Magnetically Levitated Hysteresis Motor Driven Linear Stage for In-Vacuum Transportation Tasks

by

Lei Zhou

B.S., Tsinghua University (2012)
S.M., Massachusetts Institute of Technology (2014)

Submitted to the Department of Mechanical Engineering
in partial fulfillment of the requirements for the degree of

Doctor of Philosophy in Mechanical Engineering

at the

MASSACHUSETTS INSTITUTE OF TECHNOLOGY

June 2019

Author .....
Department of Mechanical Engineering
May 18, 2019

Certified by .....
David L. Trumper
Professor
Thesis Supervisor

Accepted by .....
Nicolas G. Hadjiconstantinou
Chairman, Department Committee on Graduate Theses

Magnetically Levitated Hysteresis Motor Driven Linear Stage for In-Vacuum Transportation Tasks

by

Lei Zhou

Submitted to the Department of Mechanical Engineering
on May 18, 2019, in partial fulfillment of the
requirements for the degree of
Doctor of Philosophy in Mechanical Engineering

Abstract

This thesis presents a new in-vacuum reticle transportation mechanism for extreme ultraviolet (EUV) photolithography machines. In the photolithography process, the reticle is a quartz plate that contains a pattern of the integrated circuit, which needs to be transported between a storage position and the exposure stage. In next-generation EUV lithography machines, the reticle handling system must satisfy the following requirements: (1) transport the reticle through a distance of 2 meters, (2) the height of the mechanism needs to be within 100 mm, (3) operate in vacuum, and (4) satisfy ultra-tight contamination requirements. To fulfill these requirements, a conventional robotic reticle handler is inadequate.

In this work, we designed, built, and tested a magnetically-levitated linear stage prototype, targeting at the reticle transportation application. Compared with robot manipulators, linear stages typically require less volume for long-distance transportation tasks. Magnetic suspension is used to eliminate mechanical contact and thereby avoid particle generation that can contaminate the reticle. The stage's linear motion is driven by linear hysteresis motors, which allows using solid-steel motor secondaries on the moving stage. This is desirable for in-vacuum operation, since permanent magnets can out-gas in high vacuum when not encapsulated. The magnetic suspension of the stage is achieved using a novel linear bearingless slice motor design, where the stage's magnetic suspension in three degrees of freedom, including vertical, pitch, and roll, are achieved passively. This compact design effectively reduces the number of sensors and actuators being used. The prototype system has successfully levitated the moving stage. The resonance frequency of the passively levitated degrees of freedom is approximately 10 Hz, and the suspension bandwidth of the actively-controlled degrees of freedom is about 60 Hz. The stage's maximum thrust force is 5.8 N under a 2.5 A current amplitude, which corresponds to a stage acceleration of 1200 m/s^2. This is able to satisfy the acceleration requirement for reticle transportation task. The stage was tested to track a reticle handling reference trajectory, where the maximum position tracking error of our linear stage is 50 μm. The stage's lateral displacements

during motion is below 50 μm, which is well below making mechanical contact to the side walls. To our knowledge, this work represents the first study of linear hysteresis motors, and the first linear bearingless slice motor design.

Hysteresis motors are a type of electric machine that operates using the magnetic hysteresis effect of the secondary material. Since the magnetization in the rotor lags behind the external field, a thrust force/torque can be generated. In prior usage, hysteresis motors have been operated in open-loop, which makes them unsuitable for applications where dynamic performance is critical. As a part of this thesis work, we also studied the modeling and closed-loop torque and position control for hysteresis motors. The proposed control method was tested with three rotary hysteresis motors, including two custom-made motors of different rotor materials and one off-the-shelf hysteresis motor. Experimental results show that position control for all three motors can reach a bandwidth of 130 Hz. To our best knowledge, this is the first work that enabled high-bandwidth torque and position control for hysteresis motors, which allows this motor to be used for servo applications.

Thesis Supervisor: David L. Trumper
Title: Professor

Acknowledgments

I would like to express my greatest gratitude to my advisor Professor David L. Trumper for his guidance, support, and encouragement throughout my graduate study. I am very lucky to be able to work with him. Professor Trumper has introduced me to the research field of mechatronics, and helped me to build up the knowledge and skills. He is a great role model for me as an engineer, a researcher, and also a teacher. He has also supported me with many opportunities which were important to my professional development. It has been a great pleasure and honor working together with him.

I am grateful to my thesis committee members for their help and support. Professor Alexander H. Slocum's energy and knowledge was an inspiration to me. From him I learned a great lot about machine design, and he has also been a wonderful mentor both academically and professionally. Professor Jeffery Lang has provided valuable feedback to my thesis project. In thesis committee meetings with him, he always pointed out key problems and suggested quick solutions. These feedbacks were extremely helpful in the design for our linear stage. Professor James L. Kirtley has offered valuable discussion on the modeling and control for hysteresis motors as well as the linear stage design. He has also taught me in 6.685, which has set a foundation for my thesis work.

I would like to thank ASML for their collaboration and financial support for my doctoral study. I sincerely thank Dr. Ruvinda Gunawardana and Dr. Minkyu Kim for their constant involvement and feedback. The discussion with them was extremely helpful in defining the project, setting target functional requirements, and also the detailed design phase for our project. I would also like to thank Mark Schuster and Steve Roux for their valuable help and feedback.

I also thank my collaborators during my doctoral study. Professor Wolfgang Gruber at Johannes Kepler University Linz, Austria has gave me tremendous help and support to my thesis project. He has offered valuable inputs in the modeling and control for hysteresis motors, and has helped us with the hysteresis measurement for multiple samples. I also would like to thank Dr. Yebin Wang, who was my host during my internship at MERL. From him I learned about the sensorless control for electric machines, which provided important reference for my thesis research.

My dear labmates created a very friendly atmosphere in our laboratory and offered me

their help. Mohammad Imani Nejad was a semi-advisor for me in my masters studies. From him I learned a lot about bearingless motors and hysteresis motors. His thesis on hysteresis motors was a great resource to this project. Darya Amin Shahidi was my instructor in 2.737. From him I learned so much in control and mechatronics. Jun Young Yoon always had answers for my questions on magnetic designs and control. I enjoyed the trips that we had together to ASML in Wilton. Minkyun Noh has been a great friend whom I can bounce ideas with. I really enjoyed frequent brainstorming sessions with him. Brij Bhushan was a a great team leader in our ASPE student challenge projects, and he is also always patient and willing to help with my questions in design. Daniel Rathbone was my best buddy in 2.720. I enjoyed working together with him on our desktop lathe. Tyler Hamer has brought bright energy to our lab. The digital signal analyzer (DSA) that he developed was of great help for my work too. I would also like to thank Zhen Sun, Luis Soenksen, Joseph Church, Phillip Daniel, Austin Brown, and Benjamin Weinreb for being great friends and offering their support.

I would also like to express my gratitude to Christine Slocombe and Laura Zaganjori for their efficient and friendly help on all the administrative matters. I would also like to thank the mechanical department office staff, especially Leslie Regan. I would like to thank my dear friends with whom I have spent many hours together. They have made my life a lot more interesting and enjoyable.

I am most indebted to my parents. They are my source of support, love, and encouragement, and without them I would not have been where I am at this moment. My husband, Xiangyao Yu, has been my best friend and has helped me in every step in my graduate studies. I thank him for being extremely supportive and understanding.

This work was sponsored by ASML and performed at the Massachusetts Institute of Technology.

Contents

List of Figures

List of Tables

Chapter 1

Introduction

A growing number of precision manufacturing applications require in-vacuum transportation solutions to minimize the risk of unwanted chemical reactions or contamination of the process and surrounding equipment. The design of such in-vacuum motion systems is challenging, because permanent magnets and potted motor windings need to be encapsulated to prevent out-gassing in high vacuum, which increases the system complexity. One example is reticle transportation in extreme ultraviolet (EUV) photolithography machines. In the photolithography process, the reticle is a quartz plate that contains a pattern of the integrated circuit, which needs to be transported between a storage position and the exposure stage. In next-generation EUV lithography machines, the reticle transportation system needs to satisfy the following requirements: (1) transport the reticle through a distance of 2 meters, (2) the total height of the mechanism needs to fit within 100 mm, (3) operate in vacuum, and (4) satisfy ultra-tight contamination control requirements. To fulfill these requirements, a conventional robotic reticle handler is inadequate.

Targeting at the reticle transportation application, this thesis presents the design, building, and testing of a new concept of in-vacuum transportation mechanism using a magnetically-levitated linear stage. Compared with robot manipulators, linear stages typically require less volume for long-distance transportation tasks. Magnetic suspension is used for the stage to eliminate mechanical contact and thereby avoid particle generation that can contaminate the reticle. The stage uses a novel linear

bearingless slice motor design, where the magnetic suspension of the moving stage in three degrees of freedom, including vertical, pitch, and roll, is achieved passively. The linear stage is derive with linear hysteresis motors. Such a linear stage design allows contact-free transportation in vacuum with a simple stage design, which shows promise for being used in in-vacuum transportation applications for manufacturing systems.

The rest of this chapter is organized as follows: Section 1.1 introduces background for this research, including a quick introduction to the photolithography process and the reticle transportation task. Section 1.2 presents a literature review of related works, including both reticle/wafer handling systems and magnetically-levitated linear stages. Finally we outline an overview of this thesis and list the main contributions in Section 1.3.

1.1 Background

Photolithography is a critical manufacturing technology in the semiconductor industry. In the photolithography process, a master pattern on a quartz substrate, which is often referred as the mask or reticle, is transferred onto a silicon wafer via ultra-violet light exposure. In a scanner, both the reticle and the wafer are moving relative to each other and the lenses, and the exposure is happening as both the wafer and the reticle pass through a slit of light [15]. Typically a semiconductor chip can contain 10-100 layers, and each layer uses a different reticle for its patterning. The reticles are stored in the lithography scanner in a storage position called the reticle library, and are transported between the storage position and the exposure stage through a reticle handling system. Robot manipulators are typically used for this reticle handling task in scanners to date.

In the 2010s, extreme ultraviolet (EUV) lithography scanners began to be developed to satisfy the increasing demand for finer resolution in chips. EUV scanners use radiation of wavelength 13.5 nm for the exposure, thereby offering significant improve-

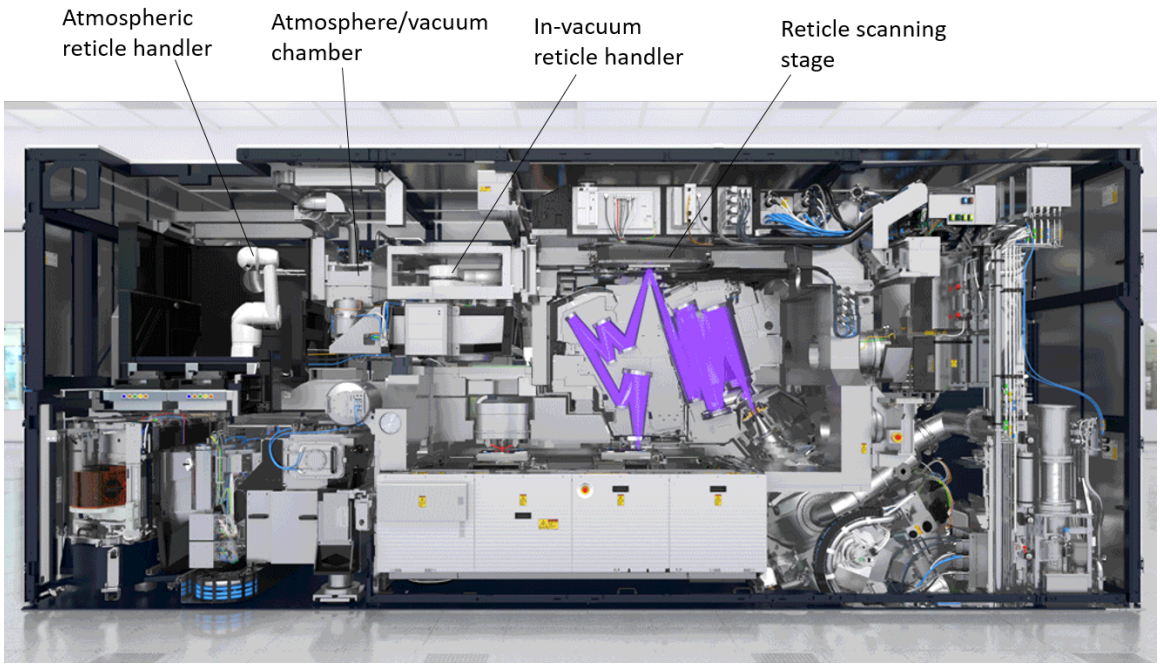

Figure 1-1: Reticle handling system in an EUV photolithography scanner from ASML. Picture of scanner is taken from www.asml.com.

ment in resolution comparing with the state-of-the-art 193 nm immersion lithography systems (deep UV scanners) [16]. The use of the EUV, however, imposes many infrastructure challenges to the scanner design. For example, the 13.5 nm wavelength EUV cannot penetrate though media such as air. As a result, the exposure process needs to happen in a vacuum chamber. In this chamber, a low pressure nitrogen atmosphere is used and circulating in the chamber mainly for particle control purposes. Such requirements, together with many other new challenges brought by the use of EUV, makes the design for the EUV scanner significantly more complex than the past-generation lithography scanners.

In the EUV photolithography scanner, the reticle handling system also needs to fulfill a series of new challenges. The reticle library is typically in atmosphere, while the scanning is happening in vacuum. Therefore the reticle handling system needs to transport the reticle between the two environments. In addition, mechanical contact and out-gassing are not allowed during the handling, especially in the vacuum environment, to prevent contamination of the reticle. Figure 1-1 shows a view of the reticle handling system in a current EUV lithography scanner from ASML. Here,

two robot manipulators are used in the reticle handling system. The reticle and its container (often referred as the reticle pod) are taken from the storage position by an atmospheric robot arm and are sent to an atmosphere-to-vacuum chamber. Then the chamber closes its doors and pulls to vacuum. After that, the chamber opens its door on the other side, and an in-vacuum robot arm is used to pick up the reticle from the pod and handle it to the reticle scanning stage. After scanning, the reticle is handled back to the reticle library using the same system in a reversed order. In such a way the reticle is able to be transported between the scanning stage in vacuum and the reticle library in atmosphere.

In the next generation EUV scanners, the design of the reticle handling system needs to face new challenges. The vision is that the distance between the reticle library and the scanning stage is as long as 2 meters, and the reticle must be transported in vacuum through a channel that is 500 mm in width and 100 mm in height. Such a new reticle handling system will have a reduced volume, and the saved space can be used for other subsystems in the lithography scanner. This new volume constraint add a lot of difficulties to the design for the reticle handling system, since robot manipulators typically have low stiffness and low-frequency dynamics for this large motion range. This thesis aims to explore an alternative solution for the reticle handling task that can satisfy this new volume requirement, and is contamination-free and vacuum-compatible at the same time.

1.2 Related Works

In this section we present a literature review of related prior works, including both reticle/wafer handling systems for semiconductor manufacturing, and magnetically-levitated linear stage for transportation and precision positioning systems.

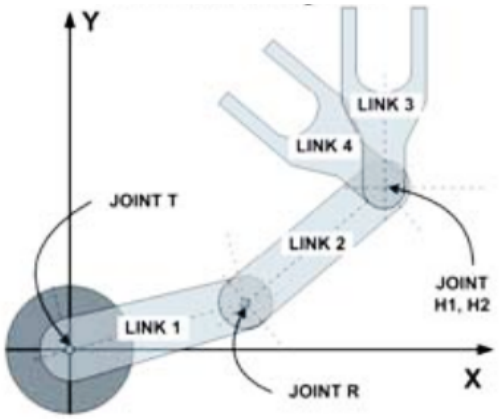

Figure 1-2: Diagram of a typical SCARA robot. Figure taken from [1].

1.2.1 Reticle/Wafer Handlers

In this section, we introduce prior art reticle and wafer handling systems for semiconductor manufacturing. Typically reticle and wafer handling in lithography scanners uses robot manipulators with SCARA-type kinematics, where SCARA stands for selective compliance assembly robot arms. Figure 1-2 shows a diagram of SCARA arm, which is taken from [1]. The SCARA configuration uses an articulated robot arm and operates in cylindrical coordinates. The arm is rigid in the vertical direction while actively controlled with joint torques in the horizontal plane. In addition, SCARA-type arms allow for a low profile, which is advantageous for highly constrained volumes, and thus makes these robots suitable for semiconductor manufacturing. Often the robot uses a frog-leg-like linkage design for stiffness purposes, and often dual robots are used for throughput improvement. Figure 1-3 shows pictures of several reticle or wafer handling robots from different manufacturers. Patent literature reporting design of various robots for semiconductor manufacturing includes [17–21].

Reticle and wafer handling devices that are not using robots have also been studied. Figure 1-4 shows a magnetic conveyor system for wafer or reticle handling designed by J. Totsch et al [2]. In this design, a moving stage is passively magnetically levitated in vertical, roll, and pitch modes using permanent magnets. The edges of the stage are in mechanical contact with the side walls. Such contact constrains the stage's position in the lateral and yaw degrees of freedom, which are magnetically

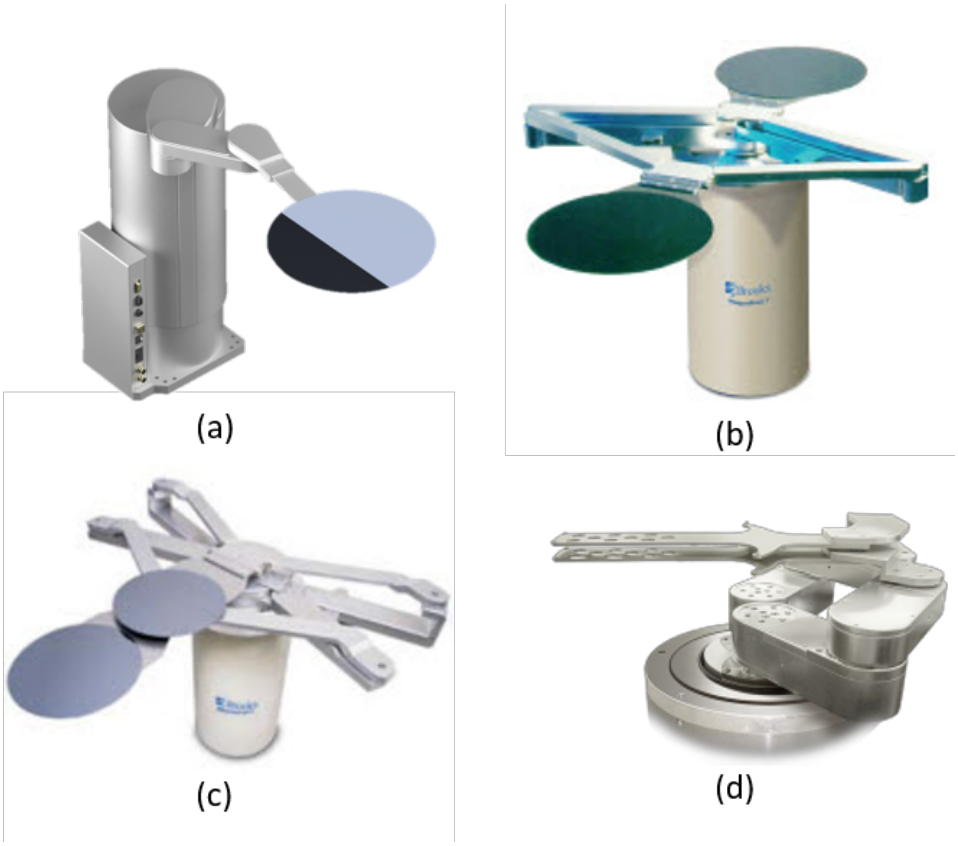

Figure 1-3: Pictures of several different robots for reticle or wafer handling. (a) RR756 SCARA atmospheric robot from Rorze. (b) MagnaTran^{TR}7 BiSymmetrik^{TR} vacuum robot from Brooks Automation. (c)MagnaTran^{TR} 7 Leapfrog^{TR} vacuum robot from Brooks Automation. (d) GPR-SMV vacuum robot from Genmark Automation.

unstable. The stage is driven passively by a magnetic coupling through the permanent magnets on the bottom of the stage and another magnetic piston beneath the stage, as shown in Figure 1-4(b). When the piston is moved along the motion direction, the attractive force between the piston and the stage can pull the stage to move in the same direction. The motion of the piston is controlled via the pressure difference between the two sides in the tube. Such a design can transport the payload in a cleanroom environment without directly driving the stage. Similar inventions include [22, 23].

Figure 1-5 shows another wafer transportation system design using a permanent magnet screw for driving. Here Figure 1-5(a) and (b) show the magnetic screw for driving the motion for the stage. There are two magnetic lead screws coupling with

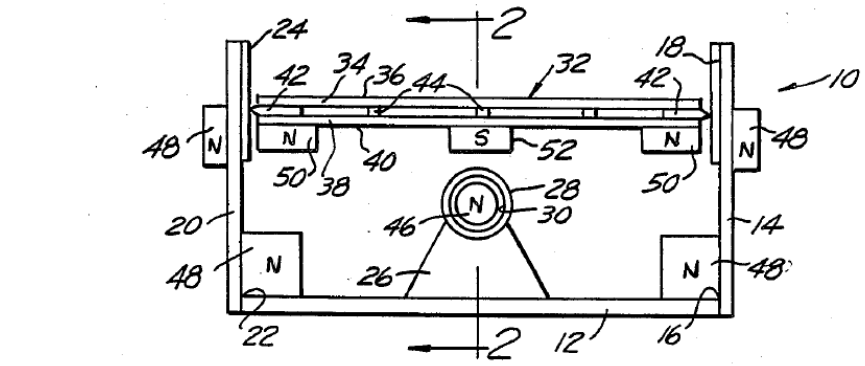

(a)

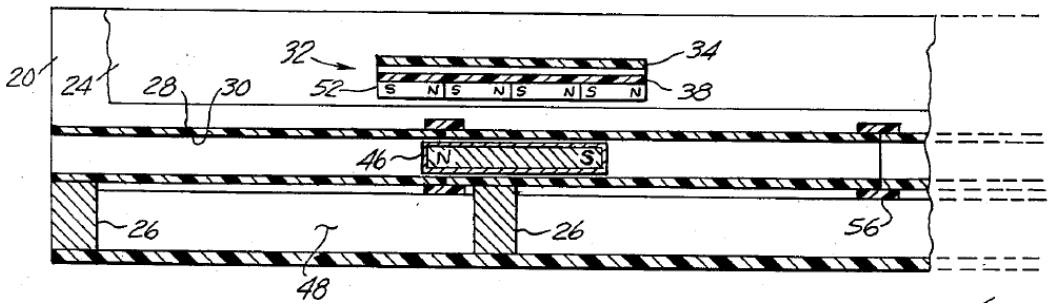

(b)

Figure 1-4: Schematic diagram of a magnetic conveyor system for wafer or reticle invented by J. Totsch. Figures are taken from [2]. (a) Front cross-section view. (b) Side cross-section view.

magnetic nuts. Driving the two lead screws in common-mode and differential, the motion of the stage and the yaw degree of freedom of the stage can be controlled. In addition, the stage uses a combination of active and passive magnetic bearings to levitate the stage and thus eliminate mechanical contact between the stage and the walls of the chamber, as shown in Figure 1-5(c).

Wafer and reticle transportation using direct-drive linear motors has also been studied. Figure 1-6 shows a wafer transportation linear stage presented by D. Belna in [4]. Here, the stage is magnetically-levitated by V-shaped magnetic bearings as shown in Figure 1-6(a), which compensates the weight of the stage and stabilizes it in all degrees of freedom except for the motion direction. The bottom of the stage is conductive, and a stator configured underneath the stage interacts with the stage for

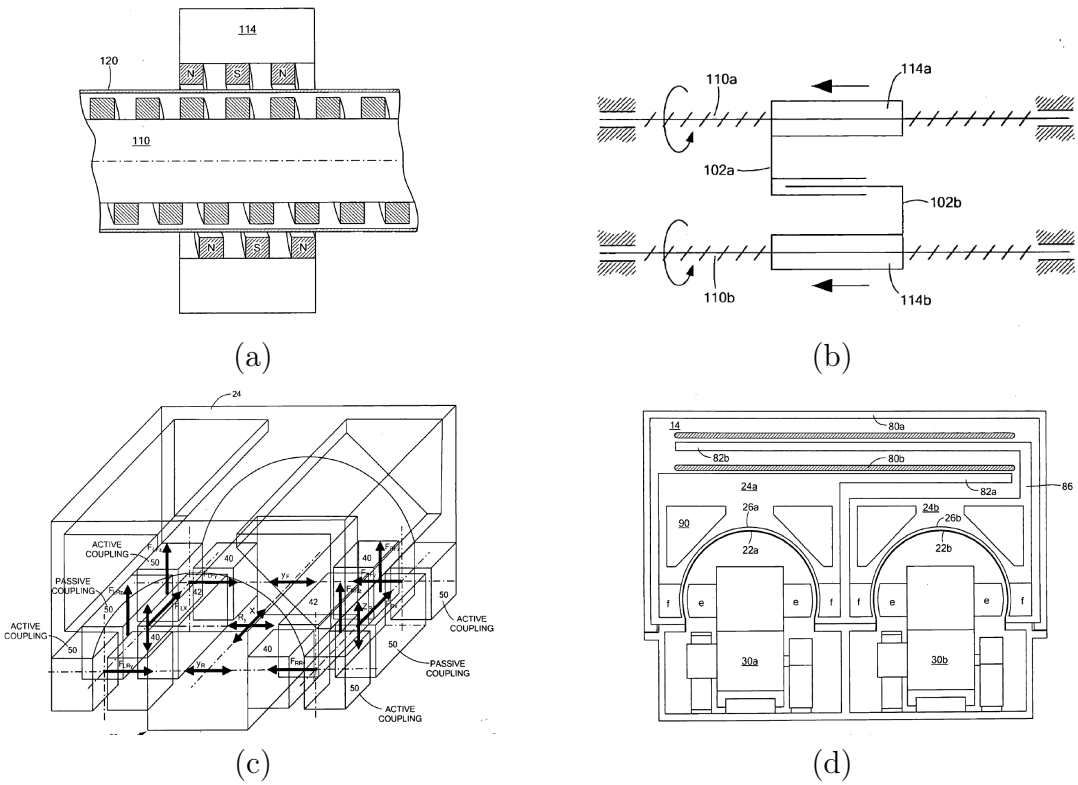

Figure 1-5: Schematic diagram of a in-vacuum wafer transportation system for invented by M. Hosek. Figures are taken from [3]. (a) Magnetic screw. (b) Motion driving principle. (c) Suspension in different degrees of freedom. (d) Cross-section view of full stage.

thrust force generation using a linear induction motor principle. Such a transportation stage resembles the configuration for magnetically-levitated trains for ground transportation. Studies on similar reticle/wafer transportation systems include [24, 25].

1.2.2 Magnetically-Levitated Linear Stages

Through the years, a number of works have reported different designs for magnetically-levitated linear or planar stages. The major application for these stages include precision manufacturing applications such as wafer and reticle scanning, and transportation and conveyance in manufacturing processes. This section discussies prior work on magnetically-levitated linear stages. According to their driving force generation principle, these stages can be categorized into: (1) permanent-magnet-motor-driven stages, (2) reluctance-motor-driven stages, and (3) induction-motor-driven stages.

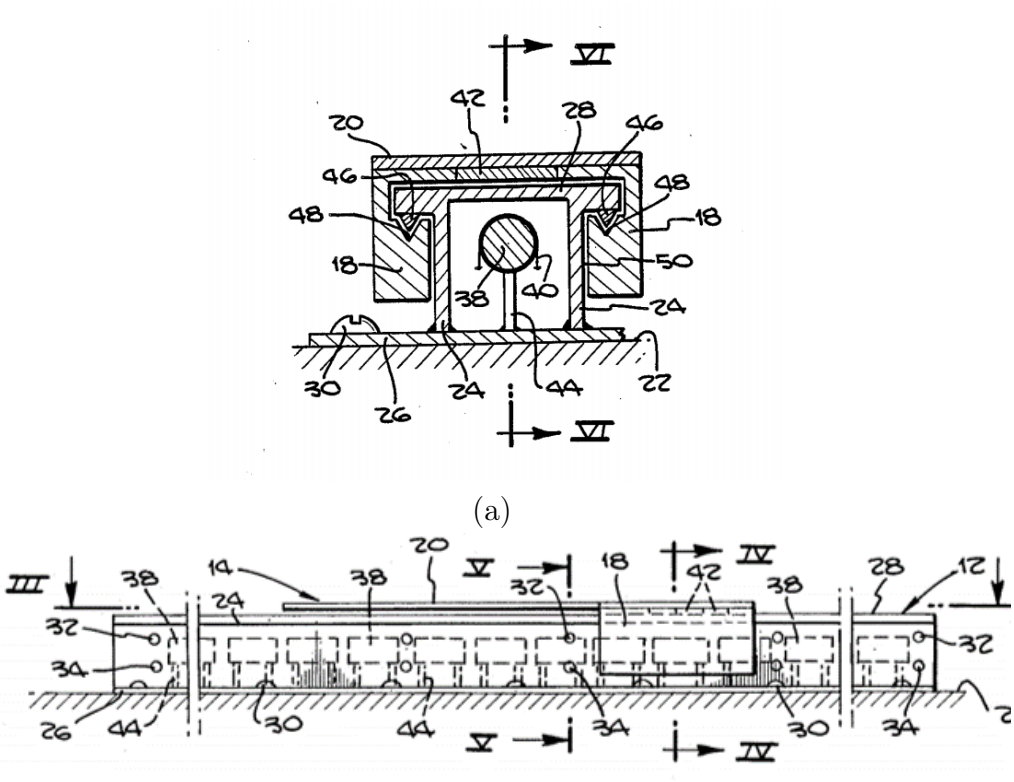

Figure 1-6: Schematic diagram of a wafer/reticle transportation system driven by linear induction motor invented by D. Belna. Figures are taken from [4]. (a) Front ross-section view of the stage. (b) Linear induction motor for driving the stage.

Permanent Magnet Motor Driven Stages

The first group of the stage designs uses linear permanent magnet synchronous motors as the driving force generation principle. These stages typically have high precision and bandwidth, and can be used for precision applications such as wafer steppers in lithography scanners. Figure 1-7 shows a magnetically-levitated planar motor designed by W. Kim and D. Trumper in [5]. In this design, four permanent magnet arrays are configured on the bottom of the moving stage, and each magnet array is interfacing with a stator on the bottom of the stage, as shown in Figure 1-7(a). Figure 1-7(b) shows a cross-section diagram of the linear motors in the stage. Each linear motor can control the thrust force and normal force generation, and all four linear motors working together can achieve the stage's magnetic suspension and motion control in all degrees of freedom. Recent work [6] by X. Lu extended this design to a long-stoke

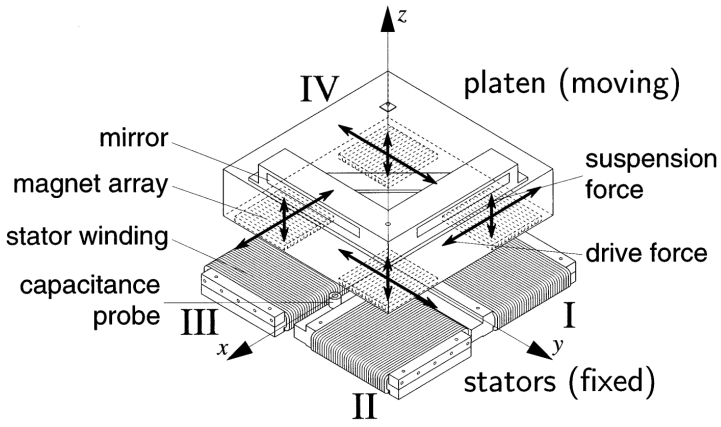

(a)

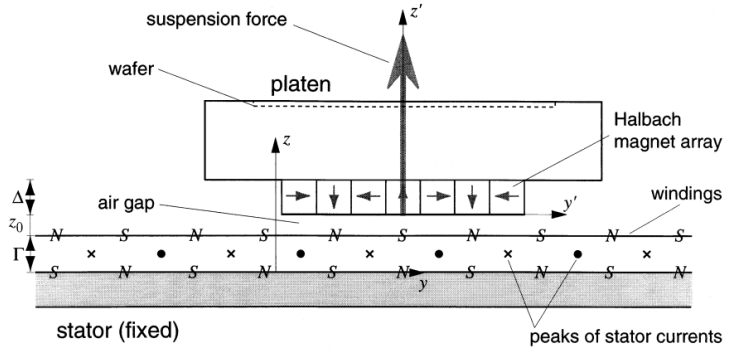

(a)

Figure 1-7: Schematic diagram of a magnetically-levitated linear stage designed by W. Kim and D. Trumper. Figures taken from [5]. (a) Perspective view diagram of the stage. (b) Linear motor and its force generation principle.

magnetically-levitated planar stage, where the stator is manufactured using printed circuit board. Figure 1-8 shows a diagram of the long-stroke magnetically-levitated planar motor design in [6]. Figure 1-9 shows another permanent magnet motor-driven planar stage design [7], where a checkerboard Halbach permament magnet array is used, and the stator coils and the magnet array are at an angle of 90 degrees.

Reluctance Motor Driven Stages

The second type of magnetically-levitated stages are driven by variable reluctance motors, where the motor secondary is made of magnetically highly permeable material and has saliency. Variable reluctance motors have the advantage of simplicity

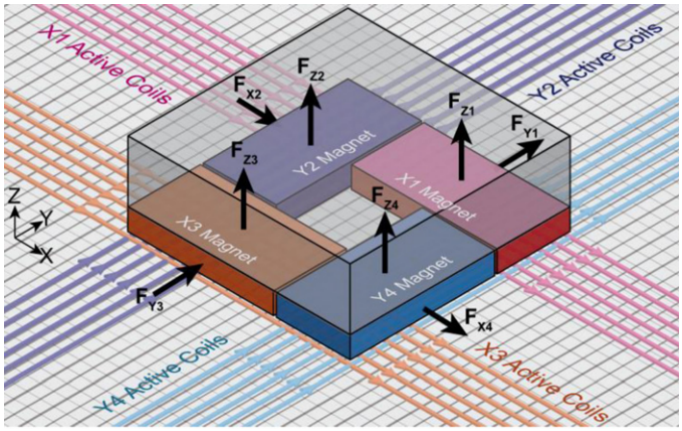

Figure 1-8: Schematic diagram a magnetically-levitated long-stroke planar motor designed by X. Lu. Figure taken from [6].

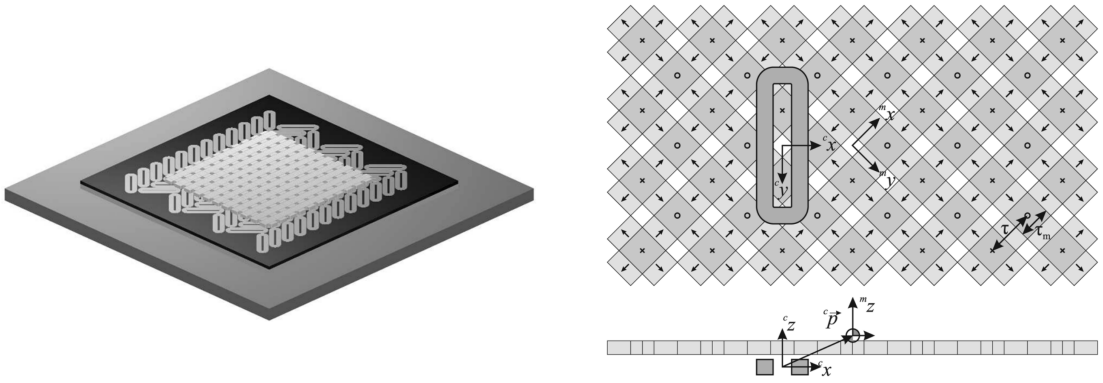

(a) (b)

Figure 1-9: A magnetically-levitated planar motor with checkerboard Halbach permanent magnet array design. Figures are taken from [7]. (a) CAD diagram of the stage. (b) Diagram of one coil and the permanent magnet array.

and ruggedness of construction, which makes these motors suitbale for general transportation uses. However they typically have large force ripple in both normal and thrust forces, which makes their integration with magnetic bearings very challenge. Figure 1-10 shows one example magnetically-levitated linear stage driven by linear reluctance motors, which is designed by Higuchi et al. [8]. Here the secondary plate on the top is made of soft magnetic material. By controlling the currents in the primary, suspension forces and thrust force can be generated.

Another early example linear stage that uses the variable reluctance motor as the driving principle is the Sawyer motor [9]. Figure 1-11 shows a schematic diagram of

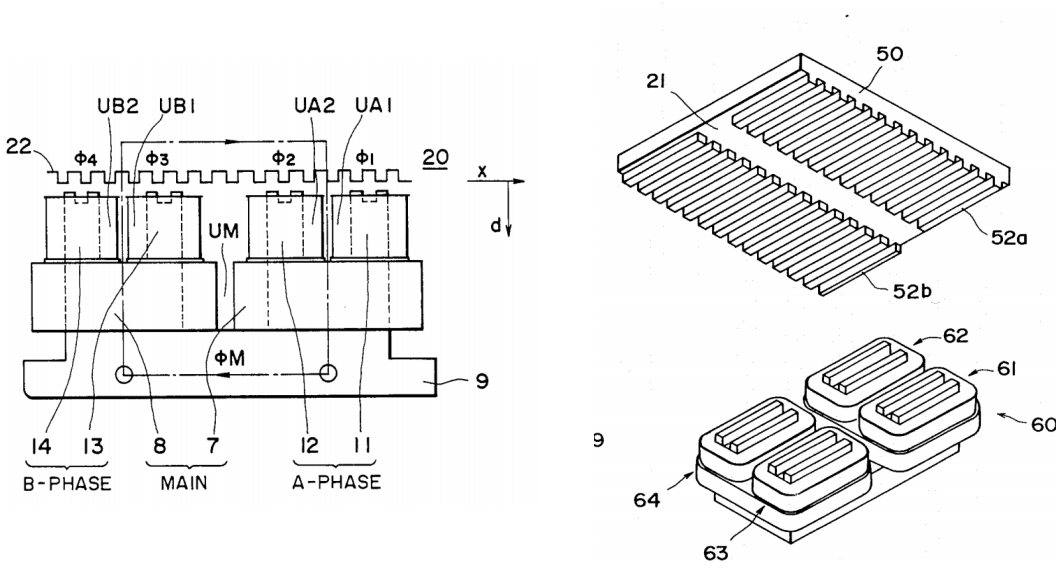

(a) (b)

Figure 1-10: A magnetically-levitated linear stage driven by variable reluctance motor designed by Higuchi et al. Figures are taken from [8]. (a) Cross-section schematic diagram of the stage. (b) Stage secondary and primary.

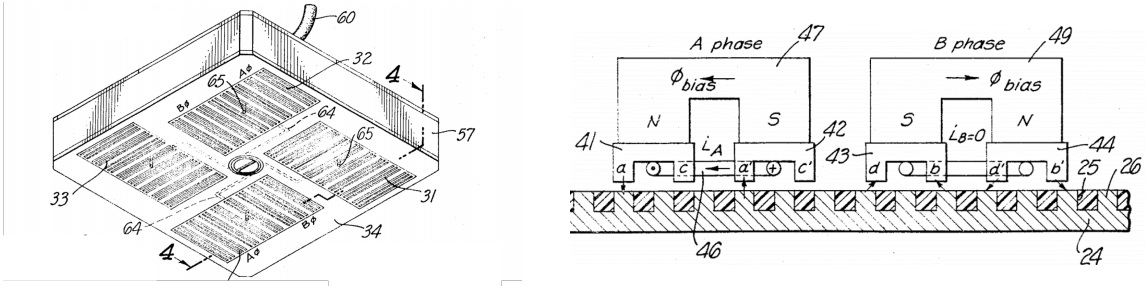

(a) (b)

Figure 1-11: A two-axis planar stage designed by B. Sawyer. Here the stage is supported by air bearings. Figures taken from [9]. (a) Primary (moving part). (b) Operating principle.

a Sawyer planar motor. The system use a secondary plate with small square pillars made of highly permeable material. The primary uses the flux steering principle for thrust force generation, as shown in Figure 1-11(b). This stage design, however, is difficult to integrate with magnetic bearings since the stage experiences a large variation in attractive force when it is operating.

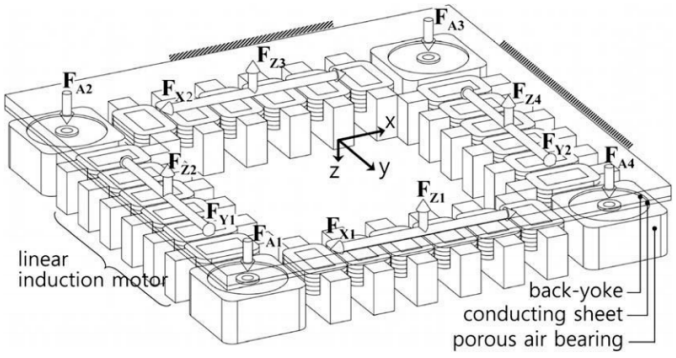

Figure 1-12: A planar stage driven by linear induction motors. Air bearings are used for supporting the stage. Figures taken from [10].

Induction Motor Driven Stages

The last group of linear stages are driven by linear induction motors. These systems are typically used for ground transportation and general conveyor systems for manufacturing applications. Linear induction motors inherently have AC force generation in both the normal and shear directions associated with the magnetic induction, which makes them difficult to be used for precision applications. One example linear-induction-motor-driven stage for wafer/reticle transportation in [4]. Other example systems include magnetically levitated trains [26–28], where typically stator coils are configured along the track, and superconducting magnets are arranged on the train. Reference [29] reports the use of magnetically-levitated linear induction motors for steel sheet conveyance in the steel painting and coating industry. Recent work [10] by KS. Jung et al. studied using linear induction motors for planar motors targeting at precision manufacturing applications, and the stage design is shown in Figure 1-12. Here the stage is supported by air bearings.

Among the prior work on magnetically-levitated linear stages, to our knowledge, there is no reported study on stages driven by linear hysteresis motors. A hysteresis motor is a kind of electric machine that uses the secondary material's magnetic hysteresis for thrust force or torque generation. These motors are typically used in open-loop and in rotary mode, and are typically limited to non-precision, open-loop,

and low-bandwidth applications. To our understanding, the reasons that to date there have been no hysteresis-motor-driven linear stage is twofold. First, there had been no developed method for controlling the thrust force or position for a hysteresis motor with relatively high bandwidth. Second, hysteresis motors typically have relatively low thrust force generation capability compared with other motor types. In this thesis work, we study the modeling and control for hysteresis motors, and present a magnetically-levitated linear stage driven by linear hysteresis motors. This work can potentially extend the application areas for hysteresis motors, and allow them to be used in precision mechatronic systems.

1.3 Thesis Overview

This thesis presents the design, building, and testing of a magnetically-levitated linear stage, targeting reticle transportation in lithography scanners. The stage's linear motion is driven by linear hysteresis motors, which allows using solid-steel motor secondaries on the moving stage. The magnetic suspension of the stage is achieved using a novel linear bearingless slice motor design, where the stage's magnetic suspension in three degrees of freedom, including vertical, pitch, and roll, are achieved passively. This compact design effectively reduces the number of sensors and actuators being used. To our knowledge, this work represents the first study of linear hysteresis motors, and the first linear bearingless slice motor designs to date.

Another contribution of this thesis work is modeling and control for rotary and linear hysteresis motors. In the past, typically hysteresis motors were operated in open-loop, which makes them unsuitable for applications where dynamic performance is critical. As a part of this thesis work, we also studied the modeling and control for hysteresis motors. To our best knowledge, this is the first work that enables the high-bandwidth torque and position control for hysteresis motors, which allows this motor to be used for servo applications.

The rest of this thesis is organized as follows:

1.3.1 Hysteresis Motor Modeling and Control

Chapter 2 presents modeling and field-oriented control (FOC) for hysteresis motors, with the goal of achieving position control of hysteresis motors for servo applications. We present an equivalent circuit model for hysteresis motors that describes the motor's transient-time dynamics, and a state-space model for hysteresis motors is developed. This model is used to construct a rotor flux orientation observer for the field-oriented control for hysteresis motors. Three methods for estimating the rotor field angle are introduced. The proposed FOC-based position control method was tested with three rotary hysteresis motors, including two custom-made motors of different rotor materials and one older commercially manufactured hysteresis motor. Experimental results show that position control for all three hysteresis motors can reach a bandwidth of 130 Hz with the proposed methods. To our best knowledge, this is the first experimental study of field-oriented control and position control for hysteresis motors.

1.3.2 Linear Stage Design

Chapter 3 presents the design process of our magnetically-levitated linear stage. We first discuss the design requirements and specifications for the reticle handling task in the next-generation EUV photolithography scanners. Then we establish the design strategies including: (1) use a magnetically-levitated linear stage for the reticle transportation task, (2) use linear hysteresis motor as the driving principle, and (3) consider using passive magnetic levitation for reducing system complexity. Starting from these general strategies, we generate a variety of design concepts, and gradually narrow down to one design concept for building and testing.

1.3.3 Modeling and Analysis

Chapter 4 presents modeling for the magnetically-levitated linear stage. We first present the operating principle for the selected linear stage design concept. Figure 1-13 shows a diagram of the magnetic fluxes in the proposed linear stage system. This

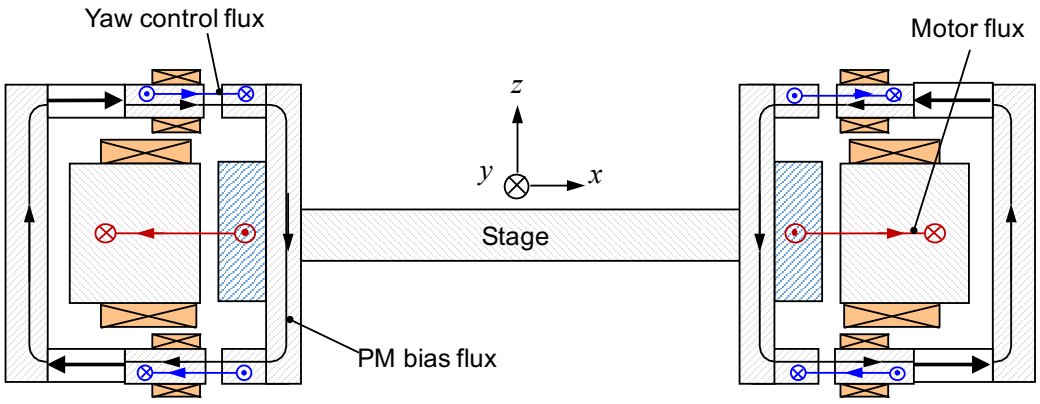

Figure 1-13: Cross section diagram of our magnetically-levitated linear stage prototype and the main magnetic fluxes.

system is configured as a linear bearingless slice motor design, where the magnetic bearing and linear motors are combined in one device, and the stage's z, θ_x, and θ_y degrees of freedom are passively stablized. The stage is driven by linear hysteresis motors in the long travel direction. Then we present a first-order analytical model for the magnetic suspension force and torque generation, which is used to guide the linear stage design. Finally, we present a finite element model for a pre-magnetized linear hysteresis motor. In this model, the pre-magnetized hysteresis secondary is modeled as a permanent magnet array, whose material property is determined by the pre-magnetization process. To our knowledge, this is the first work on modeling for pre-magnetized hysteresis motors.

1.3.4 Magnetically-Levitated Linear Stage Hardware

Figure 1-14 shows a photograph of the magnetically-levitated linear stage prototype. Chapter 5 presents the detailed design and fabrication of the prototype system, including the moving stage, stator assemblies, sensing system, power electronics, grounding and shielding, and real-time control systems.

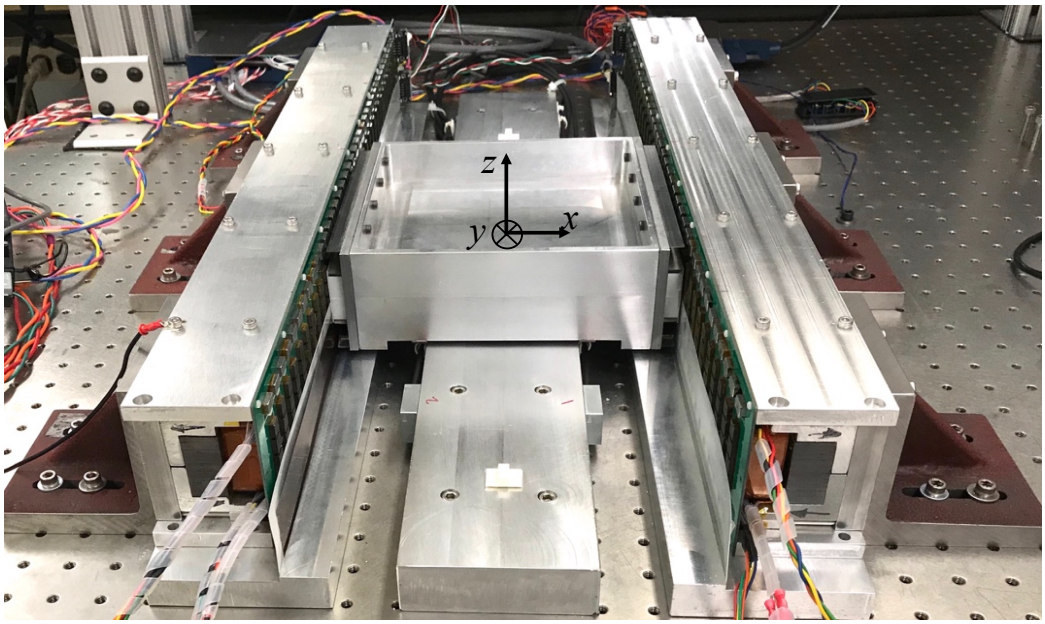

Figure 1-14: Photograph of the magnetically-levitated linear stage prototype.

1.3.5 Experimental Tests

Experimental tests for the magnetically-levitated linear stage prototype are presented in Chapter 6. The natural frequency and damping of the stage's passive magnetic suspension in vertical, pitch, and roll modes are presented. The active magnetic suspension of the stage in lateral and yaw degrees of freedom have a bandwidth of about 60 Hz. The stage's thrust force generation as a function of the stator excitation's phase is measured and compared with the model presented in Chapter 4. Good agreement between the measurement and simulation validates the model. Finally, the coupling between the stage's motion and the pitch mode is discussed and modeled, and the position control for our linear stage is tested. These tests show that our prototype is able to successfully levitate the stage, and is able to satisfy the thrust force and position control requirements.

1.3.6 Discussion and Design Variations

Although our linear stage prototype is satisfactory as a proof of concept, it still has several limitations that makes the system difficult to be used for reticle transportation

in photolithograhy scanners. In Chapter 7, we discuss the limitations for our linear stage prototype including: (1) motion and pitch mode coupling, (2) vertical mode coupled with the common-mode motor attractive force, and (3) sensing system is not vacuum compatible. Targeting at these limitations, we discuss potential methods that can improve the performance of the linear stage. We also discuss alternative system design concepts that don't have these limitations, and can potentially provide improved performance for the reticle transportation task.

Chapter 2

Rotary Hysteresis Motor Modeling and Control

As a part of this thesis, we have studied the transient-time dynamics of hysteresis motors, and propose a field-oriented control method to enable the motor's high-bandwidth torque and position control. This study forms a basis for the linear stage design and control, which uses linear hysteresis motors as the driving principle. Some content of our previously published paper [30] is partially reused in this chapter.

Among many motor drive principles, the hysteresis motor is receiving increasing attention in the past decade due to its advantages of simple structure, vibration-free operation, high rotor thermal and mechanical robustness, and self-starting capability. A hysteresis motor operates using the magnetic hysteresis of its rotor material. Since the magnetization in the rotor lags behind the external magnetizing force, a torque is generated due to the stator and rotor field interactions [31].

There are a wide range of rotor materials for hysteresis motors, including tool steel, chrome and/or cobalt alloy, AlNiCo magnets, etc. As a result, the hysteresis motor encompasses a wide range of possible constructions. Figure 2-1 shows an illustration of the motor type categorization according to the magnetic hardness of the rotor magnetic material. In this work, we study hysteresis motors of different rotor magnetic hardness using a unified framework.

The common operation state for hysteresis motors is running asynchronously in

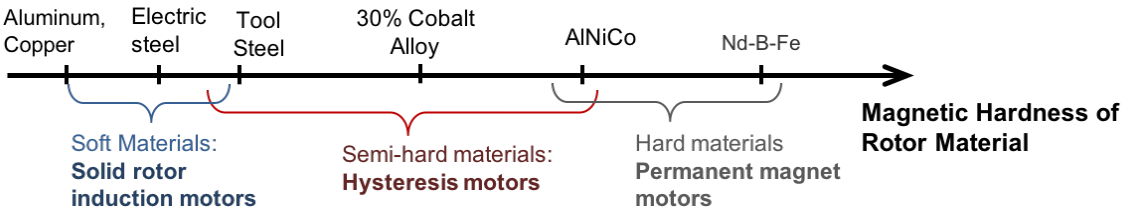

Figure 2-1: Ranges of motor concepts according to the magnetic hardness of the rotor material.

transients and synchronously in steady-state. Typical applications for hysteresis motors include tape drives [32], pumps [33,34], centrifuges [35], and flywheels [36,37]. For these operation modes, speed feedback control is typically not required, as the dynamics of a hysteresis motor are stable and robust under open-loop control. However, the open-loop dynamics of a hysteresis motor are usually relatively slow-converging and lightly damped, which makes the motor unsuitable for applications where dynamic performance is critical. This fact motivates our research for methods to control the motor's torque with high bandwidth, which is desired for some applications of hysteresis motors such as gyroscopes [38] and reaction wheels [39]. This advance can also allow hysteresis motors to be used for servo applications, which may be attractive for some special circumstances, such as high temperature or in-vacuum operations, and when smooth running and high speed is required. Prior work [40] studies sensorless field-oriented control for hysteresis motors and presents simulations of the proposed scheme. However, to our knowledge, experimental studies for field-oriented control and position control for hysteresis motors have not yet been reported in the literature.

As a part of this thesis work, we study modeling and field-oriented control to enable high bandwidth torque control for hysteresis motors, and thus enable them being used for position servo applications. The main objectives of this chapter are as follows:

1. Propose a novel equivalent circuit model that describes the hysteresis motor's transient-time dynamics, which can be used to design a real-time flux observer for hysteresis motors.

2. Introduce the field-oriented control method for hysteresis motors, and propose

Figure 2-2: Photograph of a legacy off-the-shelf hysteresis motor from Oriental Motor with the rotor taken out. The rotor consists a rotor shaft, an aluminum core, and a ring-shaped hysteresis alloy. Motor was purchased on eBay.

several approaches for rotor flux orientation estimation.

3. Experimentally test the position control method on three different hysteresis motors. Experiments show that the position control based on the proposed methods is successful for all three hysteresis motors.

To our knowledge, this work presents the first experimental study for field-oriented control and position control for hysteresis motors.

The rest of this chapter is organized as follows. Section 2.1 briefly introduces the operation principles for hysteresis motors. Section 2.2 presents the modeling for hysteresis motors. Section 2.3 focuses on the field-oriented control for hysteresis motors. Section 2.4 presents the experiments for rotary hysteresis motor control.

2.1 Hysteresis Motor Operating Principle

This section briefly introduces the operation principle of hysteresis motors. A hysteresis motor consists of a conventional poly-phase stator and a rotor of solid cylindrical or ring-shaped semi-hard magnetic material. Sometimes, the semi-hard magnetic material is in a ring around an aluminum core. Figure 2-2 shows a photograph of a legacy off-the-shelf hysteresis motor from Oriental Motor with the rotor taken out, where the hysteresis alloy forms a ring around an aluminum core. The magnetic hysteresis

effects of the rotor material causes a lag angle between the rotor magnetic field and the air-gap magnetic field, and a hysteresis torque can be generated [31]. When the rotor of the hysteresis motor is conductive, eddy current effects also contribute to the torque generation when the motor is operating asynchronously.

Figure 2-3 shows the ideal and practical hysteresis motor torque-speed curve, where T_m is the motor torque, ω_m is the motor speed, and ω_e is the electrical driving frequency. The ideal hysteresis motor demonstrates constant hysteresis torque during asynchronous operation, assuming the hysteresis lag angle equals its maximum when slip is non-zero. At synchronous speed, the motor torque can demonstrate different values, depending on the load torque and the motor excitation conditions. As a result, the ideal torque-speed curve demonstrates a torque singularity at $\omega_m = \omega_e$. In a practical hysteresis motor with a conductive rotor, eddy currents in rotor generate an additional slip-frequency dependent eddy current torque when in asynchronous operation, making the motor torque vary with the slip frequency. At the vicinity of synchronous speed, the practical hysteresis motor torque demonstrates smooth transition from the motoring mode to the generating mode. This is because that the hysteresis lag angle at the vicinity of synchronous speed is less then its maximum value, as is discussed in reference [41].

2.2 Modeling for Rotary Hysteresis Motors

2.2.1 Time Average Model of Hysteresis Motor

This section presents the equivalent circuit model for hysteresis motors. Modeling of the hysteresis motor is challenging mainly due to the nonlinearity of hysteresis material properties. Through the years, several different models have been developed to study the motor's behavior [35, 42–44]. Hysteresis motors with eddy current effects being considered have been also studied [11, 41, 43, 45].

In this work, the elliptical hysteresis loop-based model for hysteresis motors proposed in [11, 44] is used to model the motor dynamics. This model has later been

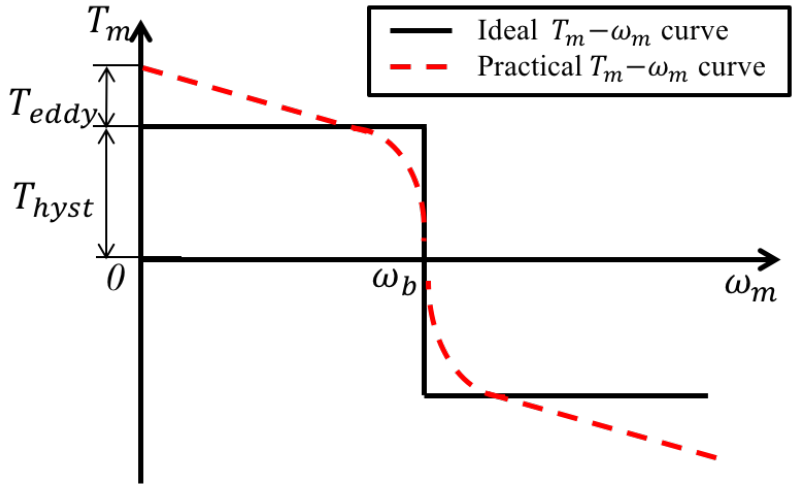

Figure 2-3: Typical single-pole-pair hysteresis motor torque-speed curve. Solid black line: ideal hysteresis motor torque-speed curve. Dashed red line: practical hysteresis motor torque-speed curve, where the effect of eddy currents is taken into account.

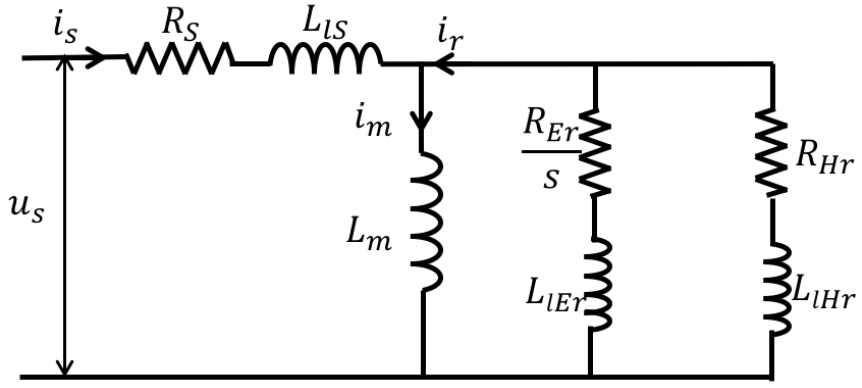

Figure 2-4: Time-average per phase equivalent circuit model for hysteresis motors as introduced in [11].

used in [46–48]. In this model, the B-H curve of the rotor material is approximated by an ellipse, as $B = B_m \cos\theta$, $H = (B_m/\mu)\cos(\theta + \delta)$, where B_m is the maximum amplitude of the flux density, μ is the permeability of the rotor material, and δ is the lag angle between field intensity H and flux density B. This model considers only the fundamental harmonics for B- and H-fields. By making μ and δ as functions of the excitation amplitude, the magnetic saturation effect can be modeled.

The elliptical hysteresis approximation allows modeling the hysteresis motor dynamics using linear circuit elements. Figure 2-4 shows the hysteresis motor equivalent

circuit model based on the elliptical hysteresis approximation with the eddy current effect considered as developed in [11]. In this model, i_s is the stator current, i_m is the magnetizing current, and i_r is the apparent rotor current. The values of the circuit elements can be calculated by

$$L_m = \frac{2m{K_w}^2 N^2 \mu_0 l r_g}{p^2 \pi g}, \tag{2.1}$$

$$R_{Hr} = \omega_e \frac{m{K_w}^2 N^2 V_r \mu}{\pi^2 {r_r}^2} \sin\delta, \tag{2.2}$$

$$L_{lHr} = \frac{m{K_w}^2 N^2 V_r \mu}{\pi^2 {r_r}^2} \cos\delta, \tag{2.3}$$

$$R_{Er} = \frac{l}{\rho A_h}, \quad L_{lEr} \approx 0. \tag{2.4}$$

Here K_w is the winding factor, m is the number of phase, p is the number of poles, r_r is mean radius of length of the magnetic field path within rotor, r_g is the mean radius of the air gap, ω_e is the reference speed, N is the number of windings per phase per pole, g is the air-gap length, l is the rotor axial length, V_r is the effective rotor volume, ρ is the specific resistivity of the rotor material, and A_h is the effective axial cross-section area of the rotor. The stator core loss is ignored in this model. Note that this model only captures the hysteresis torque of the motor when it is operating asynchronously, which is everywhere except for the "torque singularity" in Figure 2-3 at $\omega_m = \omega_e$. In order to produce a model that describes the transition from asynchronous to synchronous operation of a hysteresis motor, one needs to model the minor hysteresis loops of rotor material, which is complicated due to the nonlinearity and history-dependency of hysteresis properties. References [49] studies such a model for hysteresis motors through the finite element method.

2.2.2 Transient-Time Dynamic Model of Hysteresis Motor

The hysteresis motor equivalent circuit model shown in Figure 2-4 is a time-average model, which describes the relationships between the time-average relationships between the motor currents, fluxes and voltages. In order to design a real-time flux esti-

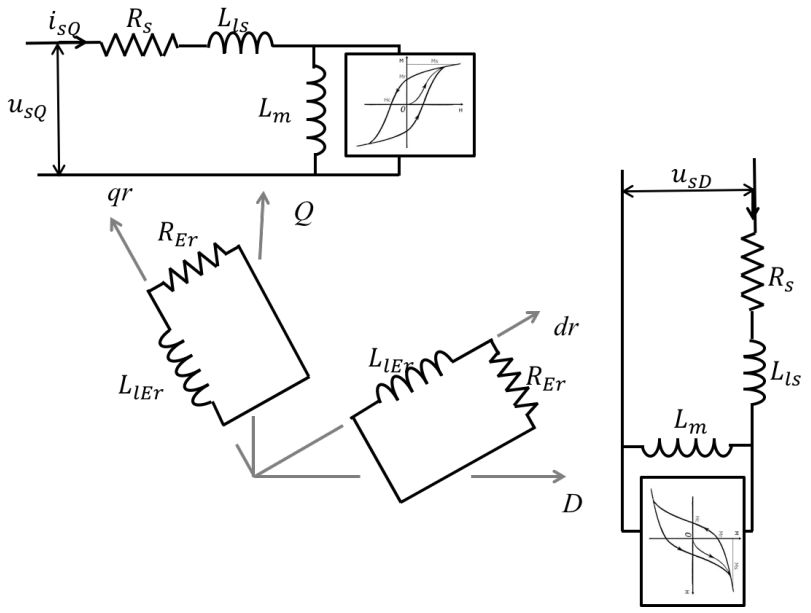

Figure 2-5: Hysteresis motor circuit diagram with hysteresis effect and eddy current effect in different coordinate systems.

mator for the motor and thus achieve a precise estimation of the rotor flux orientation, a dynamic model that describes the instantaneous current-voltage-flux relationships in a motor is needed. This model is expected to be in a form that resembles the dynamic equivalent circuit model for induction motor field-oriented control [50, 51].

The challenge of setting up a transient-time dynamic model for hysteresis motors is mainly due to the fact that the hysteresis effect and the eddy current effect need to be modeled in different reference frames. The hysteresis effect of the rotor would cause a constant lag angle between the rotor flux and the air-gap flux, and this relationship should be modeled in the stator-fixed frame. On the other hand, the eddy current effect should be modeled in the rotor-fixed frame, since the eddy currents in the rotor are created in the conductors fixed on the rotor. This separation in reference frames is depicted in Figure 2-5. This prevents us from modeling the rotor flux using unified variables as in an induction motor model.

In this work, a transient-time dynamic model for hysteresis motors with eddy current effects considered is developed. Figure 2-6 shows the transient-time equivalent circuit model for the hysteresis motor in the stationary D-Q frame. In Figure 2-6, $\boldsymbol{i_s} = [i_{sD}, i_{sQ}]^\top$ is the stator current, $\boldsymbol{i_{Hr}} = [i_{HrD}, i_{HrQ}]^\top$ is the hysteresis part

rotor current, and $\boldsymbol{i_{Er}} = [i_{ErD}, i_{ErQ}]^\top$ is the eddy current part rotor current. Define $i_m = [i_{mD}, i_{mQ}]^\top$ to be the magnetizing current as

$$\boldsymbol{i_m} = \boldsymbol{i_s} + \boldsymbol{i_{Hr}} + \boldsymbol{i_{Er}}. \tag{2.5}$$

Note that in the transient-time equivalent circuit model Figure 2-6 there are rotor speed dependent voltage sources on the eddy current part of the rotor side circuits. This is because the reference frame change for the eddy current effect relationships from the rotor-fixed frame to the stationary frame. Define $\boldsymbol{\Phi_{Hr}} = [\Phi_{HrD}, \Phi_{HrQ}]^\top$ and $\boldsymbol{\Phi_{Er}} = [\Phi_{ErD}, \Phi_{ErQ}]^\top$ as the hysteresis part and the eddy current part of the rotor flux:

$$\boldsymbol{\Phi_{Hr}} = L_m \boldsymbol{i_m} + L_{lHr} \boldsymbol{i_{Hr}}, \tag{2.6}$$

$$\boldsymbol{\Phi_{Er}} = L_m \boldsymbol{i_m} + L_{lEr} \boldsymbol{i_{Er}}, \tag{2.7}$$

and the total rotor flux is defined as

$$\boldsymbol{\Phi_r} = \boldsymbol{\Phi_{Hr}} + \boldsymbol{\Phi_{Er}} - L_m \boldsymbol{i_m}. \tag{2.8}$$

A state space model for the hysteresis motor transient-time dynamics is derived for the model given in Figure 2-5. This model is later being used to construct a flux observer for the hysteresis motor in the field-oriented control. Selecting the state variables $\boldsymbol{x} = [\boldsymbol{i_s}^\top, \boldsymbol{\Phi_{Hr}}^\top, \boldsymbol{\Phi_{Er}}^\top]^\top = [i_{sD}, i_{sQ}, \Phi_{HrD}, \Phi_{HrQ}, \Phi_{ErD}, \Phi_{ErQ}]^\top$, the state space model for the hysteresis motor transient-time dynamics is

$$\frac{\mathrm{d}}{\mathrm{d}t} \begin{bmatrix} \boldsymbol{i_s} \\ \boldsymbol{\Phi_{Hr}} \\ \boldsymbol{\Phi_{Er}} \end{bmatrix} = \begin{bmatrix} -\gamma \boldsymbol{I} & \alpha \boldsymbol{I} & \beta \boldsymbol{I} - \frac{\sigma L_m L_{lHr} \omega_r}{\kappa} \boldsymbol{J} \\ \sigma R_{Hr} L_m L_{lEr} \boldsymbol{I} & -\sigma R_{Hr} L_{Er} \boldsymbol{I} & \sigma L_m R_{Hr} \boldsymbol{I} \\ \sigma R_{Er} L_m L_{lHr} \boldsymbol{I} & \sigma L_m R_{Er} \boldsymbol{I} & -\sigma L_{Hr} R_{Er} \boldsymbol{I} + \omega_r \boldsymbol{J} \end{bmatrix} \begin{bmatrix} \boldsymbol{i_s} \\ \boldsymbol{\Phi_{Hr}} \\ \boldsymbol{\Phi_{Er}} \end{bmatrix} + \begin{bmatrix} \frac{1}{\kappa} \boldsymbol{I} \\ \boldsymbol{0} \\ \boldsymbol{0} \end{bmatrix} \boldsymbol{u_s} \tag{2.9}$$

Here R_s is the stator resistance, L_m is the mutual inductance, L_{ls} is the stator leakage

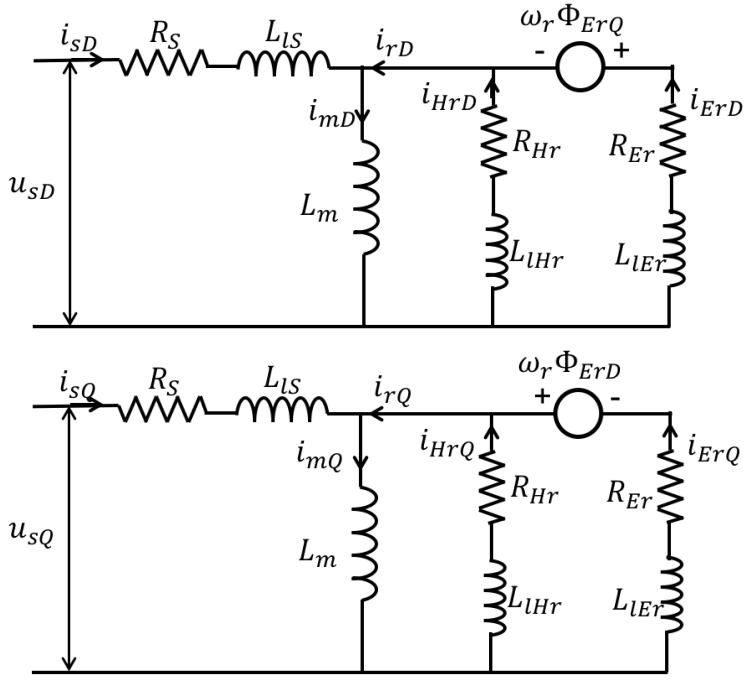

Figure 2-6: Transient time equivalent circuit modtel for hysteresis motors including the eddy current effect in the stationary D-Q frame.

inductance, R_{Hr} and R_{Er} are the rotor side hysteresis and eddy current resistances, and L_{lHr} and L_{lEr} are the hysteresis and eddy current part rotor leakage inductances. Further, $L_s = L_m + L_{ls}$ is the total stator side inductance, $L_{Hr} = L_m + L_{lHr}$ and $L_{Er} = L_m + L_{lEr}$ are the hysteresis part and eddy current part total inductances. The rest of the parameters are defined by

$$\sigma = 1/(L_{Hr}L_{Er} - L_m^2), \tag{2.10}$$

$$\kappa = L_s - \sigma L_m^2(L_{lEr} + L_{lHr}), \tag{2.11}$$

$$\gamma = \Big(R_s + \sigma^2 L_m^2(L_{lEr}^2 R_{Hr} + L_{lHr}^2 R_{Er})\Big)/\kappa, \tag{2.12}$$

$$\alpha = \Big(\sigma^2 L_m(R_{Hr}L_{Er}L_{lEr} - R_{Er}L_m L_{lHr})\Big)/\kappa, \tag{2.13}$$

$$\beta = \Big(\sigma^2 L_m(R_{Er}L_{Hr}L_{lHr} - R_{Hr}L_m L_{lEr})\Big)/\kappa. \tag{2.14}$$

The derivation of the model in (2.9) is presented below. In an elementary model of the hysteresis motor model, the stator flux $\boldsymbol{\Phi_s} = [\Phi_{sD}, \Phi_{sQ}]^\top$, hysteresis part rotor flux $\boldsymbol{\Phi_{Hr}} = [\Phi_{HrD}, \Phi_{HrQ}]^\top$, and eddy current part rotor flux $\boldsymbol{\Phi_{Er}} = [\Phi_{ErD}, \Phi_{ErQ}]^\top$

are defined as

$$\boldsymbol{\Phi_s} = L_{ls}\boldsymbol{i_s} + L_m\boldsymbol{i_m}, \tag{2.15}$$

$$\boldsymbol{\Phi_{Hr}} = L_m\boldsymbol{i_m} + L_{lHr}\boldsymbol{i_{Hr}}, \tag{2.16}$$

$$\boldsymbol{\Phi_{Er}} = L_m\boldsymbol{i_m} + L_{lHr}\boldsymbol{i_{Er}}. \tag{2.17}$$

The stator-side voltage balance equation is given by

$$\boldsymbol{u_s} = \frac{\mathrm{d}}{\mathrm{d}t}\boldsymbol{\Phi_s} + R_s\boldsymbol{i_s}. \tag{2.18}$$

The rotor side voltage balance includes two parts. The hysteresis part voltage balance relation is in the stationary frame, as

$$\boldsymbol{u_{Hr}} = \mathbf{0}_{2\times1} = \frac{\mathrm{d}}{\mathrm{d}t}\boldsymbol{\Phi_{Hr}} + R_{Hr}\boldsymbol{i_{Hr}}, \tag{2.19}$$

where $\mathbf{0}_{2\times1} = [0,0]^\top$. The eddy current part voltage balance relationship is in the rotor-fixed frame, which is similar to that of an induction motor [51]. The equation is given by

$$\boldsymbol{u_{Er}} = \mathbf{0}_{2\times1} = \frac{\mathrm{d}}{\mathrm{d}t}\boldsymbol{\Phi^r_{Er}} + R_{Er}\boldsymbol{i^r_{Er}}, \tag{2.20}$$

where $\boldsymbol{i^r_{Er}} = [i^r_{Erd}, i^r_{Erq}]^\top$ is the vector of the eddy current part of the rotor current in the rotor-fixed d-q frame. These equations are consistent with the equivalent circuit model of the hysteresis motor shown in Fig. 2-5, where the eddy current effect and hysteresis effect are in different coordinate frames.

The transform of the equation from the rotor-fixed d-q frame to the stationary D-Q frame can be done through

$$\boldsymbol{Z} = \boldsymbol{T}\boldsymbol{Z}^r, \tag{2.21}$$

where $\boldsymbol{Z}$ is a dummy variable which can represent flux or current, and the transfor-

mation matrix $\boldsymbol{T}$ is defined as

$$\boldsymbol{T} = \begin{bmatrix} \cos(\omega_r t) & -\sin(\omega_r t) \\ \sin(\omega_r t) & \cos(\omega_r t) \end{bmatrix}, \tag{2.22}$$

where ω_r is the rotor speed, and t is the time. Substituting (2.21), (2.22) into (2.20), and writing the equation in matrix form yields

$$\begin{aligned} \frac{\mathrm{d}}{\mathrm{d}t}\begin{bmatrix} \Phi_{ErD} \\ \Phi_{ErQ} \end{bmatrix} &= \begin{bmatrix} \cos(\omega_r t) & -\sin(\omega_r t) \\ \sin(\omega_r t) & \cos(\omega_r t) \end{bmatrix} \left(\frac{\mathrm{d}}{\mathrm{d}t}\begin{bmatrix} \Phi_{Erd} \\ \Phi_{Erq} \end{bmatrix} \right) \\ &\quad + \omega_r \begin{bmatrix} -\sin(\omega_r t) & -\cos(\omega_r t) \\ \cos(\omega_r t) & -\sin(\omega_r t) \end{bmatrix} \begin{bmatrix} \Phi_{Erd} \\ \Phi_{Erq} \end{bmatrix} \\ &= -\begin{bmatrix} R_{Er} & 0 \\ 0 & R_{Er} \end{bmatrix} \begin{bmatrix} i_{ErD} \\ i_{ErQ} \end{bmatrix} - \omega_r \begin{bmatrix} -\Phi_{ErQ} \\ \Phi_{ErD} \end{bmatrix}. \end{aligned} \tag{2.23}$$

Equations (2.15)-(2.19) and (2.23) fully describe the transient dynamics of a hysteresis motor with the eddy current effect being considered. There are six independent dynamic equations: (2.18), (2.19), and (2.23), and six independent variables. One can derive a state-space model for the hysteresis motor by selecting a set of state variables, and eliminating all other variables. Many different state variable selections can be made, with the model representing the same dynamics. By selecting the set of state variables as $\boldsymbol{x} = [\boldsymbol{i_s}^\top, \boldsymbol{\Phi_{Hr}}^\top, \boldsymbol{\Phi_{Er}}^\top]^\top$, the state-space model (2.9) can be derived.

2.3 Field-Oriented Control for Hysteresis Motor

The field-oriented control for hysteresis motors is similar to that of the other motor types. Figure 2-7(a) shows a vector diagram of the variable relationships . In Figure 2-7(a), D-Q is the stationary two-phase frame, and d-q is the rotor flux-oriented frame, where the d-axis is aligned with the rotor flux linkage, and the q-axis is perpendicular to the d-axis. Vector i_s represents the stator phase currents, and Φ_r is the rotor flux vector. Figure 2-7(b) shows a block diagram of the position control for the hysteresis

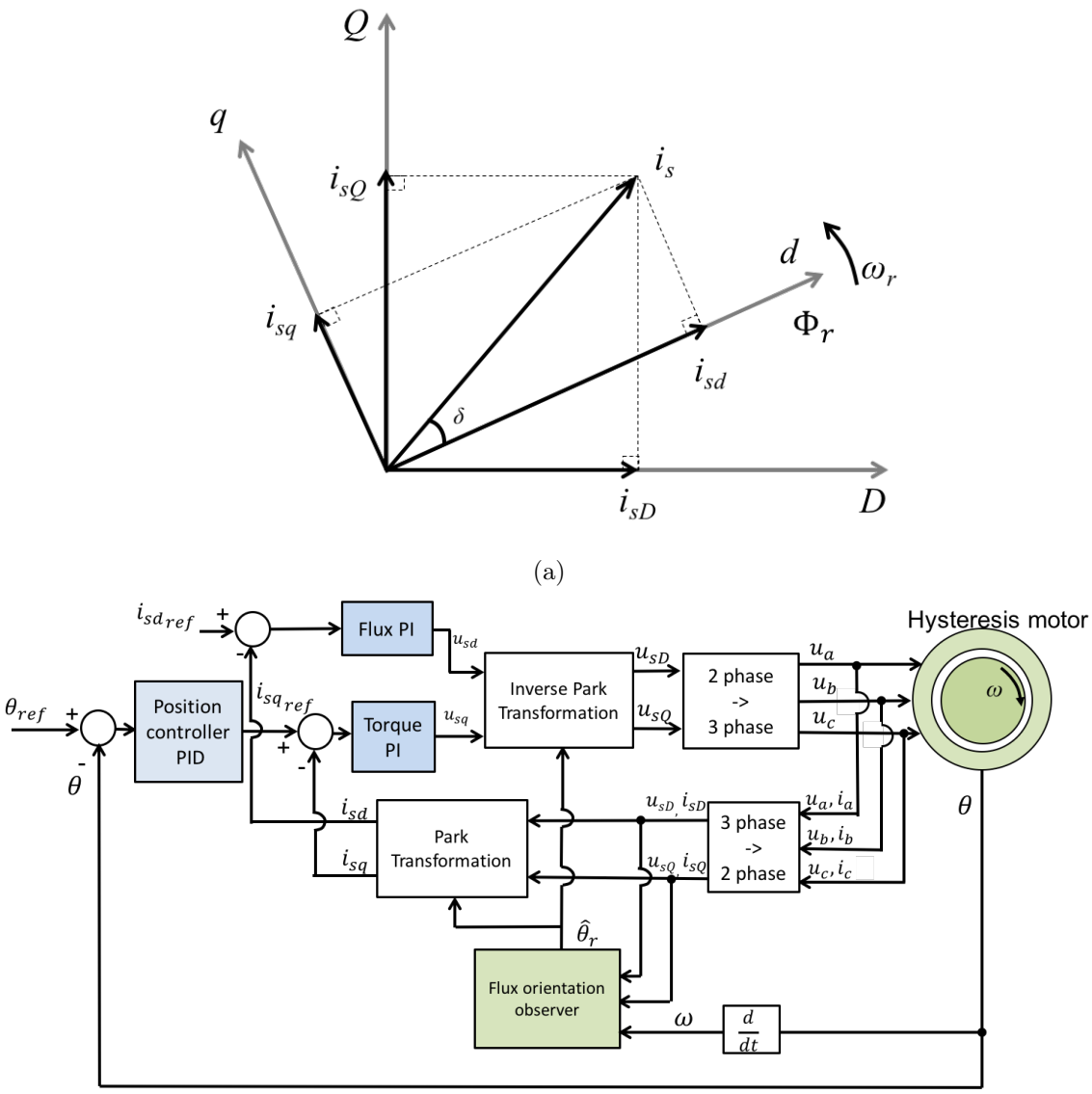

Figure 2-7: Vector diagram and block diagram of hysteresis motor position control via the field-oriented control approach. (a) Vector diagram of hysteresis motor field-oriented control. (b) Block diagram of hysteresis motor position control. The blue-shaded blocks are the PID position controller and PI current controller.

motor via field-oriented control. In Figure 2-7(b), the motor's angular position, the motor terminal currents and voltages are also measured and used to reconstruct the flux orientation through a flux orientation estimator. With the estimated rotor flux angle $\hat{\theta}$, the measured currents are transformed into the rotor flux-oriented d-q frame and are then used for current control. The reference of d-axis current is set to be

a constant. The measured motor angular position is fed-back through a position controller, and the control effort signal is set to be the reference signal for q-axis current. The two current control effort signals u_{sd} and u_{sq} are then transformed back to the stationary three-phase frame and energize the stator windings.

The most challenging element in the field-oriented control for hysteresis motors is the rotor flux orientation estimator. The flux angle estimation accuracy directly influences the motor control performance. There are three approaches to obtain an estimate of the rotor flux angle proposed in this work, as introduced below.

2.3.1 Approximate with Motor Mechanical Angle

The simplest method to obtain an estimate for the flux angle is to directly use the measured rotor angular position, as $\hat{\theta} = \theta_r$, where θ_r is the rotor's mechanical angle. This method assumes that the magnetization is fixed on the rotor surface, which resembles the case of a permanent magnet motor. Over-exciting the motor by a large d-axis current at the starting up of the motor as introduced in [52] will help improve the performance of this flux angle estimation method, as the magnetization of the rotor can be fixed along the d-axis on the rotor.

2.3.2 Estimate Flux via Back-EMF Measurements

The second method uses the back-electromotive force (EMF) in the stator coils to estimate the rotor flux orientation. When the magnetized rotor is rotating, the change of the rotor field will induce a voltage in the stator winding, which is the back-EMF. The back-EMF in the stationary D-Q frame can be calculated as

$$\boldsymbol{e} = \boldsymbol{u_s} - R_s \boldsymbol{i_s} - L_{ls} \dot{\boldsymbol{i}}_{\boldsymbol{s}}. \tag{2.24}$$

An estimate for the rotor flux linkage in the stationary two-phase frame can be calculated by

$$\hat{\boldsymbol{\Phi}}_{\boldsymbol{r}} = \int \boldsymbol{e} \mathrm{d}t, \tag{2.25}$$

where $\hat{\boldsymbol{\Phi}}_{\boldsymbol{r}} = [\hat{\Phi}_{rD}, \hat{\Phi}_{rQ}]^\top$. Finally the estimated flux angle $\hat{\theta}$ can be calculated as

$$\sin\hat{\theta} = \frac{\hat{\Phi}_{rQ}}{(\hat{\Phi}_{rD}^2 + \hat{\Phi}_{rQ}^2)^{1/2}}, \quad \cos\hat{\theta} = \frac{\hat{\Phi}_{rD}}{(\hat{\Phi}_{rD}^2 + \hat{\Phi}_{rQ}^2)^{1/2}}. \tag{2.26}$$

This method provides good rotor flux orientation estimation performance when the motor speed is relatively high. However, when the motor is standing still or operating at low speed, the back-EMF signals are small and therefore the angle estimation is not accurate. As an alternative flux orientation estimation approach, a combination of the back-EMF based estimation and the rotor's mechanical angle can reach a good rotor flux angle estimation performance. One implementation of the combined flux orientation estimation is through

$$\hat{\theta} = (1 - S(|\omega_r| - \omega_r^{sw}))\theta_r + S(|\omega_r| - \omega_r^{sw})\hat{\theta}_{EMF}, \tag{2.27}$$

where $|\cdot|$ is the absolute value operation, ω_r is the rotor speed, ω_r^{sw} is a threshold rotor speed for estimation method switching, $\hat{\theta}_{EMF}$ is the flux angle estimation using the back-EMF method, θ_r is the rotor's mechanical angle measured through a position sensor, and $\hat{\theta}$ is the resultant rotor flux angle estimation. $S(x) = 1/(1 + e^{-x})$ is the sigmoid function, which is a smooth transition function from 0 to 1 at $x = 0$. Through (2.27), an angle estimation using the mechanical angle at low speed, and using the back-EMF based estimation at high speed, can be achieved.

2.3.3 Full-Order Observer

The third method of estimating the rotor flux orientation is by constructing a state observer for the hysteresis motor. Given the hysteresis motor state space model

(2.9), a full-order state observer can be designed. Rewrite the system equation (2.9) in matrix form as

$$\dot{\boldsymbol{x}} = \boldsymbol{A}\boldsymbol{x} + \boldsymbol{B}\boldsymbol{u_s}, \boldsymbol{y} = \boldsymbol{C}\boldsymbol{x}, \tag{2.28}$$

where $\boldsymbol{A}$, $\boldsymbol{B}$ are the system matrices in (2.9), $\boldsymbol{C} = [\boldsymbol{I}, \boldsymbol{0}]$ is the measurement matrix, and $\boldsymbol{y} = \boldsymbol{i_s} = [i_{sD}, i_{sQ}]^\top$ is the measurement signal. A Luenberger observer can be designed for the system as

$$\dot{\hat{\boldsymbol{x}}} = \boldsymbol{A}\hat{\boldsymbol{x}} + \boldsymbol{B}\boldsymbol{u} + \boldsymbol{L}(\boldsymbol{y} - \boldsymbol{C}\hat{\boldsymbol{x}}), \tag{2.29}$$

where $\hat{\boldsymbol{x}}$ is the estimated state, and $\boldsymbol{L}$ is the observer gain matrix. The observer dynamics is determined by the matrix $\boldsymbol{A} - \boldsymbol{L}\boldsymbol{C}$, and the design approach for Luenberger observers can be applied to design the observer gain $\boldsymbol{L}$. System (2.28) is stable in open-loop, which means $\boldsymbol{L} = \boldsymbol{0}$ will stabilize the system. Also, the motor speed ω_r is a parameter in the system dynamics (2.9). As a result, gain scheduling with ω_r being the scheduling parameter may need to be used in the design for $\boldsymbol{L}$. The system (2.28) is fully observable even when the motor is operating at zero speed.

The flux observer method provides good rotor flux angle estimation accuracy over a large speed range, and has demonstrated the best performance in the experiments among the three flux angle estimation methods. However, the estimation performance of the flux observer will significantly degrade if the model parameter errors are large. Also, this method requires full knowledge of the hysteresis properties of the rotor material, which is often not available for off-the-shelf hysteresis machines.

2.4 Experiments with Rotary Hysteresis Motors

In this work, the position control system shown in Figure 2-7 is experimentally tested with three hysteresis motors. Motor I and Motor II are custom-made hysteresis motors, which are manufactured by replacing the squirrel cage rotor in a regular three-phase induction motor with rotors made of different semi-hard magnetic materials.The

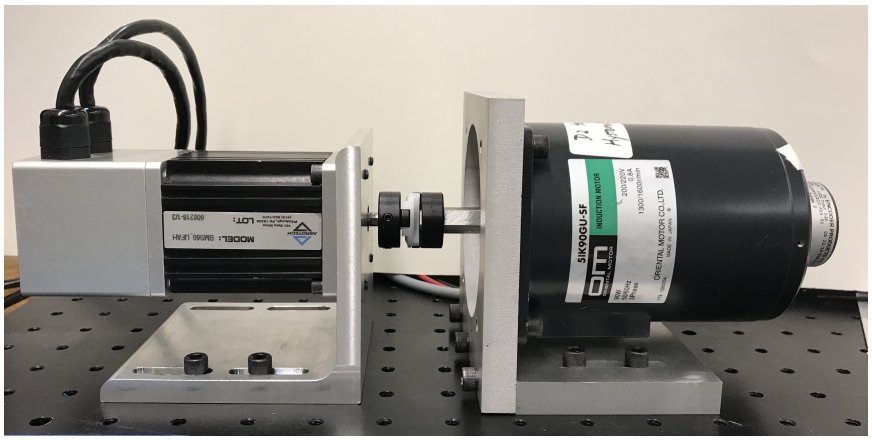

Figure 2-8: Photograph of our custom-made hysteresis motor using a 90 W induction motor stator as connected to a brushless DC load machine.

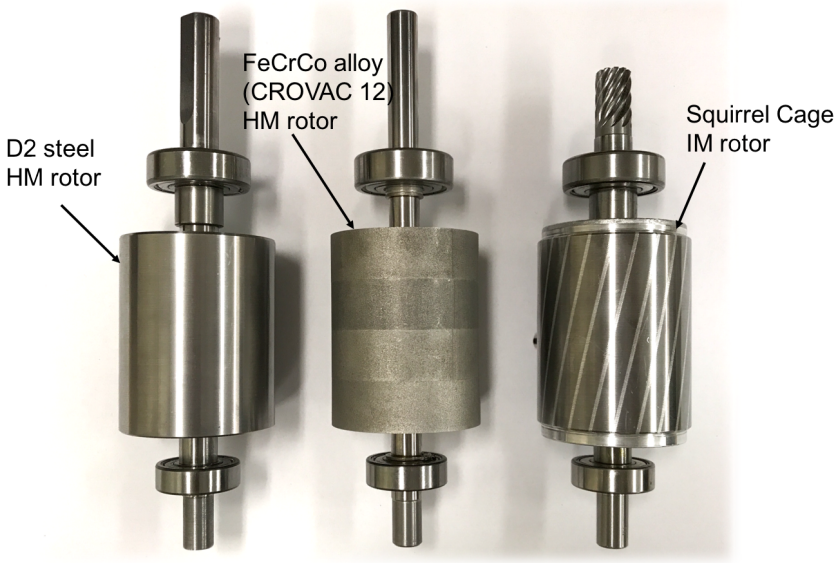

Figure 2-9: Custom-made rotors for hysteresis motors. Left: D2 hysteresis rotor for Motor I. Middle: FeCrCo alloy hysteresis rotor for Motor II. Right: the original squirrel cage rotor for the induction motor.

original induction motor is a 90 W 51K90GU-SF induction motor from Oriental Motor Co., Ltd. Motor I has a rotor made of D2 tool steel, which is a standard tool steel known for its resistance to wear. It also has relatively large magnetic hardness. Prior work studying D2 tool steel hysteresis motors include [34, 36, 39]. Motor II has a rotor of FeCrCo alloy, which is the CROVAC^{TM} 12 material from Vacuumschmeltze GmbH. Motor I and Motor II share the same stator construction and rotor geometry, and the only difference is in the rotor material. Figure 2-8 shows a photograph of the

Table 2.1: Parameters of Motor I and Motor II.

Parameter	Value
Motor power	90 W
Number of pole pairs	2
Rated voltage	200-220 V
Rated RMS current	0.8 A
Rotor diameter	47.5 mm
Air gap	0.4 mm
Number of turns per phase	8×80

induction motor stator with hysteresis rotor being tested, and Figure 2-9 shows the custom-made rotors for Motor I and II and the original rotor for the induction motor. The parameters of Motor I and II are shown in Table 2.1. The third hysteresis motor being tested, Motor III, is a commercial 250 W type GLLHNNB-3529 hysteresis motor from Elinco Inc. Figure 2-10 shows a photograph of the Motor III, and its parameters are shown in Table 2.2.

In the experiments, the hysteresis motors are driven by a PWM three-phase inverter manufactured by Linz Center of Mechatronics GmbH. The inverter operates with a DC bus voltage of 200 V. The three-phase currents of the motors are measured through shunt resistors of the inverter, and are fed back for current control. A slotless, brushless DC (BLDC) motor BMS60 from Aerotech Inc. is used as a load machine for the hysteresis motors, as is shown on the left in Figure 2-8 and Figure 2-10. The BLDC motor is driven by a current-mode linear three-phase power amplifier using a PA12 from Apex Inc., where the current controllers are implemented by analog circuits. The current control for the BLDC motor has a bandwidth of 2 kHz. A sine-cosine optical encoder on the load machine is used to measure the rotor's angular position, which can be interpolated to a resolution of 10^5 pulses per revolution. The signal of this encoder is also used for controlling the position of the hysteresis motor, and a stiff coupling is used to connect the two motors. The controllers for the hysteresis motors are implemented in LabVIEW and are downloaded to a National Instruments PXI controller with FPGA for execution. The hysteresis motor current controller, PWM signal generation, encoder interpolation, and the commutation for

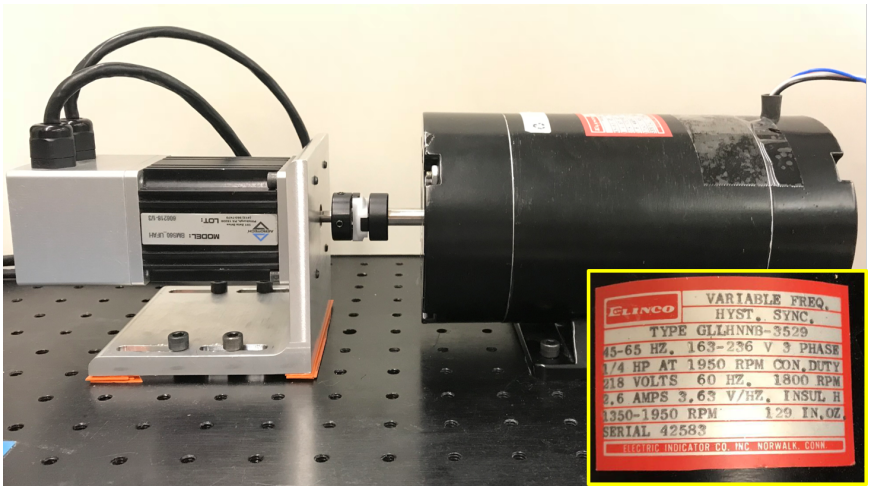

Figure 2-10: Photograph of 250 W hysteresis synchronous motor from Elinco Inc.

Table 2.2: Parameters of Motor III.

Parameter	Value
Motor power	250 W
Number of pole pairs	2
Rated voltage	163-236 V
Rated RMS current	2.6 A

the BLDC motor are implemented in the FPGA with a sampling frequency of 40 kHz, and the position controller and the flux orientation estimator are implemented in the floating point real-time control loop with a sampling rate of 10 kHz. The hysteresis motor's current control has a bandwidth of 600 Hz.

2.4.1 Hysteresis Measurement of Rotor Materials

This section presents the measurement and parametrization of hysteresis properties of the rotor materials for Motor I and Motor II: the D2 tool steel and the FeCrCo alloy. Table 2.3 shows the chemical, physical, and magnetic properties of the two rotor materials.

The B-H curves of the two rotor materials at different excitation amplitudes are measured and are shown in Figure 2-11, which is measured by Dietmar Andessner at the Linz Center of Mechatronics, GmbH. Reference [53] introduces the hysteresis measurement apparatus. It can be seen from Figure 2-11 that the FeCrCo alloy

Table 2.3: Rotor Material Properties.

Material Name	D2 steel	FeCrCo Alloy
Material chemical composition	C: 1.5%; Co: 1%; Cr: 12 %	Co: 12% Cr: 28% Mo: 1%
Conductivity	8.3×10^6 S/m	1.4×10^6 S/m
Remanence	0.85 -0.90 T	0.85 - 0.95 T
Coercitivity	1.2 - 2.3 kA/m	16-32 kA/m

has a larger magnetic coercivity than the D2 steel, while the saturation of FeCrCo alloy is lower than that of the D2 steel. Since the hysteresis torque generation of a hysteresis motor is proportional to the hysteresis loop area [31], the FeCrCo alloy hysteresis motor can potentially generate larger hysteresis torque than the D2 steel hysteresis motor, however it requires a larger H-field to fully utilize the hysteresis torque capability of the material.

There are two parameters in the elliptical hysteresis model: the permeability μ and the lag angle δ. Figure 2-12 shows the hysteresis parameters of D2 steel and the FeCrCo alloy under different B-field amplitudes. These parameters are stored in look-up tables and are used to construct the model for hysteresis motors through Eq. (2.1)-(2.4). With the two hysteresis parameters being functions of the excitation amplitude, the magnetic saturation effect can be modeled.

2.4.2 Open-loop Tests

The three hysteresis motors are first tested in open-loop, i.e. the position control loop for the motors is not closed. Under this test condition, the stator windings are energized with symmetric sinusoidal three-phase currents, and the motors are tested in a no-load condition.

Figure 2-13 presents the speed start-up curves of the three motors. In this test, the stator current zero-to-peak amplitude is 1 A for Motor I and II, and is 2.5 A for Motor III. It can be observed that the speed data of Motor II and Motor III demonstrates a larger speed oscillation amplitude than that of the Motor I, which is

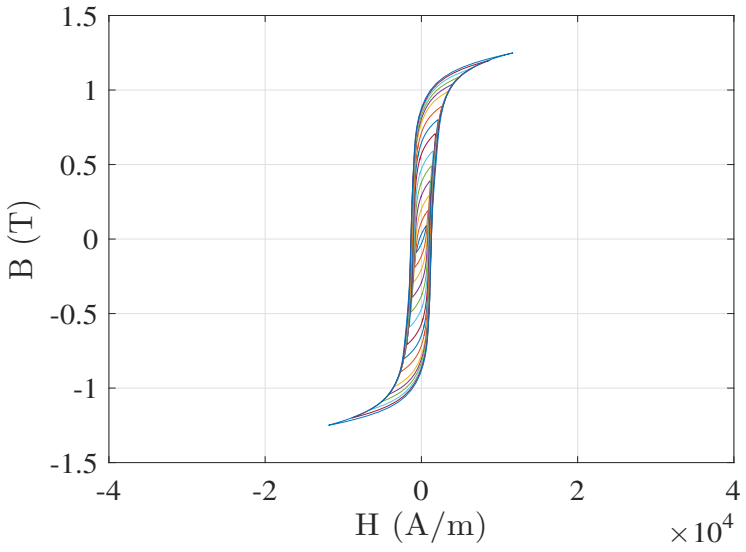

(a)

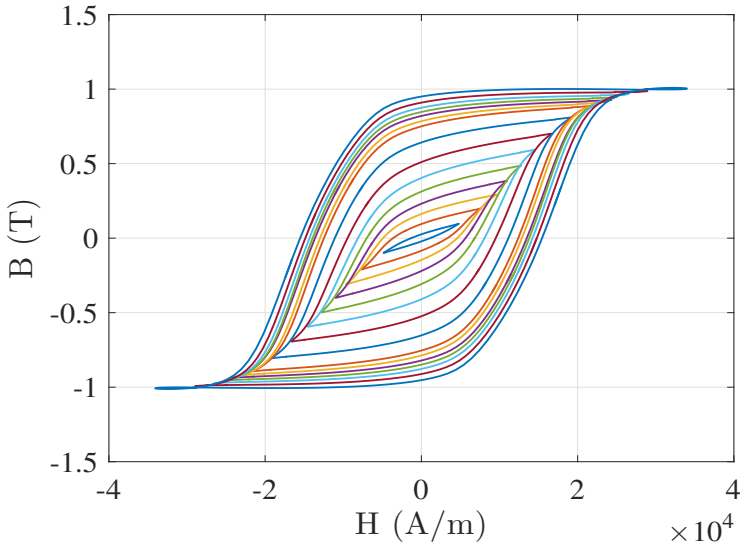

(b)

Figure 2-11: Measured hysteresis properties of the D2 tool steel and the FeCrCo alloy under different sinusoidal B-field excitation amplitudes at 10Hz. The data is measured by Dietmar Andessner at the Linz Center of Mechatronics, GmbH. (a) D2 tool steel. (b) FeCrCo alloy.

refered to as the hunting behavior for hysteresis motors [54]. Figure 2-13 also shows that the Motor I has a shorter settling time than Motor II and III. This is due to the D2 steel is having a larger conductivity than the FeCrCo alloy and the rotor material for Motor III, and thus Motor I demonstrates a larger damping than the Motor II and III.

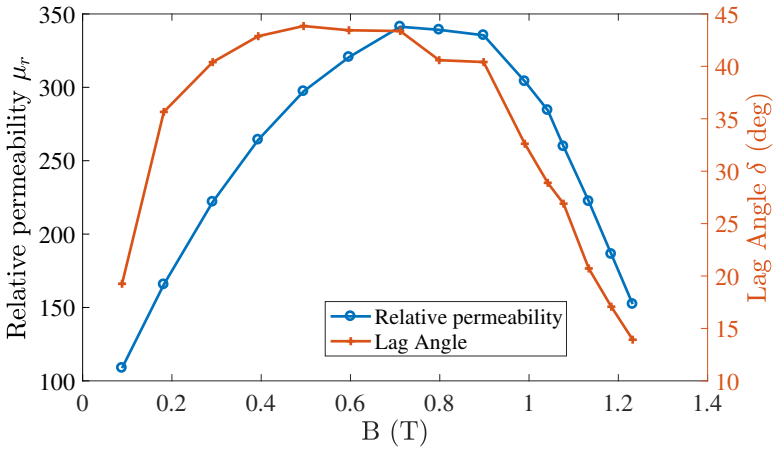

(a)

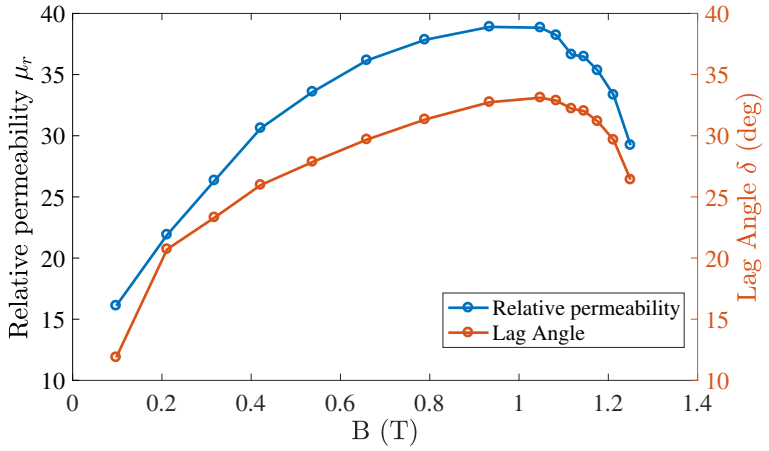

(b)

Figure 2-12: Measured μ_r and δ of the hysteresis motor rotor materials at 10 Hz under different excitation amplitude. (a) D2 tool steel. (b) FeCrCo alloy.

The motors' starting torques are estimated though measuring the slope of the speed during starting up. The drag torques to the motors, including air drag and the bearing friction, are identified through the deceleration of the motor after disconnecting from the power sources, and are considered in the calculation of the motor starting torques. Figure 2-14 shows the torque-slip frequency relationship of the three hysteresis motors. Figure 2-14(a) and (b) also present the modeled torque calculated using the time-average hysteresis motor equivalent circuit model shown in Figure 2-4, with the motor geometric parameters and hysteresis parameters of the specific rotor material being used. In Figure 2-14(a) and (b), the modeled and measured torque

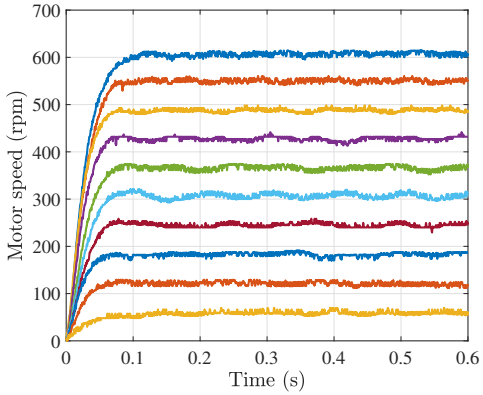

(a)

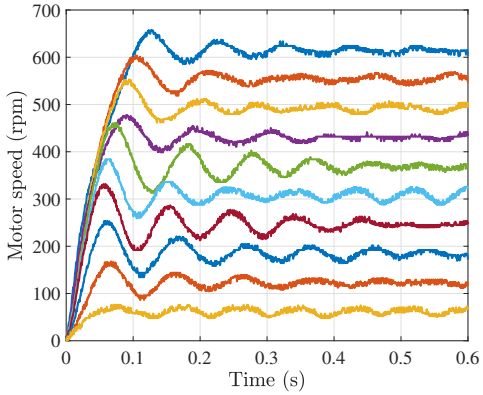

(b)

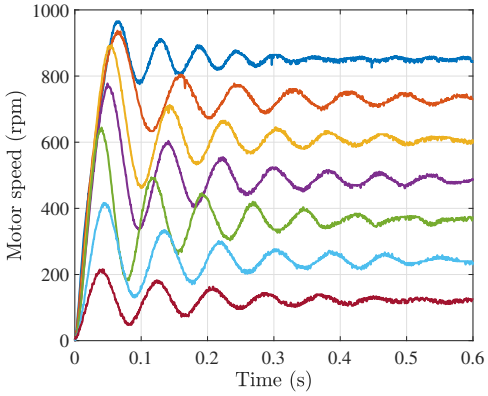

(c)

Figure 2-13: Start-up speed plots of hysteresis motors at different reference frequencies. All speed data converge to synchronous. Note speed hunting transients for lower two plots. (a) Motor I: D2 tool steel motor; peak current amplitude 1 A. (b) Motor II: FeCrCo alloy motor; peak current amplitude 1 A. (c) Motor III: Commercial hysteresis motor; peak current amplitude 2.5 A.

data agree well at high slip frequency, but have a relatively large difference at low slip frequency. This is because the model assumes the hysteresis lag angle is equal to its

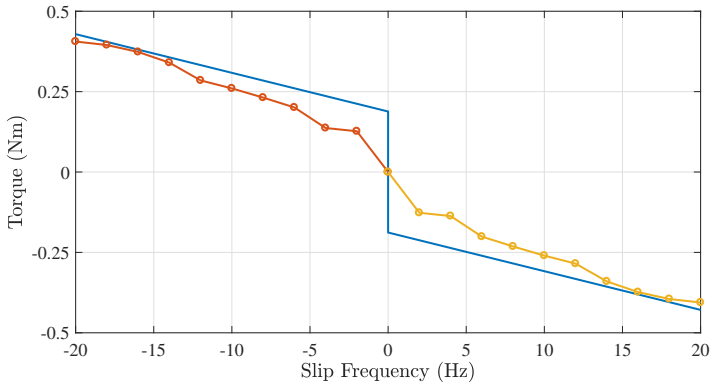

(a) Motor I: D2 steel hysteresis motor.

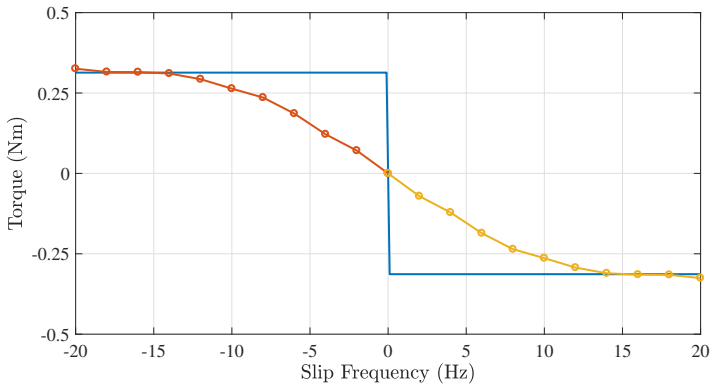

(b) Motor II: FeCrCo alloy motor.

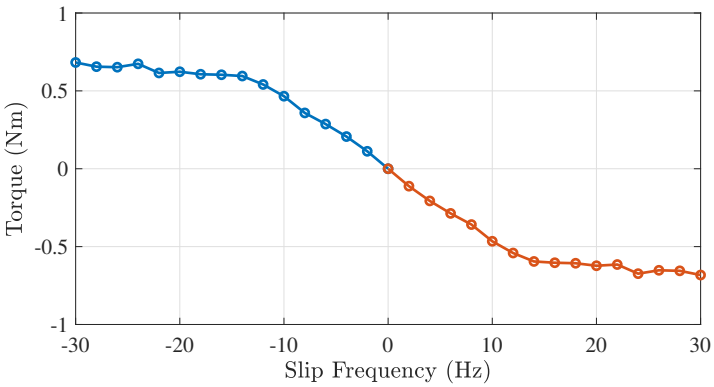

(c) Motor III: Elinco motor.

Figure 2-14: Torque-slip frequency curve of hysteresis motors. Solid line: modeled torque. Marked lines: measured torque. (a) Motor I: D2 tool steel motor; peak current amplitude 1 A. (b) Motor II: FeCrCo alloy motor; peak current amplitude 1 A. (c) Motor III: Commercial hysteresis motor; peak current amplitude 2.5 A.

maximum whenever the motor is running asynchronously, i.e., the slip frequency is non-zero. However when the motor slip frequency is small, the lag angle can demonstrate values smaller than the maximum lag angle, as discussed in reference [41].

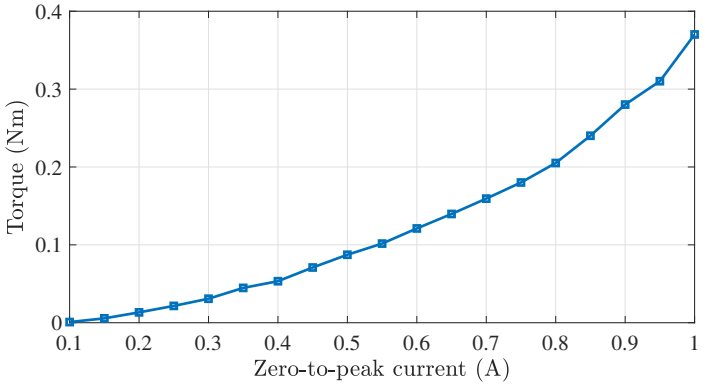

(a)

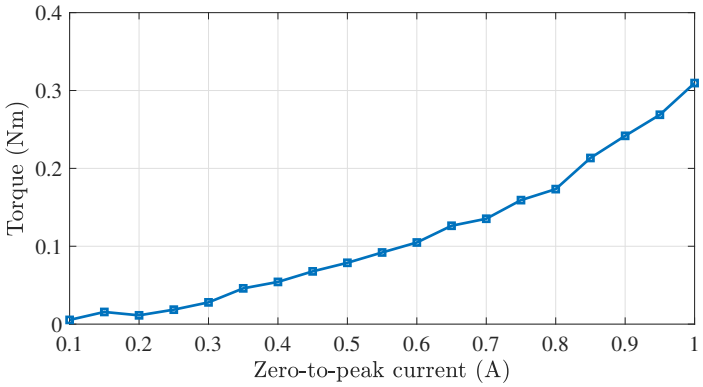

(b)

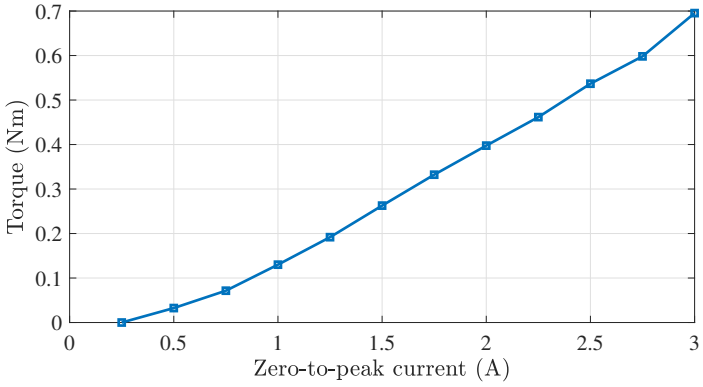

(c)

Figure 2-15: Torque-current relationships of hysteresis motors at 20 Hz driving frequency measured under a locked rotor condition. (a) Motor I: D2 tool steel motor; peak current amplitude 1 A. (b) Motor II: FeCrCo alloy motor; peak current amplitude 1 A. (c) Motor III: Commercial hysteresis motor; peak current amplitude 2.5 A

Also, as is shown in Figure 2-14(a) and (b), the torque of motor I increases almost linearly with the slip frequency, while the starting torque of motor II saturates to a certain value when slip frequency is high. This indicates that the dominant torque

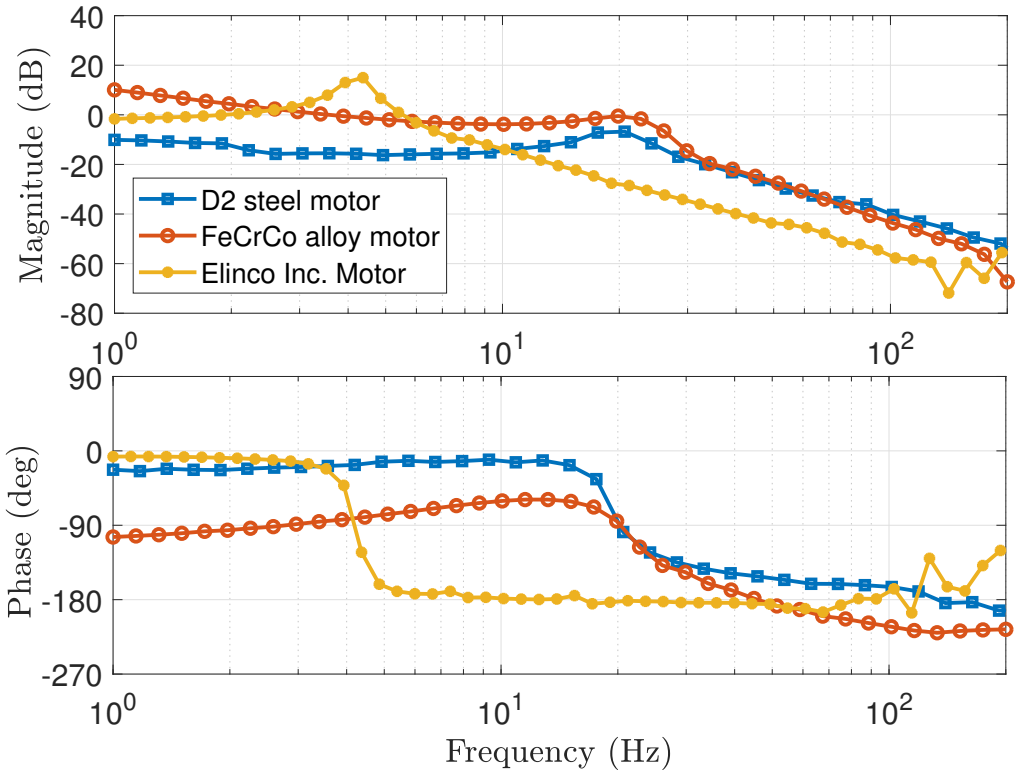

Figure 2-16: Measured plant Bode plots for three hysteresis motors. Input: q-axis current amplitude; output: measured position.

generation mechanism of Motor I is through eddy current effects, while the dominant torque generation mechanism of Motor II is through the hysteresis effect.

Figure 2-14 (c) does not show the modeled torque for Motor III since we lack knowledge about the rotor hysteresis material property for Motor III. Comparing Figure 2-14(b) and (c), it can be seen that the measured torque-slip frequency relationship of Motor III resembles that of Motor II, where both motors' torque saturates to an approximately constant value as the slip frequency increases. This indicates that the torque generation of Motor II and III is mainly through the hysteresis effect.

Figure 2-15 shows the measured torque-current relationships of the three hysteresis motors under a blocked-rotor condition with a driving frequency of 20 Hz. It can be seen that the motor torque is roughly quadratic with respect to the current amplitude.

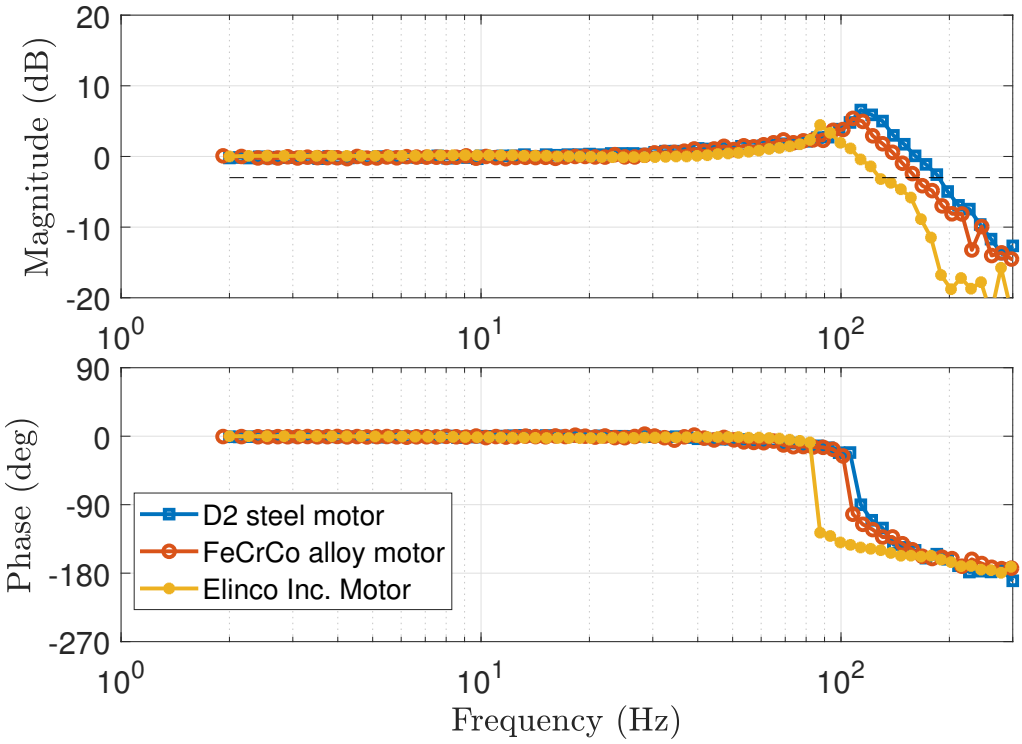

Figure 2-17: Measured closed-loop Bode plots for three hysteresis motors. Input: reference position; output: measured position. The -3 dB level in the magnitude plot is shown as a dashed line.

2.4.3 Position Closed-Loop Control

The position closed-loop control scheme shown in Figure 2-7 is tested with the three hysteresis motors. The motors are first tested under no-load condition. For Motor I and Motor II, the full-order state observer method given in (2.28) and (2.29) is used for the rotor flux orientation estimation. For Motor III, rotor flux orientation is estimated through the combination of the mechanical angle and back-EMF method, which is shown in (2.27). This is because the full hysteresis motor model is available for Motor I and II, and is not available for Motor III due to the lack of knowledge about the rotor material hysteresis properties.

Figure 2-16 shows the measured plant frequency responses of the position control for the three hysteresis motors. In this measurement, the input signal is the q-axis current in the rotor flux-oriented frame, and the output signal is the measured rotor

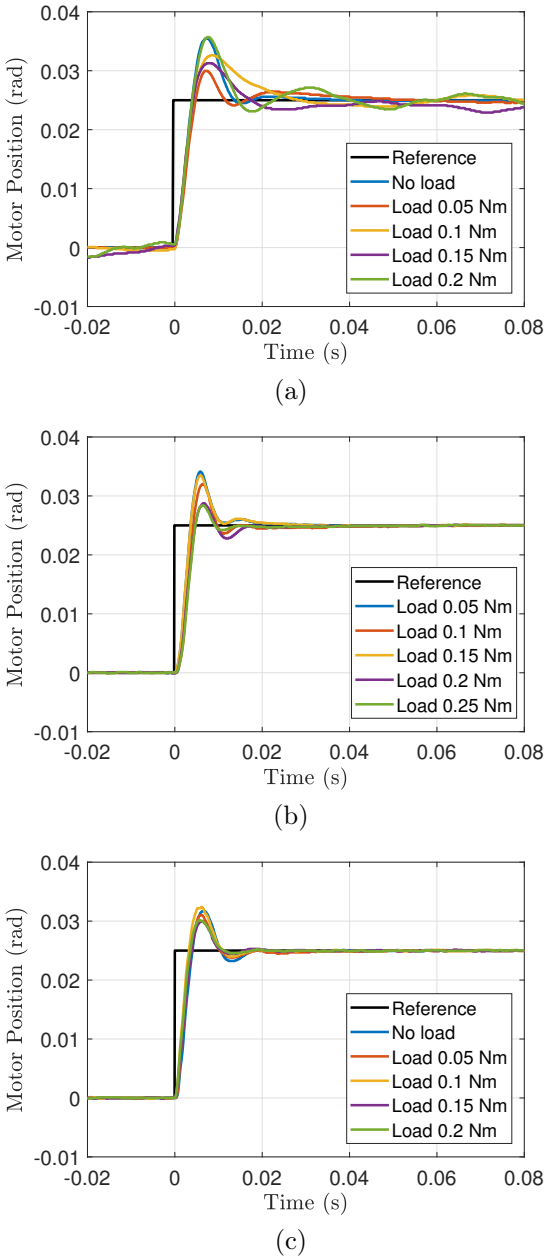

Figure 2-18: Closed-loop position step responses of three hysteresis motors under different load torque. (a) Motor I: D2 tool steel motor; d-axis current is 0.4 A . (b) Motor II: FeCrCo alloy motor; d-axis current is 0.4 A. (c) Motor III: Commercial hysteresis motor; d-axis current is 0.6 A.

angular position. It can be observed in Figure 2-16 that all three measured Bode plots demonstrate -40 dB/dec slope at high frequencies, which follows the torque-to-position Newton's second law relationship in a typical motor. The Bode plots in Figure 2-16 shows zero slope at low frequency which is believed due to the bearing

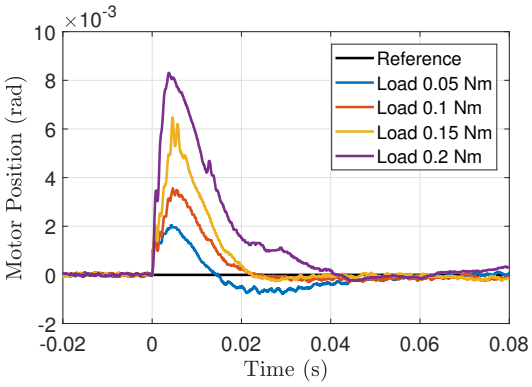

(a)

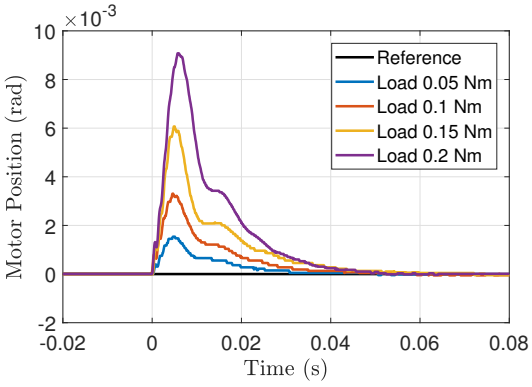

(b)

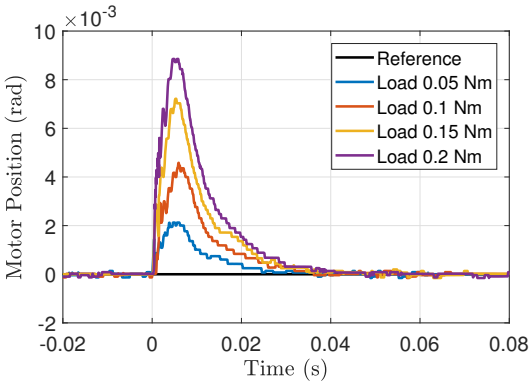

(c)

Figure 2-19: Position error signal of hysteresis motors under step change of disturbance torque in the positive direction. (a) Motor I: D2 tool steel motor; d-axis current is 0.4 A . (b) Motor II: FeCrCo alloy motor; d-axis current is 0.4 A. (c) Motor III: Commercial hysteresis motor; d-axis current is 0.6 A.

friction, in the fashion discussed in reference [55]. This measurement indicates that the q-axis current is roughly proportional to the torque of the motor. It also demonstrates that the proposed flux orientation estimation approach is successful for motors with known and unknown rotor hysteresis properties.

Figure 2-17 shows the measured closed-loop Bode plots for the position control systems for the hysteresis motors. Figure 2-17 demonstrates that the bandwidth of the position control for the three hysteresis motors are above 130 Hz.

The hysteresis motors are also tested under mechanical load. Figure 2-18 shows the measured closed-loop position step responses of the three hysteresis motors under different constant load torques, and Figure 2-19 shows the hysteresis motor's position signal under a step change of the load torque. In this experiment, the load torque is applied by the BLDC load motor, which is under current-control. The load torque magnitude is determined though the load machine's current times its torque constant. It can be seen through Figure 2-18 that Motor I demonstrates larger position ripple than the Motor II and III when under a constant torque larger than 0.05 Nm. This is because Motor I uses AC current to compensate the large torque, and it demonstrates torque ripple under this condition due to the high order harmonics of the motor winding. In contrast, Motor II and III are able to compensate the load torque with DC currents in their windings, as they are operating in the no-slip regime. This experiment shows that the hysteresis motor's position control is successful under different load conditions, and also demonstrates that the position control for the three hysteresis motors are robust with respect to load changes.

2.5 Summary

In this chapter, we studied position control for hysteresis motors by means of field-oriented control. A transient-time hysteresis motor model including both hysteresis effect and eddy current effect is developed based on the elliptical assumption of hysteresis loops. Three methods for estimating the rotor flux orientation are proposed, which are used for field orientation estimation for hysteresis motors in real-time control. Three hysteresis motors, including two custom-made hysteresis motors with a D2 steel rotor and a Cobalt alloy rotor and one commercial hysteresis motor, are tested. All three motors have achieved successful position control with bandwidth more than 100 Hz, and demonstrated good robustness with respect to external loads.

This work sets a foundation for the design and control for the linear stage driven by linear hysteresis motors, which is presented in the following chapters.

Chapter 3

Linear Stage Design

This chapter discusses the design of our magnetically-levitated linear stage. The design process include three levels: (1) strategies, (2) concepts, and (3) details. In this chapter, we focus on the first two levels of the linear stage design, which presents the process to conceive new designs for the magnetically-levitated linear stage.

In this chapter, Section 3.1 discusses the functional requirements and specifications for the reticle transportation in the EUV photolithography scanners. The established design strategies are presented in Section 3.2, and the design concepts that can implement the strategies are shown in Section 3.3. In the end, we selected one design concept and proceed with the detail design, building, and testing, which are presented in Chapter 4 to Chapter 6.

3.1 Functional Requirements

The target application of our magnetically-levitated linear stage is the in-vacuum reticle transportation in extreme-ultraviolet (EUV) photolithography scanners. Figure 3-1 shows a picture of an EUV photolithography machine from ASML Inc. In the photolithography process, the reticle, or photomask, is a 6 inch by 6 inch square reflective optical plate that contains a pattern of the integrated circuit. This pattern is transferred onto the silicon wafer using a 13.5 nm wavelength light during the ex-

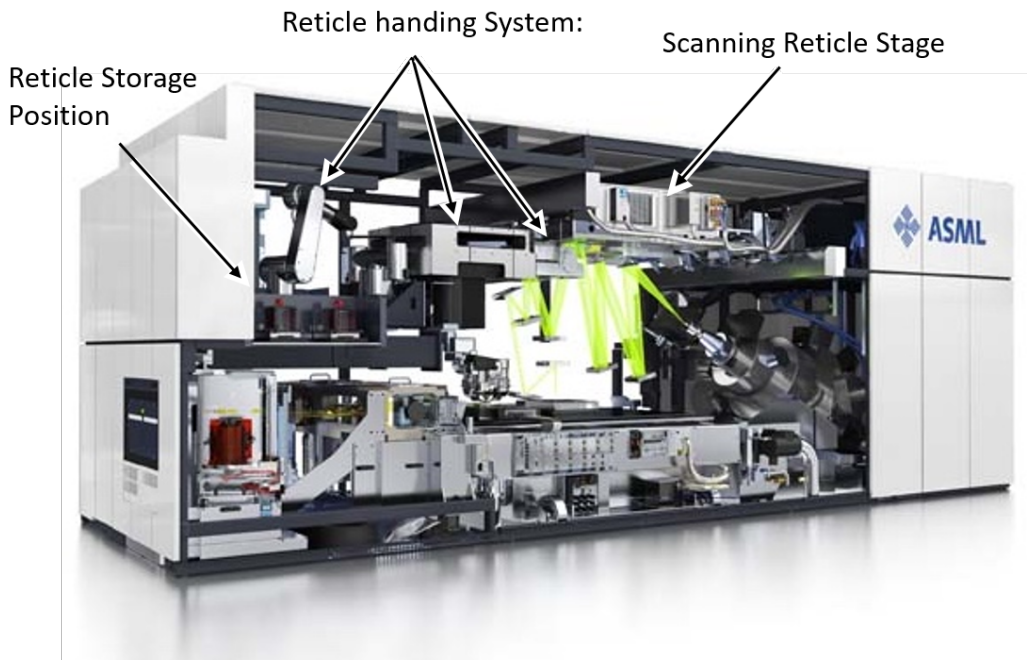

Figure 3-1: Picture of extreme-ultraviolet (EUV) photolithography machine from ASML Inc. Picture source: www.asml.com.

posure process. In lithography machines, the reticles need to be transported between a storage position and the scanning reticle stage, and typically robot manipulators are used to fulfill this transportation task, as shown in Figure 3-1.

In next-generation EUV lithography machines, due to the increased system complexity, the reticles transportation system needs to satisfy a series of new functional requirements as follows:

(1) **Handling**: The transportation system needs to transport the reticle and its container in between the storage position and the scanning stage. The transportation distance is approximately 2 meters.

(2) **Volume Efficient**: In order to accommodate other subsystems in the EUV scanner, the reticle transportation system needs to satisfy a tight volume constraint, with its vertical height below 100 mm, and the lateral width below 500 mm.

(3) **In-vacuum Operation:** The reticle needs to be transported in vacuum with a background of low pressure nitrogen, which is added to the environment for cooling and particle control purpose.

Table 3.1: Specifications for New Reticle Transportation System

Specification	Value
Transportation distance	2 m
Vertical height of the system	100 mm
Lateral width of the system	500 mm
Power dissipation in vacuum	1 W
Acceleration during transportation	500 mm/s^2
Maximum speed of trajectory in transportation	250 mm/s
Position control accuracy during docking	100 μm

(4) **Contact-free:** Mechanical contact during transportation needs to be eliminated to prevent particle generation.

(5) **Low Power Dissipation in Vacuum:** The system needs to have a low power dissipation in the vacuum, since cooling in the vacuum environment is challenging.

(6) **Eliminate Out-gas in Vacuum:** The system must have sufficiently low outgassing in the vacuum environment to prevent contaminating the reticle.

The specifications for reticle transportation system are further shown in terms of numbers in Table 3.1. With the requirements above, especially the constraint on vertical height and the long travel distance requirement, the design for a robot reticle hander is very challenging. This fact motivates the design for a novel reticle handling system that can fulfill these new requirements.

3.2 Strategy

In this section, we present the selection of strategies to conceptualize a high-level solution for the transportation system with the aforesaid design requirements. We decide to use a magnetically-levitated linear stage to fulfill the reticle transportation task. For the linear stage's driving principle, we propose to use linear hysteresis motors in order to achieve a simple and compact moving stage design. Lastly, we consider passive levitation for some degrees of freedom of the moving stage, which allows a more compact design and reduces the system cost. The rest of this section

discusses the aforesaid strategies in detail.

3.2.1 Magnetically Levitated Linear Stage

To achieve the reticle transportation task within a highly-constrained volume, we propose the idea of using a linear stage for reticle transportation. In order to fulfill the vacuum compatibility and contamination-control requirements, we further propose to use magnetic suspension for the linear reticle transportation stage. A magnetically-levitated linear stage is attractive for the reticle transportation application for two reasons:

(1) First, linear stages/motors are suitable for transportation tasks, especially for those with relatively long travel distances and small allowed height. Compared with robot manipulators, linear stages typically require less volume in the machine, and thus can satisfy the tight dimension constraint in the vertical direction with less challenge.

(2) Second, magnetic levitation is proposed for the reticle transportation stage to eliminate mechanical contact and lubrication, which are not allowed in the reticle handling environment to prevent particle generation. There are two commonly used solutions for linear motors to eliminate mechanical contact: air bearings and magnetic bearings. Due to the in-vacuum operation requirement, the use of air bearings is very challenging for the reticle transportation stage, which will increase the cost and volume of the system. On the other hand, the magnetic bearing is a convenient solution for linear stages and also allows in-vacuum operation.

In addition, we plan to configure a channel with thin walls surrounding the entire motion range of the stage. The moving stage transports the reticle inside the channel in a clean vacuum, while the stators for the moving stage are configured on the outside in a relatively dirty vacuum, as shown in Figure 3-2. In this way, we are able to separate out the contamination generation from the stator assembly, which has actuator coils and its potting, permanent magnets, cooling cables, etc.

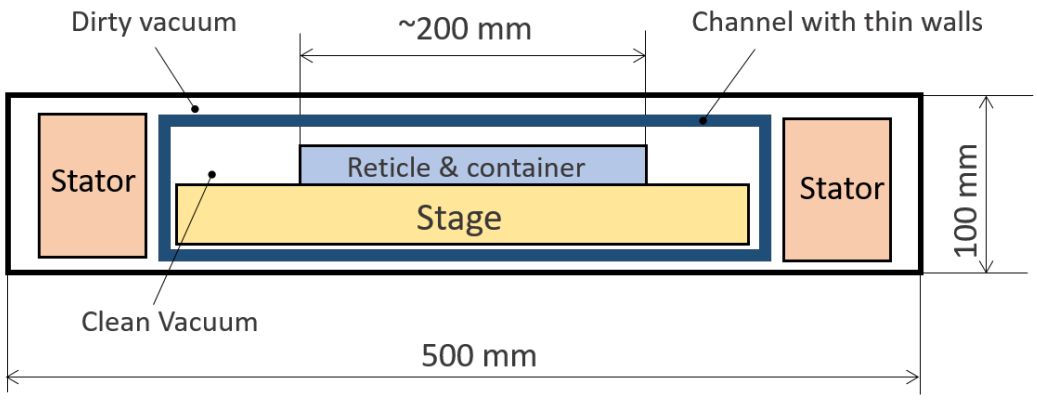

Figure 3-2: Diagram of reticle transportation channel and wall separating clean and dirty vacuum.

3.2.2 Linear Hysteresis Motor

This section presents a brief discussion about the motor driving principle selection for the magnetically-levitated linear stage for reticle transportation. Table 3.2 shows a comparison between the motor driving principles. The advantages and disadvantages of each driving principle are discussed below.

Permanent magnet linear motors for magnetically-levitated precision stage applications have been studied extensively through the years, and have demonstrated good performance in terms of thrust force generation, ease of control, and power density. However, permanent magnets can out-gas when they are exposed in vacuum, and therefore need to be encapsulated. This requires a relatively complicated moving stage design for the magnetically-levitated linear stage for reticle transportation.

Induction motors are not selected for the linear stage mainly because of the inevitable secondary loss. In an induction motor, the thrust force generation uses the induced currents in the secondary, which generates heat in the secondary. This is not favorable when the secondary needs to levitated in vacuum. In addition, induction motors require asynchronous operation, and an AC component force generation can thus exist in the motor, which can cause oscillations in the moving stage.

Reluctance motors allow a monolithic steel secondary construction, and have the advantages of relatively large shear force production capability and high secondary structural stiffness. However, when being used for magnetically-levitated

Table 3.2: Comparison between different motor types, advantages and disadvantages.

Motor	Main features
Permanent magnet motor	+ Large force generation capability and high efficiency. + Linear current-to-force relationship; simple position control method available. − Cogging force and force ripple exists. − Permanent magnet and its potting cannot expose in vacuum since outgassing should be prevented.
Induction motor	+ Relatively high efficiency typically about 90%. − AC component in shear and normal forces. − Eddy currents in the secondary can generate heat, which is challenging to cool in vacuum environment.
Reluctance motor	+ Soft magnetic material mover; no permanent magnet needed. + Simple structure. High structural and packaging efficiency. − Nonlinear thrust generation. − High force ripple in shear and normal forces; high noise when open-loop running
Hysteresis motor	+ Semi-hard solid material mover; no permanent magnet needed. + Simple structure. High structural and packaging efficiency. − Nonlinear and history-dependent current-to-force relationship. − Relatively small shear force generation capability.

linear stages, the relatively large normal and shear force ripple of the reluctance motor may lead to stage oscillations, which is undesirable when the stage is being used for reticle transportation. These disturbances also occur with high spatial frequency which makes them challenging to control.

In this thesis work, we selected linear hysteresis motors as the driving principle for the magnetically-levitated linear stage for reticle transportation. Linear hysteresis motors are attractive for this application for three reasons: (1) Hysteresis motors allow using solid-steel motor secondaries on the moving stage and do not need permanent magnets. This is desirable for in-vacuum operation, since permanent magnets can outgas in high vacuum when not encapsulated. (2) The hysteresis motor secondary uses a monolithic piece of solid steel with high stiffness, which is desirable for structural purposes. (3) Compared with induction motors, hysteresis motors do not generate steady-state heat in the moving stage due to the fundamental harmonic magnetic interaction when operating in synchronous mode, which is desirable since cooling of the stage in vacuum is challenging.

Another reason that we selected linear hysteresis motors for our linear stage is to explore the use of unconventional driving principles for linear stages. As discussed in Chapter 1, to our knowledge, there is no reported study on the linear version of hysteresis motors. However, given the fact that the hysteresis motors have many unique features, linear hysteresis motors may be attractive in some special applications, such as in-vacuum operation, high-temperature environment, tight volume constraint, etc. Targeting at these potential applications, we study the design, modeling, and control for linear hysteresis motors as a part of this thesis work, which potentially can enlarge the design space for actuation principle selection for special linear motion systems.

Linear hysteresis motors also have several drawbacks including: (1) relatively low thrust force, (2) a lack of methods to control its force and position. Among these two drawbacks, the first one is acceptable for the reticle transportation tasks, since the required acceleration of 500 mm/s^2 is not high. The second challenge is partly addressed in Chapter 2, where a high-bandwidth force and position control method is proposed and tested for rotary hysteresis motors. In the development of our linear

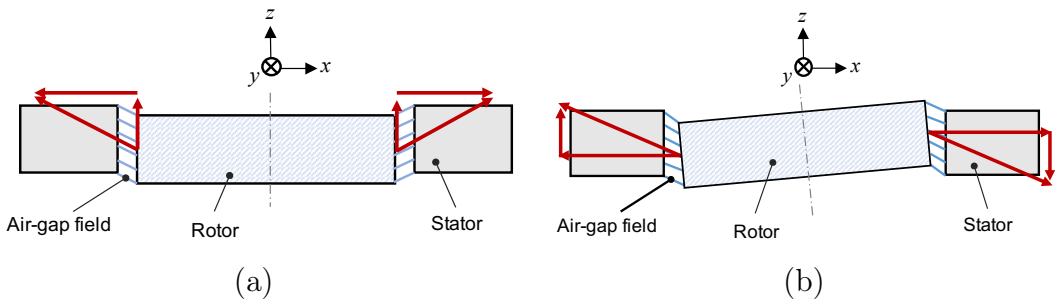

Figure 3-3: Diagram of passive magnetic suspension of axial and tip-tilt displacement in rotary bearingless slice motors. (a) Principle of axial restoring force generation. (b) Principle of tip-tilt restoring torque generation.

stage, we plan to explore control methods for linear hysteresis motors as an extension to the work in Chapter 2, thereby allowing these motors being used for linear position servo applications.

3.2.3 Passive Magnetic Suspension

In the design for the magnetic suspension mechanism for our linear stage, we consider using passive levitation for some degrees of freedom of the moving stage. An early version of passive magnetic suspension is presented by Schöb and Barletta for rotary bearingless motors in [56]. Figure 3-3 shows an illustration of the principle of passive magnetic suspension in bearingless slice motors. Here, the rotor has an axial length that is significantly smaller than the diameter, which resembles a slice of a disk. With the magnetic fields on the rotor's peripheral, such slice motor can generate restoring forces and torques when the rotor is misaligned with the stator in axial, tip, and tilt directions. In this design, three degrees of freedom of the rotor are passively stabilized: translation along the axial direction and tip and tilt of the rotor. The other two degrees of freedoms except for the rotation about the vertical axis, i.e. the translations in radial directions, are unstable in open-loop, and feedback control is required to stabilize the radial suspension of the rotor.

Several other possible configurations of passive magnetic suspension for rotary motors using ring-shaped permanent magnets are shown in Figure 3-4. The first study of passive magnetic levitation using permanent magnet ring supports is pre-

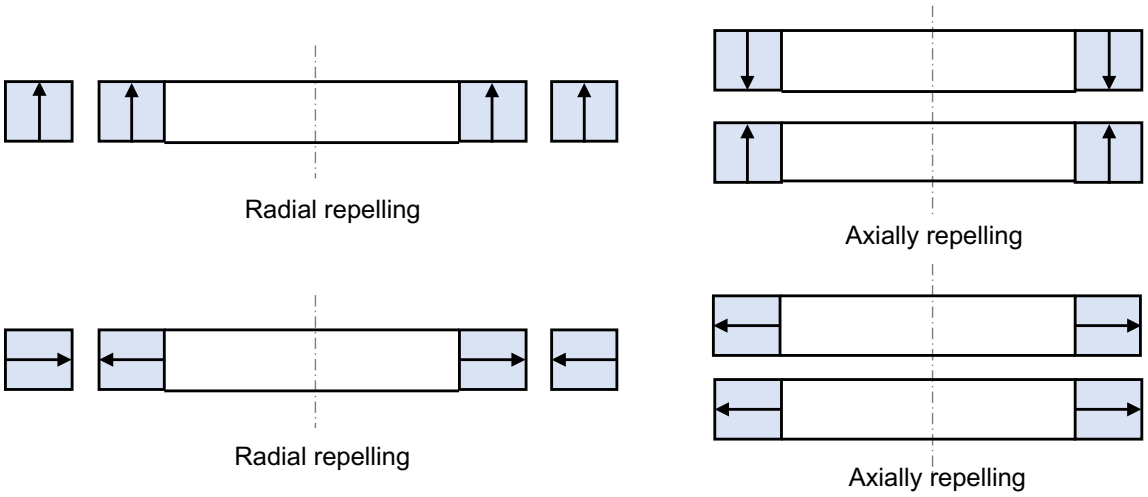

Figure 3-4: Passive magnetic bearings using ring-shaped permanent magnets introduced in [12].

sented in [12]. The proposed design uses the field and force interactions between permanent magnet rings to support the rotor in radial or axial directions. Similar to the bearingless slice motor idea, additional active magnetic bearings are necessary to stabilize the remaining unstable degrees of freedoms. This concept further enables a number of designs for one-axis active positioning in magnetic bearings and bearingless drives [57–60], where as many as four degrees of freedom of the rotor are passively stabilized.

Finally, a four degrees of freedom passive magnetic bearing can be realized via design shown in Figure 3-5. Motor designs using this suspension concept include [61] and [36]. Here the rotor has a slender geometry, and the stators are configured on the two tips of the rotor. The rotor spins about the z-axis, and its translation about the z-axis is actively controlled. Other degrees of freedom, including radial translation and tilt in x- and y-directions, are passively stabilized with the flux concentration at the tips of the rotor.

Although a number of designs have demonstrated the application of passive magnetic suspension in rotary motors, to our knowledge, few works have studied linear motors using passive magnetic suspension. To our understanding, this is because linear motors are typically used for precision manufacturing and ground transporta-

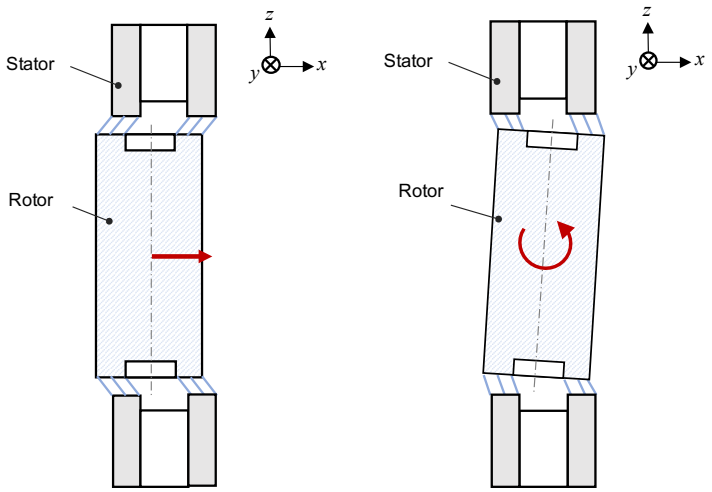

Figure 3-5: Diagram of passive magnetic suspension of slender rotor in bearingless slice motors. (a) Radial restoring force generation. (b) Tilting restoring torque generation.

tion, which requires accuracy, bandwidth, and load capacity that is usually difficult to achieve with passive magnetic suspension. However, in this work, since our magnetically-levitated linear stage does not require extremely high precision positioning during transportation, passive magnetic suspension is attractive to reduce the number of sensors, windings, and power amplifiers, and therefore reduce the overall system cost and complexity.

3.3 Design Concepts

This section presents the specific design concepts that we have explored during the design phase that can realize the design strategies discussed in Section 3.2. Some of the design concepts are presented in our patent application [62]. Note that the design concepts presented in this section is not limited to linear hysteresis motors. Same magnetic configurations can be applied to stages driven by other types of linear motors, such as linear permanent magnet motors, and linear induction motors, linear reluctance motors.

First, let us define the coordinate system of the magnetically-levitated linear stage

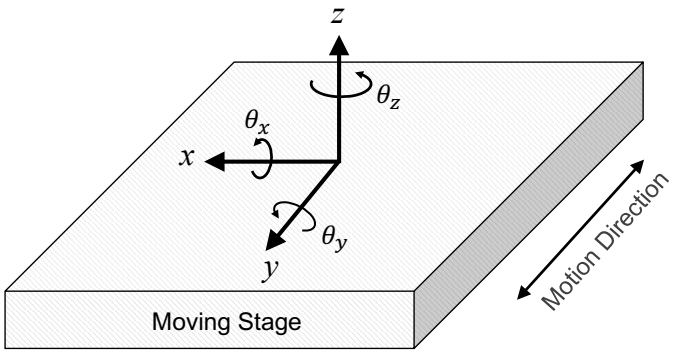

Figure 3-6: Diagram of the coordinate system of the magnetically-levitated linear stage.

as shown in Figure 3-6. Here, the y-axis is aligned with the long travel motion direction of the stage. The z-axis is aligned with the vertical direction and points upward. The x-axis is aligned with the cross-motion direction, and it forms a right-handed Cartesian coordinate with y- and z-axes. The angles θ_x, θ_y, and θ_z indicate the rotation about x-, y- and z-axes, respectively.

The design concepts presented in this section can be roughly categorized into three groups according to their magnetic suspension configuration: (1) active magnetic suspension in all degrees of freedom, (2) passive magnetic suspension in x- and θ_z-directions (lateral and yaw modes), and (3) linear bearingless slice motor design with passive magnetic suspension in z-, θ_x, and θ_y-directions (vertical, pitch and roll modes). The rest of this section describes several linear stage design concepts of each group.

3.3.1 Group I: All-DOFs Active Suspension Design

The first group of the stage design concepts use active magnetic suspension in all degrees of freedom. In these designs, the stage's motion is along y-axis, and all other degree of freedom of the stage are actively suspended via magnetic bearings.

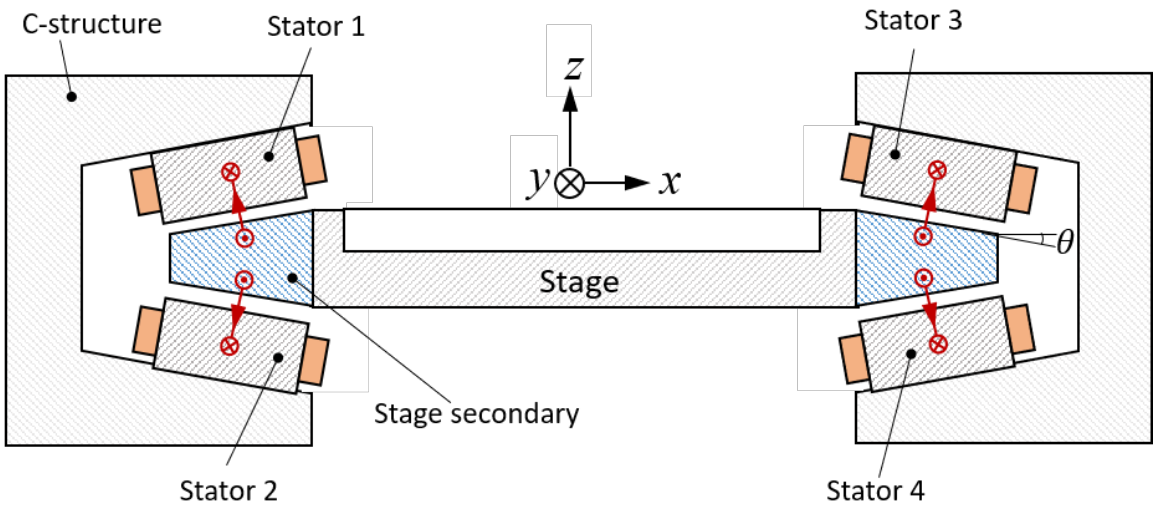

Figure 3-7: Design concept 1 of magnetically-levitated linear stage with all-DOFs actively controlled.

Group I: Design Concept 1

Fig. 3-7 shows a design concept of a magnetically-levitated linear stage using active magnetic suspension in all degrees of freedom. When the stage is driven by hysteresis motors, the stage secondaries are made of magnetically-semi-hard material with relatively large permeability. There are four stators configured around the moving stage, interfacing with the stage secondaries. The normal surfaces of the secondary are configured at an angle with the horizontal plane. Here, each stator is able to control its total normal force, total thrust force, and the torque to the secondary in the pitch direction. With all these forces and torques, all degrees of freedom of the stage can be actively controlled.

Below we discuss the winding pattern for the stator that can implement the control for required torques and forces. The winding of each stator has two possible configurations. Figure 3-8 shows the first winding configuration. Here, the stator winding consists of a series of lumped coils, and each coil is driven by independent power amplifiers. By controlling the currents in each coil, the total normal force, total thrust force, and total torque in x-direction on the stage secondary can be controlled independently. This winding pattern requires a relatively large number of

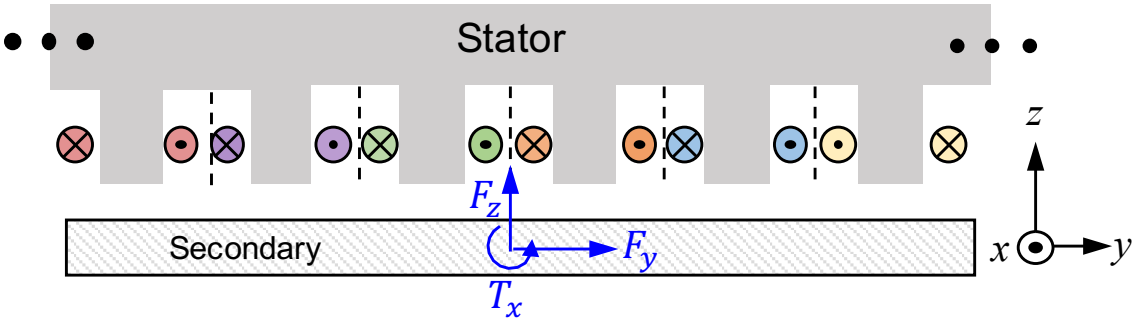

Figure 3-8: Stator winding configuration using independently-controlled lumped coils.

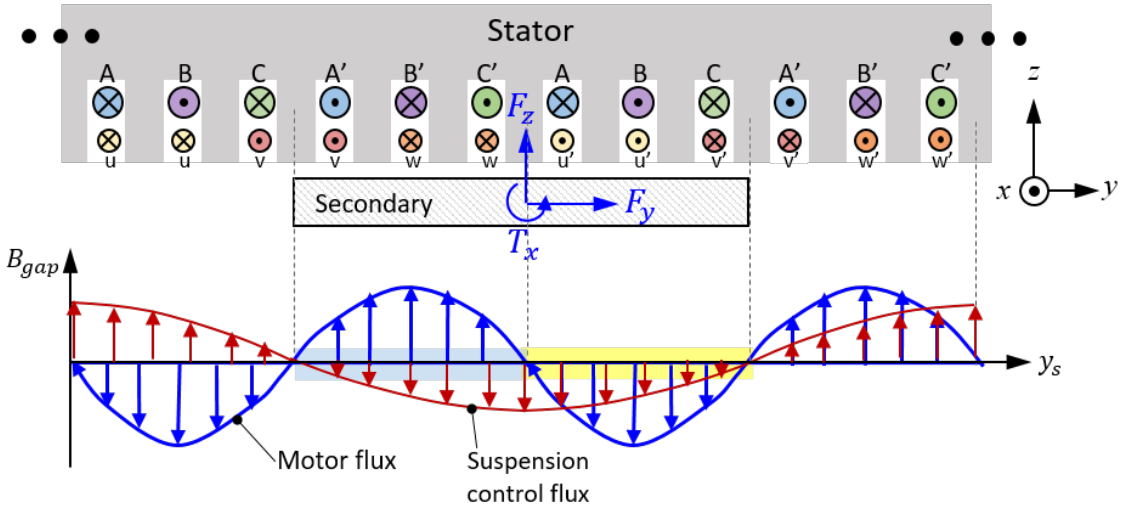

Figure 3-9: Stator winding configuration using double multi-phase windings and the corresponding air-gap flux distribution.

independent power amplifiers, especially for linear stages with long transportation distance.

The other possible winding pattern uses multiple-winding type linear bearingless motor configuration, shown in Figure 3-9. In this winding configuration, two sets of multi-phase windings are configured in the same stator, as shown in Figure 3-9. Here the windings (A, B, C) shown with large circles are the motor windings, and the windings (u, v, w) shown with small circles are the torque control windings. The wavelength of the torque control winding magneto-motive force is twice of that of the motor winding. The same phase in each set of winding are connected in series, and there are in total six independent currents in this stator. The bottom plot in Figure 3-

9 shows the air-gap fluxes generated by the two sets of windings. Here the blue lines show the motor flux, the red lines show the torque control flux. The forces and torques generated by this stator is briefly discussed below. The total normal force F_z and total shear force F_y can be controlled via the amplitude and phase, or d- and q-axis, of the motor winding excitation. The torque about x-axis can be controlled by the interaction between the motor flux and the torque control flux. For example, for flux distribution in Figure 3-9, the torque control flux intensifies the fluxes in the yellow region, and attenuates the flux in the blue region, which generates controlling torque about the x-axis in Figure 3-9. This design resembles the winding pattern of rotary bearingless motors with multiple windings [63], where the suspension flux steers the motor air-gap flux in a rotating frame for torque generation. Note that this winding pattern can only be applied for those linear motors operating in synchronous mode and has a relatively large d-axis flux, for example linear reluctance motors and linear hysteresis motors. In these circumstances, the interaction between the q-axis motor flux and the torque control flux has small amplitudes, and therefore the generated disturbance forces and torque can be rejected by feedback control.

With such stator designs, there exists several stage configurations to implement motion and active suspension in all degrees of freedom. Figure 3-10 shows several example configurations. Among these configurations, design concept 1 shown in Figure 3-7 allows a simple design for the separating channel between the stator and the stage, and allows a mechanically stiff stage design, which is favorable for our target application.

Group I: Design Concept 2

Figure 3-11 shows a linear stage design concept uses a combination of regular linear motors and flux steering magnetic bearings. Here, two stage secondaries are configured on the two wings of the moving stage. Four regular linear motor stators are configured on both top and bottom of the moving stage, interfacing with the stage secondaries. The stator's winding uses regular three-phase winding. The winding of the top and bottom stators can be connected to reduce the number of independent

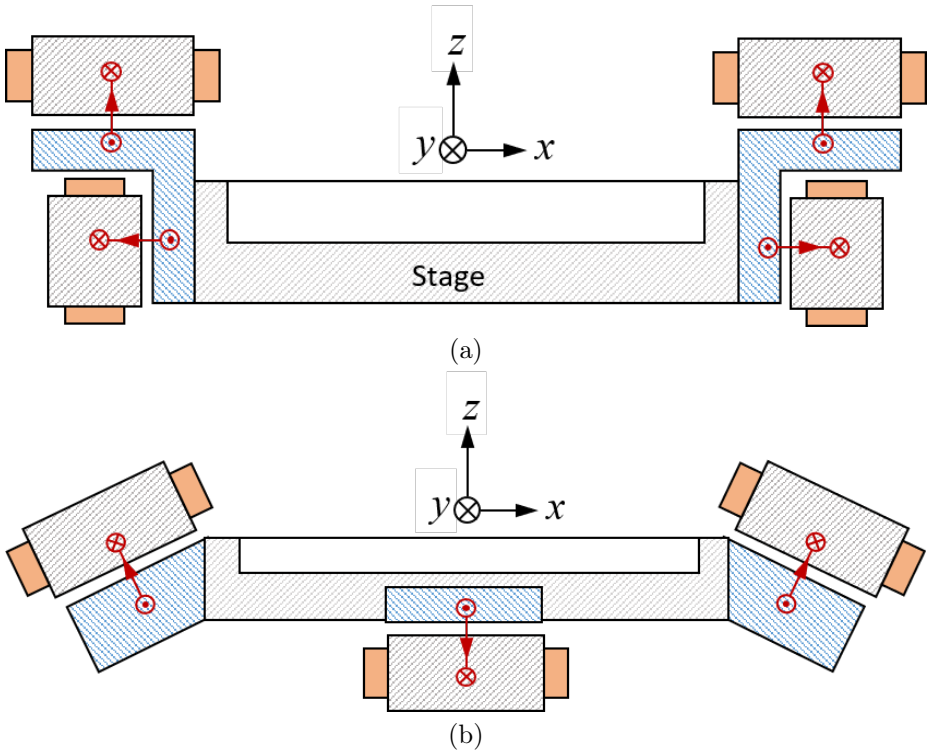

Figure 3-10: Alternative configurations of stage design concept 1 with all-DOFs actively controlled.

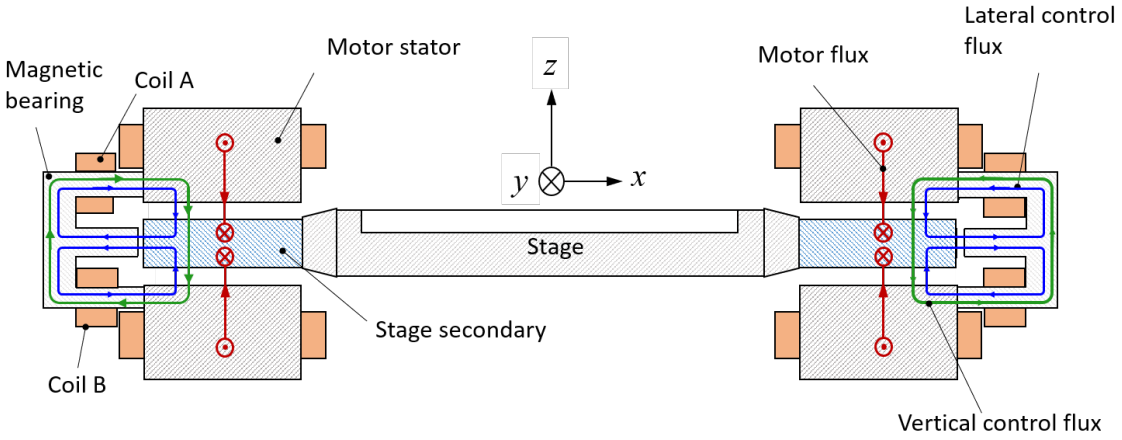

Figure 3-11: Design concept 2: magnetically-levitated linear stage with regular linear motors and flux steering magnetic bearings.

currents. These stators generate motor fluxes shown by the red lines in Figure 3-11, which interact with the stage secondaries and thereby generates thrust force in y-direction. The normal forces generated by the motor fluxes are largely canceled out by top and bottom motors when the stage is centered.

In addition to the motor stators, two rows of magnetic bearings with E-shaped cores are configured on the two sides of the moving stage, as shown in Figure 3-11. Each magnetic bearing has two coils wrapping around the top and bottom arms of the E-shaped core, as shown by coil A and coil B in Figure 3-11. The current in each coil is independently controlled. There are two kinds of magnetic fluxes generated by the E-shaped magnetic bearing. The common-code current in coil A and coil B generates lateral control flux, as shown by the blue flux lines in Figure 3-11. This flux generates normal forces on the left and right edges of the moving stage, which can control the x-directional suspension of the moving stage. With at least two magnetic bearings configured along the moving stage, the θ_z-directional magnetic suspension can also be controlled. This flux will also flow across the motor air gaps, however it does not generate net force to the stage when the stage secondary is centered vertically. In addition, the differential current in coil A and coil B generates vertical control flux, as shown by the green flux lines in Figure 3-11. This flux steers the motor flux and vertical control flux to generate vertical control force on the moving stage. For example, in Figure 3-11, the vertical control fluxes intensify the motor fluxes in the top air gaps, and weaken the motor fluxes in the bottom air gaps, thereby generates vertical suspension force pointing upwards, which can be used to compensate the weight of the stage, and to control its z- and θ_y-directional suspension. With multiple E-shaped magnetic bearings interfacing with the moving stage simultaneously, the stage's suspension in θ_x-direction can also be actively controlled. As a result, this stage configuration is able to actively control all degrees of freedom of the moving stage.

The stage design concept 2 shown in Figure 3-11 presents a relatively simple stage design, and here the suspension of the stage in different degrees of freedom are largely decoupled, which allows a simple control design. The main drawback of this stage is that its vertical suspension force relies on a non-zero motor flux. As a result, the currents in the motor windings cannot be zero even when no motion is required. This fact makes the stage less efficient in power consumption when carrying the gravity load.

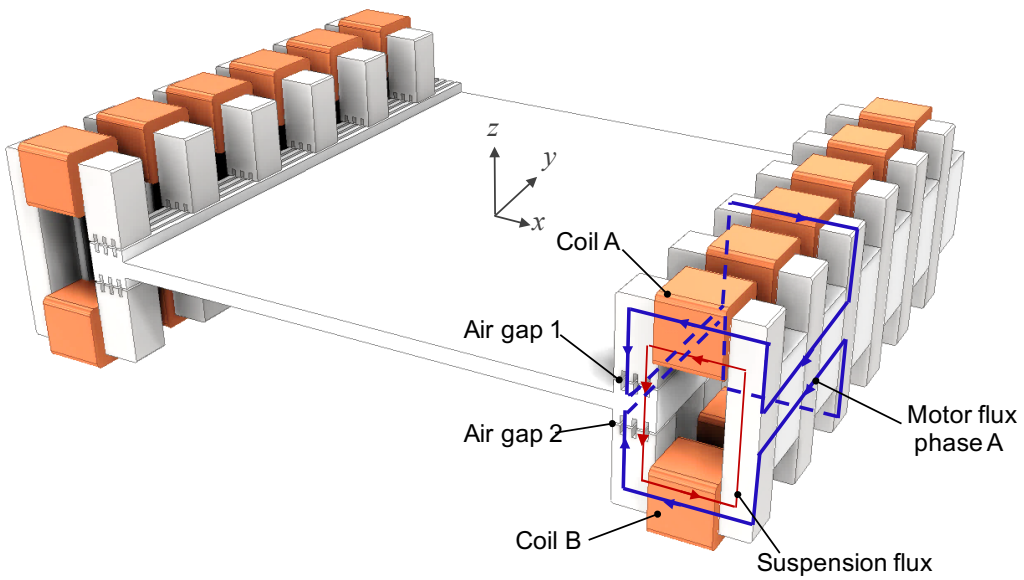

Figure 3-12: Design concept 1: magnetically-levitated linear stage with connected C-shaped core stator design.

3.3.2 Group II: Passive Suspension in x- and θ_z-direction

The second group of linear stage design concepts use passive suspension for x- and θ_z-directional levitation, and use active magnetic suspension for levitation in other degrees of freedom, including z-, θ_x-, and θ_y-directions. Note that in some of these designs the θ_z-DOF of the stage can often be actively controlled if improved stiffness is needed, although it is already stabilized passively.

Group II: Design Concept 1

Figure 3-12 shows the design concept 1 of the magnetically-levitated hysteresis linear stage in group II. Here the moving stage is magnetically suspended in the z-, θ_x-, and θ_y-directions actively, and the stage's magnetic suspension in x- and θ_z-directions are passive. When the stage uses hysteresis motor, the edges of the moving stage are made of magnetically semi-hard alloy with relatively large permeability, and thrust forces are generated along the y-direction by the hysteresis effect in the moving part.

The stator in this design consists of a row of C-shape cores with lumped windings, and the cores are connected by highly-permeable connector blocks. All stator core

segments are made of laminated electric steel. There are two coils (coil A and coil B) wound on each C-shape core, and each coil has its current controlled independently.

The operating principle of the stage design shown in Figure 3-12 is briefly discussed here. The common-mode current in the top and bottom coils in the C-core generates a two-phase alternating motor flux, as shown by blue flux lines in Figure 3-12. The motor fluxes are traveling along the y-direction for thrust force generation. The motor fluxes also stabilize the passive magnetic suspension in x- and θ_z-directions. The extrusion features on the edges of the moving stage and the saliency of the stator poles can further improve the passive stiffness. Note that the suspension in θ_z-direction can also be actively controlled by the differential of the y-directional thrust forces on two sides of the stage to improve stiffness and damping.

On top of the motor flux, the differential current between currents in coil A and coil B generates a suspension control flux, as shown by the red flux line in Figure 3-12. Magnetic suspension control forces can be generated by the superposition of the two magnetic fluxes. As is shown in Fig. 3-12, in air gap 1 the two magnetic fluxes are in the same direction, while in air gap 2 the two fluxes are in the opposite directions. As a result, a net force in the positive z-direction can be generated at the pole face of this C-core. Similarly, vertical directional forces can be generated at every pole face, and these forces can work together to control the magnetic suspension of the moving stage in the z-, θ_x-, and θ_y-directions.

The design concept 1 can achieve the suspension and motion purpose of the stage with a simple stator design. It has two major drawbacks: (1) The passive suspension of the stage relies on a bias flux which is generated by the coils. Therefore, the coil current must always on to maintain stable suspension, which results in relatively low power efficiency. (2) Each coil in the stator is independently controlled, which requires a large number of power electronics, especially for stages with long traveling distances. (3) The moving stage typically uses heavy motor secondaries on the windings for flux concentration, therefore the moving stage may have low-frequency flexible modes, which can impair the control performance.

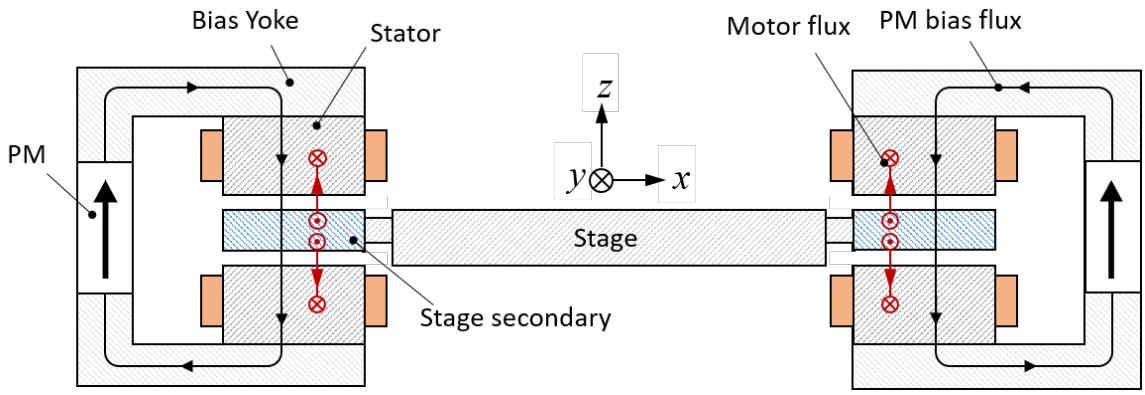

Figure 3-13: Design concept 2 for magnetically-levitated linear stage using permanent magnet flux biasing. In this design stators have independently controlled coils for suspension and thrust force generation

Group II: Design Concept 2

Figure 3-13 shows design concept 2 for magnetically-levitated linear stage in Group II. Here, the stage has two motor secondaries on its wings on both sides. When the stage is driven by linear hysteresis motors, the motor secondaries are made of magnetically-semi-hard alloy. There are four stators in this design, each has its windings implemented by a series lumped coils wrapped around the stator teeth, and each coil is independently controlled. The two stators on each side are connected with the flux biasing structure, which consists of a bias yoke and a permanent magnet. The permanent magnets generate bias fluxes as shown by the black flux lines in Figure 3-13. The bias flux generates passive stiffness in x- and θ_z-directions. In addition to the bias flux, each stator can generate a motor flux as shown by the red flux lines in Figure 3-13, which goes through the same air gaps with the bias flux. With each coil in the stators independently controlled, we are able to control the total thrust force, total normal force, and normal force generation at different y-directional locations on the stage secondaries. With all these forces and torques, the stage's suspension and motion in y-, z-, θ_x-, and θ_y-directions can be actively and independently controlled.

Compared to the design concept 1, the stage design concept 2 uses permanent magnets to provide bias flux for the passive magnetic suspension, which is effective for power saving. However, it shares the second drawback of the design concept 1,

i.e., each coil requires a separate power amplifier. This increases the complexity and cost of the system.

Group II: Design Concept 3

Figure 3-14 shows a design concept of a magnetically-levitated linear stage using separate motor stators and pitch control stators, where Figure 3-14(a) shows a cross-section diagram of the stage with magnetic fluxes, and Figure 3-14(b) shows a CAD model of this stage design concept. Here, the moving stage consists of a stage base made of non-magnetic material, four motor secondaries and four bearing secondaries. The motor secondaries and bearing secondaries are mounted on the wings of the stage base. There are two kinds of stators arranged around the stage: the motor stators and the pitch control stators. The stators are configured above and below the moving stage, and are supported with the C-shaped structure. Each motor stator has a set of three-phase windings, and each motor stator can generate independently controlled thrust and normal forces. With these forces, the stage's motion and suspension in y-, z-, θ_y-, and θ_z-directions can be actively and independently controlled.

The pitch control stator consists of two stator yokes with lumped windings connected with a horizontally-magnetized permanent magnets. The permanent magnets generate bias fluxes as shown with the black flux lines in Figure 3-14(a). This permanent magnet bias fluxes provide the stage's passive magnetic suspension stiffness in the x- and θ_z-directions. In addition, pitch control fluxes are generated by the windings in the pitch control stator, as shown by blue flux lines in Figure 3-14(a), which steer the permanent magnet bias flux to generate controlling torque about the x-direction. Figure 3-14(c) shows the air gap magnetic fluxes generated by the biasing permanent magnet and the pitch control stator windings. The pitch control flux is sinusoidally distributed in the air gaps and synchronous to the moving stage. In Figure 3-14(c), the pitch control flux attenuates the bias flux in the yellow region, and intensity the fluxes in the blue region, which generates pitch control torque about the x-axis.

Design concept 3 can fulfill the motion and suspension tasks, uses permanent mag-

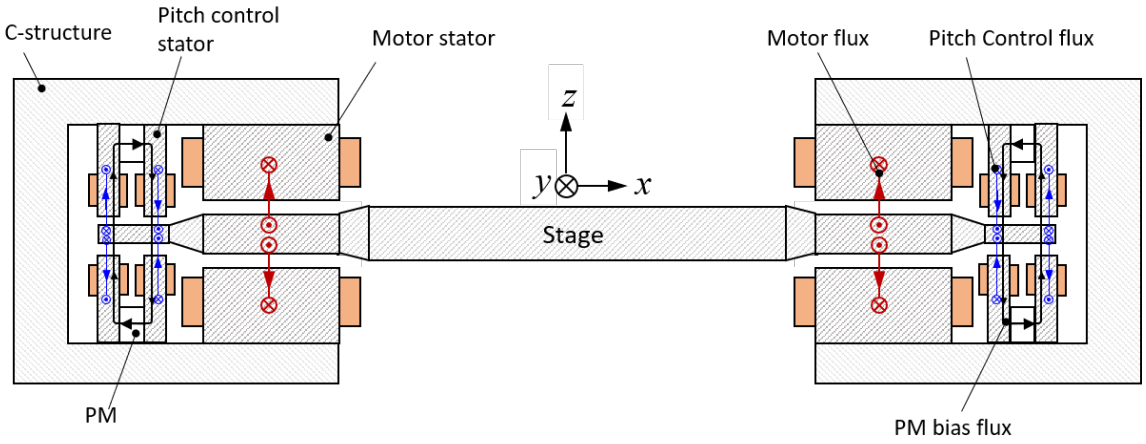

(a)

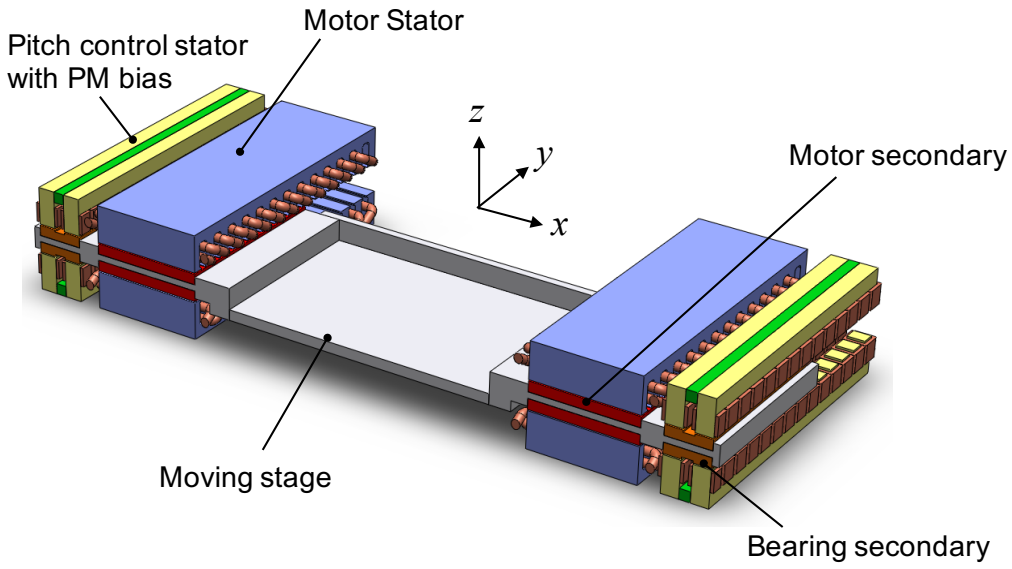

(b)

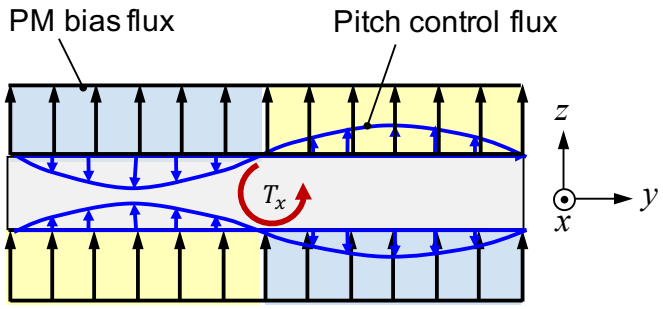

(c)

Figure 3-14: Design concept 3 for magnetically levitated linear stage with separate motor stator and pitch control stator with flux biasing. (a) Cross-section diagram of stage configuration. (b) Three-dimensional CAD diagram. (c) Air gap fluxes generated by the pitch control stator.

net flux biasing for power efficiency improvement. It also uses stators with windings connected in series, which reduces the number of independent phases compared to design concept 2. However, as shown in Figure 3-14(a) and (b), the moving stage presents a relatively wide design with secondaries on the wings, which may result in low structural stiffness and relatively low modal frequencies. In addition, there are eight stator segments in total (four motor stators and four pitch control stators) required in this concept, which is relatively complicated and expensive for manufacturing.

3.3.3 Group III: Passive Suspension in z-, θ_x-, and θ_y-directions

The third group of linear stage design concepts use passive suspension in z-, θ_x-, and θ_y-directions, and use active suspension in x- and θ_z-degrees of freedom. These designs resemble the bearingless slice motor for rotary motors, whose concept is shown in Fig. 3-3. We call these design concepts *linear bearingless slice motors*. Compared with the other two groups, linear stages using the linear bearingless slice motor typically uses less coils and sensors, since more degrees of freedom of the stage are passive. To our knowledge, there has been no prior work reporting the design for a linear bearingless slice motor stage.

Group III: Design Concept 1

Figure 3-15 shows a stage design concept using a linear bearingless slice motor. Here, the stage consists of a stage base in the center and four stage secondaries on left and right sides, which are made of magnetically-semi-hard materials. Two stator assemblies are configured on both sides of the stage, interfacing with the stage secondaries. The stator assembly consists of two stators connected with a biasing permanent magnet, and each stator has independently-controlled lumped coils. The permanent magnets in the stator assemblies provide bias fluxes as shown by the black flux lines in Figure 3-15. This bias flux provides passive suspension stiffness in z-, θ_x-, and θ_y-directions. In addition to the bias flux, driving the coils in the stators can gen-

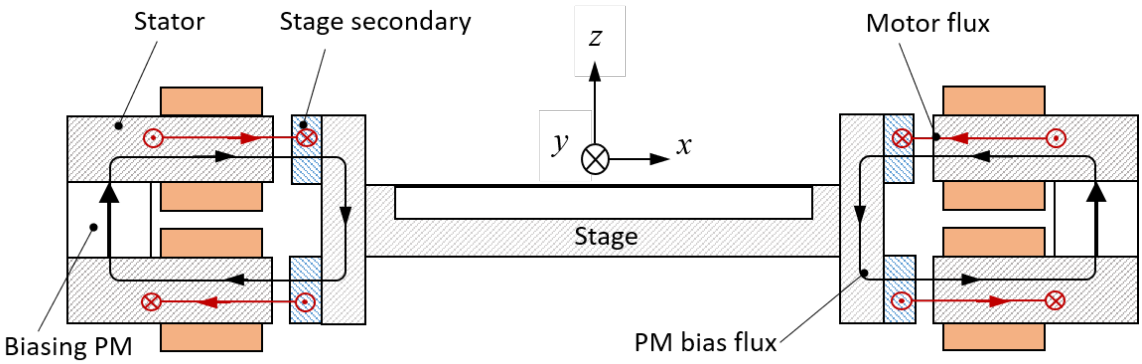

Figure 3-15: Cross-section diagram of the design concept 1 of linear bearingless slice motor. Stators have independently-controlled coils for suspension and thrust force generation.

erate motor fluxes as shown by the red flux lines in Figure 3-15. These fluxes are: (1) interacting with the stage secondaries for y-directional thrust force generation, and (2) steering the permanent magnet bias flux for x- and θ_z-directional suspension force/torque generation. Note that in this design, the magnetic suspension in the θ_y-direction can be actively controlled if additional stiffness and damping is needed. With all these magnetic fluxes, the motion and magnetic suspension of the stage in all degrees of freedom can be stabilized, either actively or passively.

The design concept shown in Figure 3-15 presents a simple stage design, and is convenient for including a separation wall between the stator and moving stage. The drawbacks of this design include: (1) The stators have coils that are driven independently, which requires a large number of power amplifiers. (2) When the stage is driven by linear hysteresis motors, the bias fluxes penetrate through the hysteresis secondaries, and thus biases the hysteresis loop. This may hurt the thrust force generation capability of the linear hysteresis motors, as it reduces the usable area of the hysteresis loop.

Group III: Design Concept 2

Figure 3-16 shows an alternative design of the linear bearingless slice motor, where Figure 3-16(a) shows a cross-section diagram, and Fig. 3-16(b) shows the top views of the magnetic fluxes in the bias flux air gaps. Here, the stage consists of a stage

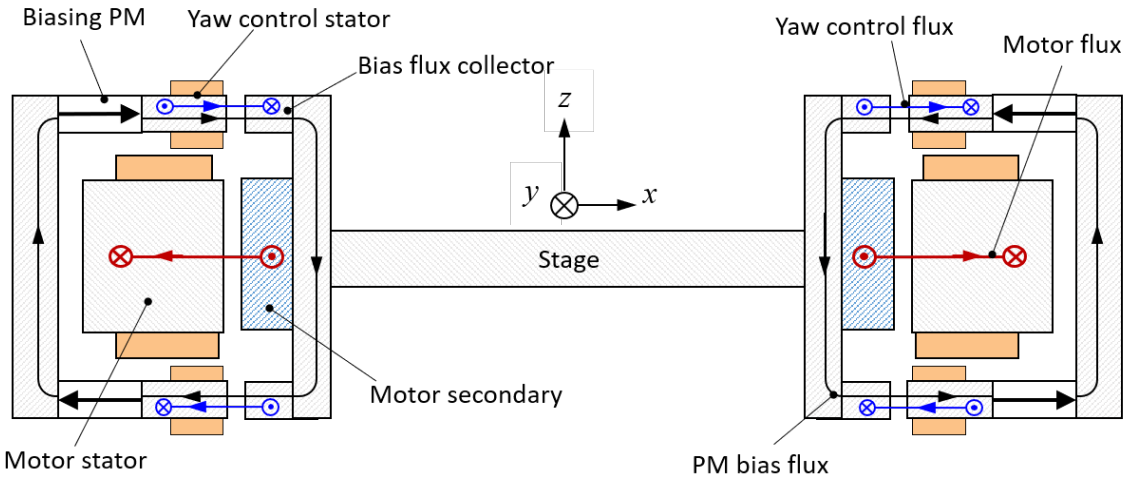

(a)

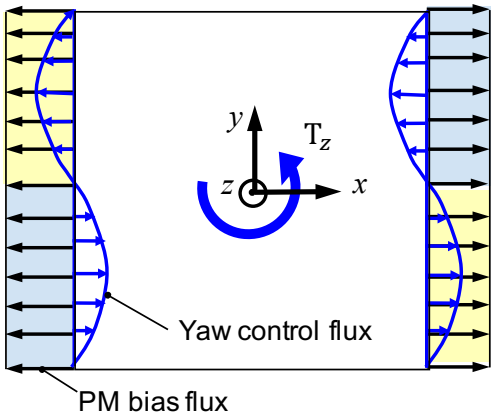

(b)

Figure 3-16: Design concept 2 of linear bearingless slice motor with separate motor stator and yaw control stator. (a) Cross section diagram of the stage. (b) Permanent magnet bias fluxes and the yaw control fluxes in the air gaps.

base and two kinds of stage secondaries: the motor secondary made of hysteresis alloy, and the bias flux collector made of highly-permeable soft magnetic material, such as low carbon steel. Two stator assemblies are configured on both sides of the moving stage. Each stator assembly includes one motor stator, two yaw control stators, two biasing permanent magnets, and a stator back iron connecting the top and bottom permanent magnets. The permanent magnets in the stator generate permanent magnet bias fluxes as shown by the black flux lines in Figure 3-16, which generates passive stiffness in z-, θ_x-, and θ_y-directions. In the same air gaps with the

bias flux, the coils in the yaw control stators generate yaw control fluxes, as shown by blue arrows in Figure 3-16(a) and (b). This flux steers the permanent magnet bias flux to generate θ_z-directional suspension torque. For example, in Fig. 3-16(b), the yaw control flux attenuates the PM bias flux in the blue region, while intensifying the flux in the yellow region. As a result, a torque about the vertical direction can be generated as shown by the T_z arrow in Fig. 3-16(b).

Finally, energizing the motor stators in the center of the stator assembly, motor fluxes as shown by the red lines in Figure 3-16(a) can be generated. Similar to design concept 2 in Group II, the common mode of the two side motor fluxes interact with the hysteresis motor secondaries to generate thrust forces in y-direction. The differential between the left and right motor fluxes generates lateral-direction reluctance force, which is used to control the x-directional magnetic suspension. With all three kinds of magnetic fluxes, we are able to stabilize all degree of freedom of the moving stage, either actively or passively.

3.4 Summary

In this chapter, we presented the functional requirements for the reticle transportation task in EUV photolithography machines, and discussed strategies and design concepts for the magnetically-levitated linear stage. We selected the design concept in Figure 3-16 for detailed design, building, and testing in this thesis work for the following reasons:

(1) In this design, three degrees of freedom of the stage are passively stabilized, which reduces the sensors and coils being used, thereby allows a simple system design.

(2) This design allows a small vertical height, which is favorable for the reticle transportation application, since the requirement of the system's vertical height is critical (< 100 mm).

(3) The control for stage's different degrees of freedom are largely decoupled, which allows simple control design.

(4) Although a number of works have studied the design for rotary bearingless slice motors, to our knowledge, there is no reported work on the design and testing for linear bearingless slice motors. In this thesis work, we would like to explore this new linear motor configuration, which potentially can be used for broader application areas, such as transportation stages in assembly lines, non-contact conveyance for metal, etc.

In the following chapters, we will discuss the modeling, design, building, and experimental testing for the selected stage design.

Chapter 4

Modeling and Analysis

This chapter presents modeling and analysis for the linear stage system, including both the magnetic suspension and the linear hysteresis motors. We first briefly rediscuss the operating principle for the stage design concept being selected in Section 4.1 to make this chapter self-contained. Then we present a first-order analytical model for the active magnetic suspension in lateral and yaw degrees of freedom in Section 4.2. Finally, the modeling for a pre-magnetized linear hysteresis motor is discussed in Section 4.3.

4.1 Operating Principle

In this section we present the operating principle of the selected magnetically-levitated linear stage design. Part of this section was discussed in Chapter 3.

Fig. 4-1 shows a CAD model for the magnetic structure in the selected magnetically-levitated linear stage design, which is comprised of two stator assemblies and one moving stage. The moving stage comprising one non-magnetic stage base, two soft iron stage backirons, four soft iron bias flux collectors, and two hysteresis motor secondaries. The stator assembly is comprised of one motor stator, two yaw control stators, and a flux-biasing structure including two rows of permanent magnets and a stage backiron. Each stator assembly also include two non-magnetic spacers for separating the bias magnetic flux path and the motor flux path.

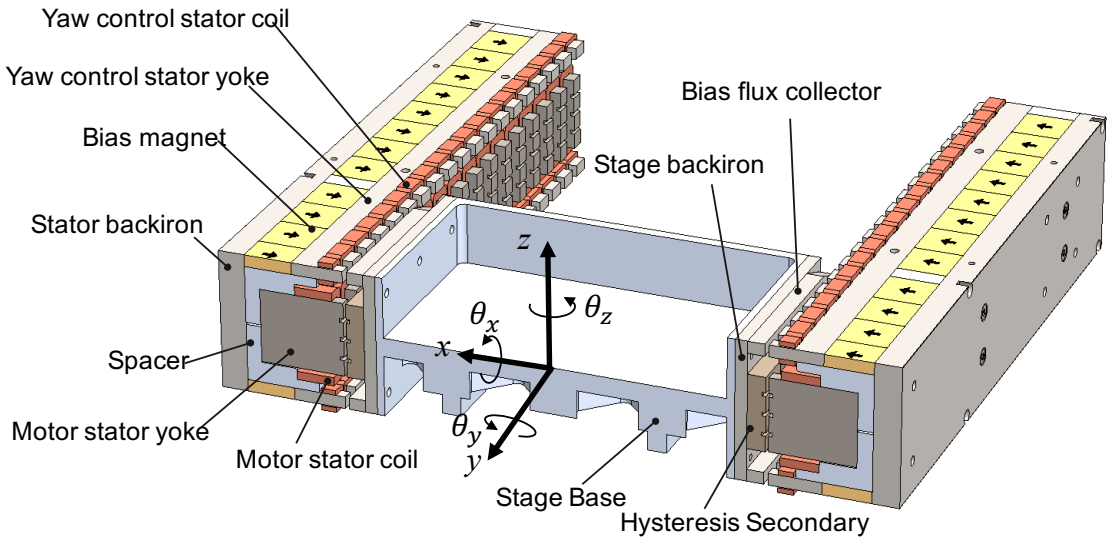

Figure 4-1: CAD model of the magnetic structures in our magnetically-levitated linear stage (cross-section view).

The coordinate system for the linear stage is shown in Fig. 4-1. The motion of the stage is along the y-axis. The system implements a linear bearingless slice motor design, with the magnetic levitation of the moving stage is active in x- and θ_z-directions, and is passive in z-, θ_x-, and θ_y-directions.

In the rest of this section, we first discuss the suspension forces/torques generation mechanisms of the linear stage in Section 4.1.1. Following this we discuss the thrust force generation mechanism of a linear hysteresis motor in Section 4.1.2.

4.1.1 Suspension Force/Torque Generation Principle

Figure 4-2 shows the magnetic fluxes in our magnetically-levitated linear stage. Figure 4-2(a) shows a cross-section diagram, and Figure 4-2(b) and (c) show the top views of the magnetic fluxes in the bias flux air gaps and motor air gaps, respectively. There are three kinds of magnetic fluxes in the system. The black lines and arrows in Figure 4-2(a) and (b) show the permanent magnet bias magnetic fluxes, which are used to generate passive magnetic suspension force and torques in z-, θ_x-, and θ_y-directions. When the stage is displaced in these directions, the bias fluxes in the air gaps provide restoring forces, and therefore stabilize the magnetic suspension

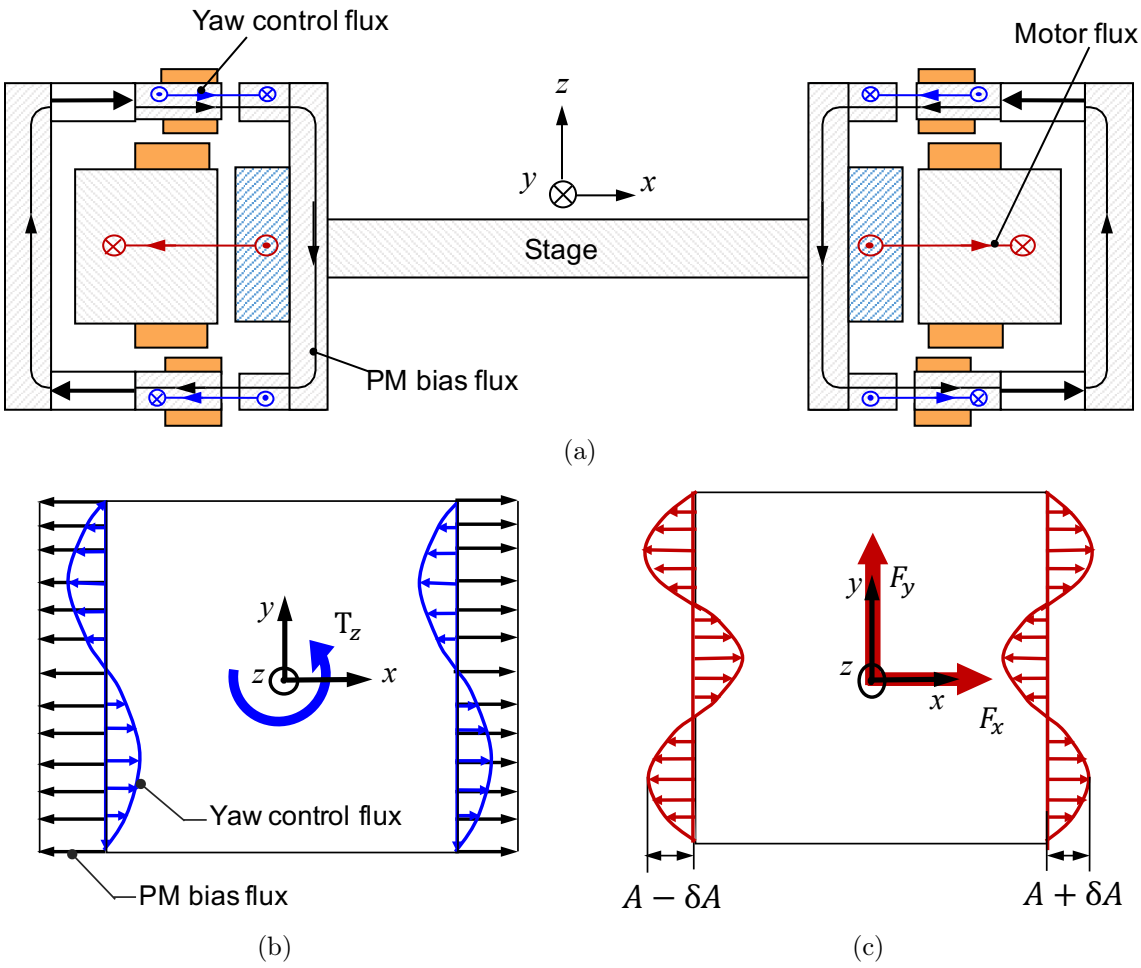

Figure 4-2: Magnetic fluxes in the magnetically-levitated linear stage. (a) Cross section diagram of the stage. (b) Top view of the permanent magnet bias fluxes and the yaw control fluxes in the air gaps. (c) Top view of the motor fluxes in the air gaps.

passively. Note that the bias fluxes also generate destabilizing force/torque in x- and θ_z-directions, and feedback control is required to stabilize the magnetic suspension in these degrees of freedom.

The blue arrows in Figure 4-2(a) and (b) show the yaw suspension control fluxes, which are generated by energizing the yaw control stators. In the top and bottom air gaps, the yaw suspension control flux is distributed sinusoidally, and is synchronous to the moving stage. This flux steers the permanent magnet bias flux (black arrows) to generate θ_z-directional suspension torque. For example, in Figure 4-2(b), the

yaw control flux intensities the bias flux in top left and bottom right areas, while attenuating the flux in bottom left and top right areas, thereby generating a torque about the vertical direction as shown by the T_z arrow in Figure 4-2(b).

The red arrows in Figure 4-2(a) and (c) represent the motor fluxes, which are generated by the windings in the motor stators. The common mode of the left and right motor fluxes is used to generate y-directional thrust force on the stage by interacting with the hysteresis motor secondaries. The differential between the left and right motor fluxes generates x-directional reluctance force, which is used to control the x-directional magnetic suspension. With all three magnetic fluxes, we are able to stabilize all degrees of freedom of the moving stage, either actively or passively.

4.1.2 Thrust Force Generation Principle

Our magnetically-levitated linear stage uses short-secondary linear hysteresis motors for the thrust force generation. Hysteresis motors have secondaries made of magnetically semi-hard materials. When the motor windings are excited, the induced magnetization in the secondaries lags behind the external field due to the magnetic hysteresis of the secondary material, thereby generating thrust forces [31]. The hysteresis motor secondaries are sometimes pre-magnetized using a large current amplitude before operation to improve the force generation capability of the motor, and these motors are often referred as ‘‘polarized hysteresis motors’’ or ‘‘pre-magnetized hysteresis motors’’ [64]. Aside from the hysteresis thrust forces, there are also additional reluctance thrust forces in linear hysteresis motors at the front and back edges of the motor secondaries due to the end effects, as shown in Figure 4-3. As a result, the force generation in a short-secondary linear hysteresis motor resembles that of an interior permanent magnet synchronous motor, where two mechanisms of thrust force generation are existing [65].

Hysteresis motors can operate in either synchronous mode or asynchronous mode. In our magnetically-levitated linear stage, we operate the linear hysteresis motors in the synchronous mode for two reasons: (1) The reluctance force in the linear hysteresis motor is oscillatory when the motor is asynchronous, which introduces undesirable

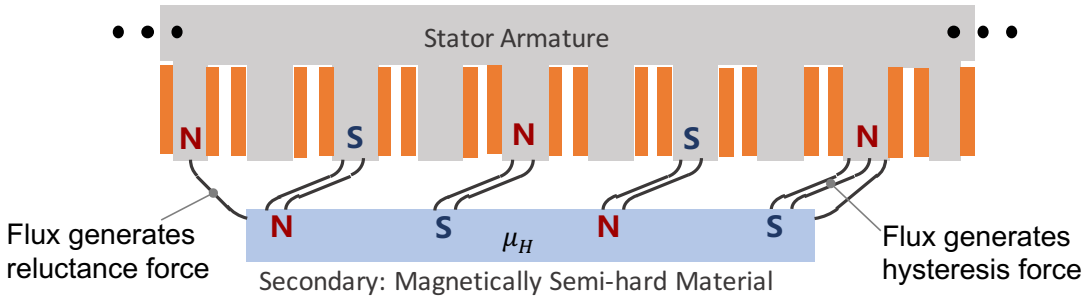

Figure 4-3: Diagram of air gap magnetic fluxes in a two-phase linear hysteresis motor showing the flux for hysteresis and reluctance thrust forces generation.

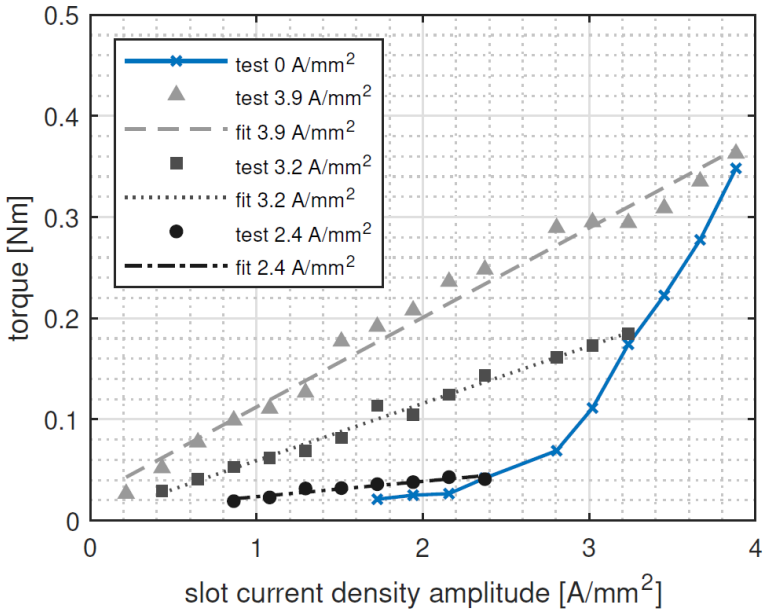

Figure 4-4: Experimental torque characteristic of a pre-magnetized rotary hysteresis motor. Figure is taken from [13].

vibrations to the stage. (2) Synchronous operation of the motor eliminates secondary hysteresis and eddy current losses due to the fundamental harmonic of the motor excitation. This is especially desirable for in-vacuum transportation systems, since cooling of the levitated moving stage is challenging when the stage is in vacuum.

In our linear stage, we operate the linear hysteresis motors with the motor secondaries pre-magnetized to improve the thrust force capability. The pre-magnetization has a very positive effect for the performance of hysteresis motors. Recent refer-

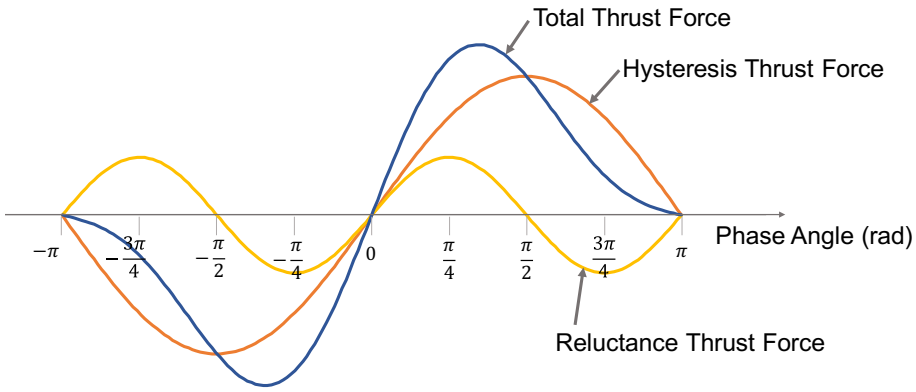

Figure 4-5: Thrust force and phase angle relationships in short-secondary linear hysteresis motors.

ence [13] has presented an experiment for a pre-magnetized rotary hysteresis motors, and Figure 4-4 shows the measured torque of a hysteresis motor pre-magnetized at different current density levels. It can be seen that the motor's torque under a certain current amplitude is significantly increased after pre-magnetization. Also, the motor's torque after pre-magnetization is largely linear with respect to the stator current density, which resembles the behavior of a permanent magnet synchronous motor. These characteristics for pre-magnetized hysteresis motors are favorable for our linear stage.

Figure 4-5 shows a diagram of the typical thrust force and phase relationship of a pre-magnetized linear hysteresis motor in synchronous operation. Here, the horizontal axis represents the phase difference between the stator excitation and the stage position, which is often referred as the force angle in linear synchronous motors. The hysteresis thrust force (orange line) is sinusoidal and has its maximum values at phase angles of $\pm\pi/2$, while the reluctance force (yellow line) is having two periods within $-\pi$ to π. The summation of two thrust forces makes the peaks of the total thrust force shift toward the center, as shown by the blue line in Figure 4-5.

4.2 Active Magnetic Suspension Modeling

This section presents a first-order model of the active magnetic suspension of the moving stage in x- and θ_z-degrees of freedom. We first derive the the first-order expression of magnetic fluxes in the air-gaps, and then we calculate the reluctance force/torque generation to the moving stage, which are the controlling force/torque applied to the stage for x- and θ_z-directional magnetic suspension. The assumptions of this model are listed as follows:

(1) The moving stage is centered in x- and θ_z-directions.
(2) The hysteresis effect of the secondary material is ignored in this analysis of normal force generation. Only reluctance force is considered.
(3) The permanent magnet bias flux is assumed to be uniformly distributed in the air gaps.
(4) Only the fundamental harmonics of the stators' winding distribution and magneto-motive forces are considered. All higher-order harmonics are ignored.
(5) Flux concentration at the front and back of the stage, i.e. end effect, is ignored.
(6) The permeability of the stator yokes and stage backiron is assumed to be infinity.
(7) The motor flux in the hysteresis secondary is assumed to be in the normal direction.

Although the model presented in this section does not capture the system's behavior in detail, it provides a first-order estimation for the suspension control force and torque, which is helpful to guide the design.

4.2.1 Lateral Suspension Force Generation

We first discuss the reluctance suspension force generation between the motor stator and the hysteresis secondary, which is used for lateral directional magnetic suspension control. Note that here only the normal directional reluctance forces are considered. The effect of the pre-magnetization of the secondaries and thrust force generation of the hysteresis motors are discussed in Section 4.3.

Define the magneto-motive forces (MMFs) generated by the left and right motor stators as $\mathcal{F}_m^L$ and $\mathcal{F}_m^R$. When the windings in both motor stators are excited with symmetrical three-phase currents, the generated MMF are

$$\mathcal{F}_m^L = N_m I_m^L \cos(\frac{2\pi}{\lambda_m} y_r + \phi_m), \tag{4.1}$$

$$\mathcal{F}_m^R = N_m I_m^R \cos(\frac{2\pi}{\lambda_m} y_r + \phi_m), \tag{4.2}$$

where y_r is the y-directional position in the stage coordinate with the origin defined in the center of the stage, N_m is the number of turns per phase per pole of the motor stator winding, I_m^L and I_m^R are the current amplitudes in the left and right motor stators, respectively, λ_m is the wavelength of the motor winding, ϕ_m is the phase of the motor stator excitation in the stage coordinate.

Then we calculate the magnetic permanences of the air gap and the hysteresis secondary. The magnetic reluctance of the hysteresis secondary over incremental length $\mathrm{d}y_r$ in the y-direction is

$$R_H = \frac{t_H}{\mu_H w_H \mathrm{dy_r}}, \tag{4.3}$$

where t_H and w_H are the thickness and width of the hysteresis secondary, respectively, and μ_H is the magnetic permeability of the hysteresis secondary. Similarly, the reluctance of the air gap at position y_r is

$$R_g = \frac{g_m}{\mu_0 g w_H \mathrm{dy_r}}, \tag{4.4}$$

where g_m is the length of the motor flux air gap, and μ_0 is the permeability in vacuum. The total permeance of the air gap and secondary stack over incremental length $\mathrm{d}y_r$ is

$$\begin{aligned} P_t &= \frac{1}{R_H + R_g} = \frac{1}{\frac{g_m}{\mu_0 w_H \mathrm{dy_r}} + \frac{t_H}{\mu_H w_H \mathrm{dy_r}}} \\ &= \frac{\mu_0 \mu_H w_H}{g_m \mu_H + t_H \mu_0} \mathrm{dy_r}. \end{aligned} \tag{4.5}$$

Then normal-directional air gap flux density distribution in the left and right air

gaps can be calculated as

$$B_m^L = \frac{P_t \mathcal{F}_m^L}{w_H \mathrm{dy_r}} \tag{4.6}$$

$$B_m^R = \frac{P_t \mathcal{F}_m^R}{w_H \mathrm{dy_r}}. \tag{4.7}$$

Substituting (4.1), (4.2), and (4.5) into (4.6) and (4.7), we have

$$B_m^L = \frac{\mu_0 \mu_H}{g_m \mu_H + t_H \mu_0} N_m I_m^L \cos(\frac{2\pi}{\lambda_m} y_r + \phi_m) \tag{4.8}$$

$$B_m^R = \frac{\mu_0 \mu_H}{g_m \mu_H + t_H \mu_0} N_m I_m^R \cos(\frac{2\pi}{\lambda_m} y_r + \phi_m). \tag{4.9}$$

The total reluctance forces on the stage generated by the left and right motor stators can be calculated using the Maxwell stress tensor method as

$$f_m^L = \int_{-L_H/2}^{L_H/2} \frac{(B_m^L)^2}{2\mu_0} w_H \mathrm{dy_r}, \tag{4.10}$$

$$f_m^R = \int_{-L_H/2}^{L_H/2} \frac{(B_m^R)^2}{2\mu_0} w_H \mathrm{dy_r}, \tag{4.11}$$

where L_H is the length of the hysteresis motor secondary. In our linear stage design, $L_H = \frac{3}{2}\lambda_m$. Substitute (4.8) and (4.9) into (4.10) and (4.11), we have

$$f_m^L = \frac{3\mu_0 \mu_H^2 w_H \lambda_m}{8(g\mu_H + t_H \mu_0)^2} N_m^2 (I_m^L)^2, \tag{4.12}$$

$$f_m^R = \frac{3\mu_0 \mu_H^2 w_H \lambda_m}{8(g\mu_H + t_H \mu_0)^2} N_m^2 (I_m^R)^2. \tag{4.13}$$

Note that when ignoring the secondary's hysteresis effect and only consider the fundamental harmonic of the motor excitations, the attractive force between the motor stator and the secondary does not depend on the force angle ϕ_m.

Define $\bar{I}_m = (I_m^L + I_m^R)/2$ and $\delta I_m = (I_m^R - I_m^L)/2$ as the common-mode and differential current amplitudes of the left and right motor stator currents. Then we have $I_m^R = \bar{I}_m + \delta I_m$, $I_m^R = \bar{I}_m - \delta I_m$. Also define constant $K_{m1} = \frac{3\mu_0 \mu_H^2 w_H \lambda_m}{8(g_m \mu_H + t_H \mu_0)^2} N_m^2$.

The total x-directional force on the stage can be calculated as

$$\begin{aligned} f_m^x &= f_m^R - f_m^L = K_{m1}\Big((I_m^R)^2 - (I_m^L)^2\Big) \\ &= K_{m1}\Big((\bar{I}_m^2 + 2\bar{I}_m\delta I_m + \delta I_m^2) - (\bar{I}_m^2 - 2\bar{I}_m\delta I_m + \delta I_m^2)^2\Big) \\ &= 4K_{m1}\bar{I}_m\delta I_m. \end{aligned} \tag{4.14}$$

When our linear stage is operating, the common-mode current $\bar{I}_m$ is typically set to a constant value for thrust force generation, and the differential current δI_m is used to control the stage's suspension in the lateral direction. Since the stage's deviation from its equilibrium position is small, typically we have $\bar{I}_m \gg \delta I_m$. Define $K_i^x = 4K_{m1}\bar{I}_m$ as the force constant in the x-direction. Then the total x-directional force on the stage is

$$f_m^x = K_i^x \delta I_m. \tag{4.15}$$

This force f_m^x is used to control the x-directional magnetic suspension of the moving stage.

Let us also calculate the yaw-directional torque generated by the motor stator excitations. The torque on the stage generated by the left and right motors can be calculated as

$$T_m^L = \int_{-L_H/2}^{L_H/2} \frac{(B_m^L)^2}{2\mu_0} w_H y_r \mathrm{dy_r}, \tag{4.16}$$

$$T_m^R = \int_{-L_H/2}^{L_H/2} \frac{(B_m^R)^2}{2\mu_0} w_H y_r \mathrm{dy_r}. \tag{4.17}$$

Substitute (4.8) and (4.9) into (4.16) and (4.17), we have

$$T_m^L = \frac{3\mu_0\mu_H^3 w_H \lambda_m^2 N_m^2}{32\pi(g_m\mu_H + t_H\mu_0)^2}(I_m^L)^2 \sin(2\phi_m), \tag{4.18}$$

$$T_m^R = \frac{3\mu_0\mu_H^3 w_H \lambda_m^2 N_m^2}{32\pi(g_m\mu_H + t_H\mu_0)^2}(I_m^R)^2 \sin(2\phi_m). \tag{4.19}$$

Define $K_{m2} = \frac{3\mu_0\mu_H^2 w_H \lambda_m^2 N_m^2}{32\pi(g_m\mu_H + t_H\mu_0)^2}$. The total yaw-directional torque to the moving stage

is

$$\begin{aligned} T_m^z &= K_{m2}\sin(2\phi_m)\Big((I_m^R)^2 - (I_m^L)^2\Big) \\ &= 4K_{m2}\bar{I}_m\sin(2\phi_m)\delta I_m. \end{aligned} \tag{4.20}$$

In our linear stage design, this torque T_m^z is a disturbance signal to the yaw-directional suspension control. More discussion about the effect of this disturbance torque is shown in Section 4.2.3.

4.2.2 Yaw Suspension Torque Generation

In this section, we present a first-order analytical model for the yaw-directional suspension torque generation using a combination of the permanent magnet bias flux and the yaw control stator excitation. Define the magneto-motive force generated by one yaw control stator as

$$\mathcal{F}_s = N_s I_s \sin(\frac{2\pi}{\lambda_s} y_r), \tag{4.21}$$

where N_s is the number of turns per phase pole in the yaw control stator, I_s is the current amplitude in the yaw control stator windings, and λ_s is the wavelength of the yaw control stator excitation, which equals to the length of the bias flux collector on the moving stage.

The bias flux air gap permeance over incremental length $\mathrm{d}y_r$ is

$$P_g^b = \frac{\mu_0 w_b \mathrm{dy_r}}{g_b}, \tag{4.22}$$

where g_b is the bias flux air gap length, and w_b is the width of the bias flux collector. Note that the yaw control stator shares the same air gap with the permanent magnet bias flux. The air gap flux distribution generated by the yaw control stator excitation can be calculated as

$$B_s = \frac{P_g^b \cdot \mathcal{F}_s}{w_b \mathrm{dy_r}} = \frac{\mu_0}{g_b} N_s I_s \sin(\frac{2\pi}{\lambda_s} y_r). \tag{4.23}$$

Assume the amplitude of the permanent magnet bias flux is B_{bias}, which is a constant

and distributed uniformly in all bias flux air gaps. Then the total flux density in the bias flux air gap is

$$B_t^b = B_{bias} + B_s = B_{bias} + \frac{\mu_0}{g_b} N_s I_s \sin(\frac{2\pi}{\lambda_s} y_r). \tag{4.24}$$

Define L_b as the length of the bias flux collector. In our linear stage design, $L_b = \lambda_s$. Then we can calculate the normal force and θ_z-directional torque generation in this air gap as

$$\begin{aligned} F_s^n &= \int_{-L_b/2}^{L_b/2} \frac{(B_t^b)^2}{2\mu_0} w_b \mathrm{dy_r} \\ &= \frac{w_b}{2\mu_0} B_{bias}^2 + \frac{w_b \mu_0 \lambda_s}{4 g_b^2} N_s^2 I_s^2, \end{aligned} \tag{4.25}$$

$$\begin{aligned} T_s &= \int_{-L_b/2}^{L_b/2} \frac{(B_t^b)^2}{2\mu_0} w_b y_r \mathrm{dy_r} \\ &= \frac{N_s w_b \lambda_s^2}{2\pi g_b} B_{bias} I_s. \end{aligned} \tag{4.26}$$

In our design, all four yaw control stators share the same current amplitude I_s. As a result, the normal forces form the yaw control stators are canceling each other when the stage is centered, and the total controlling torque on the stage about the vertical axis is

$$T_s^z = 4T_s = \frac{2N_s w_b \lambda_s^2}{\pi g_b} B_{bias} I_s \tag{4.27}$$

Define $K_i^{\theta_z} = \frac{2N_s w_b \lambda_s^2}{\pi g_b} B_{bias}$. Then the yaw-directional controlling torque on the moving stage can be written as

$$T_s^z = K_i^{\theta_z} I_s. \tag{4.28}$$

In this way, we are able to use the yaw control stator current amplitude I_s to control the stage's suspension in θ_z-degree of freedom.

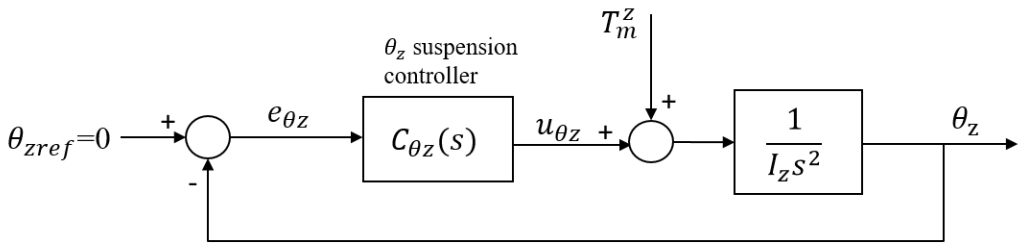

Figure 4-6: Block diagram of the θ_z-directional magnetic suspension control loop. T_m^z is injected as a disturbance signal.

4.2.3 Discussion on Torque Disturbance Generated by Motor Stators

Let us briefly discuss the effect of the disturbance torque in the θ_z-direction generated by the motor stators shown in (4.20), which is rewrite again here as

$$T_m^z = \frac{3\mu_0\mu_H^2 w_H \lambda_m^2 N_m^2}{8\pi(g_m\mu_H + t_H\mu_0)^2}\bar{I}_m \sin(2\phi_m)\delta I_m. \tag{4.29}$$

This torque is a disturbance signal in the yaw-directional magnetic suspension. We can see from (4.29) that T_m^z is proportional to δI_m, which is the control effort signal for the stage's x-directional suspension. Since the stage's displacement in the x-direction from the equilibrium is small when the stage is levitated (typically below 50 μm), the required correcting current amplitude δI_m is also small (typically below 0.05 A). This effect, together with a relatively small torque constant in (4.29), makes the effect of this disturbance torque small and therefore ignorable in our stage design.

Let us here substitute the following typical values of the parameters into (4.29) to get an estimate for the disturbance torque: $\mu_H \approx 30\ \mu_0$, $\lambda = 112$ mm, $w_H = 40$ mm, $g_m = 1.5$ mm, $N_m = 150$, $t_H = 9.5$ mm, $\bar{I}_m = 2$ A, $\phi_m = \pi/4$ rad (maximum allowed force angle in our linear stage), $\delta I_m = 0.05$ A. With these parameters, we can calculate that the typical magnitude of the disturbance torque is 0.24 mNm.

We then estimate the stage's displacement from the equilibrium in θ_z-direction caused by this disturbance torque. Figure 4-6 shows a block diagram of the θ_z-directional magnetic suspension control loop. Here, the plant being controlled is

$P(s) = 1/I_z s^2$, where I_z is the stage's inertia about the vertical axis, which equals $0.037\ \mathrm{kg} \cdot \mathrm{m}^2$ for our linear stage. The controller $C_{\theta_z}(s)$ has a unit of Nm/rad, and the control effort signal is the controlling torque in the yaw direction. Then the transfer function from the disturbance torque T_m^z to the stage's yaw-directional displacement θ_z is

$$\frac{\theta_z(s)}{T_m^z(s)} = \frac{1}{I_z s^2} \cdot S_{\theta_z}(s), \tag{4.30}$$

where $S_{\theta_z}(s)$ is the sensitivity of the θ_z-directional magnetic suspsenison loop, which is defined as $S_{\theta_z}(s) = 1/(L_{\theta_z}(s) + 1)$, where $L_{\theta_z}(s)$ the loop return ratio for yaw suspension loop.

Assume the bandwidth of the x-directional magnetic suspension is 60 Hz. Since δI_m is the control effort signal of the x-directional magnetic suspension, its typical frequency is around the bandwidth frequency. Therefore we approximate the disturbance torque T_m^z as a sinusoidal signal with a frequency of 60 Hz, and an amplitude of 0.24 mNm. Also assume the maximum sensitivity of the θ_z-directional magnetic suspension is $\max(S_{\theta_z}(j\omega)) = 5$, which is a typical value for magnetic suspension control systems. Then we can estimate the maximum yaw displacement of the stage caused by such disturbance as

$$\max(\theta_z) = \frac{1}{I_z(60 \times 2\pi)^2} \max(S_{\theta_z}) = 2.3 \times 10^{-7}\ \mathrm{rad}, \tag{4.31}$$

which corresponds to 1.3×10^{-5} degrees. Through this discussion, we can see that the effect of such disturbance torque is small, and we are able to effectively reject this disturbance through the feedback control for the stage's θ_z-directional magnetic suspension.

4.3 Linear Hysteresis Motor Modeling

This section discusses the modeling of the linear hysteresis motors in our magnetically-levitated linear stage. The comparison between the modeled force and experimental

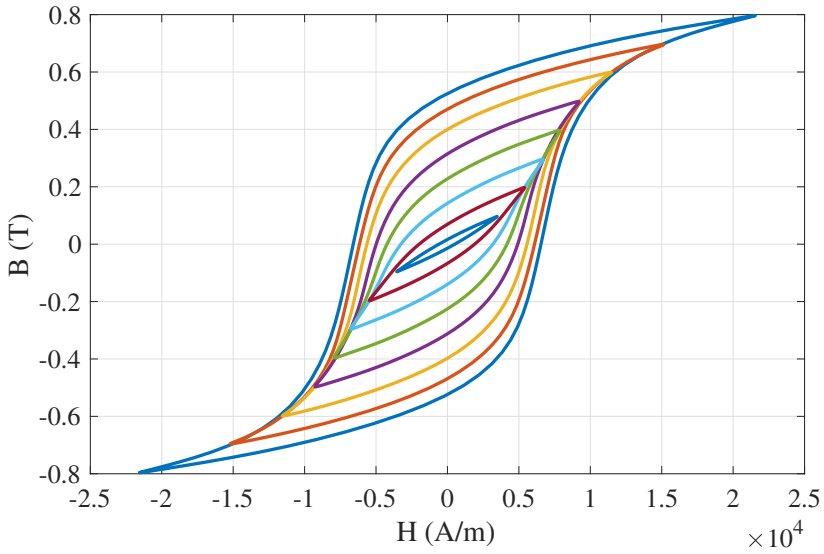

Figure 4-7: Measured hysteresis property of D2 tool steel under different excitation amplitude. Horizontal axis: field intensity (H-field). Vertical axis: flux density (B-field). Measurement taken by Dr. Gereon Goldbeck at the Johannes Kepler University in Linz, Austria.

measurements is presented in Chapter 6.

As is discussed in Section 4.1.2, in our linear stage, we pre-magnetize the hysteresis motor secondaries to improve the linear motors' thrust force generation capability. The pre-magnetization is done by setting the air gap length to zero, i.e., making the moving stage in full contact with one motor stator, and excite the motor stator with a DC three-phase current of an increasing current amplitude up to 5 A. When the pre-magnetizing field generated by the stator is removed, the magnetization inside the motor secondary does not fully vanish due to the material's magnetic hysteresis. The secondaries on both sides of the stage are pre-magnetized symmetrically. When the motor is operating, we energize the motor stators at a lower current amplitude compared with the pre-magnetization process (around 2 A), and the motor air gap length is set to 1.5 mm. Under this condition, the motor's operation does not significantly change the magnetization status of the secondaries. As a result, the pre-magnetized linear hysteresis motors operate like weak linear permanent magnet motors with relatively high secondary permeability.

In our linear hysteresis motor, hardened D2 tool steel is selected for the secondary

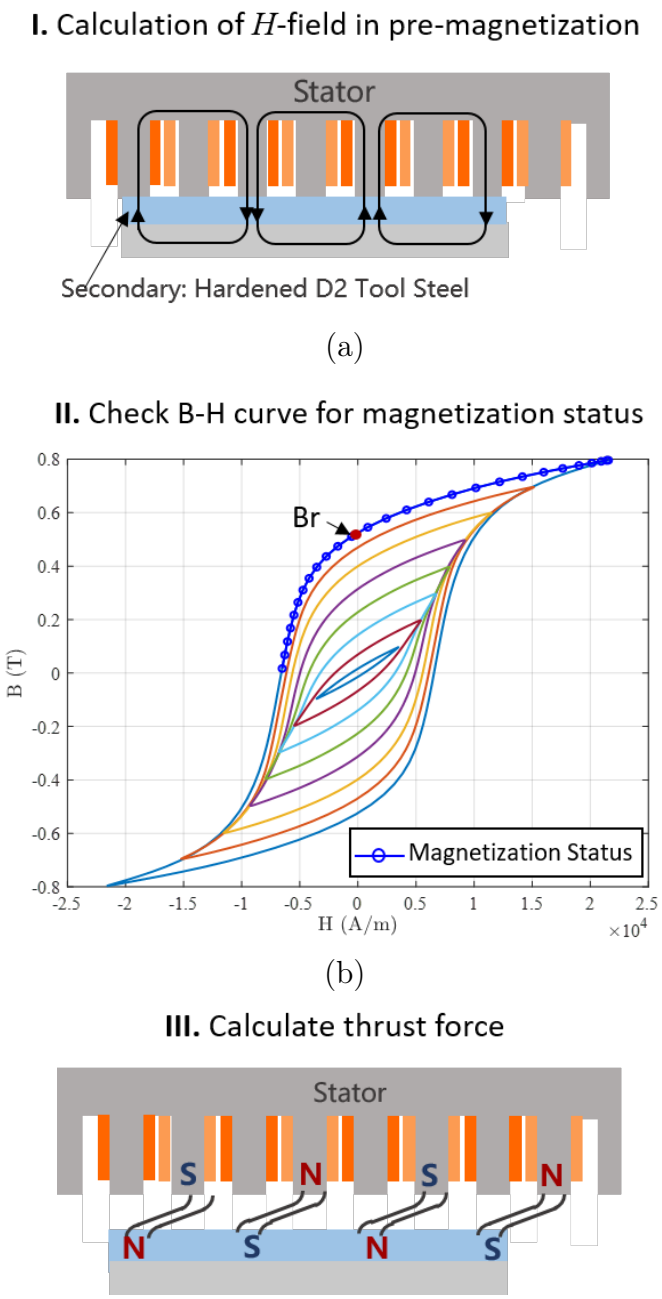

Figure 4-8: Modeling process of pre-magnetized linear hysteresis motor. (a) Calculating H-field generated by the stator during pre-magnetization process using finite element method. (b) Checking the measured B-H curve of the secondary material to determine the curve of material's magnetization status. (c) Calculate the motor's thrust force generation treating the pre-magnetized hysteresis secondary as permanent magnet with nonlinear B-H curve.

material. Figure 4-7 shows the measured hysteresis loops of the secondary material under different flux density amplitude, which is taken by Dr. Gereon Goldbeck at the Johannes Kepler University in Linz, Austria. Reference [66] introduces the hysteresis measurement setup being used.

Figure 4-8 summarizes the modeling process of the pre-magnetized linear hysteresis motors in this work. There are three steps in this modeling. In the first step, we calculate the field intensity (H-field) inside the secondary generated by the stator in the pre-magnetization process, as shown in Figure 4-8(a). In the second step, we check the measured hysteresis data of the motor secondary material, and use the calculated pre-magnetizing H-field to determine the magnetization status of the secondary after pre-magnetization, as shown in Figure 4-8(b). Finally, we model the pre-magnetized hysteresis secondary as an array of permanent magnets with its material property determined in the previous steps, and calculate the thrust force generation of the linear motor, as shown in Figure 4-8(c). Below we discuss the detailed modeling process in each step.

Step I: Pre-magnetizing field calculation.

In the first step of the modeling, we calculate the field intensity (H-field) inside the secondary generated by the stator in the pre-magnetization process. Here the finite element package FEMM [67] is used for this calculation. In this simulation, the air gap length of the motor is set to zero, and the current amplitude in the stator three-phase windings is 5 A. The frequency of the simulation is set to zero. The stator's geometric parameters are presented in Figure 5-19 and Table 5.5 in Chapter 5. The length of hysteresis motor secondary equals 9 motor stator tooth pitch, which is 1.5 times of the wavelength of motor stator MMF. The hysteresis secondary thickness is 9.52 mm, and the back iron thickness is 6.35 mm. The width of the hysteresis motor is 40 mm. Figure 4-9 shows the B-H property of the secondary material used in this simulation, which is achieved by collecting the maximum points in each measured B-H loop of the hardened D2 tool steel in Figure 4-7. Figure 4-9 is also often referred to as the ''virgin magnetization curve'' of a hysteresis material, which represents the B-H status of the hysteresis material when it is first being magnetized.

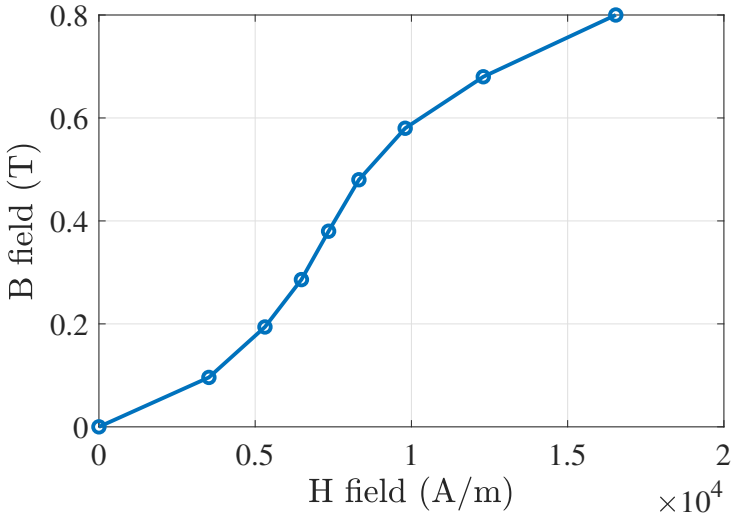

Figure 4-9: Nonlinear B-H curve of secondary material during pre-magnetization simulation. Also known as the "virgin magnetization curve" of the material.

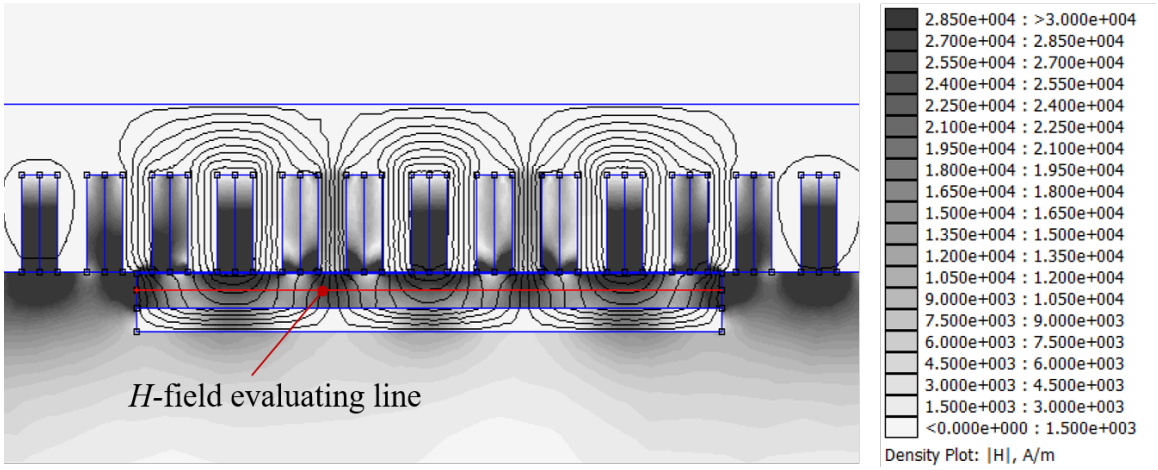

Figure 4-10: Magnetic field intensity (H-field) in the pre-magnetization process simulated with FEMM. Here magnetostatic simulation is used. The air gap length is zero, and current amplitude equals 5 A.

Figure 4-10 shows a simulated field plot of the H-field distribution in the linear hysteresis motor during the pre-magnetization process. Here the H-field evaluating line is defined as a horizontal line in the secondary through the middle of its thickness, as shown by the red line in Figure 4-10. Figure 4-11 shows the magnitude and angle of the simulated H-field along the H-field evaluating line in the secondary, i.e., the red line in Figure 4-10. The average of the H-field magnitude and the linear fit for

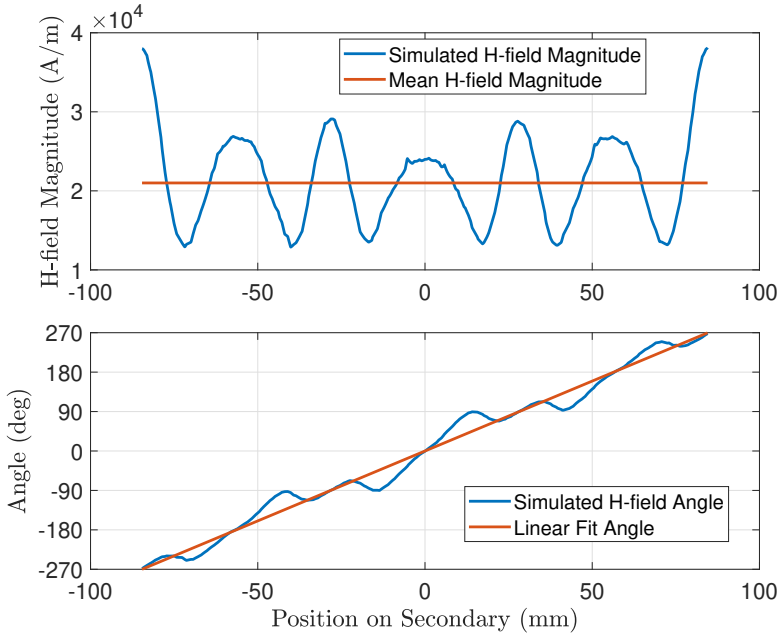

Figure 4-11: Simulated field intensity magnitude and angle in secondary along mid line during the pre-magnetization process.

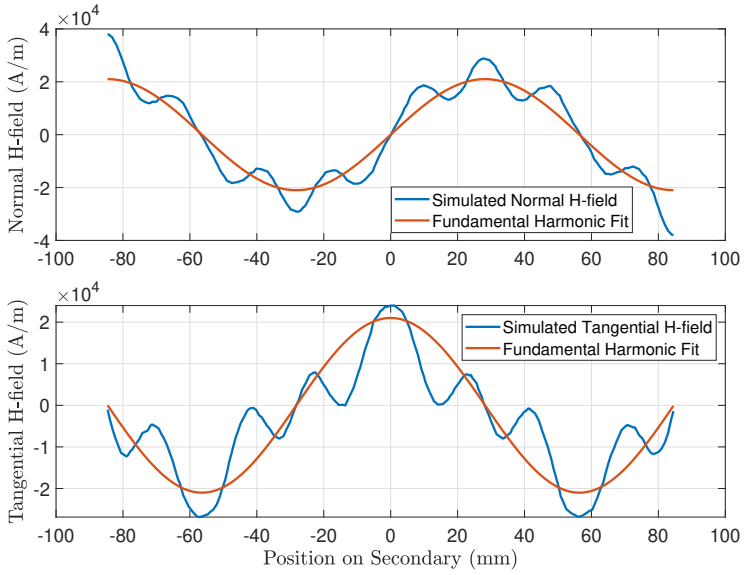

Figure 4-12: Normal and tangential components of field intensity during the pre-magnetization in secondary along mid line simulated by FEMM. Blue: simulated data. Orange: fundamental harmonic fit data calculated from magnitude $|H| = 2.1 \times 10^4$ A/m and angle $\theta = 2\pi y_r/\lambda_m$.

the angle are also plotted in orange lines in Figure 4-11. Here, the average H-field magnitude is $|H| = 2.1 \times 10^4$ A/m, and the fitted angle is $\theta = 2\pi y_r/\lambda_m$ rad, where $\lambda_m = 112$ mm is the wavelength of the motor stator windings. Figure 4-12 shows the normal (vertical) and tangential (horizontal) components of the simulated H-field. The fundamental harmonic fit of the H-field components calculated from the average magnitude and the fitted phase are also plotted in Figure 4-12. It can be seen that the two components of the simulated H-field are in general matching well with their fundamental harmonic fits.

Step II: Checking B-H curve for magnetization status.

In the second step of the modeling, we check the measured B-H curve of the hysteresis secondary material to find its magnetization status after the pre-magnetization. The measured B-H curve of the secondary material is shown again in Figure 4-13. In Step I, we calculated that the average magnitude of the H-field in the secondary during pre-magnetization is $|H| = 2.1 \times 10^4$ A/m. Checking the data in Figure 4-13, it can be seen that the magnetization status of the material after pre-magnetization can be represented by the outmost loop in Figure 4-13, specifically the region highlighted with blue circles. When the external pre-magnetizing field generated by the stator is removed, the magnetization of the material is $B_r = 0.53\ T$, which is the remanence of the material.

Step III: Thrust force calculation.

In the last step, we model the hysteresis secondary as a permanent magnet array, and calculate the thrust force of the motor using finite element method. Here, the magnetic property of the magnets representing the secondary is set with the magnetization status curve in shown in Figure 4-13. Note that unlike typical rare-earth magnets, this B-H curve is nonlinear. When an alternating external field is generated by the stator, such secondary can exhibit hysteresis when they are demagnetized. That is, when an external H-field pushes the material's magnetization status to a lower point in the demagnetization curve, the flux density level does not recover to the previous magnitude when the external H-field changes direction. Instead, the magnetization status follows a minor hysteresis loop, thereby generating secondary

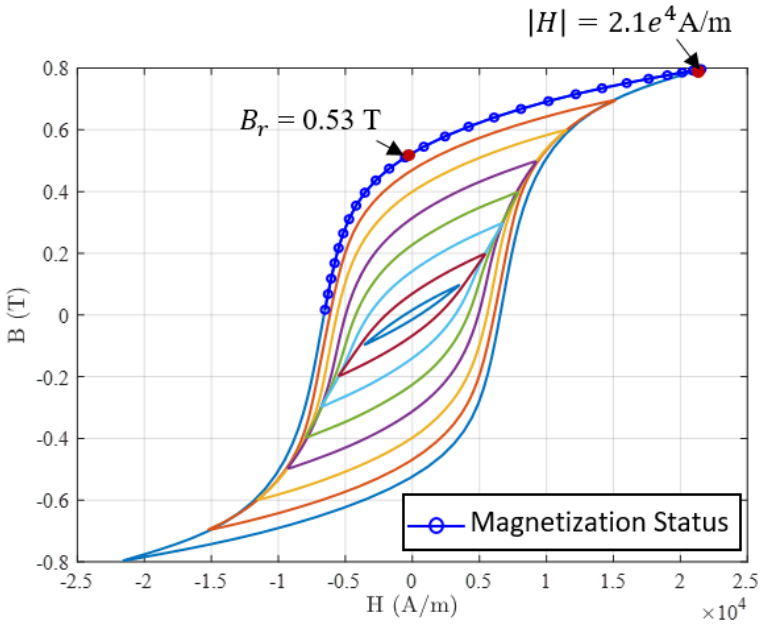

Figure 4-13: Measured B-H curve of the D2 tool steel. The material's magnetization status curve after pre-magnetization is highlighted in blue circles.

loss. In our model for pre-magnetized linear hysteresis motors, this effect is not captured. This is acceptable here for two reasons. First, the H-field magnitude generated by the stator when the motor is operating is significantly smaller than the stator field during the pre-magnetization phase. This allows us to approximate the B-H curve in of the material in the operating range with a linear curve without significant loss of accuracy. Second, in our linear stage, we operate the motor synchronously, where the fundamental harmonic of the external magnetic field does not slip with respect to the secondary material, and only has a phase difference with respect to the secondary material when the stage is accelerating or decelerating. This fact further reduces the magnitude of the external H-field variation range in the material. As a result, the model presented here is able to capture the behavior of the linear hysteresis motors in our linear stage with sufficient accuracy.

The calculation of the thrust force also uses FEMM. In this simulation, the hysteresis secondary is modeled as an array of permanent magnets comprising 40 segments, as shown in Figure 4-14. The material of all segments are the same, and the magnetization direction of each segment is determined the H-field direction during the

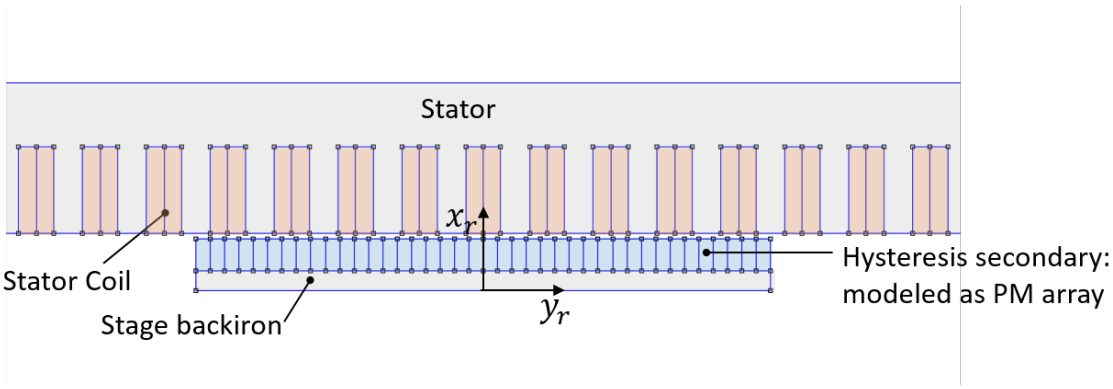

Figure 4-14: Finite element model for linear hysteresis motor thrust force calculation in FEMM. Here the pre-magnetized hysteresis secondary is modeled as a permanent magnet array of 40 segments. The material of all segments are the same, while the direction of the magnetization is determined by the H-field during pre-magnetization, i.e. $\theta = 2\pi y_r/\lambda_m$ rad.

pre-magnetization phase. Specifically in this model, we set the magnetization angle as $\theta = 2\pi y_r/\lambda_m$ rad, where y_r is the position of the center point of each segment in the stage coordinates. Figure 4-15 shows the method of setting the nonlinear permanent magnet property in FEMM, where the blue solid line shows the target material property, which has $H_c = 6.6\times10^3$ A/m and $B_r = 0.53$ T. The method to set such material property is: (1) set the secondary material's coercivity as $H_c = 6.6 \times 10^3$ A/m, and (2) set the material's B-H property as the B-H curve of the material shifted to the right by H_c, as shown by the orange dashed line shown in Figure 4-15. Note that this simulation will include both hysteresis and reluctance thrust force generation, since the secondary material has magnetization for hysteresis thrust force generation, and has relatively high permeability for reluctance force generation.

We simulated pre-magnetized linear hysteresis motor using FEMM while sweeping the phase of the stator current. The amplitude of the motor current is set to 2 A. Figure 4-16 shows the simulated field distribution in the pre-magnetized linear hysteresis motor at different phase difference ϕ_m between the stator and secondary magneto-motive forces. The phase difference ϕ_m is often referred as force angle for linear synchronous motors. As shown in Figure 4-16(a), when $\phi_m = 0$, the motor field and secondary field are along the same direction, and the air gap field is largely in the

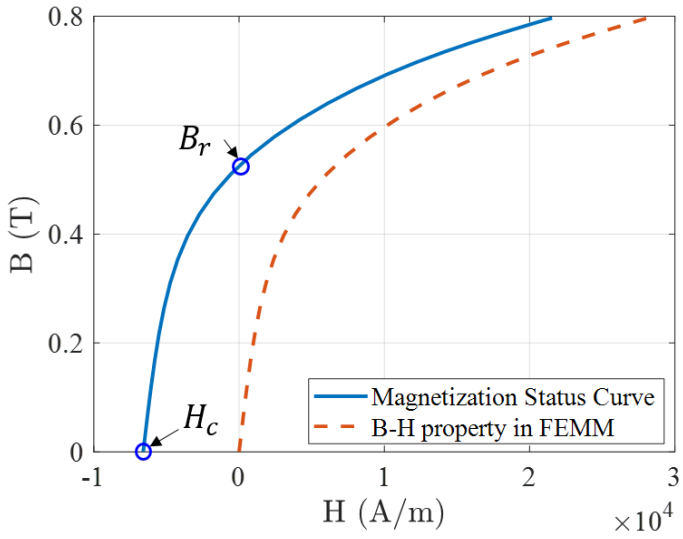

Figure 4-15: The method of setting secondary material property in FEMM. Blue solid line: target nonlinear permanetn magent material property with $H_c = 6.6 \times 10^3$ A/m and $B_r = 0.53$ T. Orange dashed line: B-H property of hysteresis secondary material in FEMM model. Note that the material's coercivity is set to $H_c = 6.6 \times 10^3$ A/m in FEMM.

normal direction. There is no thrust force generated at this moment, and the normal attractive force generation of the motor reaches its maximum. When $\phi_m = \pi/2$, the field lines are tilted in the air gap including both normal and tangential components as shown in Figure 4-16(b), and the hysteresis thrust force generation reaches its maximum. When $\phi_m = \pi$, the stator field and secondary field are opposed to each other. As shown in Figure 4-16(c), the secondary field is largely returning through the stage backiron. There is no thrust force generation at this moment, and the normal attractive force reaches its minimum. This total normal attractive force is a sum of an attractive reluctance force between the stator and secondary, and a repelling normal force between them due to the same polarity are facing each other.

Figure 4-17 shows the simulated thrust force of the pre-magnetized linear hysteresis motor as we sweep the phase of the current excitation using the finite element model shown in Figure 4-14. The amplitude of the stator current is set to 2 A. Note that this is the force generated by one linear motor, while our linear stage consists two linear hysteresis motors on both sides. It can be seen that the peaks of the

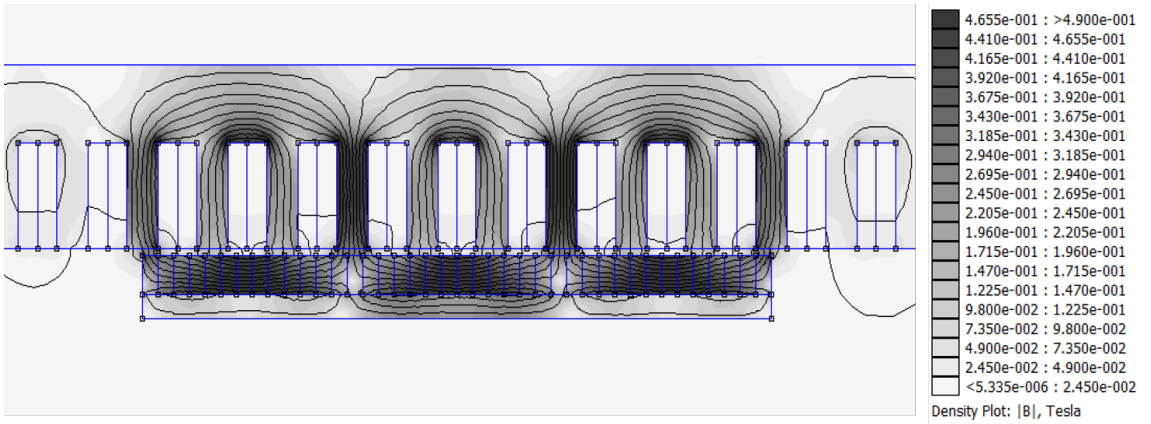

(a)

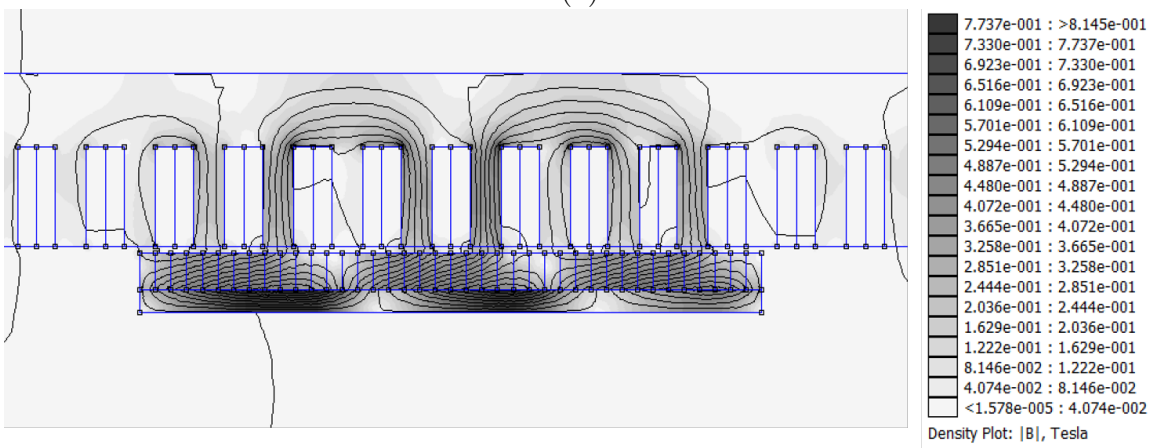

(b)

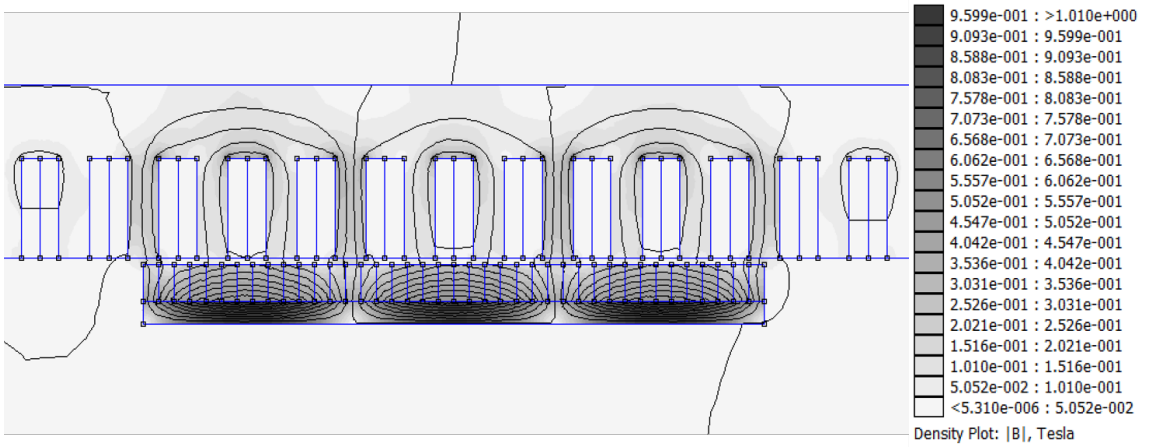

(c)

Figure 4-16: Simulated magnetic field distribution of pre-magnetized linear hysteresis motor under different phase difference ϕ_m between stator and secondary magneto-motive force. (a) $\phi_m = 0$ rad. (b) $\phi_m = \pi/2$ rad. (c) $\phi_m = \pi$ rad.

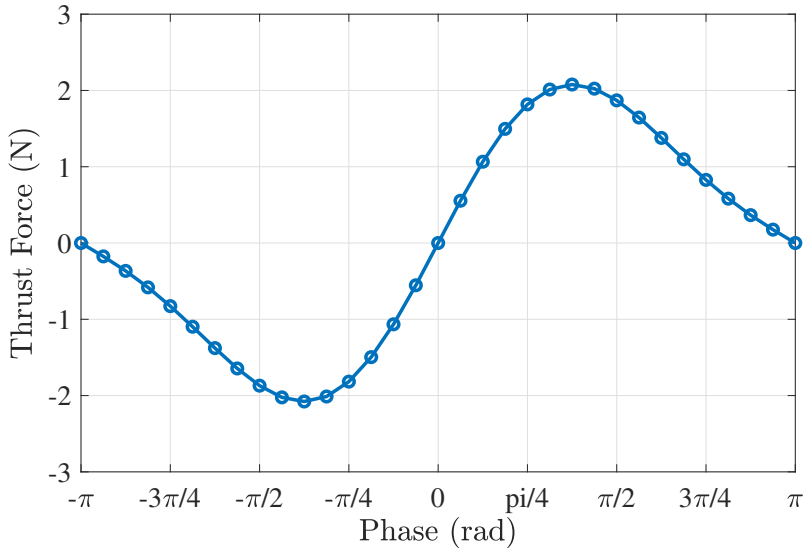

Figure 4-17: Simulated total thrust force generation in pre-magnetized linear hysteresis motor as a function of the phase of motor stator excitation using finite element method. Stator current amplitude is 2 A.

thrust force are in between $\pm\pi/4$ and $\pm\pi/2$, which matches with the discussion in Section 4.1.2.

We then calculate the thrust force generated by reluctance force only to separate the reluctance effect in the total thrust force generation. In this simulation, the coercivity of the secondary material is set to zero. The material's property is assumed to be linear, and its permeability is set to the slope of the nonlinear B-H curve around the remanence point B_r, which is $\mu_H = 29\mu_0$. Figure 4-18 shows the simulated magnetic field intensity distribution when the stator current amplitude is set to 2 A. It can be seen that the H-field range in the secondary material is within -3000 A/m to 3000 A/m, which is small compared with the H-field range in Figure 4-15.

Figure 4-19 shows the simulated thrust force decomposition in a pre-magnetized linear hysteresis motor using our model. The stator current amplitude in simulation is set to 2 A. In Figure 4-19, the blue line shows the simulated total thrust force generation. The orange line shows the simulated reluctance thrust force generation. The yellow curve shows the estimated hysteresis thrust force generation, which is calculated by subtracting the simulated reluctance thrust force from the simulated

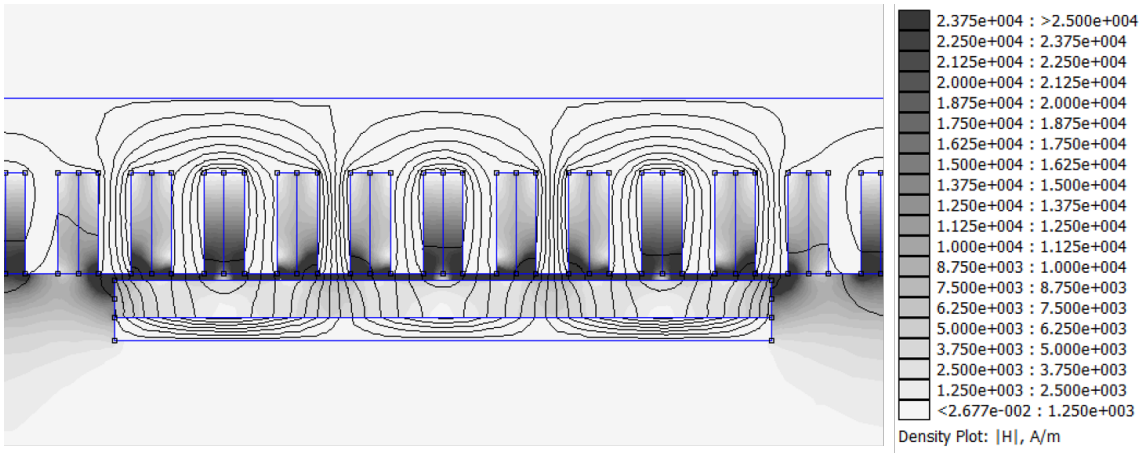

Figure 4-18: Field intensity (H-field) distribution of in reluctance-force-only simulation for pre-magnetized linear hysteresis motor. Here the secondary material is set to $H_c = 0$ and $\mu_H = 29\mu_0$. The maximum H-field intensity is 3000 A/m in motor secondary.

total thrust force. It can be seen that this simulated reluctance force demonstrates two periods between $\phi_m = -\pi$ to $\phi_m = \pi$. The estimated hysteresis thrust force is sinusoidal with respect to the phase of excitation, and its peaks are at $\phi_m = \pm\pi/2$. These observations match our prediction in Section 4.1.2.

This model for pre-magnetized linear hysteresis motors is developed after we built and tested the magnetically-levitated linear stage prototype. The experimental measurements of the linear hysteresis motors in our linear stage is used to validate this model. The comparison between the simulated and experimental measurements are presented in Chapter 6.

4.4 Summary

In this chapter, we first presented the operating principle of our magnetically-levitated linear stage. We then presented a first-order analytical model for the active magnetic suspension of our linear stage, which shows the expression for the suspension controlling force/torque generation using reluctance force principle. Lastly, we present the modeling for pre-magnetized linear hysteresis motor using finite element method. Here, the pre-magnetized hysteresis secondary is modeled as a permanent magnet

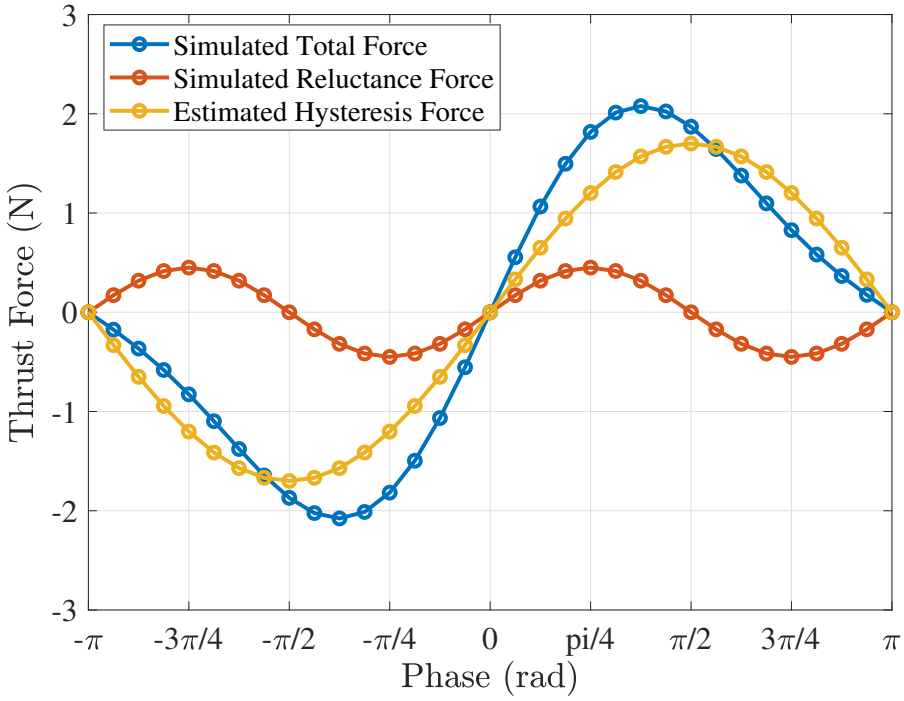

Figure 4-19: Simulated thrust force generation in pre-magnetized linear hysteresis motor as a function of the phase of motor stator excitation. Stator current amplitude is 2 A. Here the total thrust force is simulated using the model shown in Figure 4-16. The reluctance force is simulated using the model shown in Figure 4-18. The hysteresis thrust force is estimated by subtracting reluctance force from the total force.

array, where the material property and the magnetization direction of each magnet is determined by the H-field in the pre-magnetization step. To our knowledge, this work presents the first model for pre-magnetized hysteresis motor including in both linear and rotary form.

In the next chapter, we will describe the design and building of our magnetically-levitated linear stage prototype.

Chapter 5

Magnetically Levitated Linear Stage Hardware

This Chapter introduces the design and fabrication of the magnetically-levitated linear stage prototype, whose operating principle and analysis are presented in Chapter 4. This chapter is organized as follows: Section 5.1 presents a system overview. Section 5.2 shows the design and fabrication of the moving stage. Section 5.3 presents the stator assembly, including the bias flux structure, motor stator, and yaw control stators. Section 5.4 discusses the sensing system for the linear stage, including both air gap sensors and travel-directional displacement sensor. Section 5.5 presents the power electronics. Section 5.6 discusses the grounding and shielding of the linear stage system. Finally the real-time control system design is introduced in Section 5.7.

5.1 System Overview

Fig. 5-1 shows the CAD model of the magnetically-levitated linear stage design, and Fig. 5-2 shows a photograph of the prototype system. Our magnetically-levitated linear stage prototype comprising two stator assemblies, one moving stage, and a sensing system. The stators are mounted on an optical table. Devices not shown

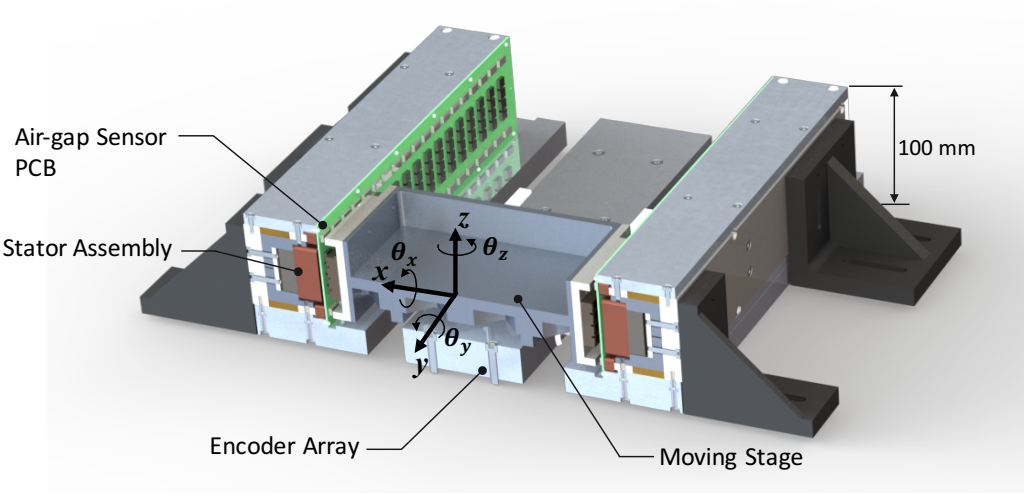

Figure 5-1: Cross-section view of the CAD model for magnetically-levitated linear stage system.

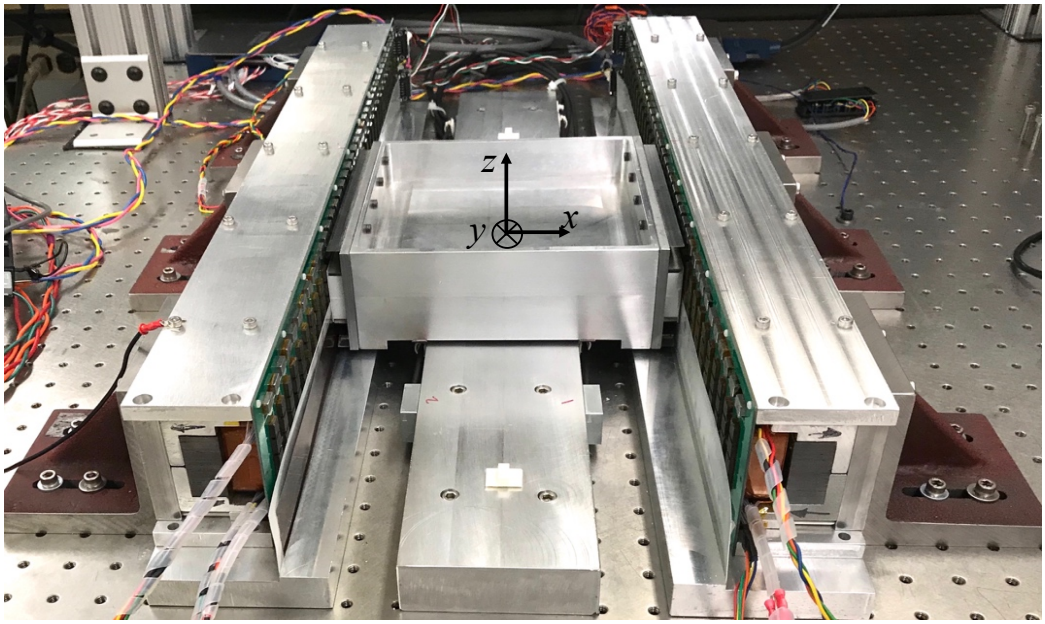

Figure 5-2: Photograph of the magnetically-levitated linear motor prototype.

in the figures include the power electronics for energizing the stators, and a real-time controller and its break-out boards. The coordinate system for the linear stage is shown in Fig. 5-1 and 5-2. Here, the moving stage is driven along the y-axis. The magnetic levitation of the moving stage is active in x- and θ_z-directions, and is passive in z-, θ_x-, and θ_y-directions. The overall design parameters of our linear stage prototype are shown in Table 5.1.

Table 5.1: Key design parameters of the magnetically-levitated linear stage prototype.

Parameter Description	Variable	Value
Linear stage total length	L_{MLLS}	650 mm
Linear stage total width	W_{MLLS}	420 mm
Linear stage total height	H_{MLLS}	100 mm
Hysteresis motor air gap length	g_{motor}	1.5 mm
Bias flux air gap length	g_{bias}	2.0 mm
Bias magnetic flux density	B_{bias}	0.45 T
Weight of the moving stage	m_{stage}	4.8 kg
Vertical sag length due to stage's weight	Δ_{sag}	0.75 mm

Our moving stage design is vacuum compatible, however the sensing system for the prototype was not designed to best fit the vacuum environment. When the system needs to operate in vacuum, different sensors need to be used. Possible alternative sensing methods are discussed in Chapter 7. In addition, when the linear stage is used for in-vacuum transportation, a channel with thin walls (not shown in figures) needs to be configured along the motion range of the moving stage. The moving stage is levitated and transports the reticle inside the channel in clean vacuum, while the stators are configured outside the channel, and are in a relatively dirty vacuum environment. This channel is able to separate out the contamination generation from the stator assemblies.

5.2 Moving Stage

Moving Stage Design and Fabrication

Figure 5-3 shows the CAD model of the moving stage, and Figure 5-4 shows the photos of the moving stage. The moving stage is mainly comprised of a stage base, two stage back irons, two hysteresis motor secondaries, and four bias flux collectors. Two magnetic encoder scales are fixed on the bottom of the moving stage for displacement measurement, as shown in Figure 5-3(b). The parts in the moving stage that are not shown in Fig. 5-3 are: (1) two copper plates for passive electrodynamic damping in the passively-levitated degrees of freedom, and (2) the optical sensor targets made

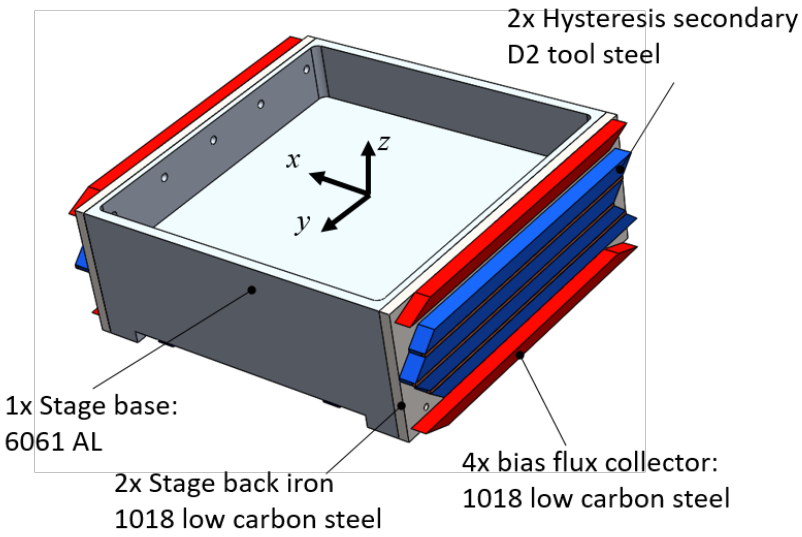

(a)

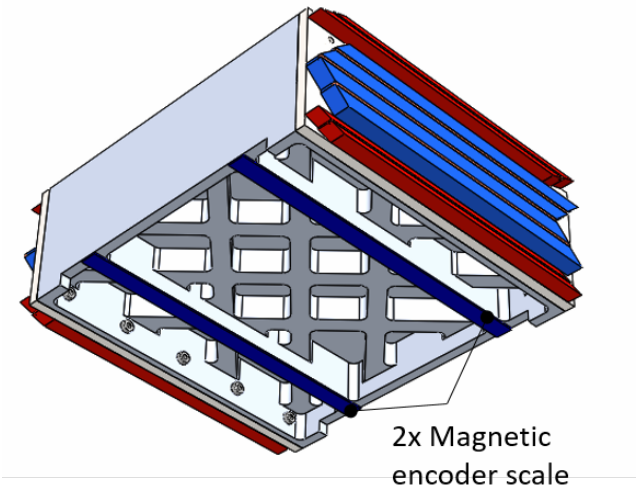

(b)

Figure 5-3: CAD model of the moving stage. (a) Top view. (b) Bottom view.

of 0.5 mm thick white polyacetal (Delrin) sheets, which is covering the hysteresis secondary and to improve the optical air gap sensor sensitivity. These parts are shown in the photos in Figure 5-4. The major geometric parameters of the moving stage are shown in Figure 5-5, and their values are shown in table 5.2. The total mass of the stage is 4.8 kg.

The stage base is made of 6061-T6 aluminum. On the bottom of the moving stage, a honeycomb reinforcement structure is included to improve the stiffness of the

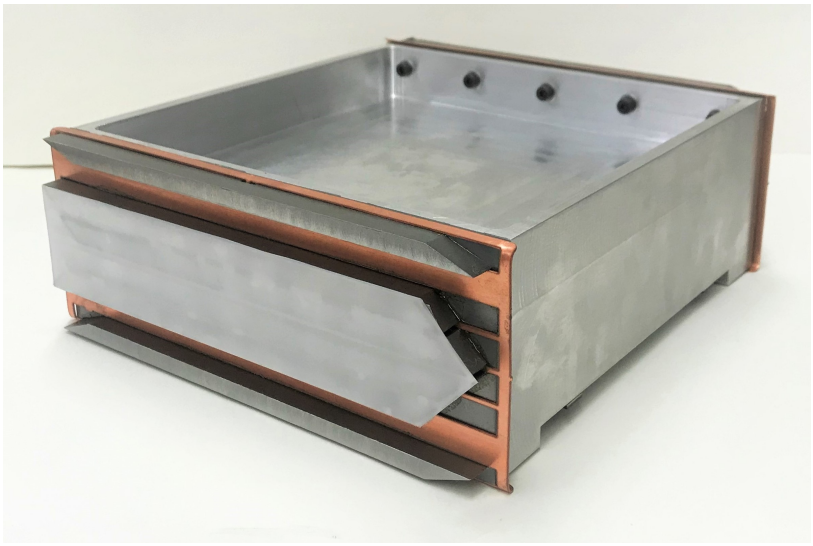

(a)

(b)

Figure 5-4: Photos of the moving stage. (a) Top view. (b) Bottom view.

moving stage, as shown in Figure 5-3(b) and Figure 5-4(b).

The moving stage has two stage secondary assemblies on both sides of the stage base. Each stage secondary consists of one stage backiron, two bias flux collectors, one hysteresis secondary, one copper damping plate, and one white Delrin sheet. Figure 5-6 shows a photo of the stage secondary without the Delrin optical sensor target sheet. The stage back iron and bias flux collectors are made of ANSI 1018 low carbon steel,

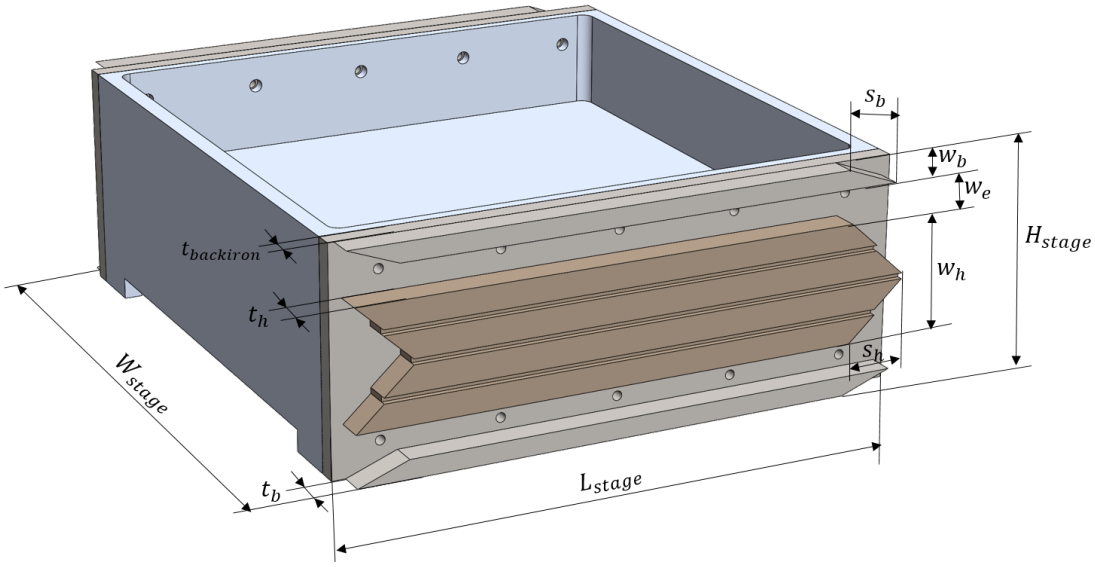

Figure 5-5: Major geometric parameters of the moving stage.

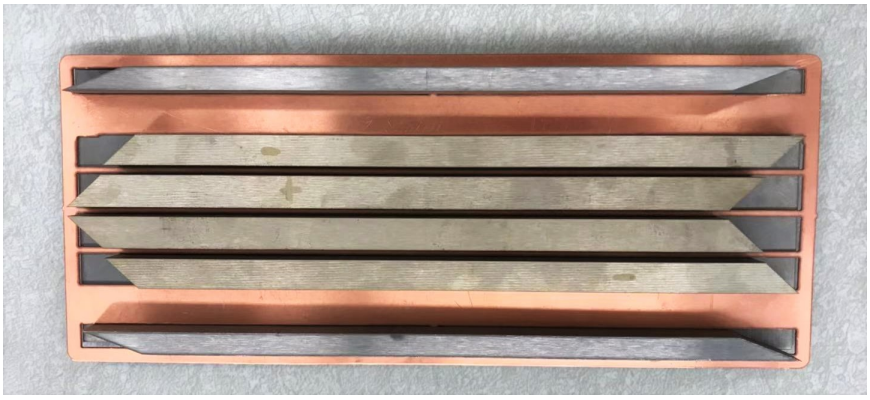

Figure 5-6: Photo of stage secondary without the Delrin optical sensor target sheet.

whose relative permeability is approximately $\mu_{1018} = 850\mu_0$ [68]. Although better soft magnetic materials exist, we selected 1018 steel for its high availability, low cost, and the ease of manufacturing in our prototype. The edges of the bias flux collectors are skewed with one full tooth pitch of the yaw control stator to reduce the cogging force generation due to the permanent magnet bias flux. The effect of such skewing is simulated in Section 5.3.3.

The hysteresis motor secondaries are made of hardened D2 tool steel. D2 tool steel has relatively large magnetic hysteresis, which allows it to be used for the secondary

Table 5.2: Major geometric parameters of the moving stage.

Parameter Description	Variable	Value
Stage length	L_{stage}	192 mm
Stage width	W_{stage}	188 mm
Stage height	H_{stage}	80 mm
Hysteresis secondary width	W_h	40 mm
Hysteresis secondary thickness	t_h	9.5 mm
Hysteresis secondary skew length	s_h	18.8 mm
Bias flux collector width	w_b	6.35 mm
Bias flux collector thickness	t_b	9 mm
Bias flux collector skew length	s_b	17 mm
Stage backiron thickness	t_{sb}	6 mm

of hysteresis motors. It also has relatively high magnetic permeability, which is advantageous for reluctance force generation for magnetic suspension purposes. Fig. 5-7 shows the measured hysteresis loop of D2 tool steel hardened to Rockwell 65, which is measured by Dr. Gereon Goldbeck from Johannes Kepler University in Linz, Austria. The hysteresis data is used to estimate the thrust force capability of the linear hysteresis motors using the model introduced in Chapter 4. The edges of the hysteresis secondaries are also skewed by one motor stator tooth pitch to reduce tooth harmonic reluctance force ripples. There are three slots in the hysteresis secondary along the motion direction, and each has a width of 2 mm. These slots are matching with the slots in the motor stator yokes, which can concentrate the motor magnetic fluxes and thus improve the passive magnetic suspension stiffness.

The hysteresis secondaries and the bias flux collectors are assembled onto the stage back irons via epoxy. Here the structural adhesive Loctite 326 is being used together with primer Loctite 7649 for the assembly. In addition, we used micro solid glass spheres with 80 μm-diameter, or bond line controller, from Rock West Composites to set the thickness of the epoxy layer.

Moving Stage Structural Analysis

In this section we discuss the structural analysis for the moving stage. When the linear stage is in operation, the moving stage is under stretch due to the attractive

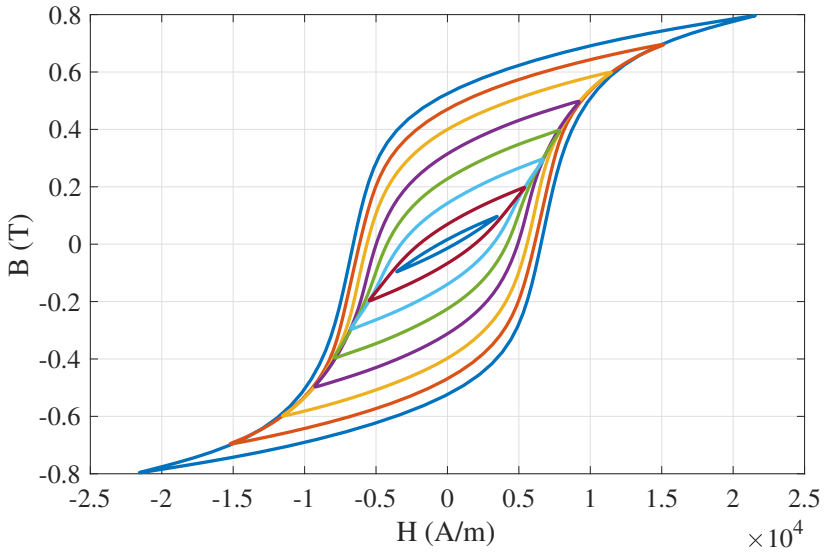

Figure 5-7: Measured hysteresis property of hardened D2 tool steel under different excitation amplitude. Horizontal axis: field intensity (H-field). Vertical axis: flux density (B-field). Measurement took by Gereon Goldbeck from Johannes Kepler University in Linz, Austria.

magnetic forces on both sides. Figure 5-8 shows a static structural finite element simulation for the moving stage assembly using Solidworks. In this simulation, we assumed the magnetic flux density in all air gaps are 1.2 T and is in the normal direction, which is an over-estimated value. Under this circumstance, the normal directional magnetic force per unit area on all stage secondaries is 0.57 MPa. It can be seen that when under such tension the maximum deformation of the moving stage is below 5 μm, which is acceptable for the reticle transportation application. The calculated maximum stress under this condition is 7.4 MPa, which is safely below the yield stress of the stage materials.

We also conducted dynamic finite element analysis for the moving stage to predict its resonance frequencies and mode shapes, which is critical for the magnetic suspension performance of the linear stage. Our design goal is to set the resonance frequency of the stage's first flexible mode's about 10 times higher than the target suspension control bandwidth (90 Hz), and all mode shapes are not excitable or detectable using our stators and air gap sensors. Figure 5-9 shows the flexible modes of the moving stage as well as their corresponding frequencies simulated with the dynamic finite

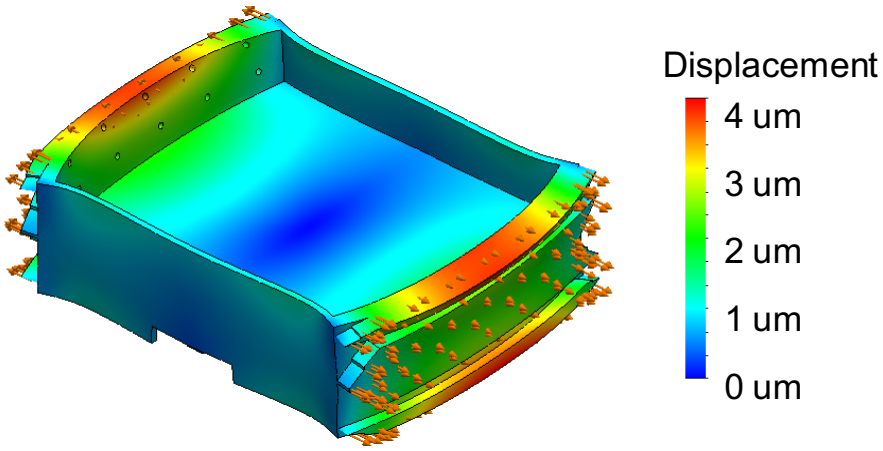

Figure 5-8: Deformation of the moving stage under attractive magnetic forces assuming all air gap flux are 1.2 T simulated using Solidworks finite element tools.

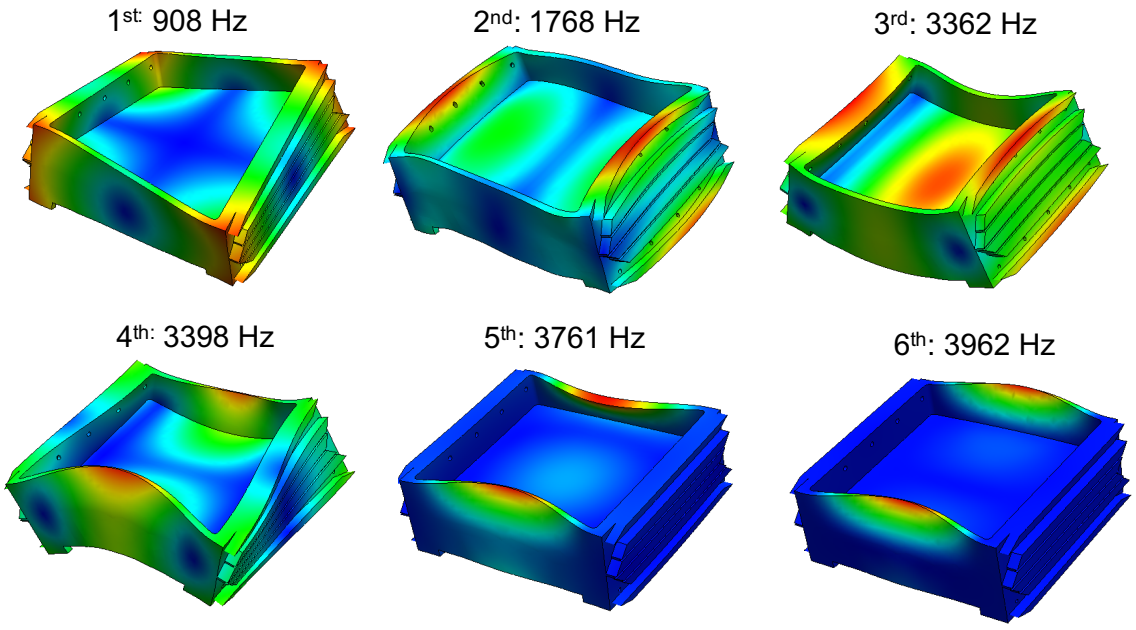

Figure 5-9: The first six flexible modes of the moving stage and their corresponding resonance frequencies predicted using Solidworks finite element tools.

element tool in Solidworks. It can be seen that the first flexible mode of the stage has a resonance frequency of 908 Hz, which satisfies the design target. All modes shown in Figure 5-9 are not excitable with the attractive forces from the motor stators, and are not detectable using the air gap sensors aligned with the centerlines of the stage on the two sides (sensing system is introduced in Section 5.4).

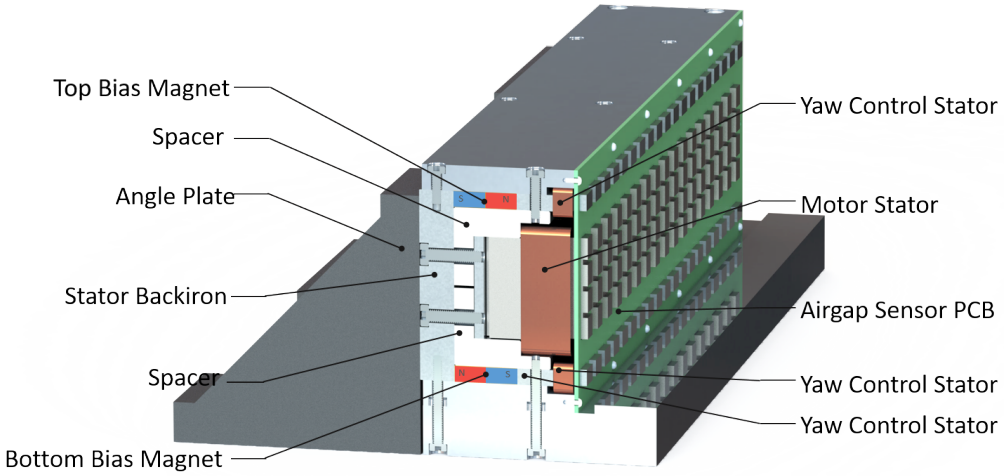

Figure 5-10: CAD cross-section view of the stator assembly.

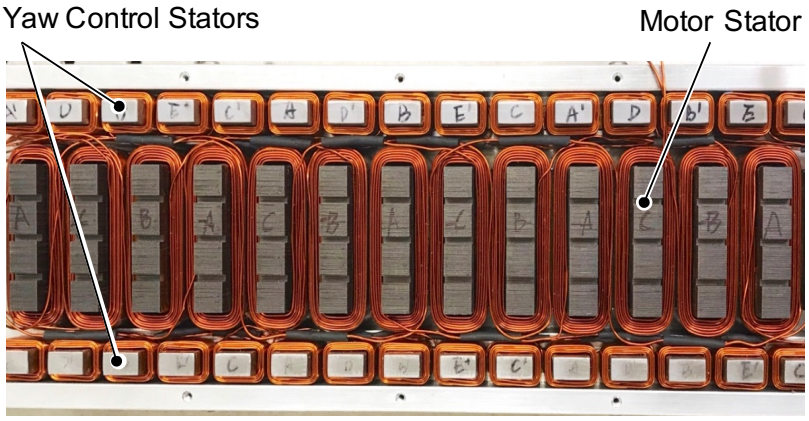

Figure 5-11: Photograph of front view of the stator assembly without the optical air gap sensor printed circuit board.

5.3 Stator Assembly

In this section, we discuss the analysis, design, and fabrication of the stator assembly. Figure 5-10 shows a cross-section view of the CAD model of the stator assembly, and Figure 5-11 shows a front view photograph of stator assembly with the air-gap sensor printed circuit board removed. The stator assembly mainly consists of a motor stator, two yaw control stators, and a flux-biasing structure comprising two rows of permanent magnets and one stator back-iron, as shown in Figure 5-10. Each stator assembly is fixed on the base optical table via three angle plates.

5.3.1 Flux Biasing Structure

This section discusses the design of the flux biasing structure, which includes two rows of permanent magnets and a stator backiron in each stator assembly. The main design parameters for the flux-biasing system include: (1) permanent magnet height h_{pm}, i.e. the magnet's dimension in the vertical direction; (2) permanent magnet thickness t_{pm}, i.e. the magnet's dimension in the magnetization direction; (3) the bias flux air gap length g_b (same with yaw control flux air gap). Other variables, such as separation distance between the bottom of magnets and the top of motor stator, motor flux air-gap, yaw control stator height, and stage backiron thickness, can also influence the bias flux's performance through changing the leakage reluctance of the bias flux.

In the design of the flux biasing structure, we sweep the design parameters using three-dimensional finite element simulation via Ansys Maxwell. First, we set the bias flux air gap length at 2 mm, which is a typical value for our linear stage, and then we swept the height and the thickness of the bias magnet. In this simulation, other geometric parameters for the stage are set as follows: hysteresis secondary thickness is 9 mm, hysteresis secondary width is 40 mm, stator back iron thickness is 14 mm, stage back iorn thickness is 6 mm, motor stator total height 56 mm, motor stator width is 40 mm, and stage total height is 75 mm. Figure 5-12 shows the calculated passive stiffness in the vertical direction and the negative stiffness in the lateral direction under different magnet geometries, and Figure 5-13 shows the ratio between the negative stiffness and the passive stiffness with respect to the magnet dimension. It can be seen that while both negative stiffness and passive stiffness increase as the magnet's thickness and height increase, minimizing the ratio between the negative stiffness and the passive stiffness would prefer a design with large magnet thickness and small magnet height. In our linear stage design, we selected to use a magnet thickness of 25.4 mm (1 inch) and a magnet height of 6.35 mm (1/4 inch). This selection is close to the optimal design in terms of the ratio between the negative stiffness and the passive stiffness, while satisfying a minimum passive

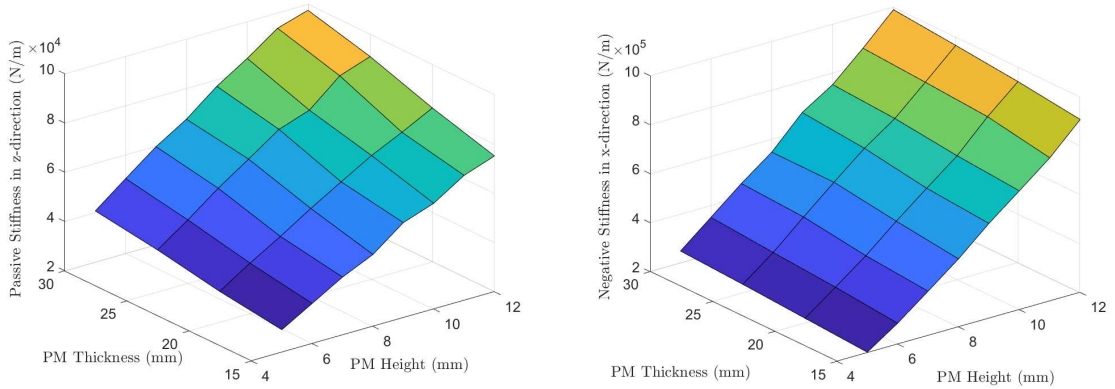

(a) (b)

Figure 5-12: Simulated flux bias structure performance with different permanent magnet dimensions. (a) Passive stiffness in z-direction (vertical). (b) Negative stiffness in x-direction (lateral).

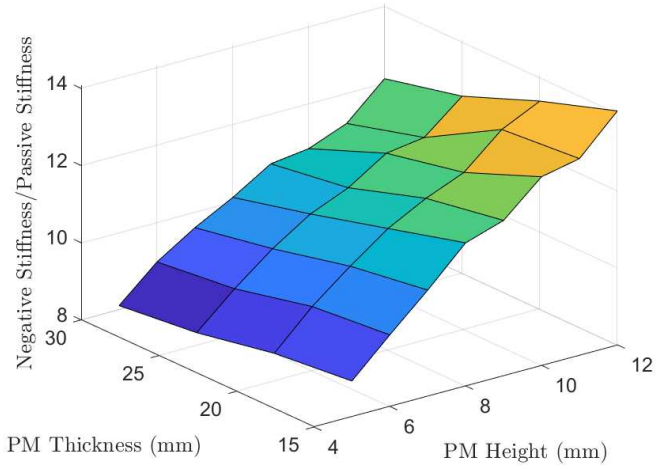

Figure 5-13: Simulated ratio between the negative stiffness and passive stiffness with respect to the dimension of biasing permanent magnet.

stiffness requirement of 2×10^4 N/m, which provides a vertical mode natural frequency of 10 Hz. We selected magnets with such dimension since they are available off-the-shelf, therefore no custom-made magnets are required, which typically have higher cost and take a longer lead time for manufacturing.

The next step is to set the air gap length for the bias flux path. Figure 5-14 shows the simulated vertical-directional restoring force generated by the permanent magnet bias fluxes when the stage is displaced from the equilibrium position in the vertical

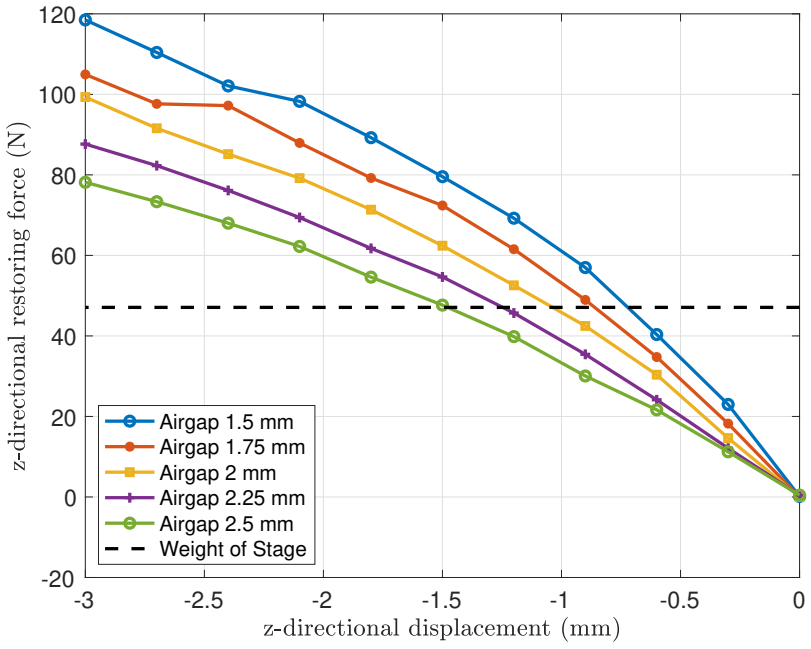

Figure 5-14: Simulated vertical-directional restoring force at different bias flux air gap lengths. Weight of the moving stage is plotted with dashed line.

Table 5.3: Simulated bias flux performance at different air gaps.

g_{bias}	Δ_{sag}	k_z	f_{nz}	$\lvert k_x \rvert$	f_{nx}
1.5 mm	0.7 mm	4.8×10^4 N/m	16.2 Hz	5.1×10^5 N/m	51 Hz
1.75 mm	0.9 mm	3.8×10^4 N/m	14.0 Hz	3.7×10^5 N/m	44 Hz
2 mm	1.0 mm	2.7×10^4 N/m	12.1 Hz	2.6×10^5 N/m	37 Hz
2.25 mm	1.2 mm	2.0×10^4 N/m	10.3 Hz	2.0×10^5 N/m	32 Hz
2.5 mm	1.5 mm	1.5×10^4 N/m	9.1 Hz	1.6×10^5 N/m	29 Hz

direction at different air gap lengths. Note that the stage's weight is compensated with the vertical directional restoring force. As a result, the gravity-induced sag of the moving stage can change with respect to the air gap length. Table 5.3 shows the simulated gravity-induced sag distance Δ_{sag}, passive stiffness in vertical direction k_z, negative stiffness in lateral direction $|k_x|$, natural frequency in vertical direction f_{nz}, and unstable natural frequency in lateral direction f_{nx} at different air gap lengths. In our final design, we selected an air gap length of 2 mm for the bias flux path due to a trade-off between the negative stiffness and passive stiffness.

Finally, we simulate the performance of the stage with bias flux only using three-

Table 5.4: Simulated bias flux performance with the selected parameters.

Parameter Description	Variable	Value
Air gap flux density	B_{bias}	0.45 T
Gravity induced sag	Δ_{sag}	1.0 mm
Passive stiffness in z-direction	k_z	2.7×10^4 N/m
Passive stiffness in roll direction	k_{θ_y}	112 Nm/rad
Passive stiffness in pitch direction	k_{θ_x}	72 Nm/rad
Negative stiffness in lateral direction	$\lvert k_x \rvert$	2.6×10^5 N/m
Negative stiffness in yaw direction	$\lvert k_{\theta_z} \rvert$	527 Nm/rad

dimensional finite element method with the selected design parameters, and the results are shown in Table 5.4. Note that in the final linear stage system, both passive and negative stiffnesses can further increase when the effect of the motor flux is included.

5.3.2 Motor Stator

This section introduces the motor stator, including the winding scheme and detailed design and fabrication for stator yoke and coils.

Motor Stator Winding Scheme

We first discuss the winding scheme design for the motor stator. Due to the constraint in the vertical directional dimension of the stator assembly, lumped winding is selected for the motor stator since it has relatively small end-turn volume. Fig. 5-15 shows the selected winding scheme of the motor stator and the corresponding magnetomotive force (MMF) waveform $\mathcal{F}_s$ generated by the motor stator. As shown in Fig. 5-15, the stator armature has three phase windings A, B, and C wound on the stator teeth. Here $-A$ indicates a coil in the same phase with A, while its current is in a reversed direction. In the motor stator, one full period consists of six stator teeth, and the winding pattern is $(A, -C, B, -A, C, -B)$. The stator coils excite the armature to magnetically interact with the hysteresis secondary on the moving stage for thrust force generation.

Figure 5-16 shows a phasor diagram of the six excitation currents in the motor

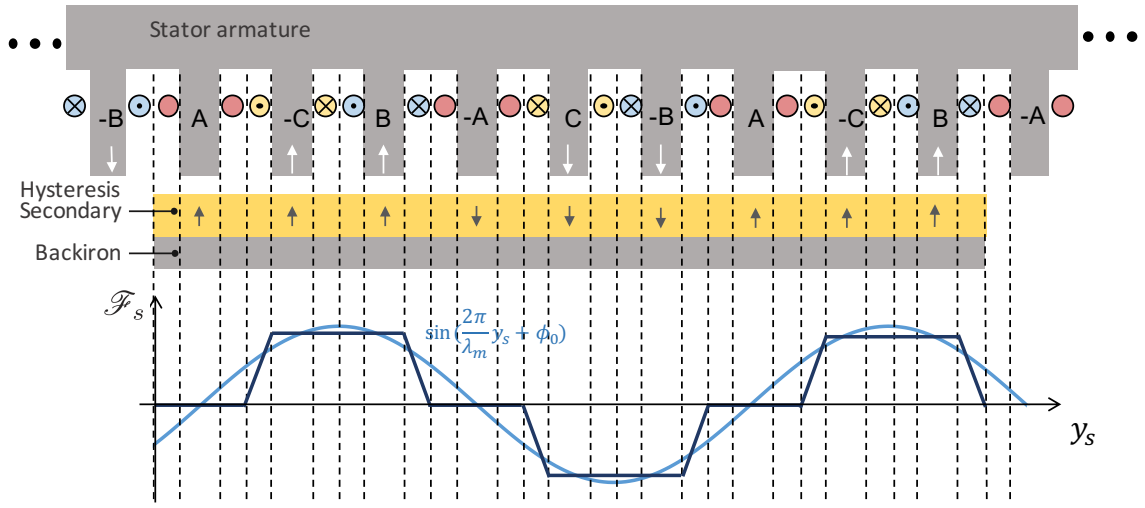

Figure 5-15: Winding diagram of the motor stator and the generated magneto-motive force distribution.

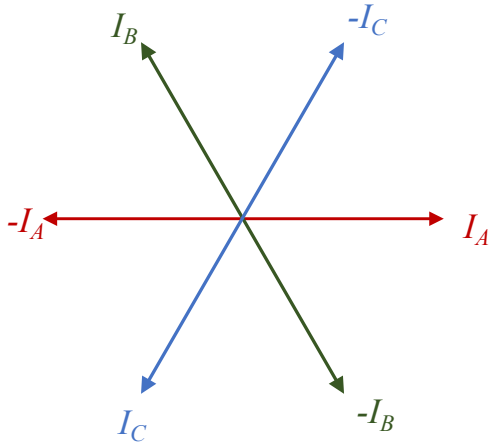

Figure 5-16: Phasor diagram of the motor stator currents.

stator, which corresponds to the currents in six adjacent coils in one full wavelength. It can be seen that such a winding scheme implements a six-phase winding using three independent currents. The reason for such a winding pattern selection, appose to a typical three-phase pattern (A, B, C, A, B, C), is discussed below.

Assume the motor stators are excited with balanced three-phase currents:

$$i_A = I_m \cos(\omega_m t), \tag{5.1}$$

$$i_B = I_m \cos(\omega_m t - \frac{2\pi}{3}), \tag{5.2}$$

$$i_C = I_m \cos(\omega_m t + \frac{2\pi}{3}), \tag{5.3}$$

where I_m is the amplitude of the motor currents, and ω_m is the electrical frequency for the motor stator excitation. The n-th harmonic of the magneto-motive force (MMF) generated by the stator excitations are

$$\mathcal{F}_A^n = \underline{\mathcal{F}_A^n} \cos\Big(\frac{2\pi n y_s}{\lambda_m}\Big) \cos\Big(\omega_m t\Big), \tag{5.4}$$

$$\mathcal{F}_B^n = \underline{\mathcal{F}_B^n} \cos\Big(\frac{2\pi n y_s}{\lambda_m} - \frac{2\pi}{3}\Big) \cos\Big(\omega_m t - \frac{2\pi}{3}\Big), \tag{5.5}$$

$$\mathcal{F}_C^n = \underline{\mathcal{F}_C^n} \cos\Big(\frac{2\pi n y_s}{\lambda_m} + \frac{2\pi}{3}\Big) \cos\Big(\omega_m t + \frac{2\pi}{3}\Big), \tag{5.6}$$

where $\underline{\mathcal{F}_A^n}$, $\underline{\mathcal{F}_B^n}$, and $\underline{\mathcal{F}_C^n}$ are the complex amplitudes of the n-th order harmonics of MMF generated by the phase A, B, and C, respectively, y_s is the coordinate along the motor stator, and λ_m is the wavelength of the motor stator MMF.

Knowing that $\cos(x)\cos(y) = \frac{1}{2}\Big(\cos(x+y) + \cos(x-y)\Big)$, the MMF expressions (5.4) to (5.6) can be written as

$$\mathcal{F}_A^n = \frac{\underline{\mathcal{F}_A^n}}{2}\Big(\cos(\frac{2\pi n y_s}{\lambda_m} + \omega_m t) + \cos(\frac{2\pi n y_s}{\lambda_m} - \omega_m t)\Big), \tag{5.7}$$

$$\mathcal{F}_B^n = \frac{\underline{\mathcal{F}_B^n}}{2}\Big(\cos(\frac{2\pi n y_s}{\lambda_m} + \omega_m t - \frac{2\pi}{3}(n+1)) + \cos(\frac{2\pi n y_s}{\lambda_m} - \omega_m t - \frac{2\pi}{3}(n-1))\Big), \tag{5.8}$$

$$\mathcal{F}_C^n = \frac{\underline{\mathcal{F}_C^n}}{2}\Big(\cos(\frac{2\pi n y_s}{\lambda_m} + \omega_m t + \frac{2\pi}{3}(n+1)) + \cos(\frac{2\pi n y_s}{\lambda_m} - \omega_m t + \frac{2\pi}{3}(n-1))\Big). \tag{5.9}$$

In the MMF expressions (5.7) to (5.9), the first terms are backward traveling waves, and the second terms are forward traveling waves. Substituting in $n = 1, 2, ...$, one can find that the 1st, 4th, 7th, ... harmonics for each MMF are forward traveling waves, while the 2nd, 5th, 8th, ... harmonics are backward traveling waves. The 3rd, 6th, 9th, ... harmonics for all MMFs have zero amplitude.

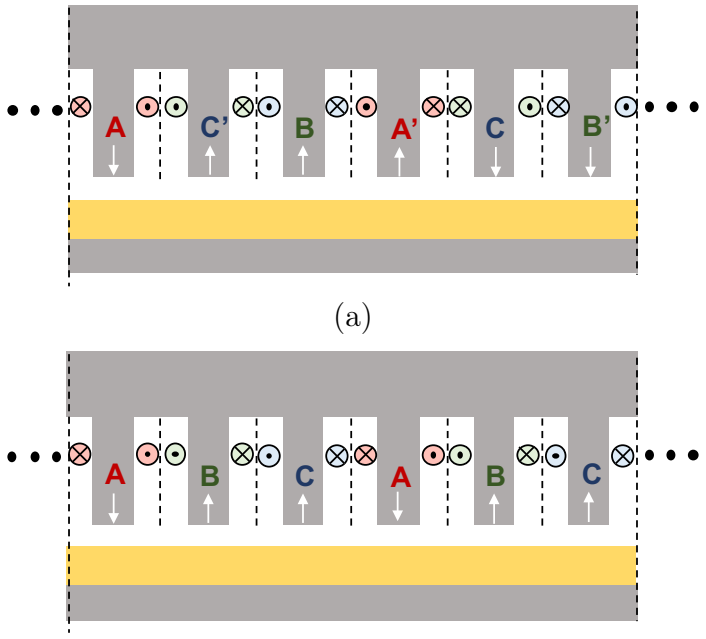

Figure 5-17: Motor winding scheme candidates. (a) Winding I: three-phase equivalent of six-phase lumped winding. (b) Winding II: three-phase lumped winding.

Now we discuss the force generation of the motor with such stator magneto-motive force. The thrust force in a linear motor is generated by the interaction the primary and secondary fields as [65]:

$$F_{thrust} \propto \mathcal{F}_s \times \mathcal{F}_r, \tag{5.10}$$

where $\mathcal{F}_s$ and $\mathcal{F}_r$ are the magneto-motive force of the primary and secondary, respectively. This thrust force relationship can be rewritten as

$$F_{thrust} \propto \sum_{n=1}^{\infty} |\mathcal{F}_s^n||\mathcal{F}_r^n| \sin \phi_m^n, \tag{5.11}$$

where $|\mathcal{F}_s^n|$ and $|\mathcal{F}_r^n|$ are the magnitudes of the n-th harmonic of $\mathcal{F}_s$ and $\mathcal{F}_r$, respectively, and ϕ_m^n is the difference in the electrical angle between the two n-th order harmonics. Equation (5.11) shows that the thrust force can only be generated through the interaction between the same order harmonics of the primary and secondary magneto-motive force.

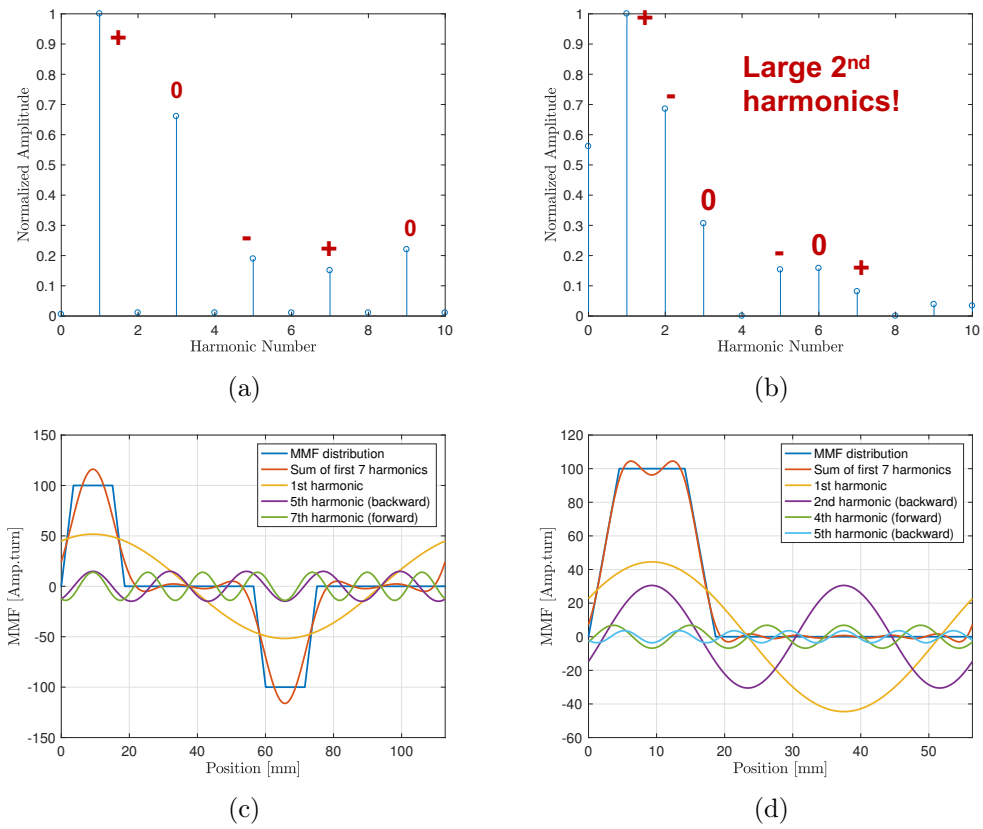

Figure 5-18: Harmonic analysis of the stator magnetio-motive force of two winding schemes. (a) and (b): Normalized amplitudes of the first 10 harmonics of stator MMF generated by phase A in Winding I and Winding II, respectively. (c) and (d) Superposition of first seven harmonics of MMF generated by phase A in Winding I and Winding II, respectively.

In a linear hysteresis motor, the secondary is magnetized with the stator's excitation, therefore the induced magnetization has the same MMF distribution with the stator. As a result, all harmonics in the stator MMF are able to generate force. In an asynchronously-operated hysteresis motor, the forward traveling waves in the stator MMF are able to generate thrust force, while the backward traveling waves can generate braking force. In a pre-magnetized, synchronously-operated hysteresis motor, only the fundamental harmonic of the stator MMF is able to generate thrust force, while all high-order harmonics of the stator MMF are generating oscillatory forces. In both cases, the high order harmonics in the stator MMF are undesired, and we should minimize their magnitude to improve the stage's performance.

Let us now compare the harmonics of the stator MMF generated by the two wind-

ing pattern candidates: Winding I: the three-phase equivalent of six-phase winding, as shown in Figure 5-17(a), and Winding II: the three-phase winding scheme, as shown in Figure 5-17(b). Figure 5-18 shows a comparison between the harmonic analysis of the two stator MMF. Here, Figure 5-18(a) and (b) show the normalized amplitudes of the first ten harmonics of stator MMF generated by phase A winding in Winding I and Winding II, respectively, and the direction of each traveling wave are labeled. Figure 5-18(c) and (d) show the superposition of first seven harmonics of MMF generated by phase A in Winding I and Winding II, respectively. It can be seen that the stator MMF of Winding II has a relatively large second-order harmonic, which can significantly hurt the motor's performance. In contrast, the stator MMF of Winding I does not have even-number harmonics. Although the third harmonic of the Winding II stator MMF is large, it does not generate disturbance force in the motor due to the three-phase symmetry. Based on this discussion, the Winding I scheme is selected since it has less high order harmonics compared to Winding II, which generates less disturbance forces in the linear hysteresis motors.

Motor Stator Yoke and Coil

This section introduces the detailed design and fabrication for the motor stator, including both motor stator yoke and the winding coils. Figure 5-19 shows the CAD diagram of the motor stator yoke and its major geometric variables, and the values of the motor stator yoke design parameters are shown in Table 5.5. Figure 5-20 shows a photograph of the motor stator yokes. The motor stator yoke is fabricated by stacking 80 layers of lamination, which is laser cut from 0.5 mm-thick M19 electric steel sheets. The lamination sheets are bonded via EB-548 bonding varnish, and are tig welded on the back-side of the stator yoke. Note that each stator yoke has three indents with 2 mm width and 3 mm depth distributed in its stacking direction, as shown in Figure 5-20, where each slot is achieved via stacking four layers of lamination with their stator teeth being 3 mm shorter than the nominal stator teeth length. These slots are interfacing with the slots on the hysteresis secondaries (shown in Figure 5-4) to improve the passive stiffness of the stage's suspension.

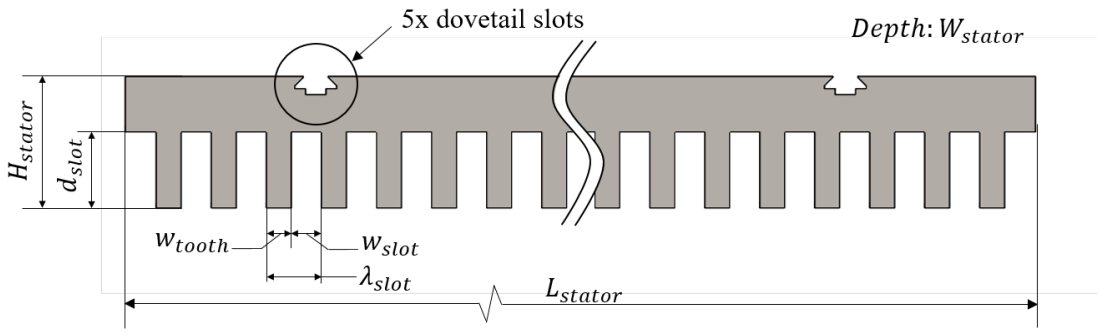

Figure 5-19: CAD diagram of the motor stator yoke with the major design parameters.

Table 5.5: Values for major geometric parameters of the motor stator yoke.

Parameter Description	Variable	Value
Stator length	L_{stator}	650 mm
Stage width	W_{stator}	40 mm
Stage height	H_{stator}	45 mm
Slot pitch	λ_{slot}	18.8 mm
Slot width	w_{slot}	10.3 mm
Tooth width	w_{tooth}	8.5 mm
Slot depth	d_{slot}	26 mm

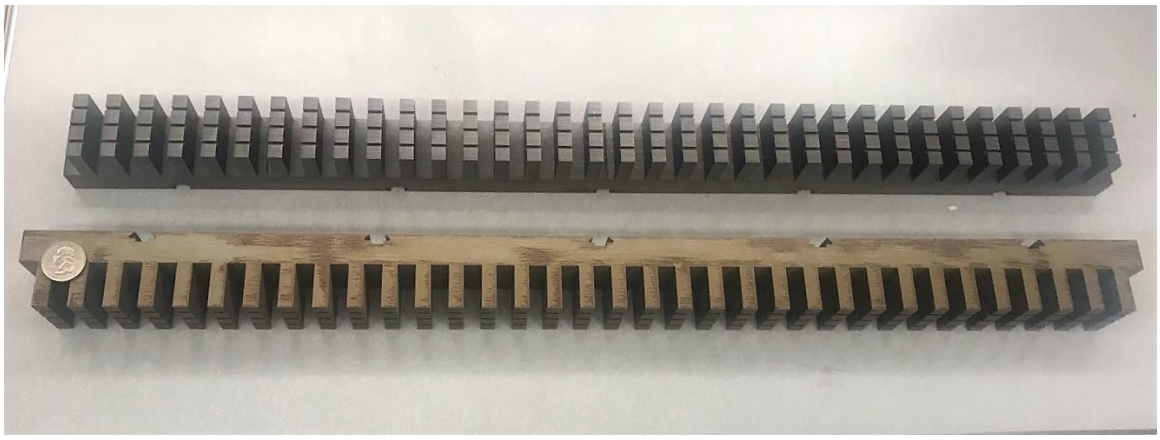

Figure 5-20: Photograph of motor stator yoke. A US quarter coin is included in the picture for size reference.

The winding in each motor stator consists of 34 coils, where the phase A is containing 12 coils, and phase B and phase C are each containing 11 coils. The coils are fabricated by Mr. Fred Sommerhalter, who has fabricated many different coils for research projects at the Precision Motion Control Lab at MIT. The motor coils are made of AWG 21 bondable magnetic wire, and each motor coil has 151 turns.

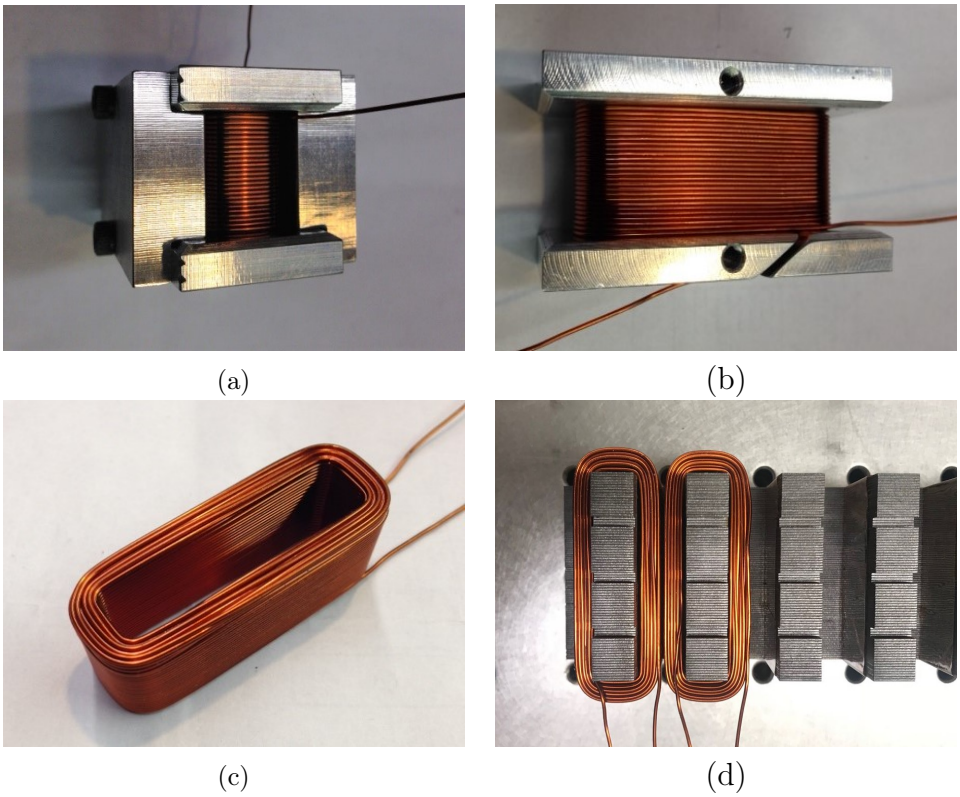

Figure 5-21: Photos of motor coil. (a) and (b): Motor coil in its winding tool courtesy of Mr. Fred Sommerhalter. (c) Photograph of one motor coil. (d) Motor coil on motor stator yoke.

Figure 5-21 shows the photos of the winding tool, motor coil, and coils on the motor stator yoke.

Figure 5-22 shows a photo of the assembled motor stator. Here the motor stator is fastened to the stator backiron and spacers via five dovetail-shaped nuts. During the assembly of the motor stator, two layers of Kapton polyimide film are wrapped around each stator tooth, each slot, and the aluminum spacers. Then the coils are slid on to the insulated stator teeth, and are bonded to the insulated stator yoke using epoxy to prevent relative motion, since such motion can risk scraping off the insulating enamel layer on the magnetic wires and cause insulation failure. The coils of the same phase are connected via soldering, and the soldering joints are insulated using heat shrink tubes. The leads of each phase are coming out from the stator assembly on the end as shown in Figure 5-22, and the leads are covered with PTFE tubings to protect the insulating enamel on the wires from scraping off. In the full

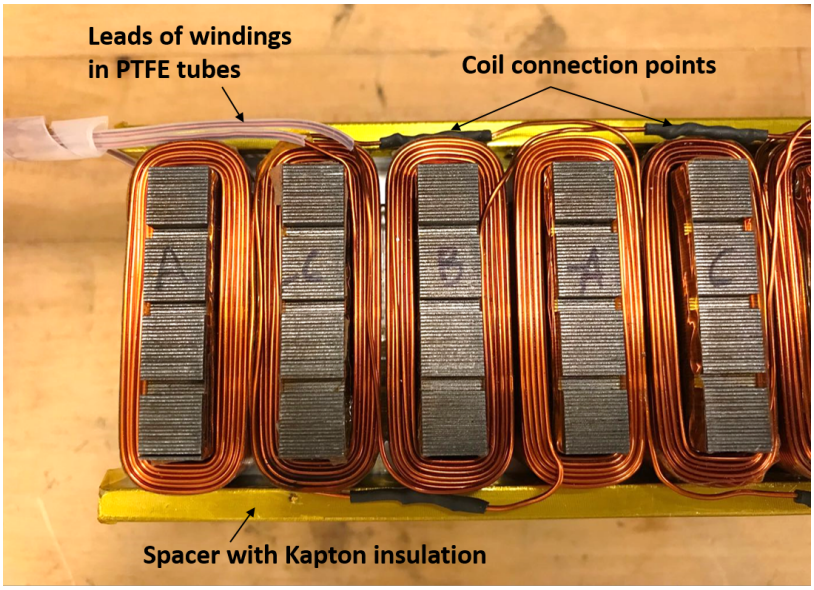

Figure 5-22: Photograph of motor stator assembled to the stator backiron and spacers.

motor stator assembly, when interfacing with the moving stage at an nominal motor flux air gap of 1.5 mm, the total per phase resistance and inductance of the motor stator winding are $R_s = 8.4\ \Omega$ and $L_s = 75.6$ mH, respectively.

5.3.3 Yaw Control Stator

This section introduces the design for yaw control stator, including cogging force reduction, winding scheme, and detailed design and fabrication for yaw control stator yokes and coils.

Cogging Force Reduction

One challenge in the design for the yaw control stator is to minimize the cogging force generation due to the stator's saliency. As shown in Figure 5-10, the yaw control stators are in the flux path of the permanent magnet bias flux. As a result, the strength of the bias flux in the air gaps are modulated by the yaw control stator teeth, which can generate reluctance forces at the front and back edges of the bias flux collectors on the moving stage. This effect can generate a cogging force to the moving stage, which has a spatial period equals to the yaw control stator tooth pitch.

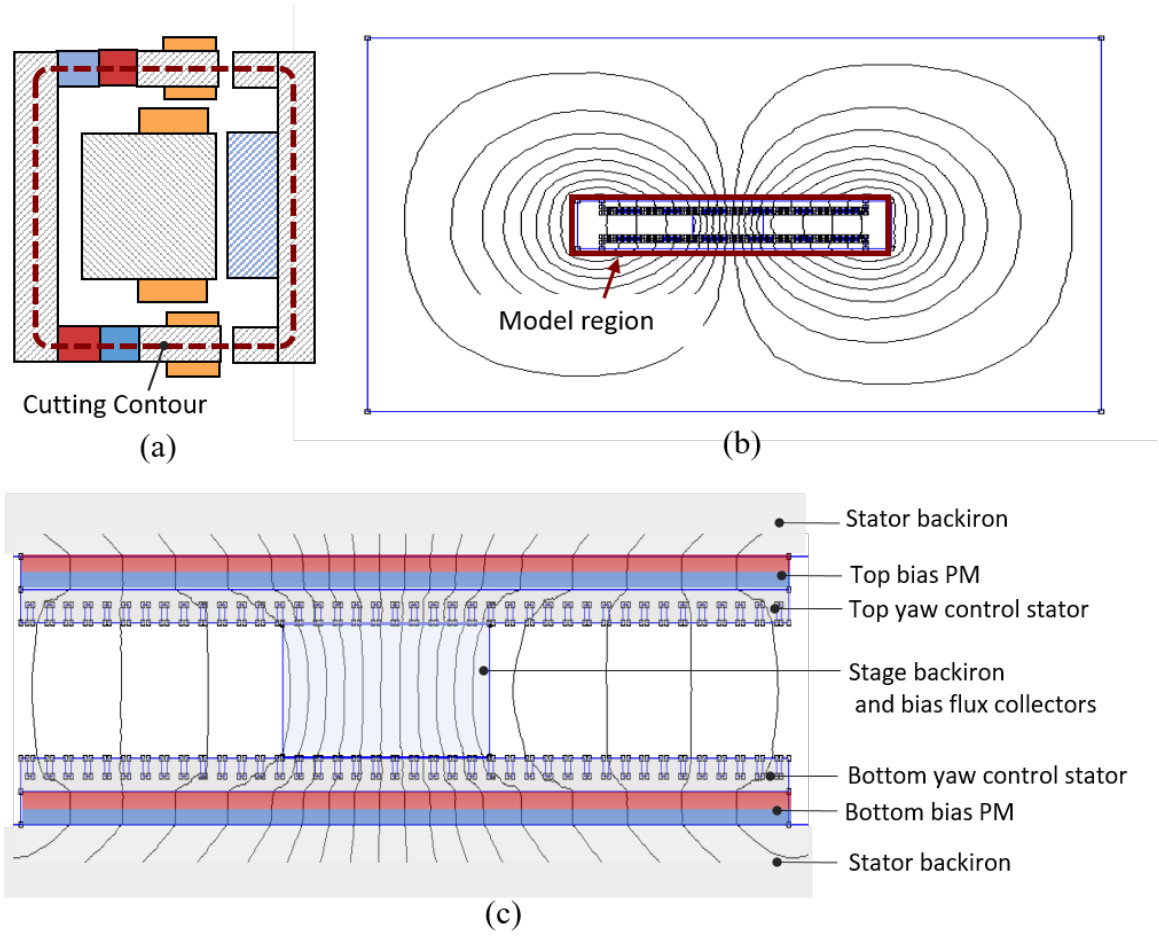

Figure 5-23: Two dimensional finite element model for the bias flux structure and yaw control stators. (a) Cross-section diagram of left stator and left stage secondary and cutting contour. (b) Full two dimensional model cutting along the cutting contour. The stator back iron is modeled as a large yoke surrounding the zoom in region. (c) Two-dimensional model for bias permanent magnets, yaw control stators, stage backiron, and bias flux collector. Here (c) is a zoomed in picture of the model region in (b).

In this section, we introduce the design for yaw control stator yoke and the bias flux collectors for minimizing the cogging forces.

First we introduce the model being used for the cogging force simulation. Here we selected to use two-dimensional finite element simulation based on FEMM [67], since it requires less computation time than a three-dimensional finite element simulation. Figure 5-23 shows the two-dimensional finite element model construction. This model is set up in the following three steps: (1) Cut the stage and stator's flux biasing

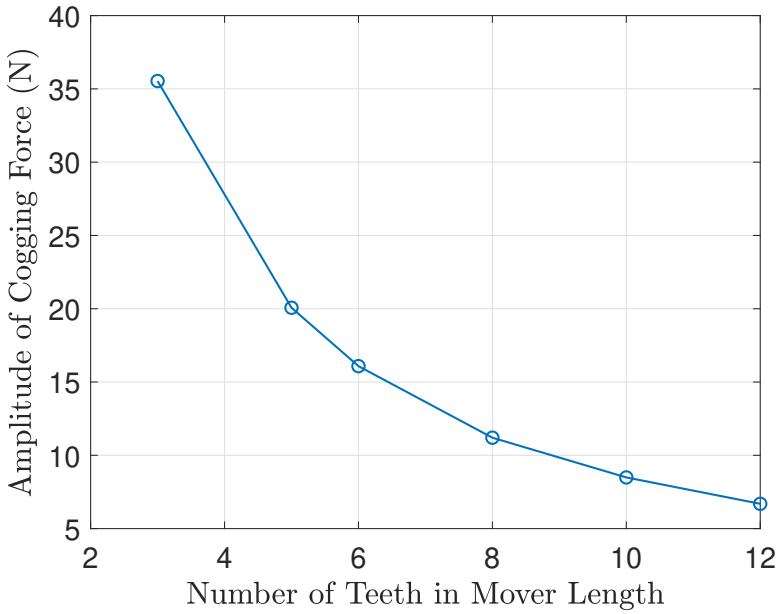

Figure 5-24: Simulated total cogging force in the motion direction under different number of yaw control stator teeth number over the moving stage length.

structure along the contour shown in Figure 5-23(a). (2) Spread all parts along the contour except for the stator backiron in a 2D plane, as shown in Figure 5-23(c). (3) Add a large, highly-permeable yoke connecting the top and bottom bias permanent magnets to represent stator backiron, which provides a flux return path for the bias flux, as shown in Figure 5-23(b). This model can be used to calculate the bias and yaw control magnetic fields in our magnetically levitated linear stage system. Note that this two-dimensional model does not capture the leakage path for the permanent magnet bias flux accurately, since the effect of the motor stator and motor secondary are ignored. Here we set the remanence of the permanent magnets to 0.8 T to reach an air gap bias flux density of 0.45 T, which matches the air gap bias flux density calculated by a three-dimensional finite element simulation. Also note that the model shown in Figure 5-23 only represents one side of the stage. The total cogging force in the y-direction will be approximately twice of the force calculated from the model. This model's computation time is about 40 times faster than a three-dimensional finite element model for the bias and yaw control fluxes.

With the model in hand, we can design the yaw control stator yoke and bias

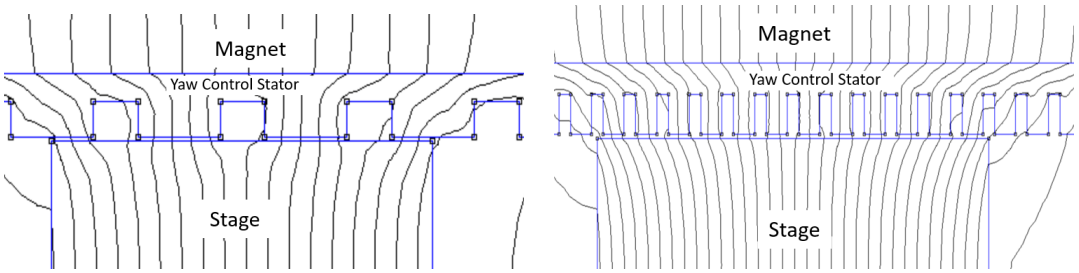

(a) (b)

Figure 5-25: Yaw control stator geometry and magnetic field distribution under different number of stator teeth number over the moving stage length. (a) Three teeth over stage length. (b) Twelve teeth over stage length.

flux collectors based on the simulation results. We used two methods to reduce the cogging force on the moving stage, which are discussed below.

(1) Finer teeth – The first method of reducing the cogging force is to use a yaw control stator with finer teeth. Since the cogging force is generated by the saliency of the yaw control stator yoke, the cogging force's wavelength and magnitude can be reduced with a smaller tooth pitch in the yaw control stator. Figure 5-24 shows the simulated cogging force peak-to-peak amplitude at different number of teeth covering the full stage length, and Figure 5-25 shows the bias magnetic field distribution in the stator and stage when the number of stator teeth over the stage length equals to 3 and 12. It can be seen that the cogging force amplitude is reduced as the yaw control stator teeth are becoming finer.

As discussed in Chapter 4, the wavelength of the yaw control flux should match with the length of the moving stage for yaw control torque generation. As a result, using finer yaw control stator teeth typically requires a larger number of phases in the yaw control stator winding. This also requires more power amplifiers and making the system more complex. In our design, we selected to use 10 stator teeth over the length of the moving stage due to a trade-off between the system complexity and cogging force amplitude.

(2) Edge skewing – The second method for cogging force reduction is skewing the edges of the bias flux collectors. As shown in Figure 5-4, the edges of the bias flux collectors are skewed by one yaw control stator tooth pitch. The effect of skewing is

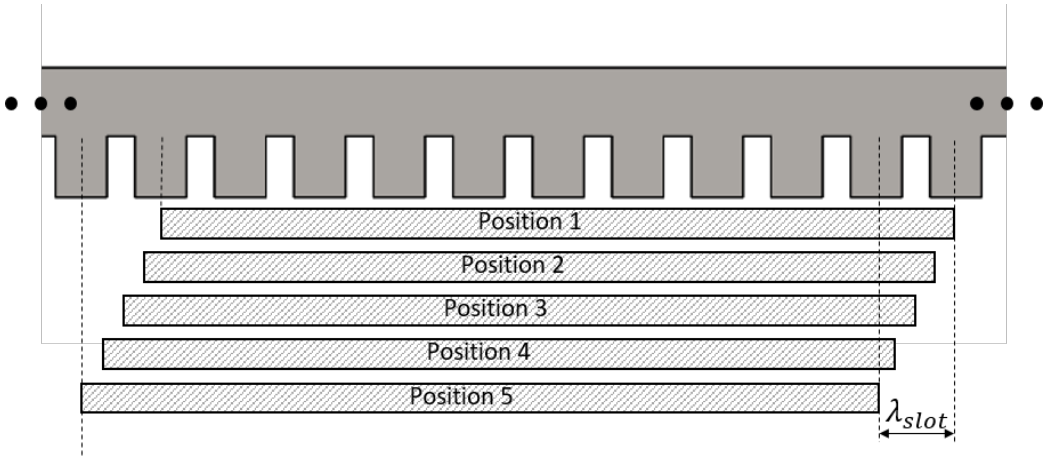

Figure 5-26: Estimation for effect of skewing secondary for cogging force reduction with 2.5-dimensional finite element simulation.

simulated using the two-dimensional finite element model by the following method: First, we calculated the thrust force generation on the stage at five evenly-distributed positions within one stator tooth pitch, as shown in Figure 5-26. Then, we averaged the five calculated forces to get an estimated force generated with skewed bias flux collectors. This method is referred as the 2.5-dimensional simulation in [69], where the skewing effect is simulated for linear permanent magnet synchronous machine for cogging force reduction. Figure 5-27 shows a comparison between the simulated non-skewed and skewed y-directional force generated on the stage by the bias flux as the stage is moved by one tooth pitch. It can be seen that with a skewed edge in the bias flux collectors, the cogging force is significantly reduced, with its peak-to-peak value reduced from 16 N to 0.3 N.

Yaw Control Stator Design and Fabrication

This section introduces the detailed design and fabrication for the yaw control stators. Figure 5-28 shows the CAD diagram of the yaw control stator yoke and its major design parameters, and Table 5.6 shows their values. In the yaw control stator yoke, we selected a large ratio between the tooth width and slot width, i.e. $w^s_{tooth}/w^s_{slot} = 11/6$. This design is selected for two reasons: (1) The yaw control stator coil does not need large ampere-turns, since the yaw control flux does not require large amplitude

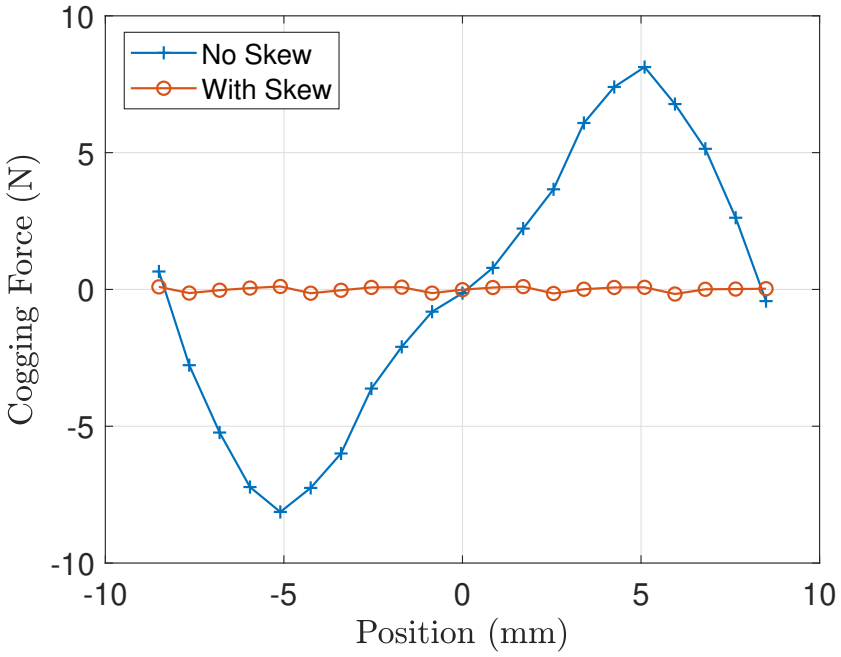

(a)

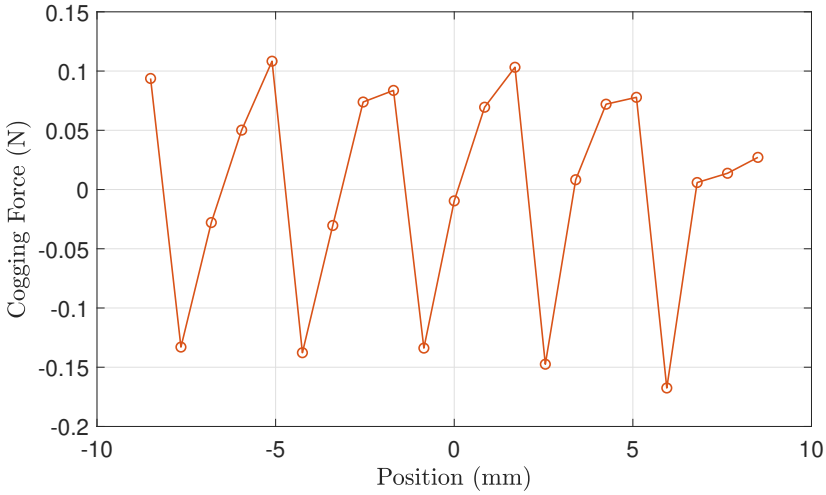

(b)

Figure 5-27: Simulated cogging force on the moving stage with skewing on the bias flux collectors. (a) Comparison between cogging force with and without skewing. (b) Zoomed in cogging force data with skewing.

to generate a steering flux for yaw control torque generation. Therefore small slot width is acceptable for the yaw control stator. (2) The permanent magnet bias flux can concentrate in the yaw control stator teeth, and a relatively large stator teeth width can help prevent severe saturation in the yaw control stator teeth.

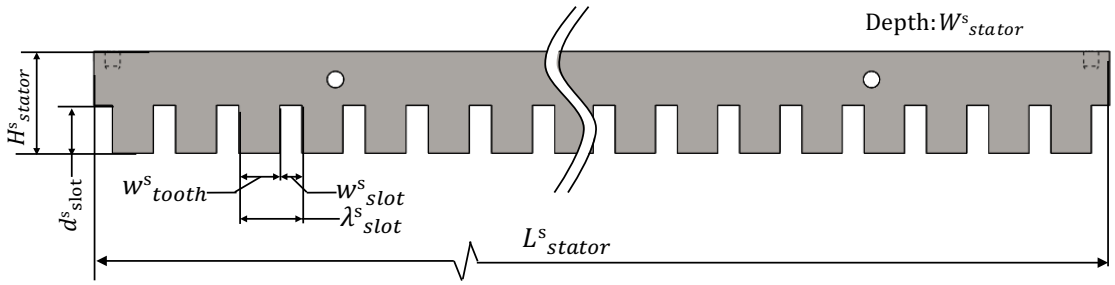

Figure 5-28: CAD diagram of the yaw control stator yoke and its major dimensions.

Table 5.6: Major geometric parameters of the yaw control stator yoke.

Parameter Description	Variable	Value
Yaw control stator length	L^s_{stator}	650 mm
Yaw control stator width	W^s_{stator}	6.35 mm
Yaw control stator height	H^s_{stator}	27.6 mm
Slot pitch	λ^s_{slot}	17 mm
Slot width	w^s_{slot}	6 mm
Tooth width	w^s_{tooth}	11 mm
Slot depth	d^s_{slot}	13 mm

The windings of the yaw control stators use a five-phase equivalent of ten-phase winding, where five independent current are being used. There are 10 stator teeth in one full wavelength, and the yaw control stator windings are in the pattern: *(A, -D, B, -E, C, -A, D, -B, E, -C)*. Figure 5-29 shows a winding diagram of the yaw control stator, and Figure 5-30 shows a phasor diagram of the currents in the yaw control stators windings. The windings in the same phase in all four yaw control stators are connected in series.

Figure 5-31 shows the photos of the assembled yaw control stator, including both the yaw control stator yoke and the coils. The yaw control stator yoke is fabricated with ANSI 1018 low carbon steel. Compared with electrical laminations, a stator yoke made of solid steel has a significantly lower cost. We simulated the yaw control stator iron loss with a low carbon steel yoke, and the calculated total iron loss in four yaw control stator yokes is 2.6 W when the electrical frequency of the yaw control stator excitation is 10 Hz, which is acceptable for our linear stage prototype.

There are in total 38 coils in each yaw control stator. The phase A, B, and D in

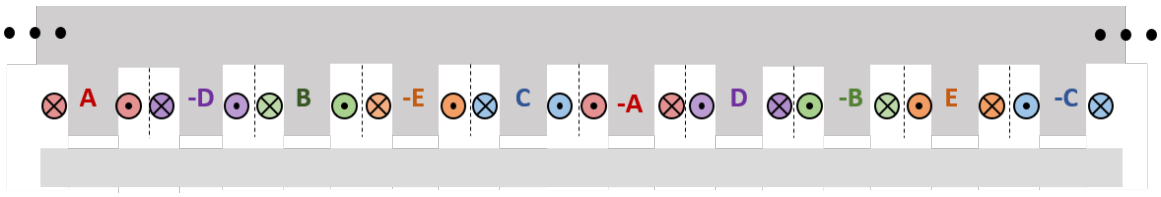

Figure 5-29: Winding scheme of the yaw control stator.

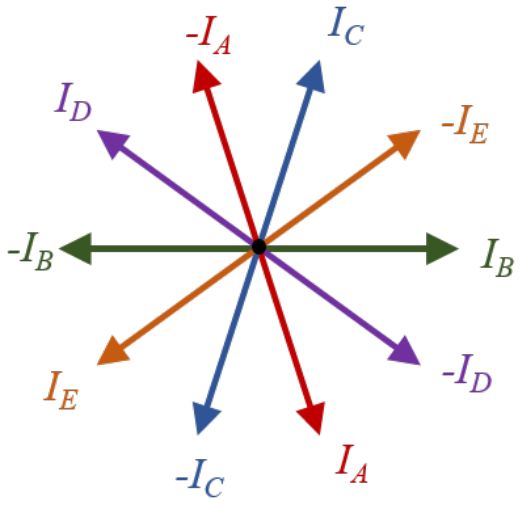

Figure 5-30: Phasor diagram of the winding currents in yaw control stator.

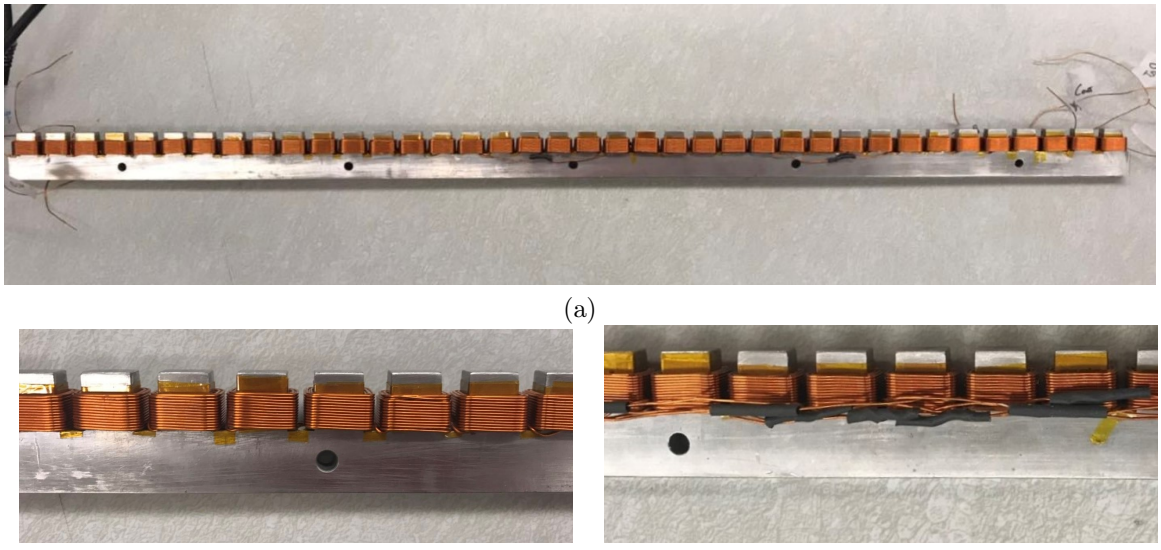

(a)

(b) (c)

Figure 5-31: Photographs of the yaw control stator. (a) Full yaw control stator. (b) Zoomed-in photo of yaw control stator. (c) Zoomed-in photo of the yaw control stator showing the coil connections.

(a)

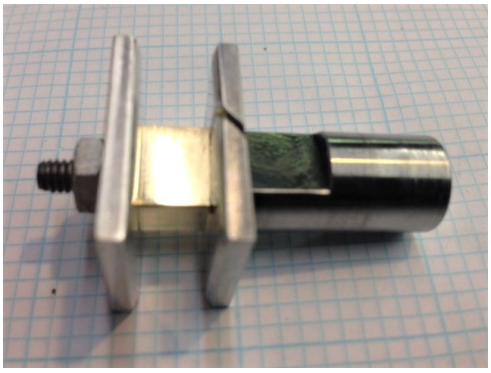

(b)

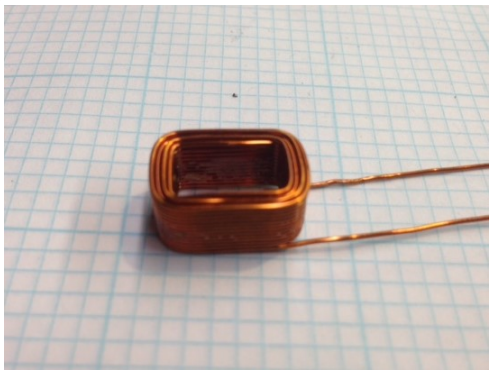

(c)

Figure 5-32: Photographs of the winding tool of the yaw control coil. Photograph courtesy of Fred Sommerhalter. (a) Parts of the yaw control coil winding tool. (b) Assembly of yaw control coil winding tool. (c) Photo of the yaw control coil.

each yaw control stator has 8 coils, and phase C and E has 7 coils. Figure 5-32 shows the photos of the yaw control coil and its winding tool. The coils are also fabricated by Mr. Fred Sommerhalter, who has fabricated the motor stator coils as well. The yaw control coils are made of AWG 23 bondable magnetic wire. The coil's height is 8 mm, and its outer length and width are 16.5 mm and 12 mm, respectively. The number of turns of each yaw control stator coil is 50.

When assembling the coils to the stator yoke, similar to the motor stator, we wrap two layers of Kapton polyimide insulating tape to each stator slot and stator teeth. The coils are bonded to the stator teeth to prevent vibration. Figure 5-33 shows the procedures of making the connection between two coils in the same phase. The

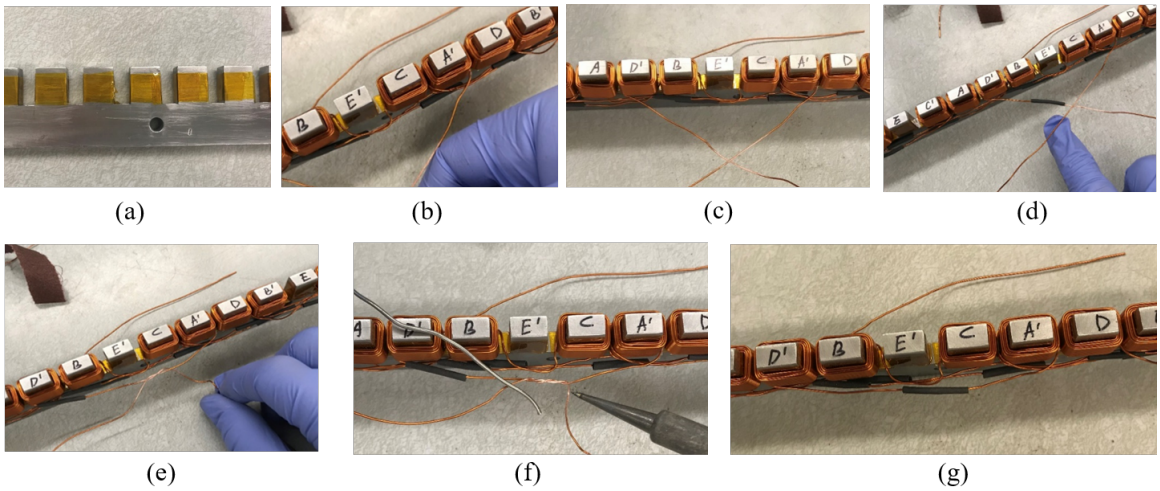

Figure 5-33: Procedures of connecting coils in the yaw control stator. (a) Wrap each tooth with two layers of Kapton tape for insulation. (b) Remove enamel on magnetic wire in the middle of two leads using sand paper. (c) Make sure enamel on wire is removed all around the wires. (d) Put heat shrink tube on one lead. (e) Tie the two leads together and make a knot in wires with the insulation removed sections together. (f) Solder the two wires at the knot. (g) Cut off left over leads, and heat up the heat shrink tube at the connection point.

same method is used for connecting the coils in the motor stator. The same phase windings of all four yaw control stator are connected in series. The leads of each yaw control stator are covered with PTFE tubes, and are connected to another yaw control stator. The total per phase resistance and inductance of all four yaw control stators' windings are 5.2 Ω and 5.7 mH, respectively.

5.3.4 Mechanical Design and Assembly Process

This section introduces the mechanical design and assembly process of the stator assembly. The over-all design is shown in Figure 5-34. Aside from the magnetically involved parts, each stator assembly include two L-shaped aluminum spacers, two housing plates, ten magnet spacers (not shown in Figure 5-34), five dovetail-shaped nuts, a bottom spacer plate, and three angle plates. The stator assembly is mounted on the optical table, which is not shown in the picture.

In each stator assembly, two L-shaped aluminum spacers are included to separate the bias flux path and the motor flux path. Figure 5-35 shows the CAD model of

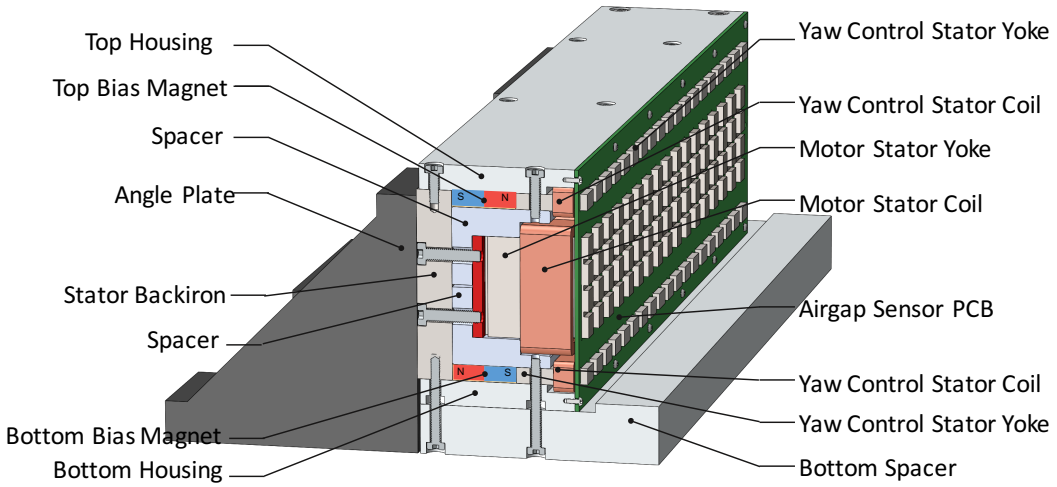

Figure 5-34: Cross-section view of the stator assembly CAD model.

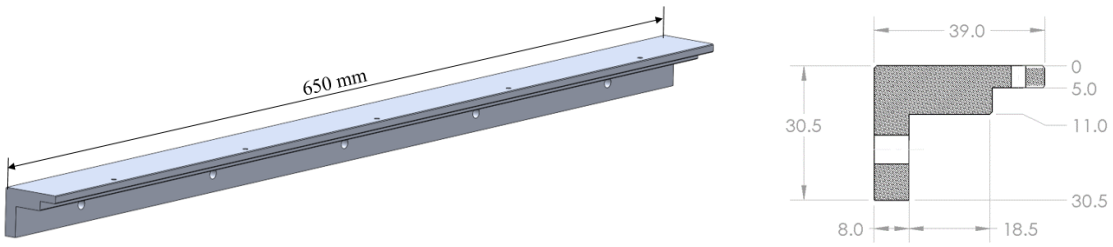

(a) (b)

Figure 5-35: Aluminum spacer for stator and its critical dimensions. (a) CAD model of the aluminum spacer. (b) Cross-section of the spacer and its dimensions in millimeters.

the aluminum spacer and its major dimensions. In the stator assembly, there is a gap designed in between the two L-shaped spacer. This is included to ensure contact between the motor stator yoke and the internal surfaces of the L-shaped aluminum spacers.

The assembly process of the stator is briefly introduced here. We first assemble the motor stator and two aluminum L-shaped spacers to the stator backiron. There are five dovetail-shaped slots arranged on the back side of the stator yoke, as shown in Figure 5-19 and Figure 5-20. Five dovetail-shaped nuts made of ANSI 1018 low carbon steel, as shown in Figure 5-36(a), are inserted in the slots, and are used to fasten the motor stator to the spacers and the stator backiron. The CAD model of

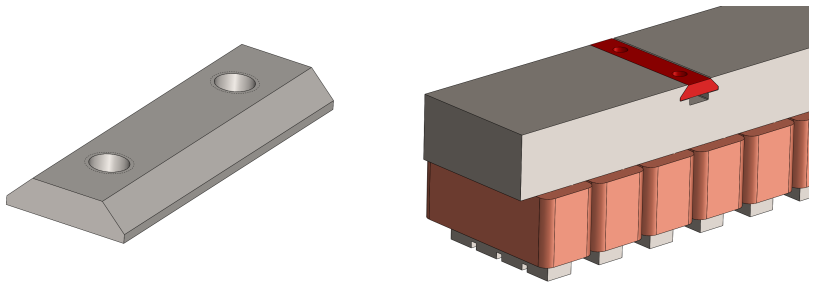

(a) (b)

Figure 5-36: Fixture of motor stator. (a) CAD model of dovetail-shaped nut for motor stator fixture. (b) Dovetail-shaped nut in stator yoke.

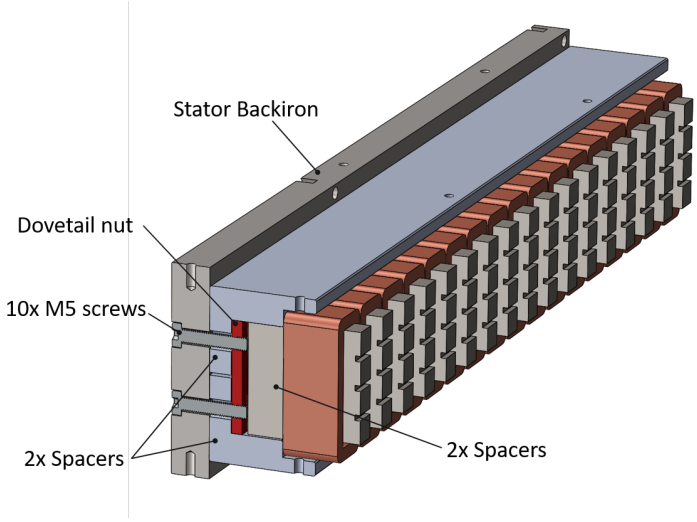

Figure 5-37: CAD model of motor stator, aluminum spacers, and stator backiron.

the assembled motor stator, aluminum spacers, and the stator backiron is shown in Figure 5-37.

Next, the yaw control stators can be assembled into the stator assembly as shown in Figure 5-38 through the screws and four 1 inch-long magnet spacer tubes. Then, permanent magnets with 1 inch $\times$ 1 inch $\times$ 1/4inch dimension can be placed one by one into the pockets on the back of the yaw control stator yoke with their magnetization direction aligned, as shown in Figure 5-39. Finally, the stator top and bottom housing plates, bottom spacer plate, angle plates, and the optical sensor printed circuit board can be assembled into the stator assembly.

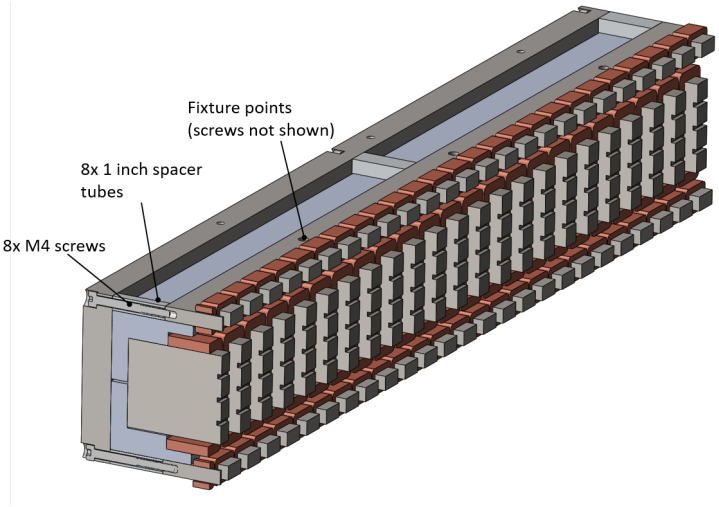

Figure 5-38: CAD model of the assembly of yaw control stators.

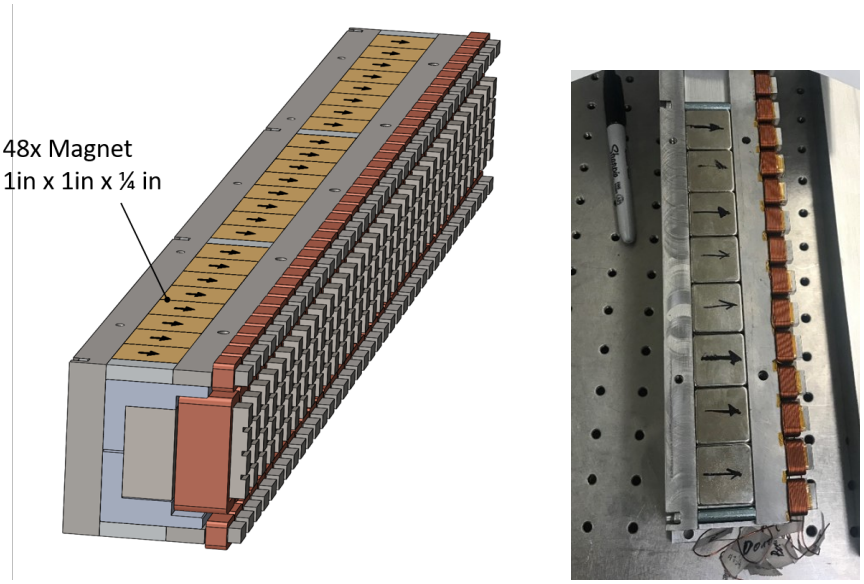

(a) (b)

Figure 5-39: Assembly of the biasing permanent magnet in the stator assembly. (a) CAD model of the stator showing the permanent magnets. (b) Photograph of the assembly process for biasing permanent magnets.

5.4 Sensing System

This section introduces the sensing system for the magnetically-levitated linear stage prototype. There are two kinds of displacement sensors used to measure the stage's motion in x-, y-, and θ_z-directions: optical reflective sensors are used to mea-

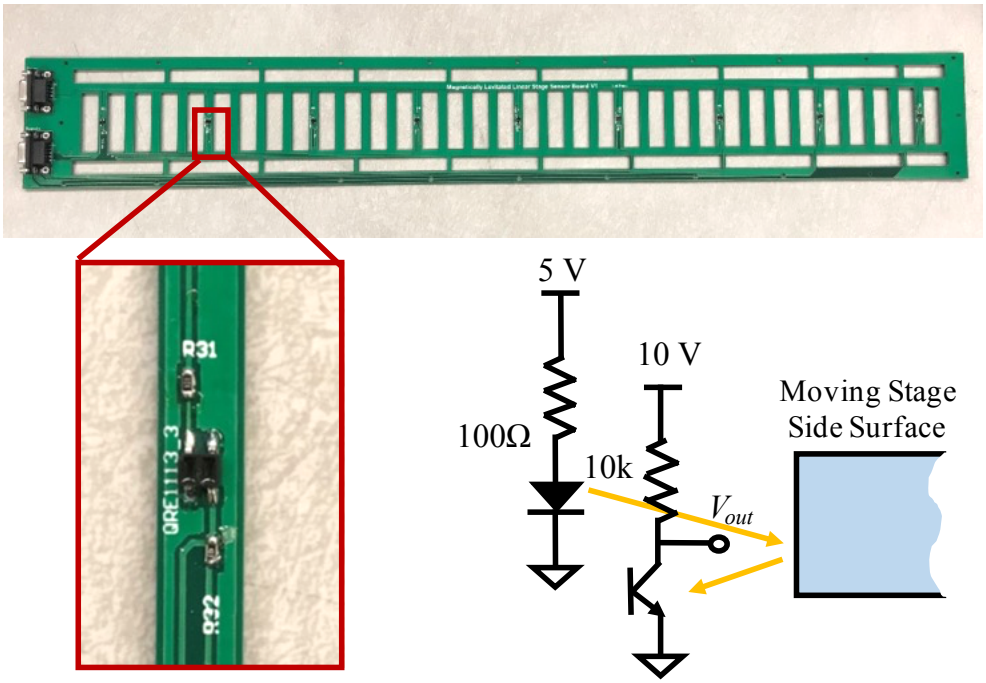

Figure 5-40: Photograph of the printed circuit board for the optical air-gap sensors (QRE1113GR from On Semiconductor) and the circuit diagram of the optical sensor.

sure the air gap length of the linear stage at different y-directional position, and magnetic encoders are used to measure the stage's y-directional displacement.

5.4.1 Optical Displacement Sensors

To measure the x- and θ_z-directional displacements of the moving stage at different y-positions, 16 reflective-type optical displacement sensors (QRE1113GR from On Semiconductor) are arranged along the stator on two printed circuit boards (PCBs), and the PCBs are mounted on the front surface of the two stators assemblies, as shown in Figure 5-1. With this configuration, there are two optical sensors arranged face to face at the same y-directional position, and the sensor pair is to measure the stage's x-directional displacement differentially. Figure 5-40 shows a photograph of the optical sensor PCB and a schematic diagram of the optical sensor's circuit. The sensor QRE1113GR consists of an infrared LED and a phototransistor facing the same direction. With the circuit diagram shown in Figure 5-40, the LED shines an infrared beam on the side surface of the moving stage, and the phototransistor

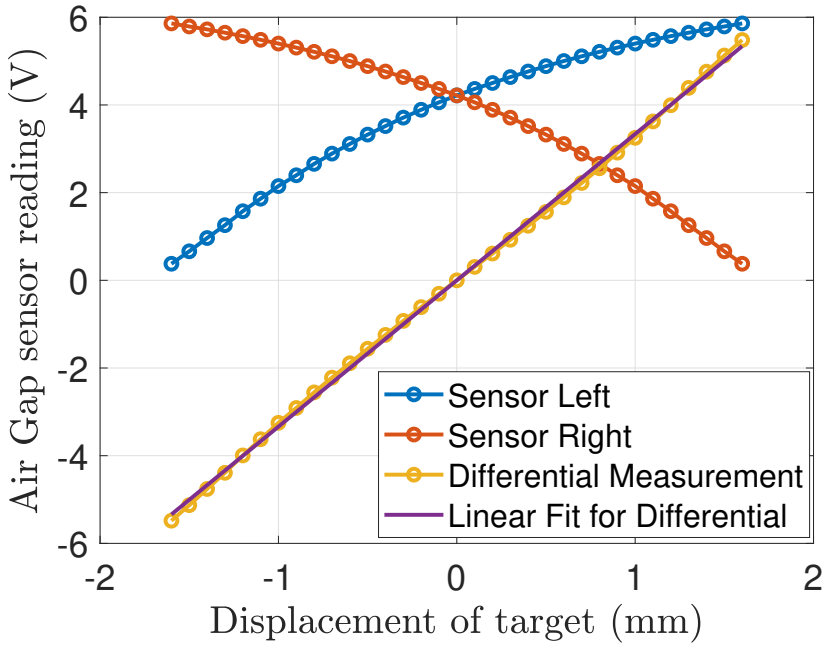

Figure 5-41: Calibration data of the reflective optical air-gap sensors (QRE1113GR). Linear fit equation: $V_{diff} = 3.34\Delta x$.

detects the reflected light. Two 0.5 mm-thick white Delrin polyacetal sheets are epoxied on the two side surfaces of the moving stage for better reflectivity, as shown in Figure 5-4. Figure 5-41 shows the calibration data of the optical sensors on two sides of the moving stage with respect to the lateral displacement of the stage, and the differential signal of two sensor's outputs is also plotted. It can be seen that the differential signal of left and right optical sensor outputs is largely linear with respect to the lateral displacement of the moving stage.

In the design of our stage, at least two pairs of optical sensors are engaged with the moving stage at any position. When the linear stage is operating, the stage's x- and θ_z-directional displacements are calculated from the readings of the optical sensors that are engaged with the stage, as shown in Fig. 5-42. The measured y-directional position of the stage is used to determine which two pairs of optical sensors are engaged with the stage. The encoders for stage's y-directional displacement measurement is introduced in Section 5.4.2. In order to prevent step changes in the air-gap signals due to errors in optical sensor calibration, a sigmoid function is used to blend the optical

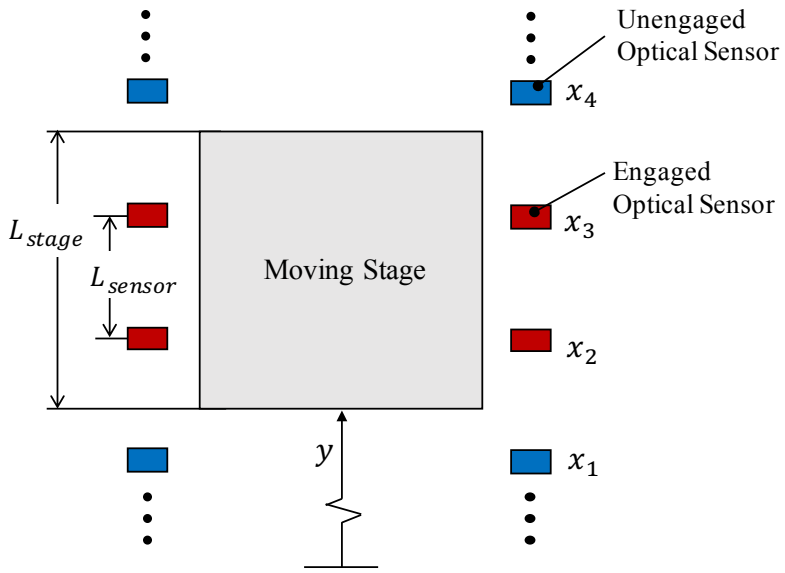

Figure 5-42: Top view diagram of optical sensors and moving stage. In this configuration, $\hat{x} = (x_2 + x_3)/2$, and $\hat{\theta}_z = (x_2 - x_3)/L_{sensor}$.

sensor readings as the stage is moving. The stage's x- and θ_z-directional displacements are estimated through the sensor readings as follows: Define the estimated stage's displacements in x- and θ_z-directions as $\hat{x}$ and $\hat{\theta}_z$, respectively. x_i is the differential signal of the i-th optical encoder pair. Define $\hat{x}_i = (x_{i-1} + x_i)/2$ and $\hat{\theta}_{zi} = (x_{i-1} - x_i)/L_{sensor}$ as the stage's displacements estimated by the $i-1$-th and i-th sensor pair readings, where L_{sensor} is the y-directional distance between two optical sensor pairs. Also define y_{sw_i} as the switching threshold for i-th air gap sensor, i.e. if $y_{sw_{i-1}} < y < y_{sw_i}$ then $\hat{x} = \hat{x}_i$ and $\hat{\theta}_z = \hat{\theta}_{zi}$. Define sigmoid function $S(x)$ as

$$S(x) = \frac{1}{1 + e^{-\beta x}}, \tag{5.12}$$

which is a smooth transition from 0 to 1 switching at $x = 0$, and β is a positive constant setting the steepness of the switching. The x- and θ_z-displacement estimation can be calculated using Algorithm 1:

Algorithm 1 Air gap sensor switching for N sensor pairs.

$\hat{x} = 0$

$\theta_z = 0$

for i := 1 to N-1 **do**

$$\hat{x} = \hat{x}\Big(1 - S(y - y_{sw_i})\Big) + \hat{x}_i S(y - y_{sw_i})$$
$$\hat{\theta}_z = \hat{\theta}_z\Big(1 - S(y - y_{sw_i})\Big) + \hat{\theta}_{zi} S(y - y_{sw_i})$$

return $\hat{x}$, $\hat{\theta}_z$

With this air gap sensor switching algorithm, a smooth transition from one set of sensor readings to the next set can be achieved when the stage is moving. The outputs of Algorithm 1, $\hat{x}$ and $\hat{\theta}_z$, are used for feedback control for the stage's magnetic suspension.

5.4.2 Magnetic Encoders

The stage's y-directional displacement is measured by linear magnetic encoders. In order to achieve a design where no cable is attached to the moving stage, we configured two magnetic encoder scales on the bottom of the moving stage. Two rows of encoder readheads, with four encoder readheads in each row, are configured along the moving direction of the stage, as shown in Figure 5-43. Here we selected the LM15 magnetic encoder from Renishaw Inc. for our linear stage. The reason for this selection is because this magnetic encoder allows a large ride height tolerance up to 4 mm, which is the distance between the encoder readhead and the scale. This is favorable for our linear stage prototype, since the stage's suspension in vertical direction is achieved passively, which has relatively low stiffness and damping. The resolution of the encoder is 8192 counts per full wavelength (10 mm), i.e. 1.2 μm. In our testing, we found that the selected encoder can demonstrate a hysteresis of about 10 μm per 100 mm when we move back and forth of one cycle, and the amount of hysteresis can vary between the encoder scales. Such error is not acceptable for the reticle transportation application. However, this encoder is used in our prototype

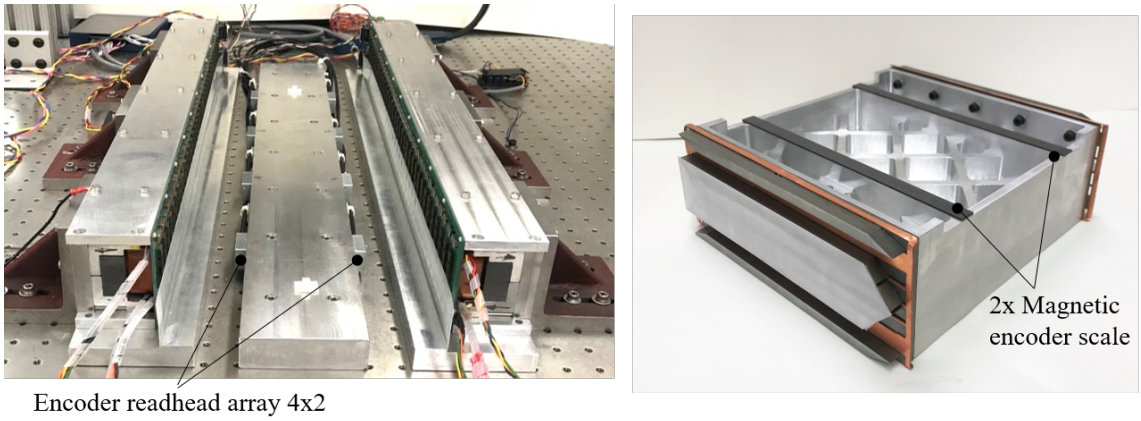

Figure 5-43: Magnetic encoders in magnetically-levitated linear stage. (a) Photograph of the encoder readhead array. (b) CAD model of the moving stage showing the encoder scales.

system as a proof of concept. During the experimental tests, we zero the encoder readings after every 3 cycles of motion.

The y-directional position signal of the moving stage is calculated by integrating the increment of the encoder reading from an readhead that is engaged with the stage. Define y_1, y_2, y_3, and y_4 as the readings for the four encoder readheads in one row, $\Delta y_i(k) = y_i(k) - y_i(k-1), i = 1, ..., 4$ as the increment of each encoder reading at time step k, and $y_{sw_1}, y_{sw_2}, y_{sw_3}$ as the three threshold positions that the encoder being used is switched. Note that at these threshold positions the moving stage must engage with two encoder readheads simultaneously. Then the stage's position measured by this row of encoder readheads can be calculated using Algorithm 2:

Algorithm 2 Encoder handing

$\Delta y_i(k) = y_i(k) - y_i(k-1)$; i = 1,...,4

if $\hat{y}(k-1) < y_{sw_1}$ **then**

    $\hat{y}(k) = \hat{y}(k-1) + \Delta y_1(k)$

else if $y_{sw_1} \leq \hat{y}(k-1) < y_{sw_2}$ **then**

    $\hat{y}(k) = \hat{y}(k-1) + \Delta y_2(k)$

else if $y_{sw_2} \leq \hat{y}(k-1) < y_{sw_3}$ **then**

    $\hat{y}(k) = \hat{y}(k-1) + \Delta y_3(k)$

else

    $\hat{y}(k) = \hat{y}(k-1) + \Delta y_4(k)$

end

Finally, we average the measurements of the left and right rows of encoders to get the y-directional displacement measurement of the stage. Note that typically magnetic encoder scales are not vacuum compatible. When the linear stage needs to operate in vacuum, different vacuum-compatible displacement sensors are needed. Alternative sensing system design options are discussed in Chapter 7.

5.5 Power Electronics

This section introduces the power electronics being used in our magnetically-levitated linear stage prototype. There are in total eleven phases in our linear stage: each motor stator is driven by three-phase currents, and all yaw control stators are connected in series, and are driven by five-phase currents. We used eleven single-phase power amplifiers to drive the stators. The power amplifier being used is the B30A40 switching-type amplifier from Advanced Motion Control (AMC). This amplifier can be used either in single-phase or three-phase mode. In our prototype, we selected to use the amplifier in single-phase and current control mode, which takes an analog signal as the current command, and outputs a high-voltage PWM signal which energizes the stator winding. The DC bus voltage is supplied by the DC power supply PS30A from Advanced Motion Control, which takes a 120/208V three-phase AC power as

Table 5.7: Specifications of power amplifier B30A40.

Specification	Value
Rated continuous power	5.7 kW
Continuous current	15 A
Peak current	30 A
Switching frequency	20 kHz
DC bus voltage range	60-400 V
Operating DC bus voltage	300 V

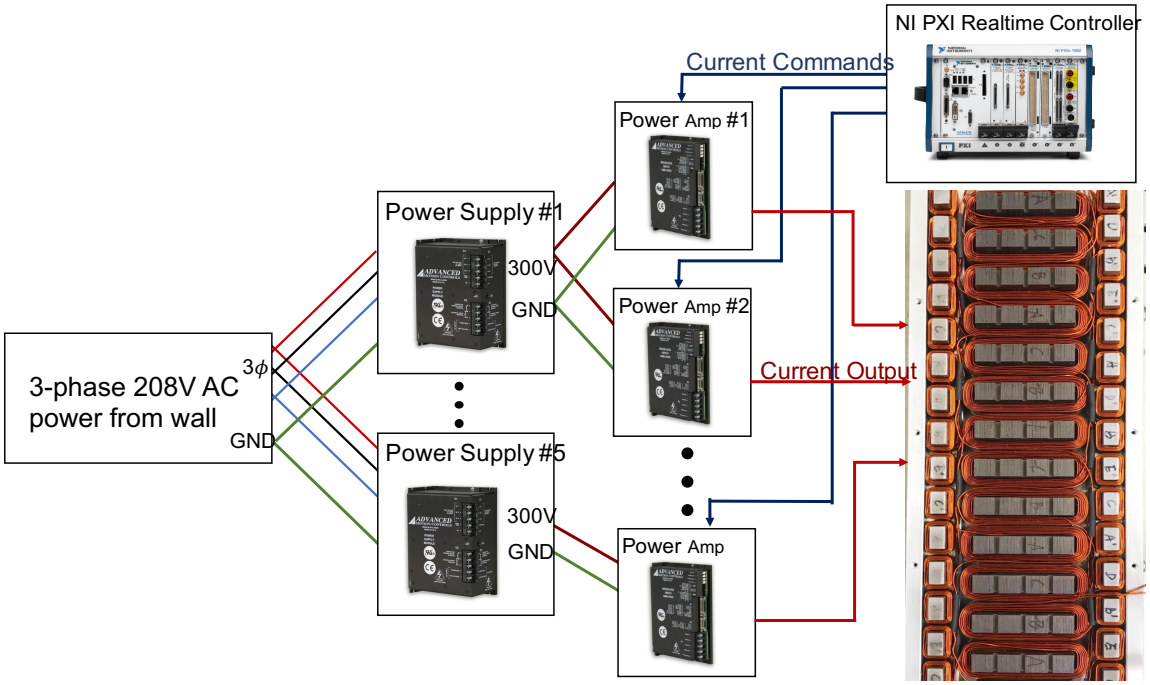

Figure 5-44: Connection diagram of power electronics for magnetically-levitated linear stage.

the input, and the output is 300 V. The specifications of the current-controlled power amplifier are shown in Table 5.7.

The power electronics for our magnetically-levitated linear stage are configured by Dr. Jun Young Yoon. Figure 5-44 shows the power electronics connection diagram for our magnetically-levitated linear stage prototype. The 120/208 V three-phase AC power supplies from the wall are connected to five DC power supplies (PS30A by AMC), whose output is a 300 V DC voltage. Then the DC bus voltages are connected into the high-voltage input of the power amplifiers (B30A40 by AMC). The current command signals sent out from real-time controller's D/A channels are connected into

Figure 5-45: Photograph of the rack for power electronics, including DC power supply, power amplifiers, and fuses.

the signal input of the power amplifiers. Finally the outputs of the power amplifiers are connected to the stator windings. Fast-acting fuses are connected to the outputs of each power amplifier for safety. Figure 5-45 shows a photograph of the rack for the power electronics. Readers are referred to Dr. Jun Young Yoon's thesis [69] for more details about the power electronics.

5.6 Grounding and Shielding

This section discusses the grounding and shielding for the magnetically-levitated linear stage prototype. In our linear stage, the optical air gap sensor QRE1113GR has an analog output, and the PCBs for air gap sensors are mounted on the front face of

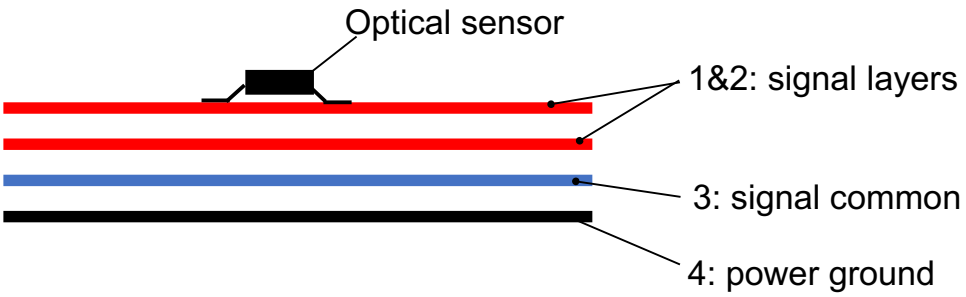

Figure 5-46: Diagram of layers in the optical air gap sensor printed circuit board.

the stator assemblies, which is close to the stator coils. In addition, the stator coils are excited with high-voltage switching-type power amplifiers. As a result, the air gap sensors' reading can be influenced by the switching noise from the power amplifiers if the grounding and shielding are not properly configured, and this effect can significantly influence the performance of our linear stage prototype.

The first shielding effort in our prototype is the design for the air gap sensor PCBs. Figure 5-46 shows a diagram for the layers in an air gap sensor PCB. As shown in Figure 5-46, there are four layers in the PCB. Define the layer with the sensor elements soldered on as the first layer. In this PCB, the first and the second layers are the signal layers for sensors' power and readings. The third layer is a full layer of copper connected to the signal common, and the fourth layer is another copper layer connected to the power common. The intention is that the currents due to the parasitic capacitive coupling between the stator coils and the PCB can flow back to the power common in the last layer of the PCB, and therefore reduce its interference with the signal ground and the air gap sensor signals.

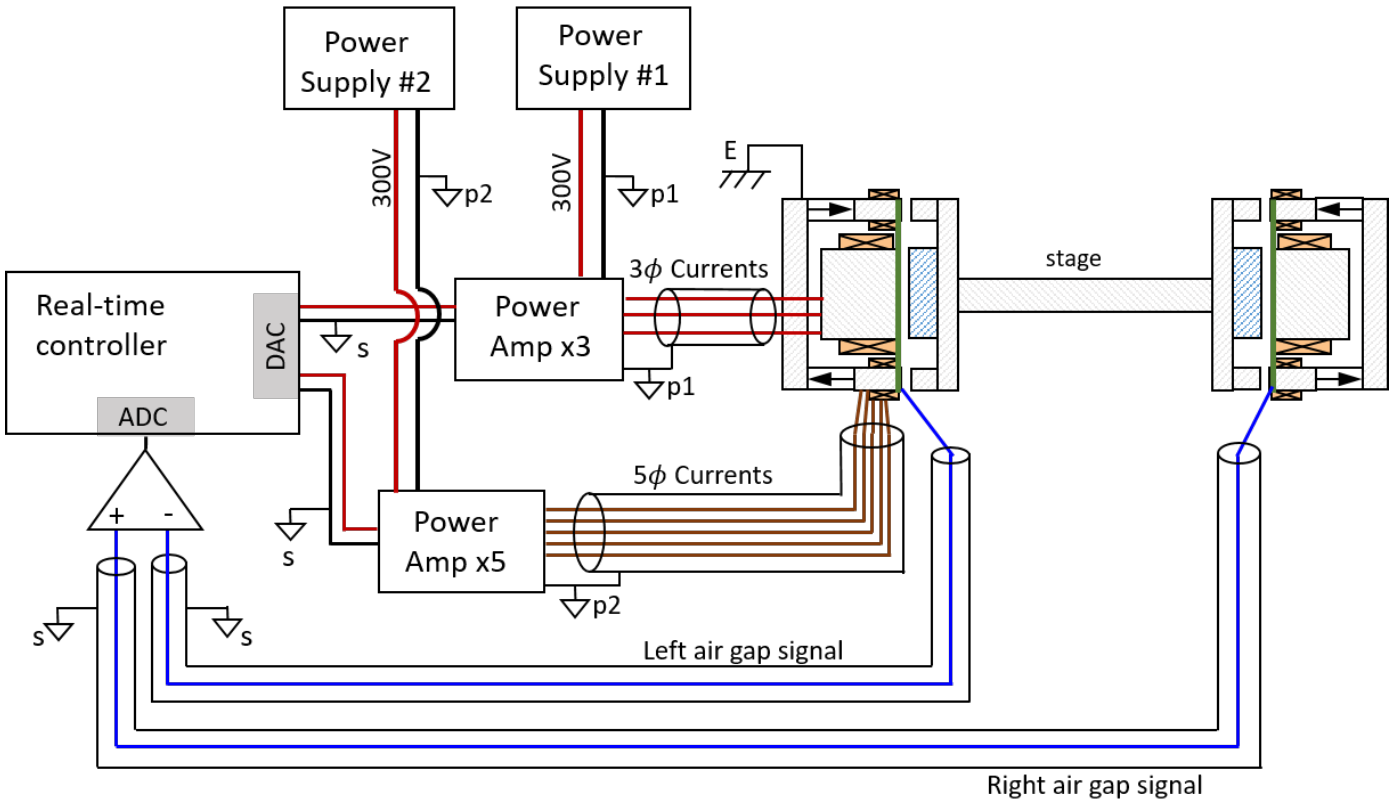

Figure 5-47: Diagram of connection in our magnetically-levitated linear stage prototype. Note that here only the power electronics for left stator is shown. The right stator uses symmetrical connections.

Figure 5-47 shows a diagram of the connections in our prototype system. Note that in this figure we only show the power electronics for the left side stator. The right side stator uses the same configurations. The triangles labeled with s indicate the signal common, triangles labeled with p indicate the power common, and the ground symbol with E indicates the earth ground. In our system, these three commons are not connected. The power supplies here provide two outputs: 300 V and a power common. These outputs are connected to the power amplifiers. The current command analog signals and the signal ground from the real-time controller are connected to the signal ports of the power amplifiers. The power amplifiers' output are connected to the stator windings through shielded cables to energize the stator windings, and the shields are connected to the corresponding power common.

The blue lines in Figure 5-47 represent the cables carrying the output signals of air gap sensors. These signals are connected to the A/D converters of the real-time controllers through shielded cables, where the shield is connected to the signal common. As discussed in Section 5.4, we only need the differential signal of the two optical sensors on two sides at the same y-directional position for suspension control. Therefore here we connect the outputs of the sensors pairs to the two terminals of the differential analog inputs, and rely on the differential amplifiers in the A/D interface to reject the common-mode noise from the switching power amplifiers.

Finally, oversampling is applied for the air gap sensor readings to further filter the noise due to the interference from the switching power amplifiers. In our system, we over-sampled the air gap sensor readings at 100 kHz using the FPGA, averaged every 10 samples to one signal, and passed the averaged signal to the feedback control loop. Since the switching frequency of the power amplifiers is 20 kHz, such over-sampling method can take five samples in one switching cycle and then average the readings, which can and effectively reduce the noise level in the air gap sensor signals. Figure 5-48 shows the measured air-gap sensor reading with and without the over-sampling filter. It can be seen that using such over-sampling technique, the amplitude of the noise in the air gap sensor reading is effectively reduced. Figure 5-49 shows a histogram of the optical air gap sensor reading. The signal's standard deviation is

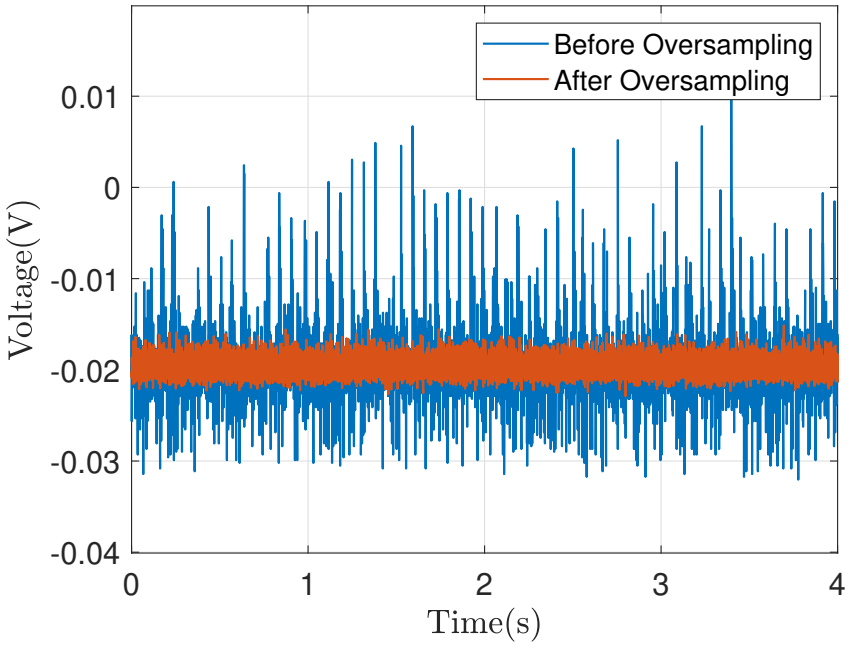

Figure 5-48: Measured optical air gap sensor output signal with and without oversampling.

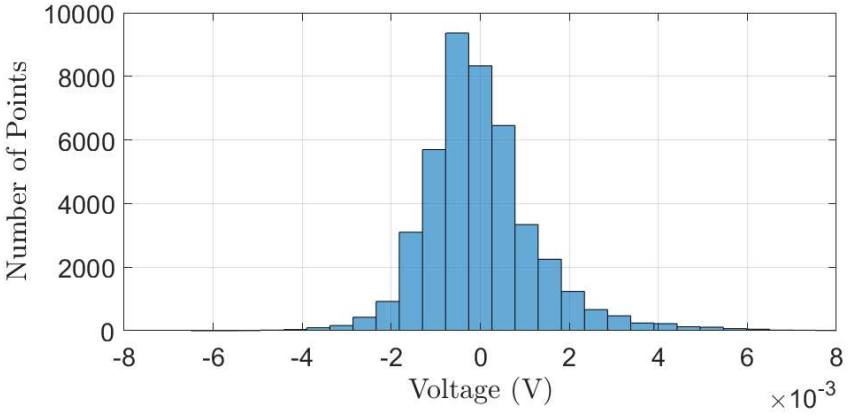

Figure 5-49: Histogram of final optical air gap sensor output signal. Standard deviation: 1.3 mV (0.4 um).

1.3 mV, which corresponds to 0.4 um in stage's lateral displacement.

In our linear stage prototype, the optical table's surface and the housing of stator assemblies are connected to the earth ground for safety. Since the yokes of the motor stators and yaw control stators are all electrically connected to the stators' housing, they are also connected to the earth ground. Before turning on the power of the

linear stage prototype, a high-voltage insulation test using an insulation meter is recommended between each phase and the earth ground to avoid insulation failure.

5.7 Control Design

This section introduces the control system design for our magnetically-levitated linear stage prototype, including an overview of the linear stage control system, and implementation details for the real-time controller in our prototype.

5.7.1 Control System Overview

Fig. 5-50 shows a control system block diagram for our linear stage prototype. Here, the x- and θ_z-directional displacements of the moving stage are estimated from the encoder and air-gap sensor measurements as described in Section 5.4, and are fedback for suspension control. The x-directional error signal is amplified by the x-DOF suspension controller $C_x(s)$, and the control effort signal u_x is used as the differential magnitude of the left and right motor current amplitudes. In addition to the x-directional control effort signals, a constant bias current I_{bias} is injected to the motor stator' current amplitude for thrust force generation and maintaining magnetic suspension.

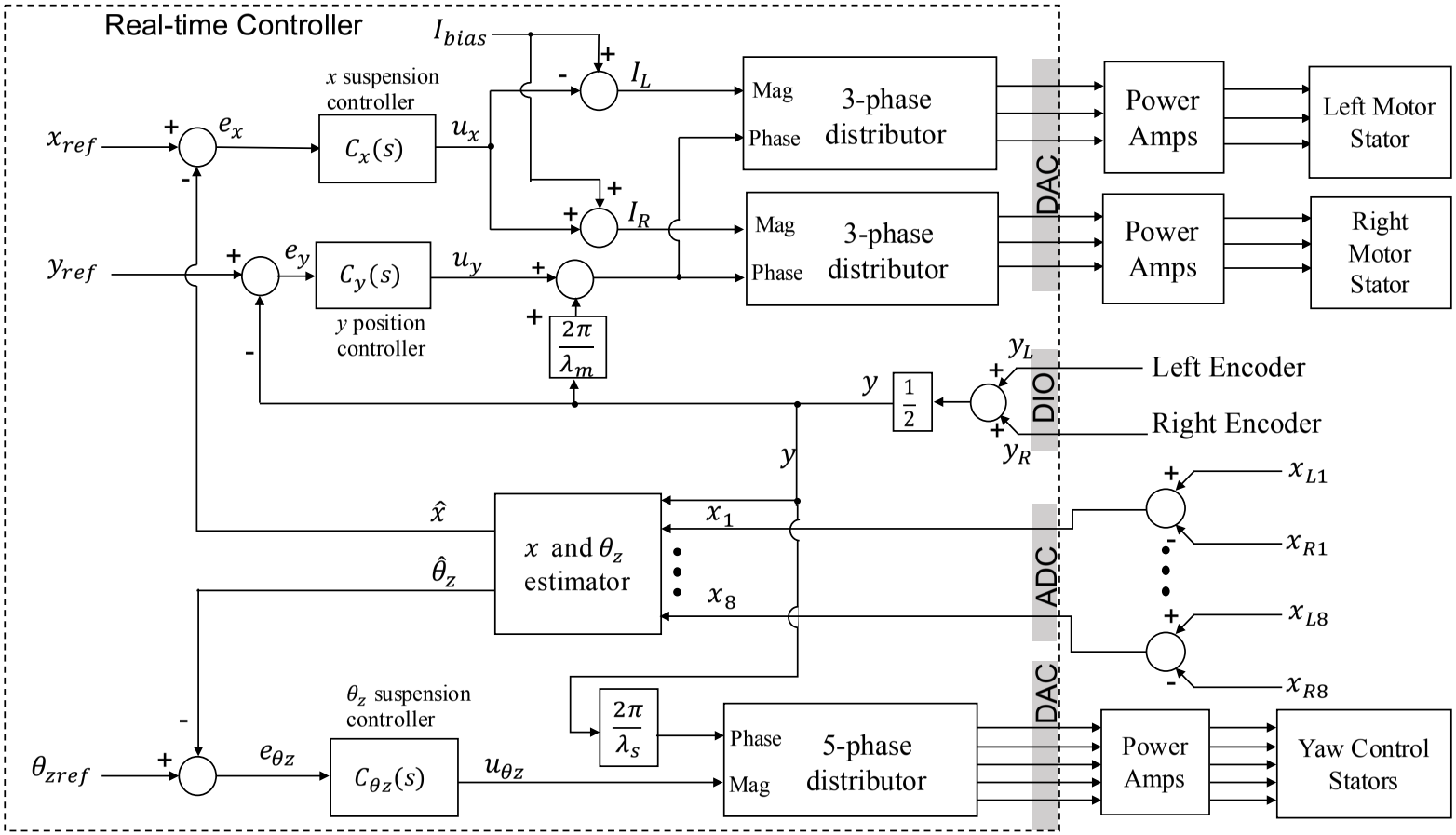

Figure 5-50: Block diagram of the control system for our magnetically-levitated linear stage prototype.

The hysteresis motors in our linear stage operate in synchronous mode. The position control loop for the linear stage is closed with the encoder measurement y being used for feedback, and the position control effort signal u_y is used to determine the phase difference between the motor stator excitation and the position of the linear stage. Therefore the phase of the motor stators is calculated as $\phi_{motor} = \frac{2\pi}{\lambda_m} y + u_y$, where λ_m is the wavelength of the motor stator magneto-motive force.

With the amplitude and the phase of the motor current determined, the current commands for the three-phase windings in the left and right motor stators $(I^*_{Lu}, I^*_{Lv}, I^*_{Lw})$ and $(I^*_{Ru}, I^*_{Rv}, I^*_{Rw})$ are determined as

$$I^*_{Lu} = (I_{bias} - u_x)\cos(\frac{2\pi}{\lambda_m} y + u_y), \tag{5.13}$$

$$I^*_{Lv} = (I_{bias} - u_x)\cos(\frac{2\pi}{\lambda_m} y + u_y + \frac{2\pi}{3}), \tag{5.14}$$

$$I^*_{Lw} = (I_{bias} - u_x)\cos(\frac{2\pi}{\lambda_m} y + u_y - \frac{2\pi}{3}), \tag{5.15}$$

$$I^*_{Ru} = (I_{bias} + u_x)\cos(\frac{2\pi}{\lambda_m} y + u_y), \tag{5.16}$$

$$I^*_{Rv} = (I_{bias} + u_x)\cos(\frac{2\pi}{\lambda_m} y + u_y + \frac{2\pi}{3}), \tag{5.17}$$

$$I^*_{Rw} = (I_{bias} + u_x)\cos(\frac{2\pi}{\lambda_m} y + u_y - \frac{2\pi}{3}). \tag{5.18}$$

These current command signals are then sent to the current-controlled power amplifiers and energize the motor stators.

The suspension of the stage in θ_z-direction is discussed below. The estimated yaw displacement $\hat{\theta}_z$ is injected into the yaw suspension controller $C_{\theta_z}(s)$, and the control effort signal u_{θ_z} is used to determine the yaw control stators' current amplitude. The winding excitations of the yaw control stators are synchronous to the moving stage, with their phases being $\phi_{yaw} = \frac{2\pi}{\lambda_s} y$, where λ_s is the wavelength of the yaw control stator magneto-motive force. The current commands for the yaw control

stator windings $(I_a^*, I_b^*, I_c^*, I_d^*, I_e^*)$ are generated by the five-phase distributor as

$$I_a^* = u_{\theta_z} \cos(\frac{2\pi}{\lambda_s} y), \tag{5.19}$$

$$I_b^* = u_{\theta_z} \cos(\frac{2\pi}{\lambda_s} y + \frac{2\pi}{5}), \tag{5.20}$$

$$I_c^* = u_{\theta_z} \cos(\frac{2\pi}{\lambda_s} y + \frac{4\pi}{5}), \tag{5.21}$$

$$I_d^* = u_{\theta_z} \cos(\frac{2\pi}{\lambda_s} y + \frac{6\pi}{5}), \tag{5.22}$$

$$I_e^* = u_{\theta_z} \cos(\frac{2\pi}{\lambda_s} y + \frac{8\pi}{5}). \tag{5.23}$$

These signals are then sent to the power amplifiers as current commands and used to energize the yaw control stators.

5.7.2 Real-time Controller

This section introduces the implementation details for our real-time controller. The controllers shown in Figure 5-50 are implemented in LabVIEW, and the real-time controller being used is NI 8108 controller with NI 1031 PXI chassis from National Instruments, and two FPGA modules NI-7845R are included.

Figure 5-51 shows a diagram of the real-time control code structure. The controller code is implemented in two hardwares: the real-time processor (RT target) and FPGA. The FPGA in our controller is used for interfacing with signal inputs/outputs, over-sampling for air gap sensor readings, encoder signal interpolation, and encoder handling as shown in Algorithm 2. The rest of the control code, including air gap sensor handing, digital controllers for suspension and motion, multi-phase distributing, trajectory generation, data plotting and recording, and Bode measurements, are implemented in the RT target. Below we briefly introduce the implementation details for these tasks.

Oversampling is applied for all air gap sensor readings to filter the noise due to the interference from the switching power amplifiers. As we discussed in Section 5.6, the power amplifiers we used have a switching frequency of 20 kHz. In our system, we

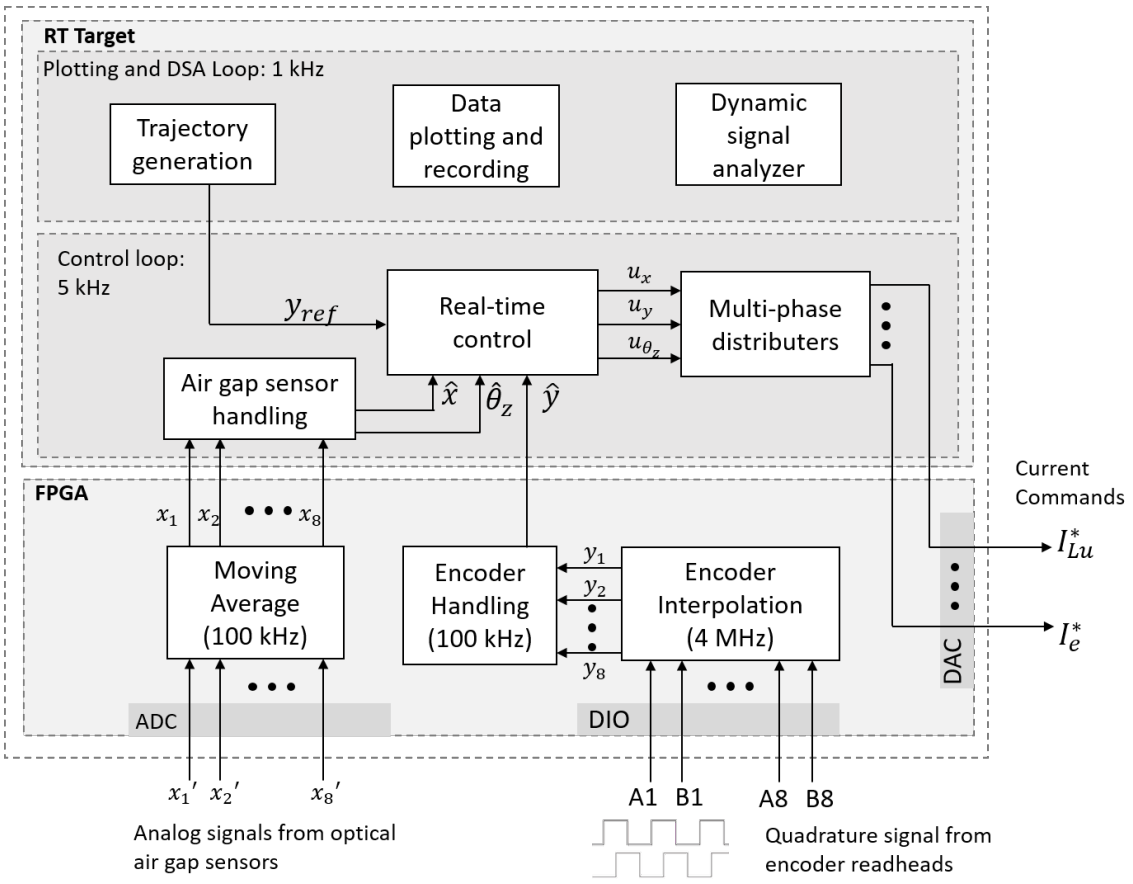

Figure 5-51: Diagram of real-time controller code structure for magnetically-levitated linear stage.

over-sampled the air gap sensor signals at 100 kHz using the FPGA, averaged every 10 samples to one signal, and passed the averaged signal to the real-time controller for feedback control. Using such over-sampling technique, the noise in the air gap signals are effectively reduced.

The magnetic encoder we selected provides quadrature digital signals, and the interpolation for the encoders is implemented in the FPGA. Figure 5-52 shows the encoder interpolation LabVIEW code for one encoder readhead. Note that there are in total eight encoder readheads in our system, and each requires its own encoder interpolation code. Therefore there are eight encoder interpolation loops running in the FPGA in parallel. The encoder interpolation loops run at a loop rate of 4 MHz, which corresponds to 10 tick counts for a 40 MHz on-board clock.

The encoder handling algorithm shown in Algorithm 2 is also implemented in

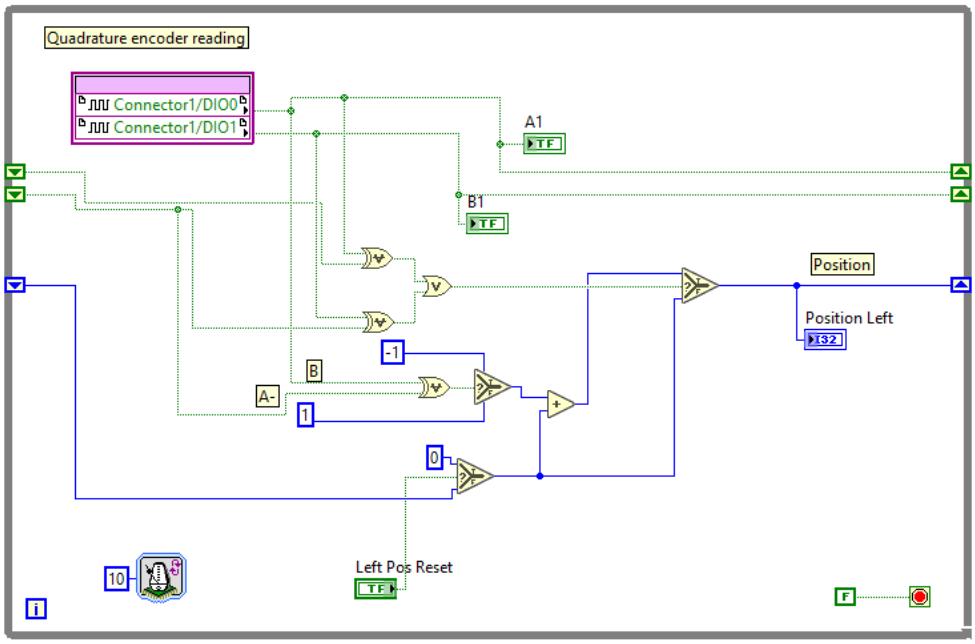

Figure 5-52: LabVIEW code for encoder interpolation.

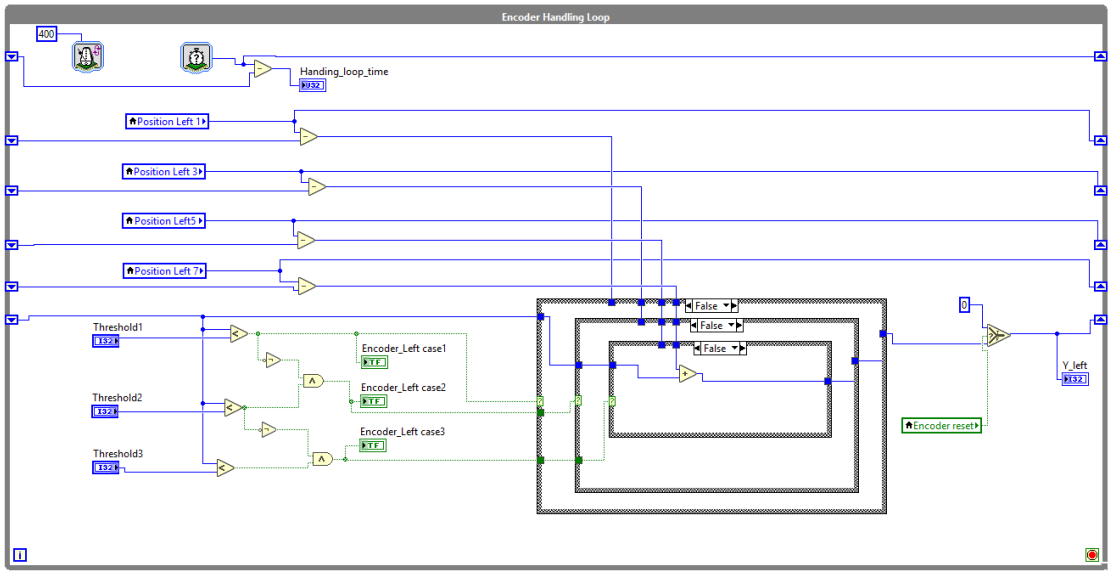

Figure 5-53: LabVIEW code for encoder handling algorithm.

FPGA via LabVIEW, as shown in Figure 5-53. Note that there are two rows of encoder readheads in our prototype, each has four encoder readheads, and there are two parallel encoder handling loops in the FPGA to get the left and right encoder readings. Each encoder handling loop runs at a loop rate of 100 kHz.

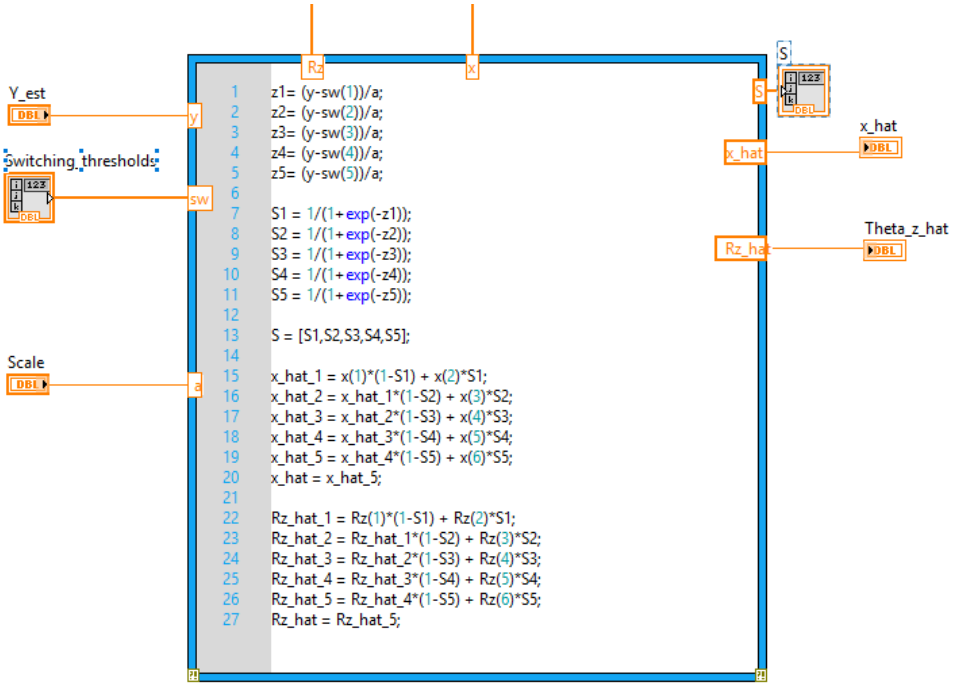

Figure 5-54: LabVIEW code for air gap sensor handling considering the first six air-gap sensors.

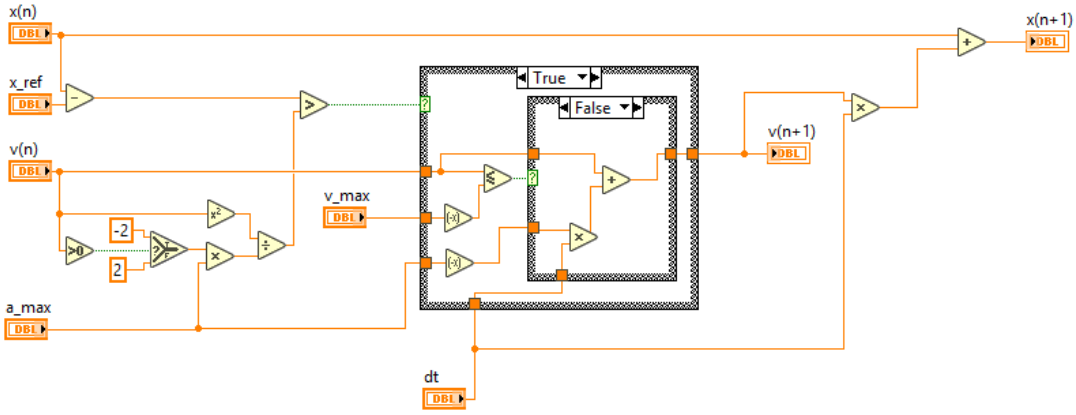

Figure 5-55: LabVIEW code for reference trajectory generation.

The rest of the control code are implemented in LabVIEW in the real-time target. Note that in our system the number of deterministic loops are limited to two, which is the number of cores in the real-time controller NI 8108. The code in the RT target includes two loops. The control loop operates at a loop rate of 5 kHz, in which we

implement the x- and θ_z-directional displacements estimation, the digital controllers for the suspension and motion control, and the generation for three-phase and five phase current commands for stators. In another real-time loop running at 1 kHz, we implement the trajectory generation for stage motion, data plotting and recording, and dynamic signal analyzer for frequency response measurements.

Figure 5-54 shows the LabVIEW code for air gap sensor switching algorithm as shown in Algorithm 1. Here the MathScript in LabVIEW is used. The inputs include the measured stage position y, the signals from the air gap sensors, and a constant β, and the outputs are the estimated stage position in x- and θ_z-directions. These outputs are then used for feedback control to stabilize the stage's magnetic suspension.

The suspension and motion controllers implements lead-lag form of PID controllers with high-frequency cut-off as

$$C(s) = K_p(1 + \frac{1}{T_i s})\frac{\alpha\tau s + 1}{\tau s + 1} \cdot \frac{1}{T_f s + 1}, \tag{5.24}$$

where K_p is the proportional controller gain, T_i is the integral time constant, α is the lead pole-zero separation constant, τ is the lead time constant, and T_f is the time constant for the low pass filter. The controllers for each loop are designed in continuous time, and are then converted to discrete-time through matched z-transform using the pole-zero mapping method with a sampling time of 5 kHz. The outputs from the controllers are then fed into the multi-phase distribution fucntions, which implements (5.16) to (5.23). The control performance of the magnetic suspension and motion for the stage are discussed in Chapter 6.

The rest of the code are configured in a slower loop with lower priority, which include the trajectory generation, data plotting and recording, and frequency response measurement. Figure 5-55 shows the reference trajectory generation code, which generates a S-shaped second-order polynomial trajectory in real-time with a maximum acceleration a_{max} and a maximum velocity v_{max}. The generated value is being used as the reference for stages' motion control. The frequency response measurement uses the LabVIEW Dynamic Signal Analyzer code written by Tyler Hamer in Precision

Motion Control Lab at MIT [70], which can be downloaded from GitHub.

5.8 Summary

This chapter presented the hardware design and fabrication for our magnetically-levitated linear stage prototype. The magnetic design process for the bias flux paths, motor stators, and yaw control stators are discussed. The mechanical design and manufacturing for moving stage and stator are presented. We also discussed the design and configuration for the sensing system, power electronics, grounding and shielding, and controllers.

With the magnetically-levitated linear stage prototype designed and built, in the next chapter we discuss the experimental tests.

Chapter 6

Experimental Tests

This chapter presents the experimental tests for our magnetically-levitated linear stage prototype. We first present the magnetic suspension tests in Section 6.1. Then the tests for the linear motors are presented in Section 6.2.

6.1 Suspension Tests

This section discusses the magnetic suspension of our linear stage prototype, including both the passive magnetic suspension in z-, θ_x-, and θ_y-directions and the actively-controlled suspension in x- and θ_z-directions.

6.1.1 Passive Magnetic Suspension

Table 6.1 shows the measured resonance frequency, damping ratio, and the estimated passive stiffness of the stage in the passively-levitated degrees of freedom. These measurements are taken when the motor stator bias current I_{bias} is set to 2 A. The bias flux air gap is 2 mm, and the air gap of the motor flux is 1.5 mm. The stage is sagging below its equilibrium position by 0.75 mm due to its weight in steady state.

Below we introduce the measurement setup for the passive magnetic suspension performance. To measure the stage's displacements in z- and θ_y-degrees of freedom,

Table 6.1: Measured magnetic levitation performance of the stage in the passively-levitated degrees of freedom under $I_{bias} = 2$ A.

DOF	Resonance Frequency	Passive Stiffness	Damping Ratio
z (Vertical)	12.9 Hz	3.1×10^4 N/m	0.1
θ_x (Pitch)	10.6 Hz	76 Nm/rad	0.018
θ_y (Roll)	9.0 Hz	118 Nm/rad	0.03

three eddy current displacement sensors from Contrinex, Inc. are configured above the moving stage and interfacing with the aluminum stage base, as shown in Figure 6-1. Note that these sensors are not included as a part of the setup when the stage is operating. The stage's displacement in the θ_x-direction is measured by the encoders arranged at the bottom of the stage, which is described in Section 5.4. Since the encoders are not aligned with the stage's center of gravity, the stage's pitch mode motion is detectable by the encoders. During the measurement, we hit the stage in a certain direction while it is magnetically levitated, and measure the stage's displacements in the passively levitated degrees of freedom. Figure 6-2 shows the measured stage's impulse responses in z-, θ_y-, and θ_x-directions. The natural frequency and damping ratio can be calculated from the measured impulse responses. The passive stiffnesses are estimated by the natural frequency measurements and the stage's inertia in different degrees of freedom.

The data in Table 6.1 shows that the stage's magnetic suspension in the passive directions have relatively low stiffness. This is mainly because the linear stage is operating at a relatively large air gap length, which is required for configuring separation walls between the stator and the moving stage. It can also be seen from Table 6.1 and Figure 6-2 that the passive damping ratio of the stage are also relatively low, especially in the pitch mode. This is an inherent limitation for the passive magnetic suspension in bearingless slice motors. Potential methods to improve the passive damping are discussed in Chapter 7 .

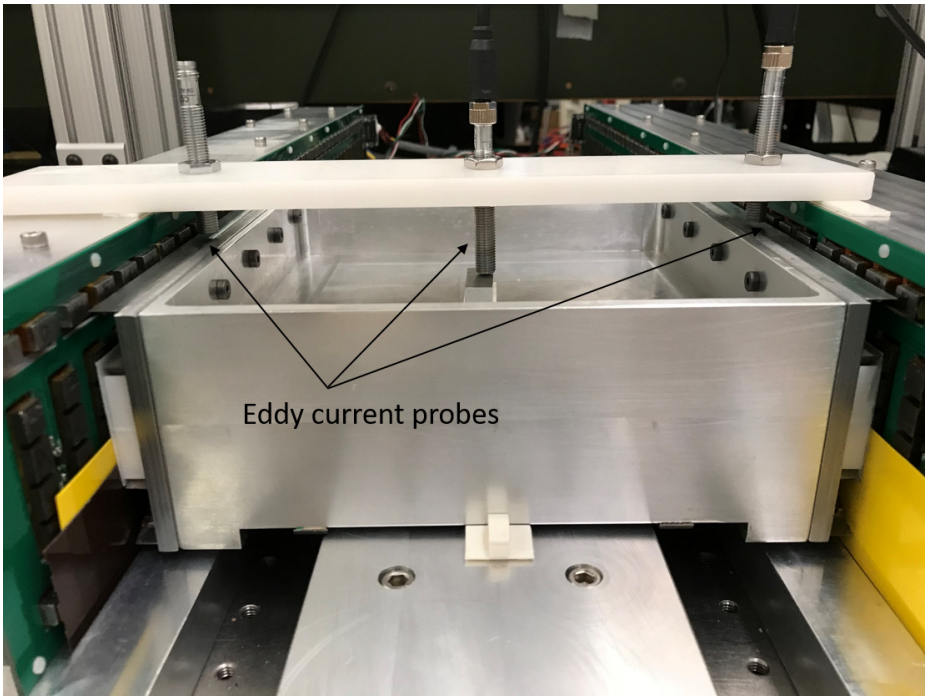

Figure 6-1: Eddy current probes for in the z- and θ_y-directional displacement measurement.

6.1.2 Active Magnetic Suspension

This section presents the experimental tests for the active magnetic suspension of the moving stage in x- and θ_z-degrees of freedom. In our linear stage prototype, we attach a 0.5 mm-thick plastic shim on the pole face of each motor stator, and a 0.5 mm-thick Delrin sheet is attached on each stage secondary as the optical sensor target. When the power is not turned on, the stage is touching on one side of the plastic shim in the air gap due to the negative stiffness caused by the permanent magnet bias fluxes, and the maximum off-centering displacement of the stage in the x-direction is 0.5 mm. As we turn on the suspension controllers, the stage is able to take off from the wall and levitates at the center position between two stator assemblies.

Figure 6-3 shows the measured plant and loop frequency responses of the stage's magnetic suspension in x- and θ_z-direction under a bias current of 2 A, which are obtained from a dynamic signal analyzer (DSA) implemented in a real-time processor

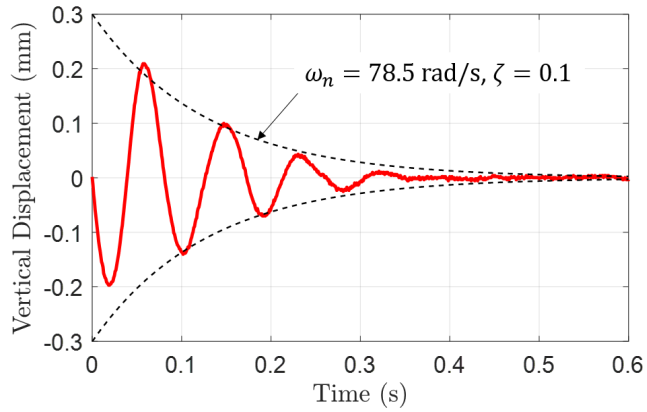

(a)

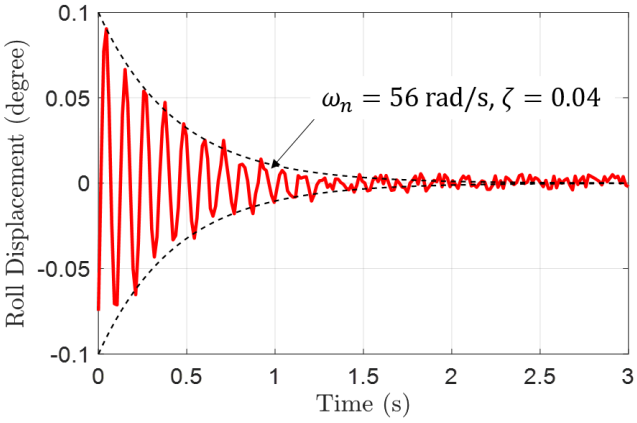

(b)

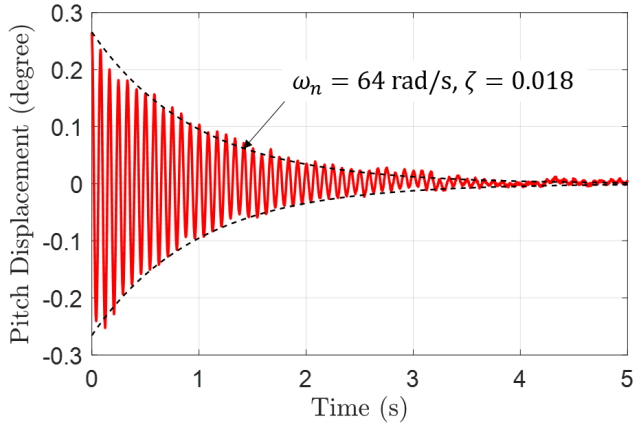

(c)

Figure 6-2: Measured impulse responses of the stage's passive magnetic suspension. Note the time scale in three plots are different. (a) Vertical directional mode (z-direction). (b) Roll mode (θ_y-direction). (c) Pitch mode (θ_x-direction).

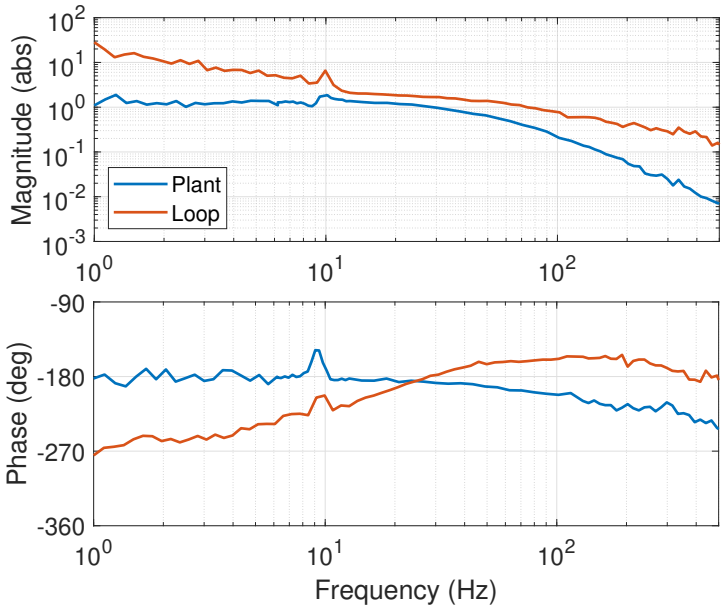

(a)

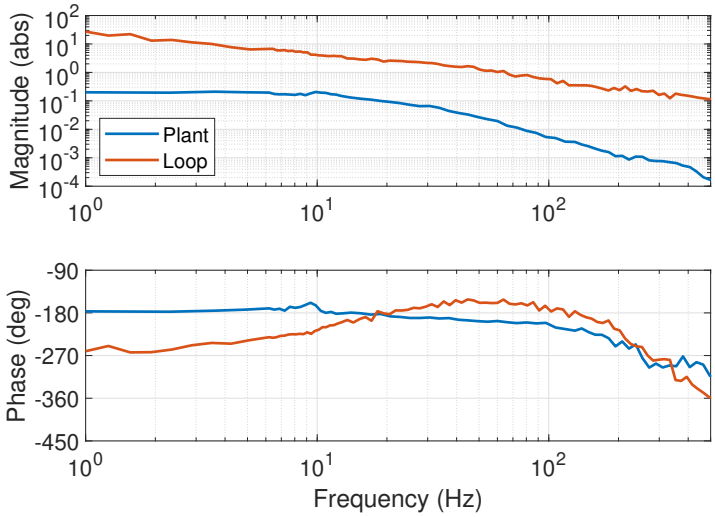

(b)

Figure 6-3: Measured plant and loop Bode plots of the magnetic suspension in actively controlled degrees of freedom. (a) x-directional magnetic suspension. (b) θ_z-directional magnetic suspension.

(NI 8108) at 1 kHz. Note that this plant measurement is taken with the magnetic suspension control loops closed, since the systems are unstable under open-loop. In the x-directional suspension plant frequency response, the magnitude curve shows a notch and a peak around 9 Hz, and the phase curve shows a peak at this frequency.

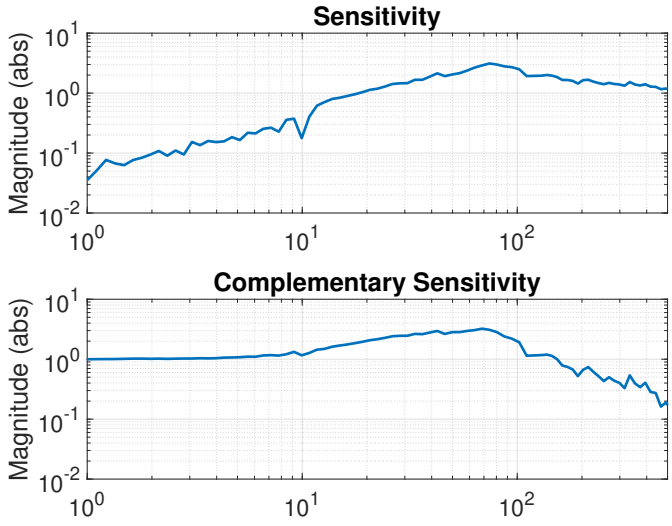

(a)

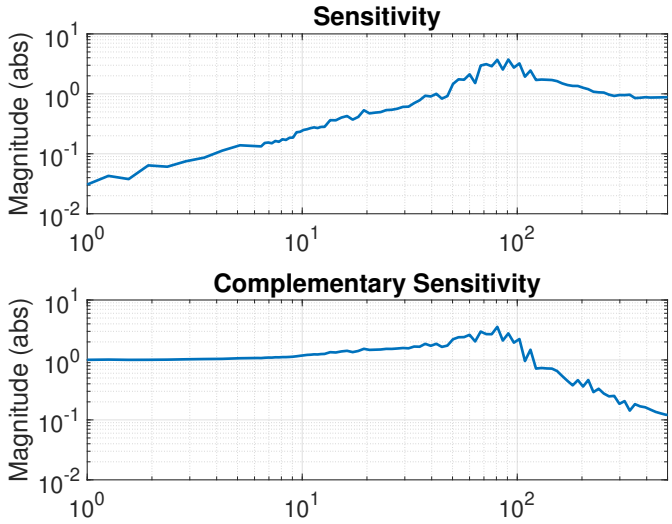

(b)

Figure 6-4: Measured sensitivity and complimentary sensitivity functions of the active magnetic suspension systems. (a) x-directional magnetic suspension. (b) θ_z-directional magnetic suspension.

This indicates that there are a pair of complex zeros and poles in the x-directional magnetic levitation plant. To our understanding, this is due to the second-order θ_y-directional mode is being added to the measured mode. Data show the cross-over frequencies of the x- and θ_z-directional magnetic levitation are 70 Hz and 60 Hz, respectively, and the phase margin of both loops are around 20 degrees.

We also measured the sensitivity of the magnetic suspension control loops in x- and θ_z-directions. Figure 6-4 shows the measured magnitude frequency response of the sensitivity and complementary sensitivity functions, which are defined as

$$S(s) = \frac{1}{1 + L(s)}, \tag{6.1}$$

$$T(s) = \frac{L(s)}{1 + L(s)}, \tag{6.2}$$

where $L(s)$ is the loop return ratio. The measured peaks of the sensitivity curves of x-directional magnetic suspension are of $\max(|\mathrm{S_x}(\mathrm{j}\omega)|) = 3.0$ at 74 Hz and $\max(|\mathrm{T_x}(\mathrm{j}\omega)|) = 3.1$ at 68.5 Hz, and the peaks for θ_z-directional magnetic suspension are $\max(|\mathrm{S}_{\theta_z}(\mathrm{j}\omega)|) = 3.7$ at 80 Hz and $\max(|\mathrm{T}_{\theta_z}(\mathrm{j}\omega)|) = 3.5$ at 80 Hz. These values indicate the worst-case amplification of sinusoidal external disturbance signals.

6.2 Linear Motor Tests

This section introduces the experimental tests of the linear hysteresis motors in our magnetically-levitated linear stage prototype, including the thrust force measurements in Section 6.2.1, and position control tests for the linear stage in Section 6.2.2.

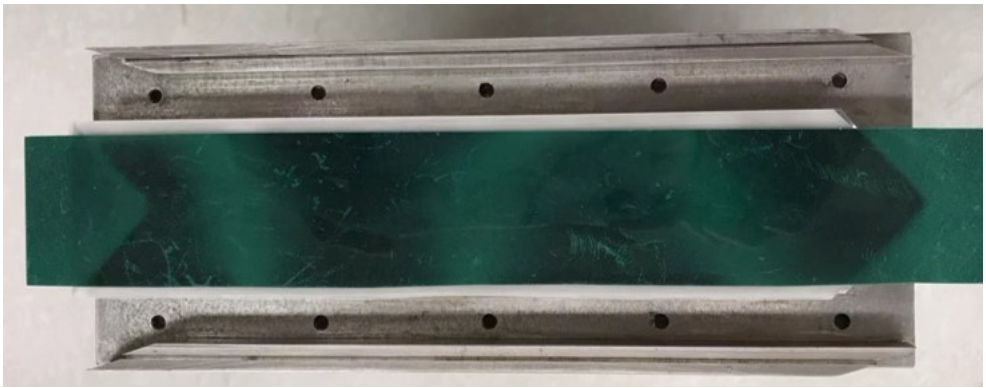

Figure 6-5: Photograph of pre-magnetized hysteresis secondary under a magnetic viewing film.

Figure 6-6: Photograph of thrust force measurement process for the linear stage.

6.2.1 Thrust Force Measurement

This section discusses the thrust force measurement of the linear hysteresis motors. In our linear stage, the hysteresis secondaries are pre-magnetized to improve the motors' thrust force capability. The pre-magnetization of the hysteresis secondary is achieved by setting the corresponding air gap to zero, i.e. pushing the stage in full contact with the motor stator on one side, and gradually increase the current amplitude of the three-phase windings in the motor stator up to 5 A. The hysteresis secondaries on both sides of the stage are magnetized symmetrically. Figure 6-5 shows a photograph of a pre-magnetized stage secondary under a magnetic viewing film. It can be seen that the arrow-shaped hysteresis secondary is having a periodical magnetization pattern.

We first measure the linear motor's thrust force as a function of the phase difference between the stator excitation and the secondary magnetization. This phase is often referred as the force angle ϕ_m for linear synchronous motors. In this measurement, the stage is magnetically levitated, and a force gauge is used to measure the

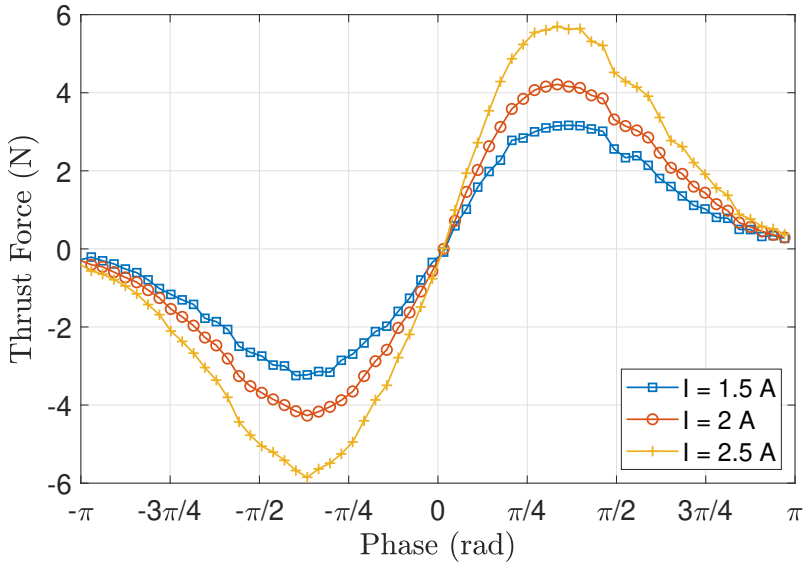

Figure 6-7: Measured thrust force and phase relationship of the linear stage under different bias current amplitudes.

thrust force while sweeping the phase of the excitation, as shown in Figure 6-6. Note that the stage's position does not move during the measurement. Figure 6-7 shows the measured thrust force and phase relationship for the linear stage under different bias current amplitudes. Here, the phases of the peak thrust forces are in between $\pm\pi/4$ and $\pm\pi/2$. This is a result of the combination of hysteresis thrust force generation and reluctance thrust force generation, as discussed in Section 4.1.2 in Chapter 4. The maximum thrust force that our stage has demonstrated is 5.8 N under 2.5 A bias current amplitude, which corresponds to an acceleration of 1200 mm/s^2. This test shows that our stage's thrust force is able to satisfy the acceleration requirement for the reticle transportation application (500 mm/s^2).

We then compare the measured thrust force and the simulation using the finite element model presented in Section 4.3, where the pre-magnetized hysteresis secondary is modeled as a permanent magnet array, whose material property is determined by the pre-magnetization process. Figure 6-8 shows the simulated and measured thrust forces of the linear stage plotted together. It can be seen that the simulation results and the measurements are agreeing well. This comparison validates the model for pre-magnetized linear hysteresis motors presented in Section 4.3.

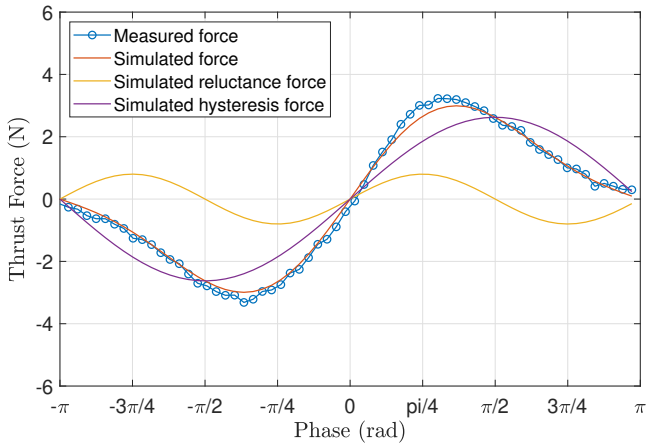

(a)

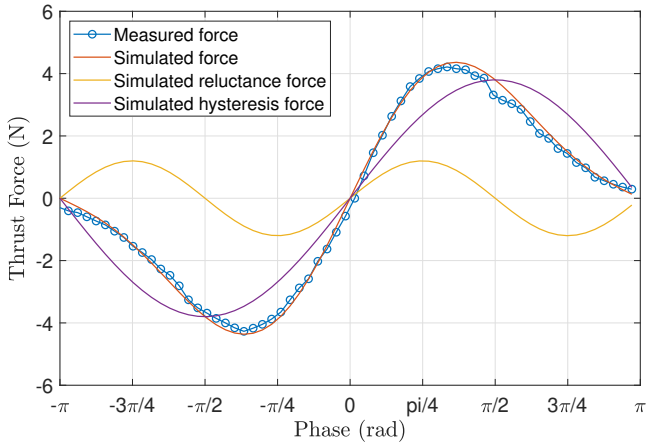

(b)

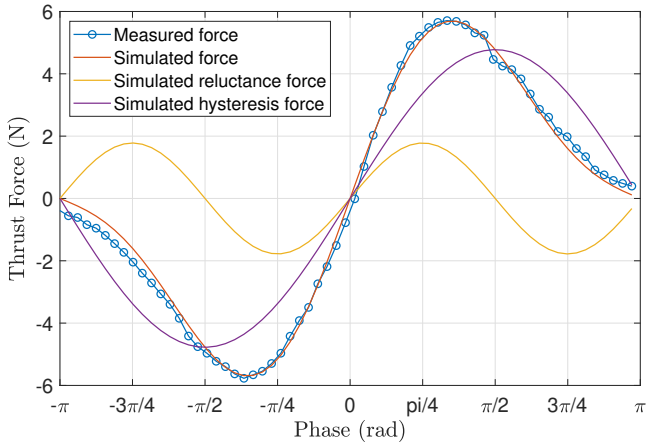

(c)

Figure 6-8: Comparison between measured and simulated thrust forces of the linear stage under different current amplitudes. (a) Current amplitude 1.5 A. (b) Current amplitude 2 A. (c) Current amplitude 2.5 A.

6.2.2 Linear Stage Position Control

This section discusses the position control experiments for the magnetically-levitated linear stage in the motion direction, including the system identification for the plant dynamics, and the closed-loop position control for the moving stage.

Plant System Identification and Modeling

The stage's position control uses the measurement from the encoders as the feedback signal. As discussed in Section 5.7, when the stage is operating, we maintain a constant bias current amplitude I_{bias}, and use the phase between the stator and secondary magnto-motive force, or the force angle ϕ_m, as the control effort. As shown in Figure 6-7, the thrust force generation is largely linear with respect to ϕ_m when $\phi_m \in [-\pi/4,\ \pi/4]$. Therefore in this test we limit the position control effort signal in $[-\pi/4, \pi/4]$. With such settings, we expect the thrust force of the linear stage is approximately linear with respect to the position control effort signal.

Figure 6-9 shows the measured plant frequency response of the linear stage position control, with the force angle ϕ_m being the input, and the stage's position measured by the magnetic encoders on the bottom of the stage as the output. The stage is magnetically levitated during the measurement. The frequency response in Figure 6-9 shows a resonance around 2 Hz. To our understanding, this resonance is generated by the cogging force between the stage and the stators. The stage's position is at an equilibrium generated by the periodical cogging force at steady state. When the stage is having a displacement from the equilibrium position, a restoring force is generated due to the interaction between the pre-magnetized hysteresis secondaries and the stator yoke, which behave like a weak stiffness to the stage. In the frequency range above the low-frequency resonance in Figure 6-9, the data demonstrates a slope of -2 in magnitude and a phase around $-180°$, which resembles the relationship between force and displacement on a free mass. This indicates that the input signal ϕ_m is largely proportional to the thrust force generation to the moving stage as expected.

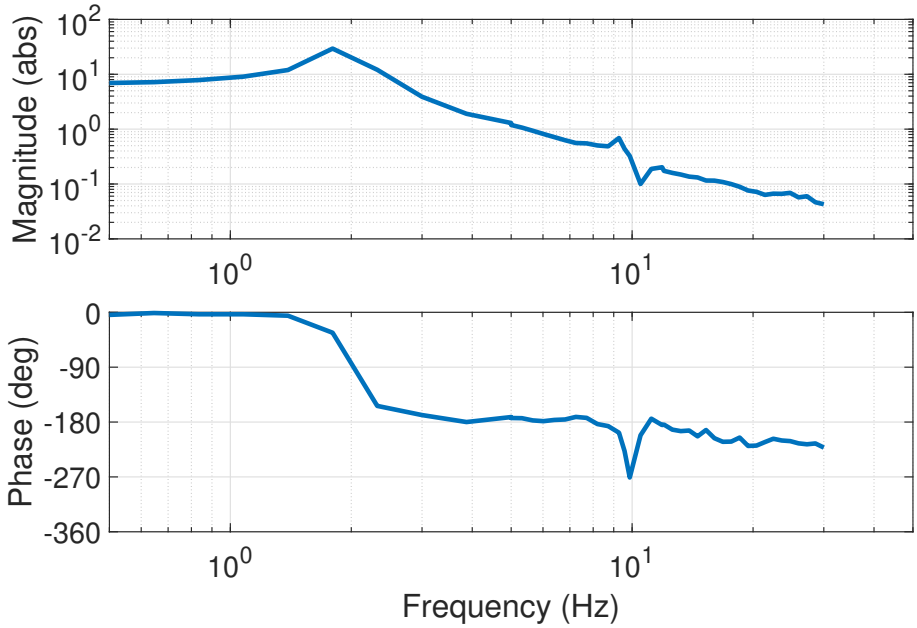

Figure 6-9: Measured frequency response from the force angle ϕ_m and the measured position using the magnetic encoders underneath the moving stage.

Finally, there are a complex pole pair and a complex zero pair in the measurement at around 10 Hz, with the pole pair being at a lower resonance frequency. The measured phase demonstrates a notch at 10 Hz due to this complex pole-zero pair. This is due to the coupling between the stage's motion in y-direction and the pitch motion of the stage.

Below we discuss the modeling for the coupling between the stage's motion in y-direction and the pitch mode. Figure 6-10 shows a diagram of the stage's motion in the y-direction and rotation about the x-axis. Here, the stage's center of gravity is CG, the mass of the stage is m, and its inertia about x-axis is I_x. The displacements of the stage include y and θ_x in the corresponding directions. The thrust force to the stage is F_y, which is acting above the point CG by l_1. The stage's motion is measured by the encoder placed on the bottom of the stage, and the vertical distance between the point CG and the measurement is l_2. The displacement measured by the bottom encoders is y_b.

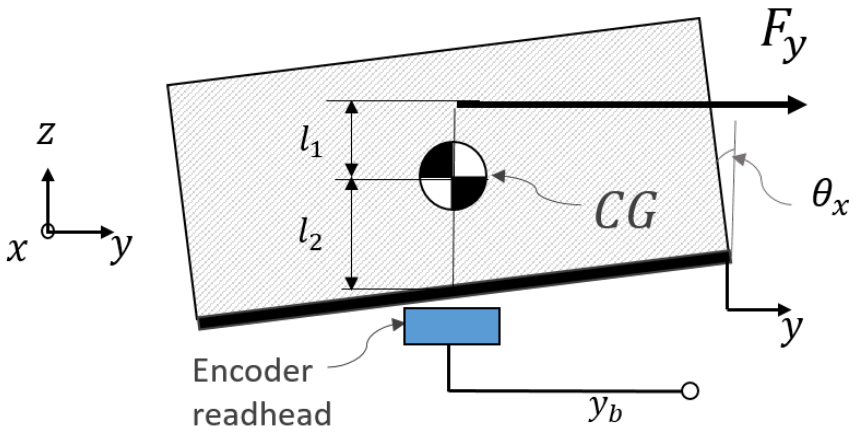

Figure 6-10: Diagram of stage's motion in y-direction and θ_x-direction and their coupling. CG is the stage's center of gravity, y is the stage's motion-directional displacement, θ_x is the stage's pitch displacement, F_y is the thrust force, y_b is the encoder measurement, l_1 is the distance between F_y and CG, and l_2 is the distance between the encoder to CG.

The stage's dynamics in the y-direction is

$$\ddot{y} = F_y/m. \tag{6.3}$$

Since the thrust force is not aligned with CG, a torque $T_x = -F_y l_1$ is generated to the stage about the x-axis. Then the stage's dynamics in θ_x-direction is

$$I_x\ddot{\theta}_x = -F_y l_1 - b_{Rx}\dot{\theta}_x - k_{Rx}\theta_x, \tag{6.4}$$

where k_{Rx} is the passive magnetic suspension stiffness in the θ_x-direction, and b_{Rx} is the passive damping. Applying Laplace transformation to (6.3) and (6.4), we can calculate the transfer function from F_y to y and θ_x as

$$\frac{y(s)}{F_y(s)} = \frac{1}{ms^2}, \tag{6.5}$$

$$\frac{\theta_x(s)}{F_y(s)} = -\frac{l_1}{I_x s^2 + b_{Rx}s + k_{Rx}}. \tag{6.6}$$

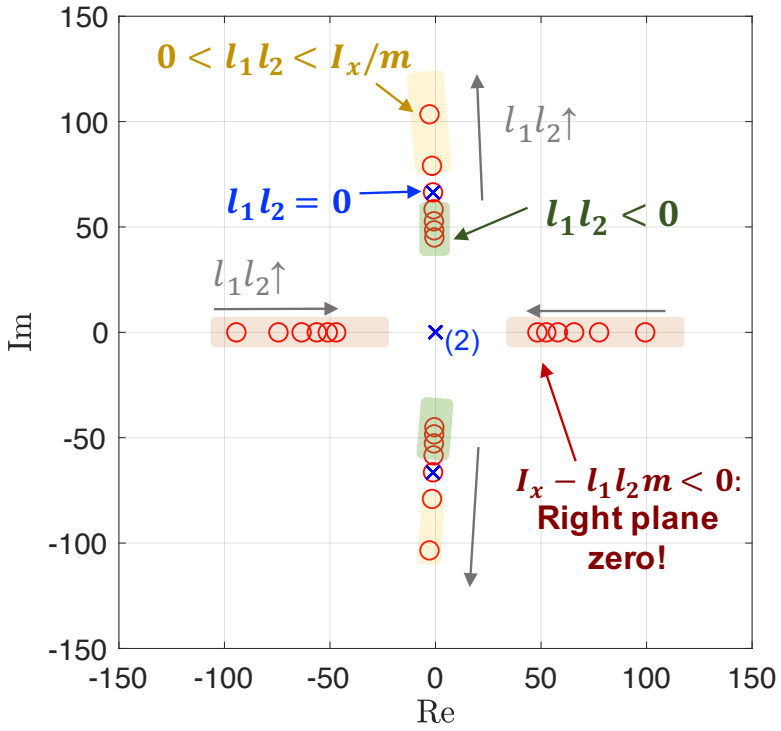

Figure 6-11: Pole-zero plot of linear stage control plant system in equation (6.8) as $l_1 l_2$ changes. The blue crosses indicate the poles, and red circles indicate possible zero positions.

The measured position using the encoder arranged underneath the moving stage is

$$y_b = \theta_x l_2 + y. \tag{6.7}$$

Substituting (6.5) and (6.6) into (6.7), the transfer function from F_y to y_b can be found as

$$\begin{aligned} \frac{y_b(s)}{F_y(s)} &= l_2 \frac{\theta_x(s)}{F_y(s)} + \frac{y(s)}{F_y(s)} \\ &= \frac{-l_1 l_2}{I_x s^2 + b_{Rx} s + k_{Rx}} + \frac{1}{ms^2} \\ &= \frac{1}{ms^2} \cdot \frac{(I_x - l_1 l_2 m)s^2 + b_{Rx} s + k_{Rx}}{(I_x s^2 + b_{Rx} s + k_{Rx})}. \end{aligned} \tag{6.8}$$

The transfer function (6.8) is the plant that we need to control when closing the position control loop for the linear stage. Note that the low-frequency resonance in the stage dynamics due to the cogging force is not included in this model. It can

be seen that the transfer function (6.8) has two terms. The term $1/ms^2$ corresponds to the y-directional dynamics, just Newton's second law. The other term in (6.8) demonstrates a pair of complex poles and zeros, which is due to the coupling between the θ_x-directional mode and the y-directional motion of the stage. For a given m, I_x, b_{Rx}, and k_{Rx}, the system's poles are fully determined. However, the position of the zeros depends on the parameters l_1 and l_2. Figure 6-11 shows a pole-zero plot of the system in (6.8) under different $l_1 l_2$ values. This plot is generated with substituting in the values: $m = 4.8$ kg, $I_x = 0.017$ kg.m^2, $k_{Rx} = 75.3$ Nm/rad, $b_{Rx} = 0.04$ Nms/rad, and sweeping $l_1 l_2$ from -0.008 m^2 to 0.014 m^2. Here, the blue crosses indicate the poles of the system, and the red circles indicate the possible position of the zeros as $l_1 l_2$ changes. In Figure 6-11, the two poles at the origin correspond to the stage's y-directional rigid body motion, and the complex pole pair corresponds to the stage's resonance in θ_x-direction. Below we discuss three different cases for the zeros' position and the corresponding system dynamics:

(1) Non-collocated measurement – The first case is when our linear stage is using the bottom encoder measurement as the output, where $l_1 = 4$ mm, and $l_2 = 32$ mm. Figure 6-12 shows the pole-zero plot and the frequency response of the linear stage system under this setting. As shown in Figure 6-12(a), there is a complex pole-zero pair corresponding to the pitch mode of the system, and the pole pair is having a lower resonance frequency. Figure 6-12(b) shows both the measured and modeled frequency responses of the system. Note that here the low-frequency resonance due to the cogging force is not included in the model. We can see that the system is having a pair of resonance and anti-resonance due to the pitch mode, and the corresponding phase is demonstrating a notch. In machine dynamics, this case is often referred as *non-collocated measurement* [71], indicating the actuation and measurement are on different sides. Closing the control loop around such systems can often result in low stability margin: when the resonance or anti-resonance in the loop return ratio is crossing over, the corresponding phase margin is typically negative due to the phase notch in the plant.

(2) Collocated measurement – In our linear stage prototype, an additional encoder

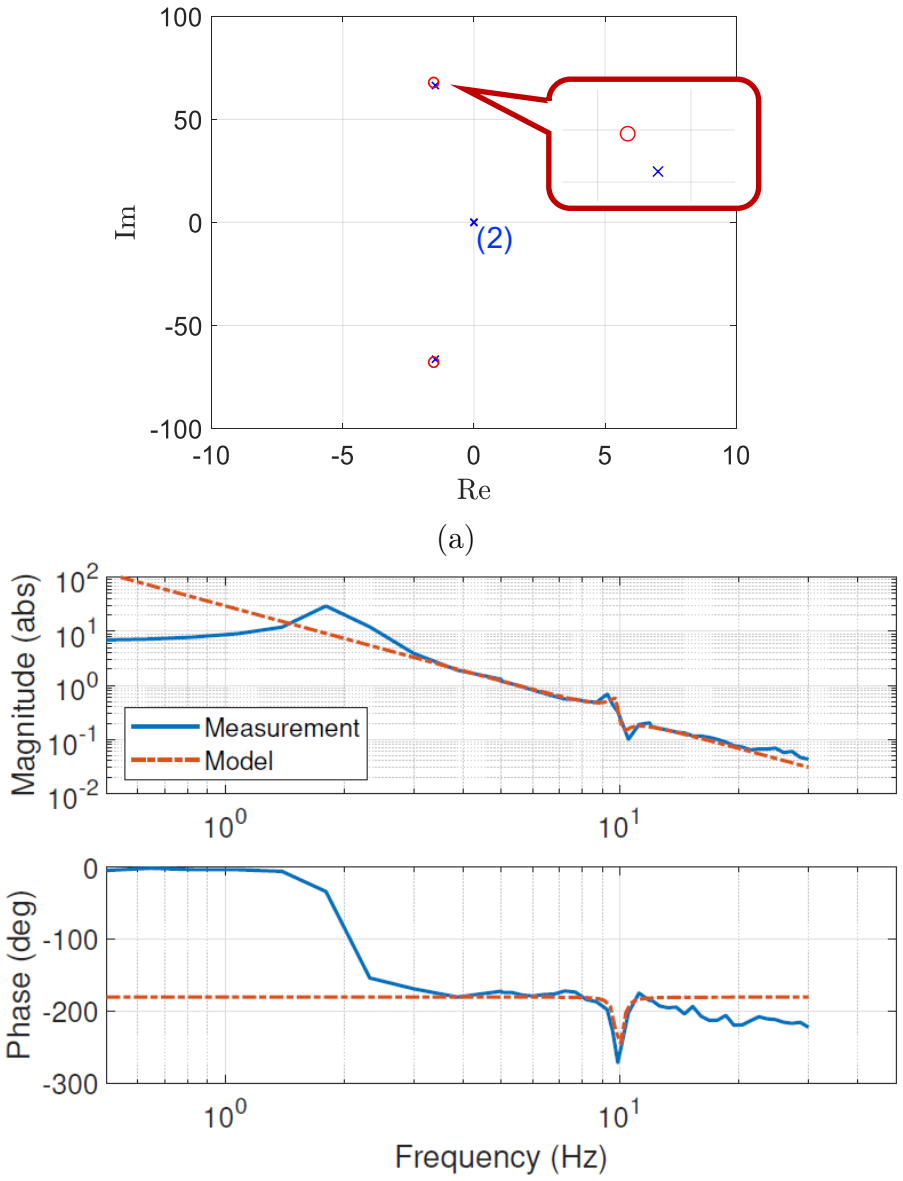

Figure 6-12: Non-collocated stage dynamics with bottom encoder reading used for output. (a) Modeled pole-zero plot. (b) Measured and modeled Bode plot. Here the low frequency resonance due to the cogging force is not included.

is configured on the top of the moving stage, as shown in Figure 6-13. The second case is when our linear stage is using the encoder configured on the top of the stage as the output. Under this condition, $l_1 = 4$ mm, and $l_2 = -40$ mm. Figure 6-14 shows the pole-zero plot and the Bode plot of the system. As shown in Figure 6-14(a), in the complex pole-zero pair corresponding to the pitch mode, the complex zero pair is

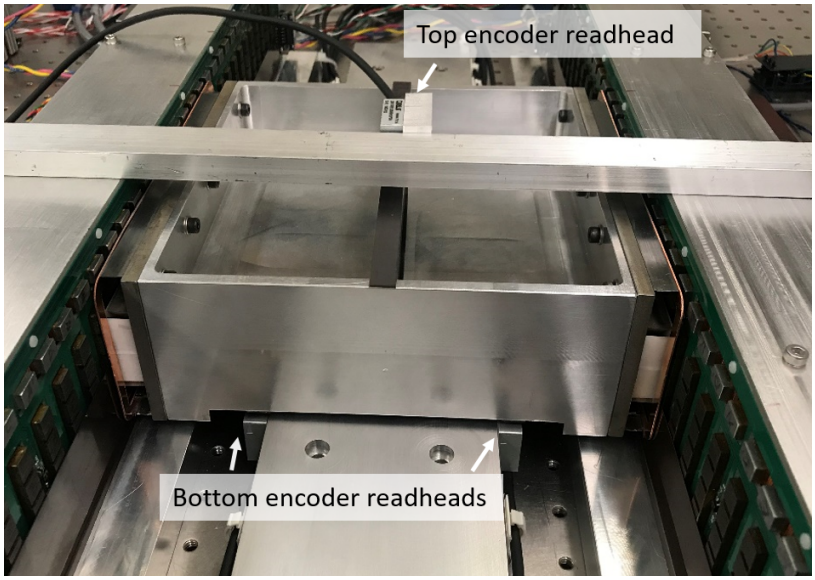

Figure 6-13: Photograph of the top encoder for the magnetically-levitated linear stage.

having a lower resonance frequency. In Figure 6-14(b), the anti-resonance has a lower resonance frequency than the resonance, and the phase is demonstrating a peak due to the pitch mode coupling. This case is called *collocated measurement* configuration in system dynamics [71].

(3) Right plane zero – When the value of $l_1 l_2$ further increases, an extreme case can happen when $I_x - l_1 l_2 m < 0$, or $l_1 l_2 > I_x/m$. Figure 6-15 shows the modeled stage dynamics with $l_1 = l_2 = 200$ mm, where Figure 6-15(a) shows the pole-zero plot of the system, and Figure 6-15(b) shows the modeled frequency response. Under this case, the two zeros of the system are moved to the real axis, as shown in Figure 6-15(a). Note that one of zeros is in the right half plane of the complex plane. Also, it can be seen in Figure 6-15(b) that the the phase of the frequency response drops to $-360°$ after the pitch mode resonance frequency, since the right plane zero is providing a negative phase change to the system (appose to a positive phase change due to a left plane zero). When closing the control loop around the system, such phase drop in the plant makes it impossible to stabilize the control loop with a cross-over frequency above the pitch mode resonance frequency. This extreme case should be avoided when designing a motion stage.

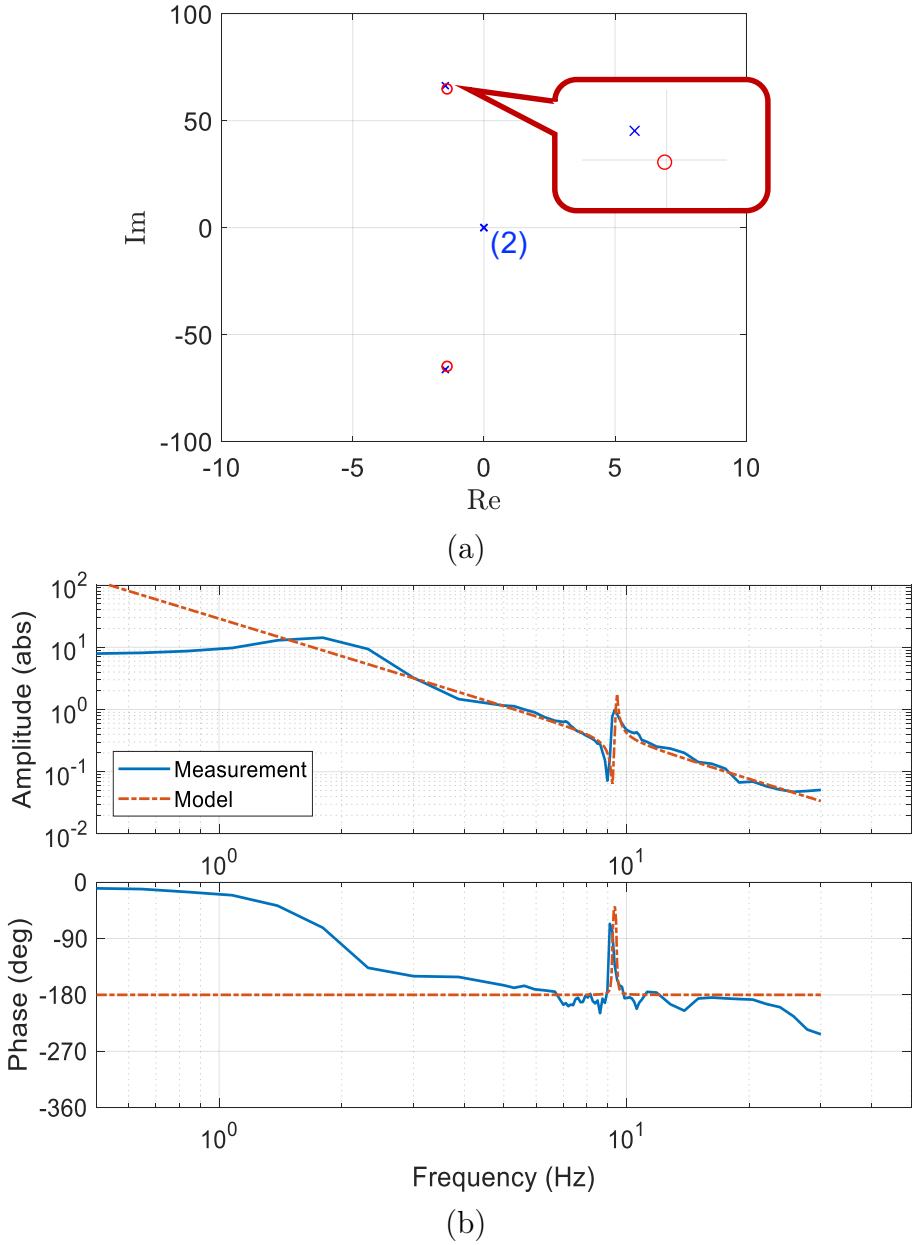

Figure 6-14: Collocated stage dynamics with encoder on the top of the stage used for output. (a) Modeled pole-zero plot. (b) Measured and modeled Bode plot.

As we have discussed before, our linear stage prototype is demonstrating a non-collocated measurement configuration. When we close the control loop around the system, the system typically has low stability margin due to the phase drop at the resonance frequency. In this work, we tested two methods to solve this stability issue: (1) Moving the position of the measurement point and align it with the stage's center

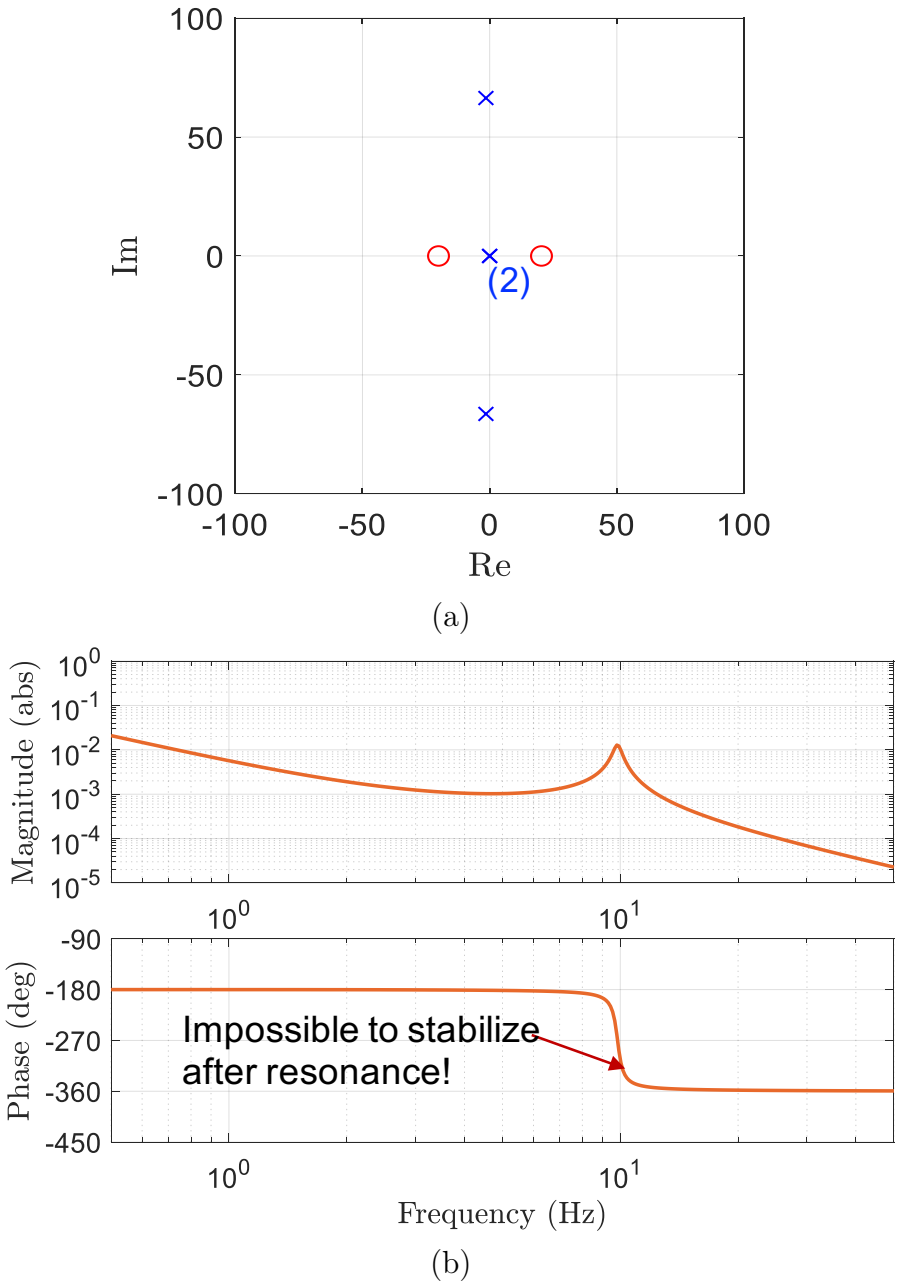

Figure 6-15: Modeled stage dynamics with $l_1 = l_2 = 200$ mm with right plane zero. (a) Pole-zero plot. (b) Frequency response.

of gravity, and therefore making the pitch mode undetectable. (2) Moving the stage's center of gravity and align it with the thrust force, and therefore making the pitch mode unexcitable. Below we discuss the experimental tests for these two methods in our linear stage prototype.

(1) Double-sided measurement: We first tested the linear stage with double-

sided encoder measurement. In this test, we define a weighted average between the top and bottom encoder readings y_{avg} being the output. The averaged y-position measurement is defined as

$$y_{avg} = (1 - \alpha)y_t + \alpha y_b, \tag{6.9}$$

where α is a constant between 0 and 1. In our experiment, the value of α is empirically tuned to make the pitch motion of the stage not detectable by the averaged measurement y_{avg}. For our experiential setup shown in Figure 6-13, $\alpha = 0.65$. Figure 6-16 shows the measured system frequency response using top, bottom, and average measurement as the system's output, where the red line is the system using the average encoder reading as the output. It can be seen that the red line in Figure 6-16 does not show resonance or anti-resonance at the pitch mode natural frequency, and its phase is also flat and around $-180°$. This measurement double confirms that the resonances and phase changes in the data are due to the coupling between the stage's y- and θ_x-modes.

(2) Stage with additional mass: The second experiment we conducted is including an additional mass in the moving stage and thus moving the stage's center of gravity upward, thereby making it aligned with the thrust force. Note that with the additional mass included, the gravity induced sag of the stage can also increase. Figure 6-17 shows the photograph of the stage with the additional mass that can make the pitch mode not excitable. The mass is added empirically by measuring the frequency response of from force angle ϕ_m to the reading of the bottom encoders, while observing the phase of the measurement around 10 Hz. The total weight of the additional mass of the stage is 0.39 kg. When the mass is included, the stage's sag below the centerline increased to 1.05 mm.

Fig. 6-18 shows the measured frequency response of the position control plant with and without the additional mass, with the force angle ϕ_m being the input, and the bottom encoder reading y_b being the output. The black line is the data measured without the payload. Here the measured phase demonstrates a notch at 10 Hz, and

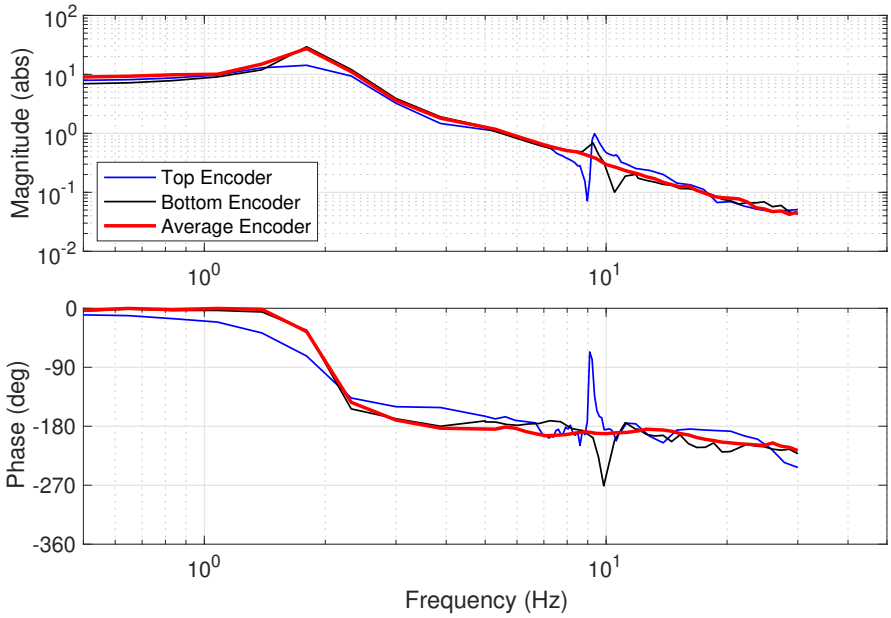

Figure 6-16: Measured frequency responses from the force angle ϕ_m to the stage position measured by different encoders. Black line: position measured by the bottom encoder. Blue line: Position measured by the top encoder. Red line: weighted average of the top and bottom encoder readings.

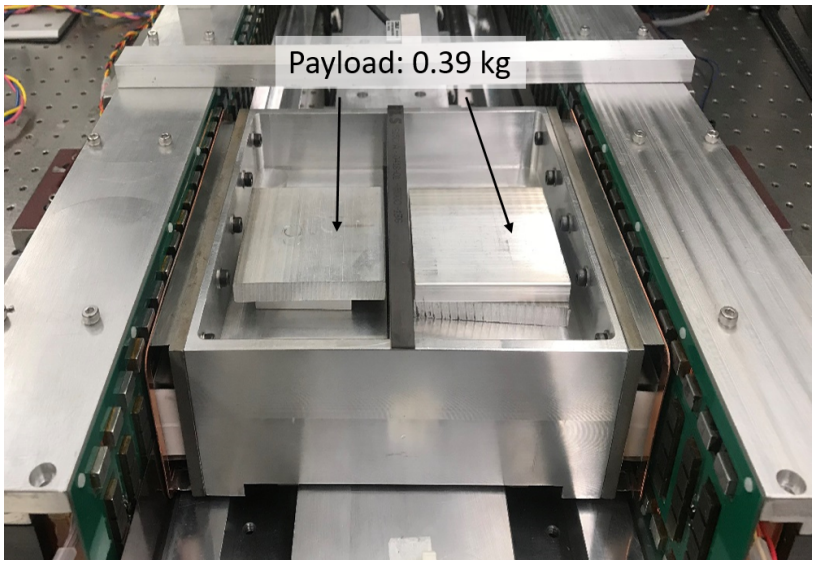

Figure 6-17: Photograph of the stage with additional mass that can make the stage's center of gravity aligned with the thrust force.

the corresponding magnitude shows resonance and anti-resonance due to the coupling dynamics. The red line in Figure 6-18 shows the measurement with the additional

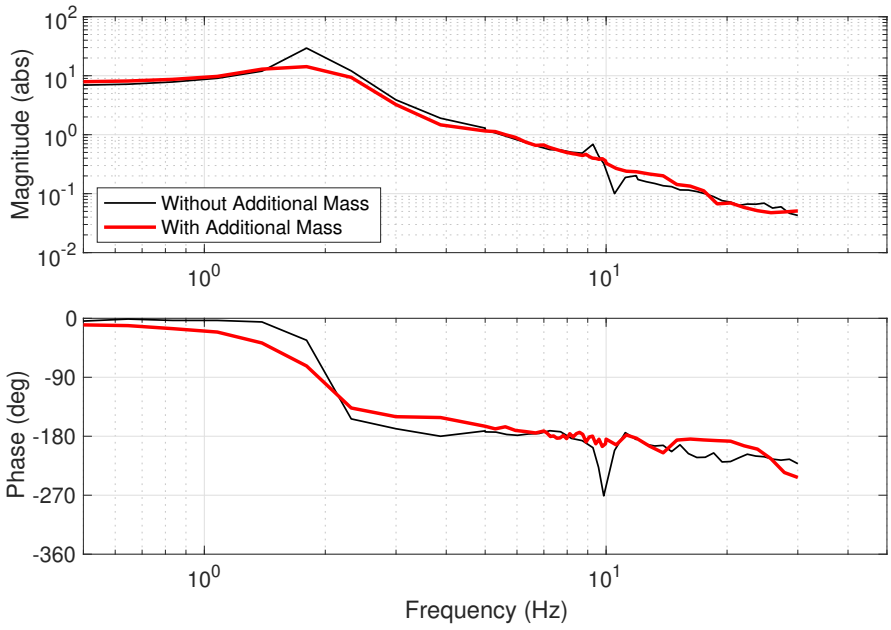

Figure 6-18: Measured frequency responses from the force angle ϕ_m to the stage position measured by bottom encoders.

mass included. It can be seen that the phase of the data does not show peak or notch at the θ_x-mode resonance frequency (10 Hz). The measured magnitude plot with the additional mass also does not show resonance or anti-resonance. This measurement confirms that when the stage's center of gravity is aligned with the thrust force, the pitch mode is no longer excitable.

Closed-loop Position Control

This section introduces the closed-loop position control for the magnetically-levitated linear stage. With the stage's pitch mode not excitable or not detectable, we are able to close the position control loop of the stage without the aforesaid stability issue. In this experiment, we closed the position control loop for the moving stage with the additional mass included, and the bottom encoder reading is used for feedback. The plant frequency response is shown in Figure 6-18 by the red line.

Figure 6-19 shows a measured position step response of the moving stage. The 10-90% rise time of this step response is 0.014 s, which corresponds to a bandwidth

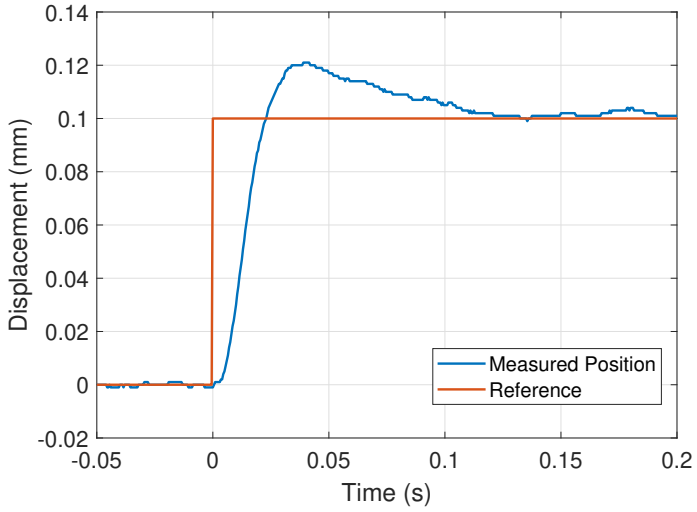

Figure 6-19: Measured position step response of our linear stage. The position control is tested with the additional mass included. The rise time of the step response is 0.014 s, indicating the position control loop's bandwidth is 25 Hz.

of 25 Hz. The reason that we did not further increase the position control bandwidth is because the control effort signal can become noisy when we further increase the position control gain due to the amplification of the quantization noise of the encoder measurement.

The stage is also tested to track a second-order polynomial reference trajectory. The trajectory's maximum acceleration and velocity are $a_{max} = 500$ mm/s^2 and $v_{max} = 250$ mm/s, respectively. The trajectory is generated by the LabVIEW code shown in Figure 5-55. Figure 6-20 shows the tracking performance of the stage's motion, where the top plot shows the reference and measured position (which are largely overlapping), the middle plot shows the position tracking error in the y-direction, and the bottom plot shows the measured x- and θ_z-directional displacements of the stage as it is moving following the trajectory. The middle plot in Figure 6-20 shows the maximum position control tracking error is about 50 μm, and the tracking error demonstrates a periodical pattern, where the spatial period of the tracking error matches with the motor stator tooth pitch. To our understanding, this error is caused by the cogging force in the pre-magnetized linear hysteresis motors. In addition, the stage's tracking error demonstrates a small amplitude oscillation of 10 Hz when the

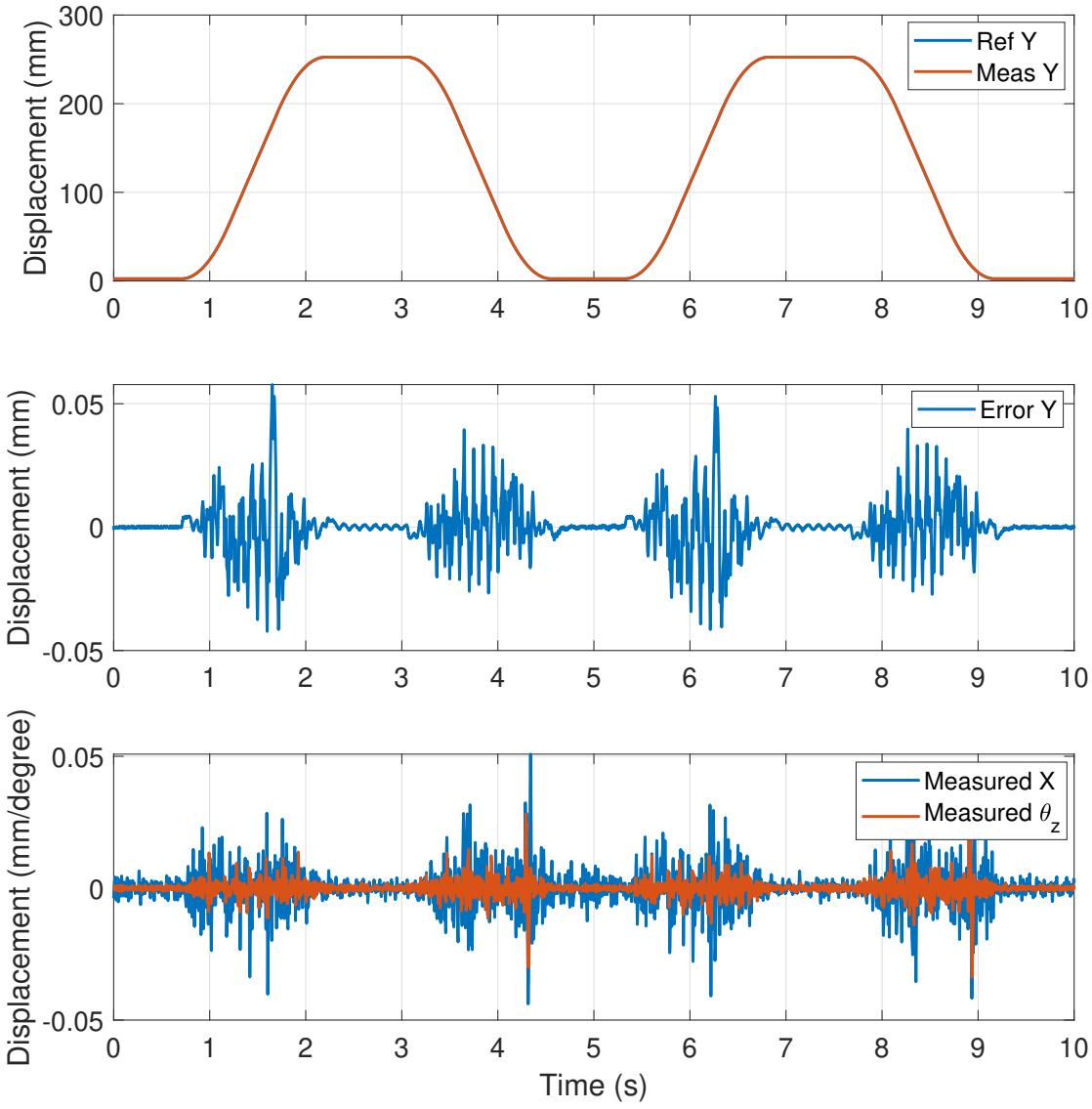

Figure 6-20: Measured tracking performance of the stage while tracking a S-shaped trajectory with $a_{max} = 500$ mm/s^2 and $v_{max} = 250$ mm/s. Top plot: reference and measured stage displacement. Middle plot: position tracking error. Bottom plot: measured stage displacements in x- and θ_z-directions.

stage is in steady-state. This is because the pitch mode is slightly excitable when the additional mass is included in the stage. The bottom plot in Figure 6-20 shows that the stage's maximum deviation from center in x-direction is about 50 μm, which is well below making mechanical contact with the side walls (mechanical air gap length is 500 μm on each side).

Table 6.2: Temperature measurement of the linear stage during operation.

Time	Coil Temperature	Lamination Temperature	Secondary Temperature
0 min	21.4 °C	21.5 °C	21.5 °C
5 min	24.2 °C	22.7 °C	21.7 °C
10 min	25.6 °C	23.6 °C	21.9 °C
15 min	26.5 °C	25.1 °C	22.1 °C
20 min	26.6 °C	25.3 °C	22.2 °C

6.2.3 Thermal Measurements

This section introduces the thermal measurement of our linear stage prototype. In this test, the temperature is measured with a type-K thermocouple probe from Fluke working together with a Fluke multimeter. In this thermal test, the moving stage is magnetically levitated and tracks a trajectory of 250 mm in length. The maximum acceleration of the trajectory is 500 mm/s^2, and the maximum speed is 250 mm/s. The stage stops at the end positions for 2 s before it moves in the reversed direction. The bias current amplitude in the motor stators is 2 A. The ambient temperature during the test is 21.5 °C. Note that in our prototype no forced cooling is included for the stators, and there is no thermal insulation between the stator and the stage. Table 6.2 shows the measured temperature of the motor stator coil, stator lamination at the teeth, and the stage secondary. It can be seen that the stator coil's temperature reaches steady-state after operating for about 20 minutes, and the steady state temperature is 26.6 °C. The secondary's temperature rises significantly slower than that of the stator lamination and coils. To our understanding, the temperature rise in the secondary is due to two reasons: (1) heat transfer from the stator, and (2) hysteresis and eddy-current secondary loss in secondary. The effect of the two mechanism is difficult to separate in experiments. Here we present a rough estimation for the power from each source.

We first estimate the power loss in the secondary due to the eddy current and hysteresis effect using finite element method. Note that our linear motors are operating in synchronous mode, and only the high-order harmonics are involved in the

generation of the secondary losses. In this simulation, the motor stator operates at a current amplitude of 2 A and a frequency of 2.3 Hz, which corresponds to a synchronous speed of 250 mm/s. Simulation shows that the power loss in each hysteresis secondary due to the high-order harmonics of the excitation is 0.04 W under this condition.

We then estimate the power of the radiative heat transfer from the stator to the secondary. Here, we assume the radiation is only from the lamination to the secondary. The area involved in the radiative heat transfer is the full area of the secondary, which is $A = 40$ mm $\times$ 192 mm. The emissivity of the secondary surface (the Delrin plate covering the secondary) is assumed to be $\epsilon = 0.8$. The steady-state temperature for lamination and secondary, $T_{lam} = 25.3$ °C$= 298.3$ K and $T_{sec} = 22.2$ °C $= 295.2$ K, are used in this calculation. Then we can estimate the radiative power as $P_{rad} = \epsilon\sigma(T_{lam}^4 - T_{sec}^4) = 0.13$ W, where $\sigma = 5.67 \times 10^{-8}\ W \cdot m^{-2}K^{-4}$ is the Stefan–Boltzmann constant. Comparing the estimated power from the radiatitve heat transfer and the secondary loss, it can be deduced that the temperature rise in the secondary in our linear stage prototype is mainly due to the heat transfer from the stator. When such heat transfer can be blocked via cooling the stators or radiation shields, we expect the temperature rise in the secondary can be significantly reduced.

The input power of in our linear stage is also estimated. Since the operating frequency of the linear motors is only 2.3 Hz and the linear motors have no load, the input power P_{in} is approximately equal to the stator power loss. The peak current amplitude of the motor windings is 2 A, and the motor stator's per-phase winding resistance is 8.4 Ω. Therefore the total power loss of the two motor stators can be calculated as

$$P_s = 2 \times 3(\frac{I_{pk}}{\sqrt{2}})^2 R_s = 100.8 \text{ W}. \tag{6.10}$$

Note that in our prototype the entire length of the stators are energized when the stage is operating. When using our linear stage for long-distance transportation tasks, the stators should be driven in sections to reduce power dissipation.

6.3 Summary

In this chapter, we presented the experimental tests for our magnetically-levitated linear stage prototype, including both magnetic suspension tests and linear motor tests. We compared the measured thrust force with the simulated force using the proposed pre-magnetized linear hysteresis motor model discussed in Section 4.3. Good agreement between the measurement and simulation validated our model. We also discovered that the stage's pitch mode dynamics is coupled to its motion along the y-axis, and conducted experiments for validation. The test results presented in this chapter shows that our magnetically-levitated linear motor prototype is able to successfully levitate the moving stage, and is able to satisfy the acceleration requirement of the reticle transportation task.

Although our linear stage prototype is satisfactory as a proof-of-concept, there are several limitations that we discovered during the experimental tests. In the next chapter, we will discuss the limitations for our current stage design, propose potential solutions, and discuss variations of stage design that potentially can deliver improved performance for the reticle transportation application.

Chapter 7

Discussion and Design Variations

In the previous chapters, we have presented the design, building, and testing of our magnetically-levitated linear stage prototype. Through this process, we have discovered several limitations for the bearingless-slice-linear-motor-based stage design, which requires a series of improvements for an application to the reticle transportiont task in EUV lithography machines. In this chapter, we first discuss the limitations for of our magnetically-levitated linear stage, and propose potential solutions for these issues in Section 7.1. Then, we present alternative design concepts that may deliver improved performance for the reticle transportation task in EUV photolithography scanners in Section 7.2.

7.1 Discussion of Limitations

Through the building and testing process, we learned that there are three major limitations in our magnetically-levitated linear stage prototype: (1) Pitch mode is coupled to the stage's motion when thrust force is not aligned with the stage's center of gravity; (2) Vertical mode of the stage is excitable by the linear motors' common-mode attractive force variation; (3) Non-vacuum-compatible sensing system. Below we discuss more details about these limitations, and suggest methods that can potentially solve these issues and therefore improve the performance for our linear stage system.

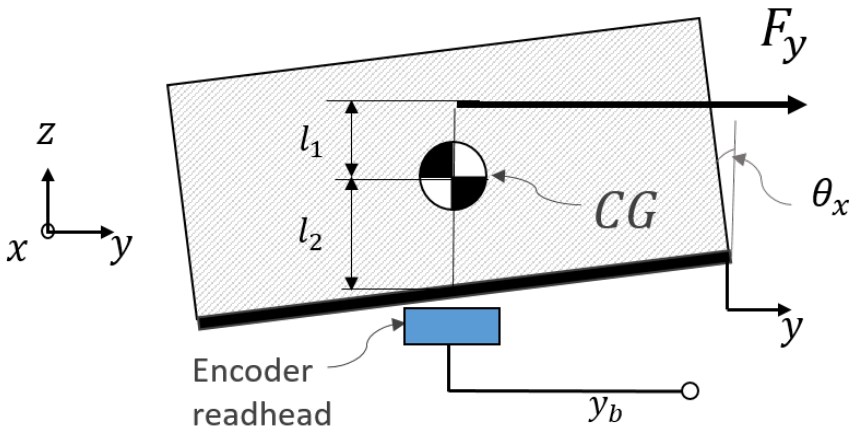

Figure 7-1: Diagram of stage's motion in y-direction and θ_x-direction and their coupling.

7.1.1 Pitch Mode Coupling

The first limitation in our linear stage is due to the coupling between the stage's pitch mode (θ_x-directional mode) and its motion along the motion direction (y-directional mode), as discussed in Section 6.2.2. Figure 7-1 shows a diagram explaining the issue. When the stage's thrust force is not aligned with the center of gravity of the moving stage, the thrust force can apply a torque to the stage when it is accelerating or decelerating, thereby exciting the stage's pitch mode. Meanwhile, in our linear stage, the pitch mode is passively levitated, which has relatively low stiffness and damping (natural frequency $\omega_{\theta_x} = 66$ rad/s, damping ratio $\zeta_{\theta_x} = 0.018$). Such lightly damped vibration is undesired for lithography application, especially when the reticle is in the transportation stage.

In order to solve this issue, the following three improvements should be applied:

(1) Pitch Mode Not Excitable When With Reticle

The first method is to make the pitch mode not excitable when the stage is carrying the reticle. When using a magnetically-levitated linear stage for reticle transportation, we should align the thrust force generation with the center of gravity of the moving stage when the reticle is in the stage. Under this condition, the lightly-damped pitch

mode is not excitable by the thrust force, and the vibration of the reticle due to the pitch mode coupling can be prevented.

(2) Pitch Mode Not Detectable in Measurement

The second method is to make the pitch mode not detectable in the measuremnet. As discussed in Section 6.2.2, when the stage is having a non-collocated measurement configuration, meaning the thrust force and measurement are on different sides of the stage's center of gravity, the stage's position control can have low stability margin due to the coupling between the pitch mode and the stage's motion. When using a bearingless slice inear motor design, we should make the passively-stabilized pitch mode not detectable by measuring through the stage's center of gravity. In this way, we are able to eliminating the stability issue in the y-directional position control. We can achieve this goal by: (a) Measuring the stage's displacement using a laser interferometer, and aligning the laser with the stage's center of gravity in the vertical direction; (b) Measuring the stage's placement on both top and bottom sides, and compute the displacement of the center of gravity, as we tested in Chapter 6.2.2 with the setup in Figure 6-13.

(3) Improve Passive Damping in Pitch Mode

In our current linear stage prototype, the pitch mode has a relatively low passive damping ($\zeta_{\theta_x} = 0.018$), which is not enough to damp out the stage's vibration in this mode when it is excited. In order to use the stage for precision applications, the passive damping of the stage in the pitch mode needs to be improved.

One potential method to increase the passive damping in the pitch mode is using a passive damper design as shown in Figure 7-2. In this design, a figure-eight-shaped short-circuited conductive loop as shown in Figure 7-3(a) is fixed on the bottom of the moving stage. Two stator rails with permanent magnets are configured on both sides of the conductive loops, as shown in Figure 7-2 and Figure 7-3(b). When the stage is having a velocity in the pitch direction, the change of the net flux coupled to the conductive loops generates electro-motive forces due to the Faraday's law of induction.

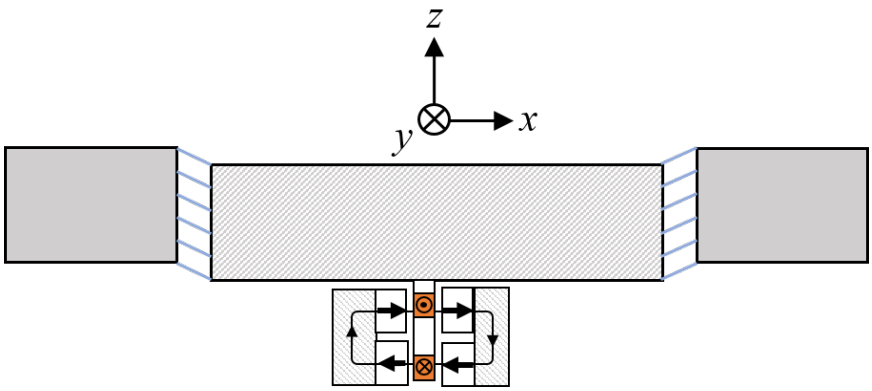

Figure 7-2: Diagram of additional passive damper design for linear stage.

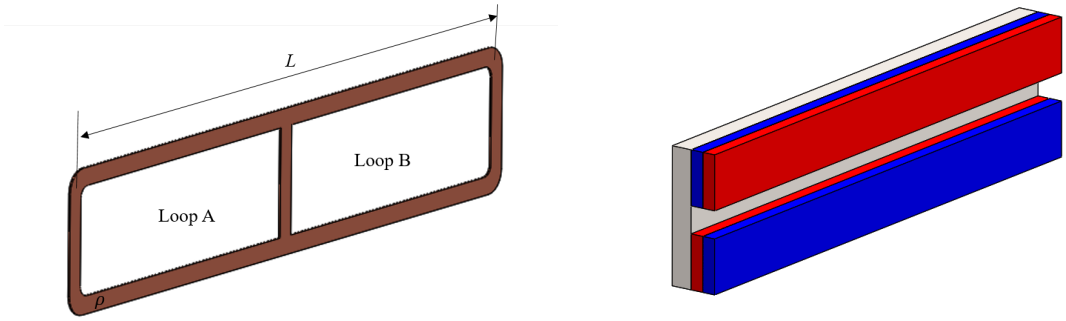

(a) (b)

Figure 7-3: CAD model of parts in the suggested additional passive damper. (a) Figure-eight-shaped conductive loop. (b) Stator rail for passive damping.

The induced currents can interact with the external field, and generates damping torque to the stage. Note that this damper design requires a relatively complicated design for the separation wall between the moving stage (including the conductor loop) and the outside stators, and therefore increases the system complexity.

Below we present a first-order calculation for the damping generation in the pitch direction using such passive damper design. Define the displacement of the stage in the pitch direction as θ_x, the flux density in the air gap between the two permanent magnet rails is B, the total length of the figure-eight-shaped conductive loop is L, the conductive loops in front and back are loop A and loop B, respectively, the resistance

of each loop is R. The the net flux variation in the loop A can be calculated by

$$\mathrm{d}\Phi_A \approx B\frac{L^2}{4}\theta_x. \tag{7.1}$$

The generated electromotive force around the conductive loop A is

$$\epsilon_A = -\frac{\mathrm{d}\Phi_A}{\mathrm{d}t} \approx -B\frac{L^2}{4}\frac{\mathrm{d}\theta_x}{\mathrm{d}t}. \tag{7.2}$$

Then the induced current around loop A is $i_A = \epsilon_A/R$. The generated restoring force on the incremental coil length $\mathrm{d}l$ is

$$\mathrm{d}f_A \approx -\frac{B^2L^2}{4R}\frac{\mathrm{d}\theta_x}{\mathrm{d}t}\mathrm{d}l. \tag{7.3}$$

The generated restoring torque in the θ_x-direction by the conductive loop A is

$$T_{xA} = 2\int_0^{L/2} l\mathrm{d}f_A = -\frac{B^2L^4}{8R}\frac{\mathrm{d}\theta_x}{\mathrm{d}t}. \tag{7.4}$$

With both conductive loops A and B, the total restoring torque in pitch mode is

$$T_x \approx -\frac{B^2L^4}{4R}\frac{\mathrm{d}\theta_x}{\mathrm{d}t}. \tag{7.5}$$

Substituting typical values $B = 1$ T, $L = 0.2$ m, $R = 0.001$ Ω, the pitch mode damping coefficient generated by this additional damper is 0.2 Nms/rad, which is five times larger than the passive damping in our current stage configuration. With such additional damper, the expected damping ratio for the moving stage in the pitch mode is 0.12. Under this condition, the pitch mode oscillations can be damped to 1% error within 0.5 s.

7.1.2 Vertical Mode Vibration

The second limitation of our linear stage prototype is due to the coupling between the common-mode attractive force generation in the linear motors and the stage's motion

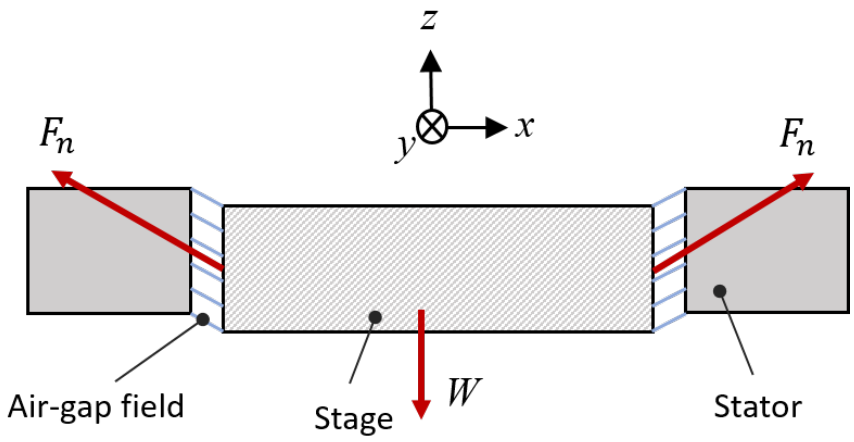

Figure 7-4: Diagram of the coupling between the linear motors' common-mode attractive force variation and the vertical-directional mode of moving stage.

in the vertical direction. Figure 7-4 illustrates such effect. As shown in Figure 7-4, the stage's weight W is balanced by the attractive forces between the stage secondaries and the stators, and the stage sags below the center of the stators for such force balance. When the motor is operating, the common-mode attractive force between the two linear motors on both sides can be position-dependent, and can vary with respect to the motors' force angle. This variation of the common-mode attractive force can excite the vertical oscillations of the moving stage, which is not acceptable for the reticle transportation device.

Below we discuss the mechanism of attractive force variation between the motor stator and the stage secondary when our linear stage is operating. The first mechanism is due to the phase change of the motor excitation with respect to the hysteresis secondary. Figure 7-5 shows the simulated thrust and attractive forces between the motor stator and the stage secondary while fixing the location of the secondary and the motor current amplitude, and sweeping the phase of the excitation. This data is simulated via the finite element model for the pre-magnetized linear hysteresis motor, which is discussed in Section 4.3. It can be seen that when thrust force is generated to the moving stage, the attractive force between the motor stator and the moving stage can vary accordingly. Here, the yellow region in Figure 7-5 shows the is the operating range for our linear hysteresis motors, as we limit the force angle ϕ_m be-

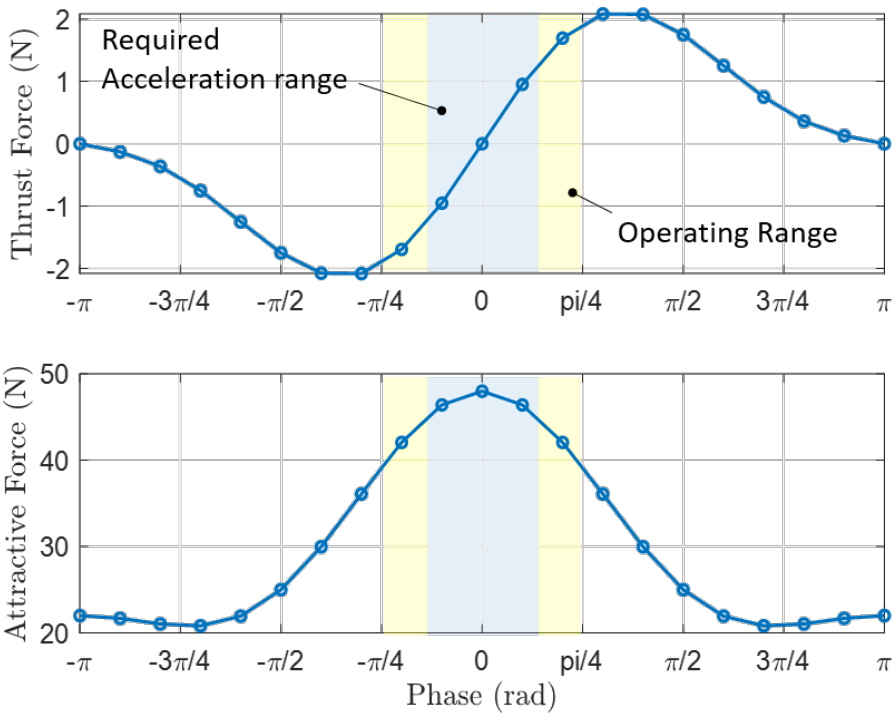

Figure 7-5: Simulated thrust and attractive force between one motor secondary and the motor stator while sweeping the motor current phase, and locking the position of the secondary. Motor current amplitude is 2 A.

tween $-\pi/4$ and $\pi/4$. The peak-to-peak attractive force variation in the full operating region is 7.6 N. The blue region in Figure 7-5 is the range when we limit the stage's acceleration within ± 500 mm/s^2, which is the acceleration requirement of the reticle transportation task. Under this condition, the peak-to-peak normal force variation is 2.8 N. This variation of the motors' common-mode attractive force happens when the stage is accelerating or decelerating.

Another source of attractive force variation is due to the cogging force in the linear hysteresis motors, which is generated by the interaction between the pre-magnetized hysteresis secondaries and the motor stator yokes. Since the hysteresis secondaries are pre-magnetized by the motor stators, their magnetization are aligned with the stator teeth and have no skew, which can generate cogging forces between the motor stator and the hysteresis secondary. Figure 7-6 shows the simulated attractive force ripple between the hysteresis secondary and the motor stator when the secondary is moved

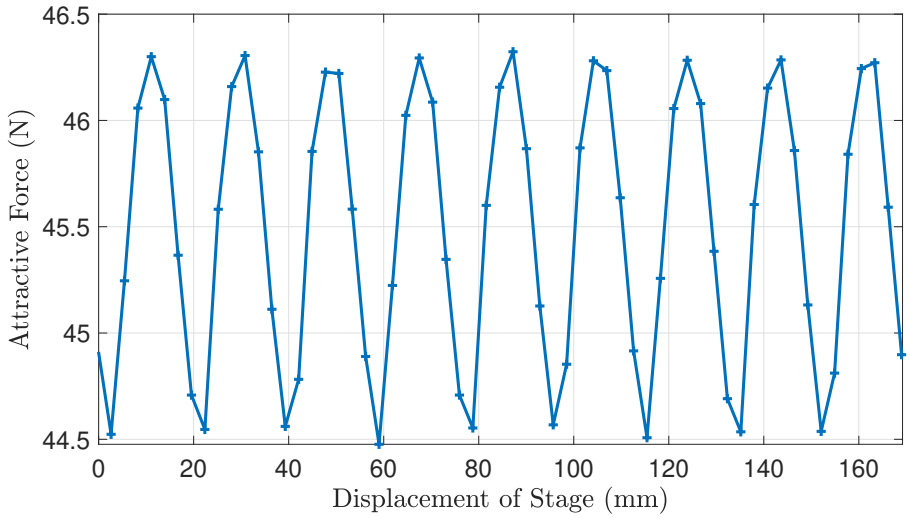

Figure 7-6: Simulated attractive force between motor secondary and motor stator as secondary is moved over one full stage length. Motor excitation is synchronous to the motor secondary.

over one full stage length, and the motor excitation is synchronous to the secondary. Here the motor current amplitude is set to 2 A, and the effect of the reluctance-force-induced force ripple is removed from the total force ripple to simulate the effect of skewed edge in the motor secondary. The simulated attractive force ripple in Figure 7-6 demonstrates a periodical pattern, and its wavelength matches with the motor stator tooth pitch. The peak-to-peak variation of this attractive force is 1.8 N. When the stage is operating, this ripple in the common-mode attractive force exists not only during the acceleration phase, but also in the constant speed phase.

Here we propose several potential solutions to the common-mode attractive force variation issue as follows:

(1) Skewed Pre-magnetization For Hysteresis Secondary

One typical method to reduce the cogging forces in permanent magnet synchronous machines is skewing. In this method, the magnet array in the secondary is skewed with one tooth-pitch of the stator. In this way, the attractive and thrust force generated by magnet-iron interaction can be averaged out as the secondary is moving relative to the stator yoke. In order to solve the attractive force variation due to the cogging effect

in the linear hysteresis motors, one can pre-magnetize the secondary in a skewed manner. This will also help reduce the position control tracking error due to the cogging force as shown in Figure 6-20, as the cogging force in both normal and shear directions can be reduced by the skewing.

(2) Feedforward Attractive Force Variation Compensation

The second method that can reduce the attractive force variation due to both phase variation and cogging effect is through feedforward cancellation. In this method, we need to model or measure the attractive force as a function of the motor current amplitude, motor current phase, and the stage's position. When the motor is operating, we vary the bias current amplitude I_{bias} and thus cancel out the normal force variation in the linear motors through a model-based feedforward method, thereby maintaining the motor's attractive force at a constant value. Prior work studied the model-based force ripple and cogging compensation for motors include [72, 73].

(3) Feedback Control for Attractive Force

In our current linear stage configuration, the attractive forces between the moving stage and the stators are not measured. If such attractive forces are measured in real-time, one potential method to reduce the attractive force variation is to feedback control the attractive force and therefore maintaining it at a constant value. In this method, load cells need to be configured in between the stators and their base to measure the reaction attractive force generated to the stator assembly. The outputs of the load cells can be used for feedback control, and we can use the bias current amplitude I_{bias} as the control effort for the attractive force regulation loop. In this method, we are able to regulate the variation for the attractive force generated by the motor, thereby reducing the vertical vibration of the stage. Note that in the linear hysteresis motors, the thrust force generation also depends on I_{bias}. As a result, the stage's position control loop and the common-mode attractive force control loop are coupled.

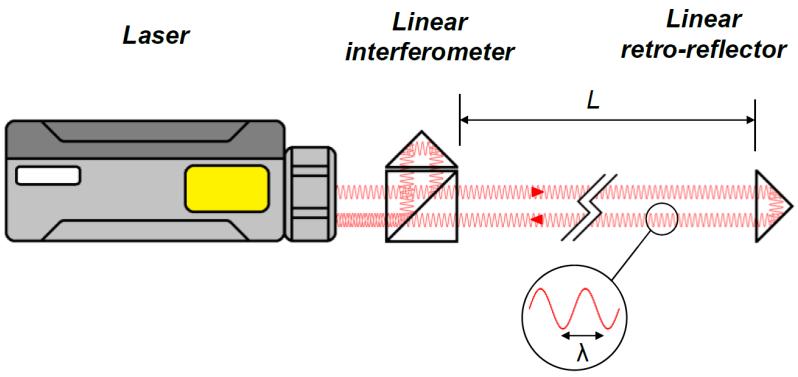

Figure 7-7: Diagram of the operating principle of laser interferometers. Figure taken from [14].

(4) Additional Steel Secondary for Normal Force Nuller

The last proposed method for the common-mode attractive force variation reduction uses an additional steel secondary. This method was initially studied in reference [74], where a steel motor forcer is added to a linear permanent magnet machine to reduce the pitch error induced by the position-dependent normal force variation in the linear motor. Future work should consider using a similar method for reducing the variation in the total normal force in linear motors.

7.1.3 Sensing System

Our linear stage prototype uses optical reflective displacement sensors for air gap measurement at different positions, and uses magnetic encoders for displacement measurement in the motion direction. Such sensing system is convenient for a proof-of-concept prototype. However, magnetic encoder scales are not compatible with the vacuum environment and cannot satisfy the contamination control requirement. In addition, the use of optical air gap sensors is challenging when a thin wall separating the stator and stage is included, since the configuration of a large number of transparent windows is difficult for such separation wall. In order to use the linear stage for reticle transportation application, different sensing system design is required. Below we discuss one possible alternative design for the sensing system.

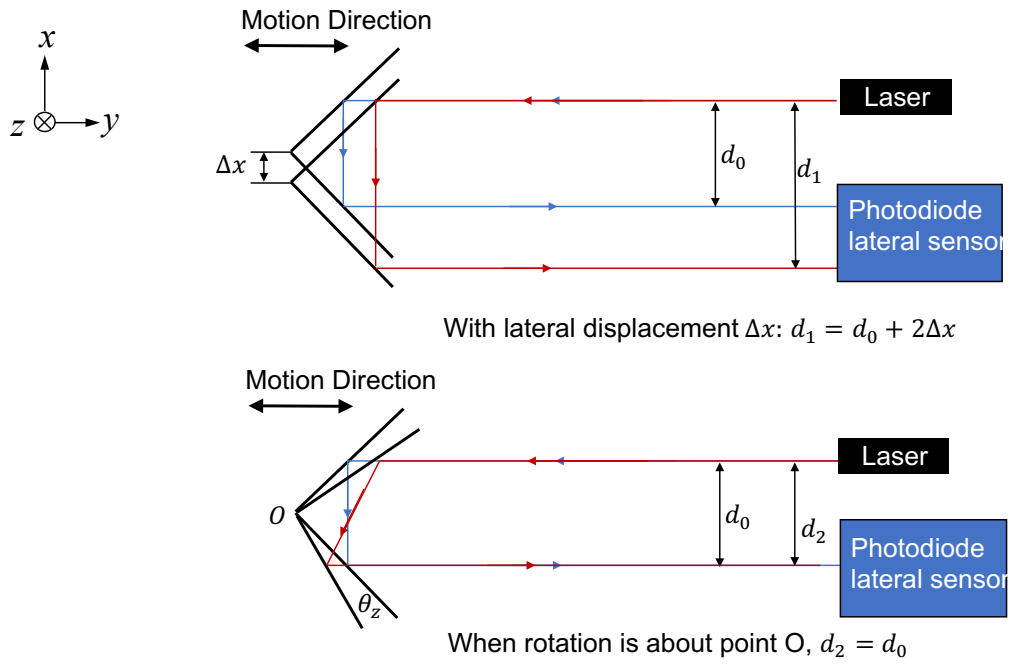

Figure 7-8: Diagram of operating principle for laser lateral displacement sensor.

To measure the stage's displacement in the motion direction, one possible alternative sensing option is to use a laser interferometer system. Figure 7-7 shows a diagram of a laser interferometer system, which is taken from [14]. Laser interferometers can measure the stage's displacement without mechanical contact. In addition, the stage is required to operate in vacuum, which is desired for interferometers since no air refractive index compensation is required. Two axis of laser interferometers can be used to also measure the stage's yaw degree of freedom motion.

For the stage's lateral displacement measurement, one possible sensor design concept is shown in Figure 7-8. Here, a reflective corner cube is configured at the center of the stage. A laser is configured to reflect twice in the corner cube, and the returning laser is detected by a photodiode lateral sensor, which measures the lateral displacement of the received laser. When the stage is having a lateral (x-directional) displacement Δx, the displacement of the reflected laser is $\Delta d = 2\Delta x$. When the stage is having a rotation about the vertical axis, the reflected laser does not move. Using such optical sensing system, no air gap sensor handling is required, which helps simplify the sensing system. The design and testings for this laser-based lateral sensor

is suggested for future work.

7.2 Alternative Stage Designs

Through designing, building, and testing for our magnetically-levitated linear stage prototype, we learned that the linear bearingless slice motor has several limitations as discussed in the previous sections. In this section, we relax the simplicity requirement for the linear stage design, and re-evaluate other linear stage design concepts based on the lessons learned in this project. These alternative stage designs inherently eliminate the aforesaid limitations of a linear bearingless slice motor, and therefore can potentially deliver improved performance for the reticle transportation application.

As presented in Chapter 3, the direct-drive linear stage design concepts can be categorized into three groups: (I) active magnetic suspension in all degrees of freedoms, (II) passive magnetic suspension in x- and θ_z-directions (lateral and yaw modes), and (III) linear bearingless slice motor design with passive magnetic suspension in z-, θ_x, and θ_y-directions (vertical, pitch and roll modes). With a relaxed requirement for system simplicity, the stage design concepts in Group I, where the stage's magnetic suspension in all degrees of freedom are actively controlled, is recommended for future efforts of reticle transportation to achieve improved performance. The reason for such recommendation is discussed as follows.

Table 7.1 shows a comparison between the three linear stage configuration groups, where the advantages and disadvantages of each group are listed. The stage designs in Group II has a relatively simple system design with two degrees of freedom passively stabilized. However, these stages typically require a moving stage with highly-permeable extruding secondaries on the wings for concentrating the flux for passive suspension, as shown in Figure 7-9. This fact can result in relatively low frequency flexible modes for the moving stage, which can hurt the the stage's magnetic suspension performance. In addition, although the passively-levitated lateral mode is not excitable by suspension control forces and thrust force in a nominal design, it may be excitable when the stage or stator has manufacturing or alignment errors. For

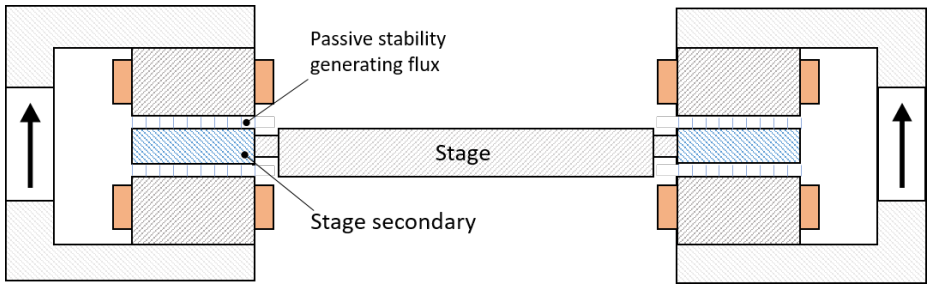

Figure 7-9: Diagram of one design concept in Group II, where the stage is passively levitated laterally. The stage requires highly permeable secondaries on the wings, which can result in stage's low frequency flexible modes.

example, if the stage secondaries are not symmetrical on the two sides, the lateral force generated by the skewing of the secondary edges may cause lateral-directional vibration. These issues of the Group II stage designs are not favored for reticle transportation in lithography applications.

Comparing with other stage configurations, Group I linear stage designs have the best magnetic suspension performance, since there is no low-stiffness and lightly-damped passive modes. In addition, it does not require additional magnetic bearings for the docking positions for the reticle transportation task, since the stage is able to provide sufficient positioning accuracy for reticle handling with active suspension control. The major drawback for the stage designs in Group I is that the system complexity is relatively high, since all degrees of freedom of the stage require actuation and sensing. However such system complexity may be accepted with for performance improvement.

Below we discuss two stage design concepts in Group I that are promising for the reticle transportation application. These design concepts were first presented in Chapter 3. Here we re-discuss the operating principles for these linear stage design concepts, and present implementation suggestions of these stage design concepts for the reticle transportation application.

Figure 7-10 shows a magnetically-levitated linear stage design concept where the stage is actively levitated in all degrees of freedom, which is first shown in Figure 3-7 in Chapter 3. The secondaries of the linear motors are configured on the wings of the moving stage, and its surfaces are at an angle θ with respect to the horizontal

Table 7.1: Comparison between stage design concept groups in advantages and disadvantages.

Stage Design Concepts	Main features
Group I: All-DOF actively controlled	+ Best performance in accuracy and vibration suppression; + No additional docking magnetic bearings required; − Relatively high system complexity: more sensors and actuators are required.
Group II: Passive: x- and θ_z-DOFs. Active: z-, θ_x-, and θ_y-DOFs.	+ Relatively high performance in vibration suppression; thrust force does not excite passive DOFs; + Relatively simple system design: no sensing/actuation in passive-DOFs required; − Lateral forces caused by manufacturing error may excite the stage's passive DOF; − Typically require stage with highly-permeable extrusions on two sides, which leads to bad stage structural dynamics.
Group III: Passive: z-, θ_x-, and θ_y-DOFs. Active: x- and θ_z-DOFs.	+ Simplest system design: only three DOFs requires sensing/actuation; + Simple stage design and allows good stage structural dynamics. − Passive pitch mode excitable by thrust force; − Passive vertical mode excitable by common-mode attractive force variation.

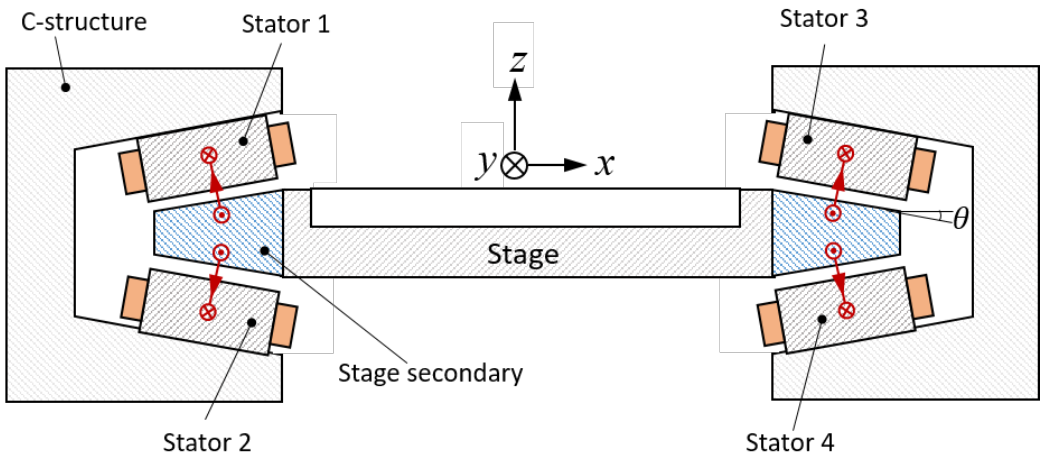

Figure 7-10: Design concept for magnetically-levitated linear stage with stage's all degrees of freedom actively controlled. Four motor stators with each coil separately driven are used. The stage's secondary has surface at an angle θ with respect to the horizontal direction.

plane. Four stators are configured around the moving stage and interfacing with the secondaries. Among the two stator winding pattterns shown in Figure 3-8 and 3-9 in Chapter 3, we recommend to use the lumped winding with each coil driven independently, as shown in Figure 3-8. This winding pattern is suggested for the following two reasons. First, this winding is flexible in controlling the normal attractive force to the stage at different positions along the motor, which can provide better suspension control performance since disturbance torque generation in the other winding is eliminated. Second, when the stage's travel range is large, the motor stators should be driven in sections to avoid stator power consumption in the range that is not interfacing with the stage. Driving each coil independently naturally allows such sectioning design for the stators. In addition, in the design for the power electronics for this linear stage, switches can be designed to allow the power electronics being handled from one section of the motor windings to another when the stage is moving. In this way, the number of power electronics being used can be effectively reduced.

Figure 7-11 shows a diagram of the normal-directional suspension forces on the moving stage in the design concept shown in Figure 7-10. The total suspension

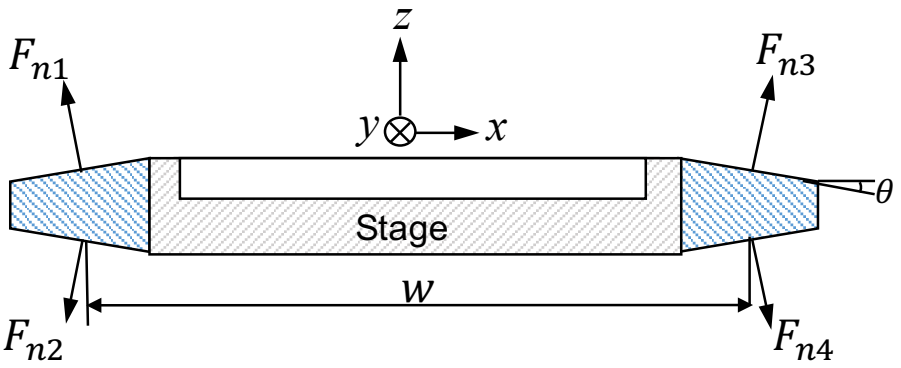

Figure 7-11: Diagram of normal suspension control forces on the moving stage.

controlling forces and torques on the stage are

$$\Sigma F_x = (F_{n3} + F_{n4} - F_{n1} - F_{n2}) \sin\theta, \tag{7.6}$$

$$\Sigma F_z = (F_{n1} + F_{n3} - F_{n2} - F_{n4}) \cos\theta, \tag{7.7}$$

$$\Sigma T_y = \frac{w}{2} \cos\theta (F_{n1} + F_{n4} - F_{n2} - F_{n3}), \tag{7.8}$$

where w is the distance between the forces acting point on two sides of the stage, and θ is the angle between the secondary's surface and the horizontal plane, as shown in Figure 7-11. Through equations (7.6) to (7.8) it can be seen that the angle θ is an important design parameter. The height constraint for the system favors a small angle θ, while the lateral force generation capability favors an angle θ close to 45°. Trade off between packaging and suspension force generation capability should be considered in the detailed design for this linear stage.

Figure 7-12 shows another suggested linear stage design concept, which was first introduced in Chapter 3. The four motor stators use regular three-phase windings. The motor fluxes are shown with the red arrows in Figure 7-12. In addition, two rows of E-shaped magnetic bearings are configured on the two sides of the moving stage, as shown in Figure 3-11. Each magnetic bearing has two coils, and the current in each coil is independently controlled. The common-code current in the two coils in one magnetic bearing generates lateral control flux, as shown by the blue flux lines in Figure 3-11. This flux generates normal force on the left and right edges of the moving

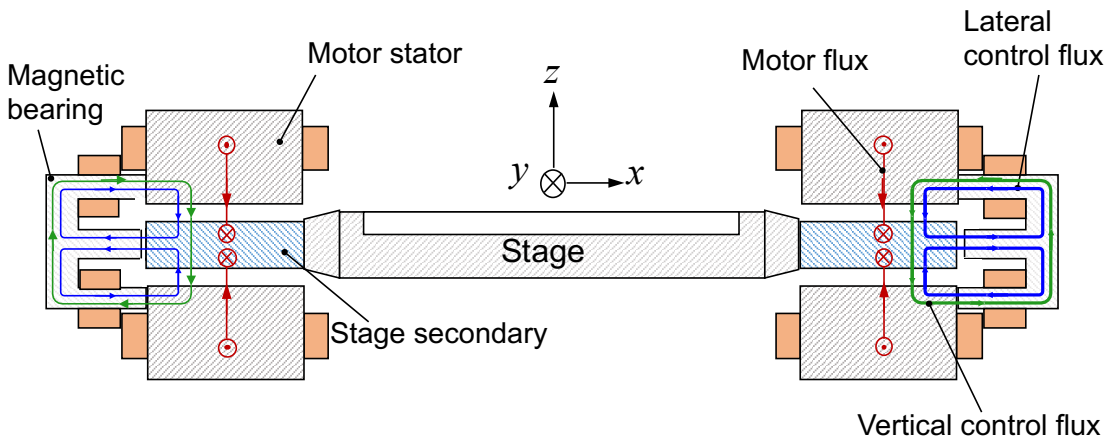

Figure 7-12: Design concept for magnetically-levitated linear stage with stage's all degrees of freedom actively controlled. Four motor stators using three-phase connected windings are used. Additional E-shaped magnetic bearings are used for the magnetic suspension.

stage, which can control the x-directional suspension of the moving stage. With at least two magnetic bearings configured along the moving stage, the yaw degree of freedom can be controlled. The differential current of the two coils in one magnetic bearing generates vertical control flux, as shown by the green flux lines in Figure 3-11. This flux steers the motor flux and vertical control flux to generate vertical control force on the moving stage. With multiple E-shaped magnetic bearings interfacing with the moving stage simultaneously, the stage's suspension in θ_x-direction can also be actively controlled. As a result, this stage configuration is able to actively control all degrees of freedom of the moving stage.

This stage design uses connected three-phase windings for thrust force generation, which reduces the number of phases independently driven compared with the design in Figure 7-10. This stage design also allow a simple control design, since the suspension force in different degrees of freedom can be generated independently and thus allow a decoupled control design. The major drawback of this linear stage design is that it uses motor flux as the bias flux. Therefore the motor current cannot be turned off even when no thrust force is needed. When power consumption on the stator side can be relaxed, this linear stage design concept presents a relatively simple stage design yet delivers good performance.

7.3 Summary

In this chapter, we discussed the limitations of our current magnetically-levitated linear stage prototype, including: (1) stage's pitch mode is excitable by thrust force, (2) stage's vertical mode is excitable by motors' common-mode attractive force, and (3) sensing system is not vacuum compatible. Potential solutions for these limitations are presented. In addition, we presented two suggested alternative linear stage design concepts which solve the aforesaid limitations inherently, and can potentially provide improved performance for the reticle transportation application in photolithography machines. The design for these linear stages are suggested for future work.

Chapter 8

Conclusions and Future Work

8.1 Conclusions

This thesis presents the design, construction, control, and testing for a new types of magnetically-levitated linear stage driven by linear hysteresis motors. The elimination of permanent magnets from the moving stage allows the stage to be vacuum compatible without encapsulation, which is advantages for the in-vacuum transportation application. The magnetic suspension of the stage is achieved using a novel linear bearingless slice motor design, where the stage's magnetic suspension in three degrees of freedom, including vertical, pitch, and roll, are passive. This compact design effectively reduces the number of sensors and actuators being used. The prototype system has successfully levitated the moving stage, and has demonstrated the required acceleration and position control capability. The limitations of our linear stage prototype are discussed, and alternative linear stage concepts that can potentially deliver improved performance are suggested for future design efforts.

8.1.1 Summary of Contributions

Below is the list of primary contributions of the thesis.

1. Developed an equivalent circuit model for hysteresis motors' transient-time dynamics (Chapter 2).

2. Proposed three methods for estimating the rotor's magnetization orientation in a hysteresis motor, including the mechanical angle method, back-electromotive force method, and the full-order observer method (Chapter 2).

3. Proposed a position control method for hysteresis motors based on field-oriented control, and tested the proposed control method with three different rotary hysteresis motors (Chapter 2). All three motors have demonstrated a position control bandwidth of more than 100 Hz. To our knowledge, this is the first work that enabled the high-bandwidth torque and position control for hysteresis motors.

4. Designed a novel magnetically-levitated linear stage using a linear bearingless slice motor configuration, where the stage's magnetic suspension in three degrees of freedom are passively stabilized. The linear stage's motion is driven by linear hysteresis motors. To our knowledge, this is the first linear bearingless slice motor design and the first work on linear hysteresis motor reported in literature (Chapter 3 and 4).

5. Developed a first-order analytical model for the active magnetic suspension control forces and torques in the our magnetically-levitated linear stage (Chapter 4).

6. Developed a finite-element-method-based model for pre-magnetized linear hysteresis motors by modeling the magnetized hysteresis secondary as an array of permanent magnets, and the magnets' material property is determined by the pre-magnetization process (Chapter 4). The model is validated by experimental measurements in our linear stage prototype (Chapter 6).

7. Designed and built a magnetically-levitated linear stage prototype driven by linear hysteresis motors (Chapter 5). Experimentally characterized the suspension and motion performance of the linear stage prototype (Chapter 6). Our linear stage prototype has successfully levitated the moving stage. The resonance frequency of the passively levitated degrees of freedom is approximately 10 Hz,

and the suspension bandwidth of the actively-controlled degrees of freedom is about 60 Hz. The stage's maximum thrust force is 5.8 N under a 2.5 A current amplitude, which corresponds to a stage acceleration of 1200 m/s^2. This is able to satisfy the acceleration requirement for reticle transportation task. The stage was tested to track a reticle handling reference trajectory, where the maximum position tracking error of our linear stage is 50 μm. The stage's lateral displacements during motion is below 50 μm, which is well below making mechanical contact to the side walls.

8. Discussed the limitations in our linear stage prototype including pitch mode coupling, vertical mode vibration, and the sensing system limitation, and proposed possible methods that can potentially solve these issues (Chapter 7). Discussed alternative stage design concepts that can eliminate these limitations and potentially can provide improved performance (Chapter 7).

8.1.2 Typical Specifications for Hysteresis Motors

As a part of the conclusion of this thesis work, we would like to summarize the typical hysteresis motor specifications based on the knowledge learned in this thesis project. This summary is targeting at providing a reference for selecting hysteresis motors for general use.

Hysteresis motor's torque can be calculated by [76]:

$$T_h = \frac{V_r}{2\pi} p A_h, \tag{8.1}$$

where V_r is the magnetically-involved volume of the hysteresis rotor, p is the number of pole pairs, and A_h is the area of the hysteresis loop that the rotor material is operating at, which can be calculated by $A_h = \oint B_h \mathrm{d}H_h$, where $B_h = f_h(H_h)$ is the material's hysteresis loop. The hysteresis motor encompass a large family of rotor materials and their performance can vary. Table 8.1 presents the typical hysteresis torque generation per unit rotor volume for motor with one pole pair for several hysteresis materials. In this table, the hysteresis property data for the first three materials are

Table 8.1: Hysteresis motor specifications for typical rotor materials.

Rotor Material	T_h/V_r for $p = 1$	Curie Temp.	Tensile Strength
Unhardened D2 steel	806 N/m^2	770 °C	1500 MPa
Hardened D2 steel	2.8×10^3 N/m^2	840 °C	2200 MPa
CROVAC 12	6.0×10^3 N/m^2	640 °C	620 MPa
AlNiCo II	1.0×10^4 N/m^2	820 °C	37 MPa
AlNiCo V	1.3×10^4 N/m^2	860 °C	21 MPa

measured within this thesis work, and the property of the AlNiCo magnets are taken from reference [32]. Note that here the torque generation due to the eddy current effect in the motors are not considered, that is, the values listed in Table 8.1 are the maximum rotor torque density the motors in synchronous operation. Also, it is worth mentioning that for a hysteresis motor, the required ampere-turns increases as the rotor material's hysteresis gets larger. Typically a hysteresis motor uses a ring-shaped hysteresis material for the rotor to fully utilize the hysteresis material, since the magnetic flux's penetration depth may be limited. Usually the larger the rotor material's hysteresis, the thinner the rotor thickness. Off-the-shelf hysteresis motors typically use rotor materials made of FeCrCo alloy or AlNiCo magnets, and the rotor ring thickness is typically below 5 mm.

Table 8.1 also shows the curie temperature and tensile strength for the listed rotor materials. For comparison, the Curie temperature and strength of Neodymium magnets are 320 °C and 75 MPa, respectively. It can be seen that all hysteresis materials listed in Table 8.1 have a larger operating temperature range than the Neodymium permanent magnets, and the first three hysteresis materials have significantly higher strength than the Neodymium magnets. These properties of the hysteresis motors allow them being used for high temperature circumstances, and some rotor materials can relieve the speed limit of motors from the rotor strength, and suitable for ultra high speed machines.

The efficiency of hysteresis motors in synchronous and asynchronous operations need to be discussed separately. When a hysteresis motor is operating in synchronous,

the fundamental harmonic magnetic excitation does not generate rotor loss since the magnetization status of the rotor material is fixed. Under this condition, the motor's efficiency can reach above 90% for a well designed hysteresis motor. When a hysteresis motor is operating asynchronously, the motor's efficiency drops due to the rotor's hysteresis and eddy current losses. When in asynchronous, the efficiency of a hysteresis motor is typically around 50% at the rated speed [36].

8.2 Future Work

The suggested future works are listed as follows.

8.2.1 Broader Application for Hysteresis Motors

The hysteresis motors are known for simple construction, small rotor imbalance, and high rotor strength and thermal robustness, which is attractive for special drives such as ultra-high-speed motors, high-temperature motors, and in-vacuum drives. Potential applications include high-speed spindles for precision machining, high-speed drills and centrifuges for oil and gas industry, high-temperature steam turbines, and turbochargers for combustion engines. When equipped with high-bandwidth torque and position control capability as studied in Chapter 2, hysteresis motors have great potential to be used in reaction wheels and gyroscopes, where both high speed and high control bandwidth are required. Future work should consider the usage of hysteresis motors for a broader application areas. We summarize the typical performance for hysteresis motors with different rotor materials in the conclusion of this thesis.

8.2.2 Speed Sensorless Control for Hysteresis Motors

In Chapter 2 of this thesis, we studied the field-oriented control for hysteresis motors with the motor's speed/position measured with an encoder. However, typically the encoder cannot operate in harsh environments such as high temperature or humid conditions, which limits the usage of the motors. In addition, the elimination of the

sensor can reduce the cost for the drives. The speed sensorless control for other kinds of motors, including permanent magnet synchronous machines, induction machines, and variable reluctance machines, have been extensively studied. However, to our knowledge, there is no reported work studying the sensorless control for hysteresis motors. Future work can study the speed estimator for hysteresis motors, which can enable the sensorless torque and speed control for these machines, and allow them to be used in a broader application areas.

8.2.3 Optimal Magnetic Design for Linear Bearignless Slice Motors

The magnetically-levitated linear stage prototype presented in this thesis is sufficient to proof the design, however, the prototype is not optimized to demonstrate the best performance. Potential improvement to the linear stage design include: (1) Optimize the structural design for the moving stage to minimize its inertia while satisfying structural and motor requirement, for example using thinner hysteresis secondary and use alternative stage base material with improved stiffness-to-weight ratio. This can increase the natural frequency of the passive magnetic suspension, and also improve the acceleration capability. (2) Optimize the permanent magnet bias flux path design to improve the ratio between the passive stiffness and negative stiffness.

8.2.4 Passive Damping Improvement

One of the major limitation for our current linear stage prototype is the lack of damping in the passively-levitated degrees of freedoms. This issue is especially problematic for the vertical and pitch mode, since these modes can be excited when the stage is operating, as described in Chapter 7. Future work should consider improving the damping of the stage in these degrees of freedom. One possible design of passive damper is presented in Figure 7-2 and Figure 7-3, which uses eddy-current damping in a short-circuited conductive loop interacting with permanent magnet in the rails for damping generation. Another potential method is to apply active damp-

ing for passively-levitated degrees of freedom, which is studied in recent work [75]. In this work, the target is magnetically-levitated in the vertical direction with top and bottom electromagnets. The differential current in top and bottom actuator is controlling the target's suspension in the vertical direction, and the common-mode current is depending on the horizontal velocity of the target, thereby providing active damping to the target in the lateral directions. Future work can consider applying such method for linear bearingless slice motors for damping improvement.

8.2.5 Common-mode Attractive Force Regulation for Linear Motors

As discussed in Section 7.1.2 in Chapter 7, another limitation for linear bearignless slice motors is the stage may oscillate vertically due to the variation of the common-mode attractive force of the two linear motors. This is undesirable for linear stage transportation stages for precision manufacturing applications. Possible methods to solve this issue are discussed in Section 7.1.2, including: (1) skewing the magnetization in the motor secondaries, (2) feedforward compensation for the attractive force variation, and (3) feedback control for the motor's attractive force.

8.2.6 Alternative Sensing System

The sensing system in our prototype system, including optical air gap sensors and magnetic encoders, are not compatible with the vacuum and the particle-free environment. Future work should investigate alternative sensing systems that is compatible with the vacuum and clean environment, thereby suitable for the transportation application for semiconductor manufacturing. Possible alternative sensors include laser interferometers and laser-based lateral sensor, are discussed in Section 7.1.3 in Chapter 7.

8.2.7 Alternative Magnetically-Levitated Linear Stage Configurations

Aside from the linear bearingless slice motor based stage design, some alternative linear stage designs can realize the magnetic suspension and motion requirement, and may demonstrate improved performance for the reticle transportation application. Several possible alternative linear stage design concepts are discussed in Section 7.2 in Chapter 7. Future work should consider the design, prototyping, and testing for these alternative stage configurations.

Bibliography

[1] Wisnu Aribowo and Kazuhiko Terashima. Cubic spline trajectory planning and vibration suppression of semiconductor wafer transfer robot arm. *IJAT*, 8(2):265–274, 2014.

[2] John W Totsch. Magnetic conveyor system for transporting wafers, February 21 1989. US Patent 4,805,761.

[3] Martin Hosek. Wafer transport system, May 12 2015. US Patent 9,027,739.

[4] David Belna. Linear induction semiconductor wafer transportation apparatus, November 25 1986. US Patent 4,624,617.

[5] Won-jong Kim and David L Trumper. High-precision magnetic levitation stage for photolithography. *Precision Engineering*, 22(2):66–77, 1998.

[6] Xiaodong Lu et al. 6d direct-drive technology for planar motion stages. *CIRP annals*, 61(1):359–362, 2012.

[7] JW Jansen, CMM Van Lierop, Elena A Lomonova, and AJA Vandenput. Modeling of magnetically levitated planar actuators with moving magnets. *IEEE Transactions on Magnetics*, 43(1):15–25, 2007.

[8] Toshiro Higuchi. Linear stepping motor, August 23 1988. US Patent 4,766,358.

[9] Bruce A Sawyer. Magnetic positioning device, April 2 1968. US Patent 3,376,578.

[10] Kwang Suk Jung and Sang Heon Lee. Contact-free planar stage using linear induction principle. *Mechatronics*, 20(4):518–526, 2010.

[11] S Miyairi and T Kataoka. Analysis of hysteresis motors considering eddy current effect. *Electrical Engineering in Japan*, 86(6):67, 1966.

[12] Gerald Jungmayr. *Der magnetisch gelagerte Lüfter*. PhD thesis, JKU, 2008.

[13] Renato Galluzzi, Nicola Amati, and Andrea Tonoli. Modeling, design and validation of magnetic hysteresis motors. *IEEE Transactions on Industrial Electronics*, 2019.

[14] MAV Chapman. Environmental compensation of linear laser interferometer readings. *Renishaw Technical white paper, TE329*, 2013.

[15] Hans Butler. Position control in lithographic equipment. *IEEE Control Systems Magazine*, 31(5):28–47, 2011.

[16] Christian Wagner and Noreen Harned. Euv lithography: Lithography gets extreme. *Nature Photonics*, 4(1):24, 2010.

[17] Sang-Ho Nam and Hee-Jung Moon. Wafer transport robot arm for transporting a semiconductor wafer, June 16 1998. US Patent 5,765,889.

[18] Ivo Raaijmakers, Loren Jacobs, Mike Halpin, Jim Alexander, Ken O'Neill, and Dennis Lee Goodwin. Substrate transfer system for semiconductor processing equipment, May 30 2000. US Patent 6,068,441.

[19] Wayne J Schmidt and Thomas H Oberlitner. Robots for microelectronic workpiece handling, November 20 2001. US Patent 6,318,951.

[20] Glenn M Friedman, Peter Kochersperger, and Joseph Laganza. Apparatus for transferring and loading a reticle with a robotic reticle end-effector, February 28 2006. US Patent 7,004,715.

[21] Peter van der Meulen, Christopher C Kiley, Patrick D Pannese, Raymond S Ritter, and Thomas A Schaefer. Semiconductor wafer handling and transport, June 12 2012. US Patent 8,197,177.

[22] Wendell T Blonigan and John M White. Substrate transfer shuttle having a magnetic drive, October 29 2002. US Patent 6,471,459.

[23] Arnold Kholodenko, Anwar Husain, and George Khait. Wafer carrier drive apparatus and method for operating the same, September 11 2012. US Patent 8,261,905.

[24] H Yamakawa, I Moriyama, Y Minamigawa, Y Maeba, T Takematsu, M Nishitsuji, O Fujiki, T Asaishi, and T Koike. Contamination-free transfer of silicon wafers with a magnetic levitation transport system in vacuum. *Vacuum*, 41(7-9):1843–1845, 1990.

[25] Yoshitaka Katagiri. Vacuum processing apparatus and transportation system thereof, February 11 1992. US Patent 5,086,729.

[26] Teruo Azukizawa, Mimpei Morishita, Shuji Kanda, NOBORU Tamura, and TOYOHIKO Yokoyama. A linear induction motor control system for magnetically levitated carrier system. *IEEE Transactions on Vehicular Technology*, 38(2):102–108, 1989.

[27] Motoharu Ono, Shunsaku Koga, and Hisao Ohtsuki. Japan's superconducting maglev train. *IEEE Instrumentation & Measurement Magazine*, 5(1):9–15, 2002.

[28] Kazuo Sawada. Outlook of the superconducting maglev. *Proceedings of the IEEE*, 97(11):1881–1885, 2009.

[29] Jung Soo Choi and Yoon Su Baek. Magnetically-levitated steel-plate conveyance system using electromagnets and a linear induction motor. *IEEE Transactions on Magnetics*, 44(11):4171–4174, 2008.

[30] Lei Zhou, Wolfgang Gruber, and David Lippincott Trumper. Position control for hysteresis motors: Transient-time model and field-oriented control. *IEEE Transactions on Industry Applications*, 54(4):3197–3207, 2018.

[31] Benjamin Richard Teare. Theory of hysteresis-motor torque. *Electrical Engineering*, 59(12):907–912, 1940.

[32] Herbert C Roters. The hysteresis motor-advances whick permit economical fractional horsepower ratings. *Trans. of the American Institute of Electrical Engineers*, 66(1):1419–1430, 1947.

[33] Reza Nasiri-Zarandi, Mojtaba Mirsalim, and Alberto Tenconi. A novel hybrid hysteresis motor with combined radial and axial flux rotors. *IEEE Trans. on Industrial Electronics*, 63(3):1684–1693, 2016.

[34] Minkyun Noh, Wolfgang Gruber, and David L Trumper. Hysteresis bearingless slice motors with homopolar flux-biasing. *IEEE/ASME Trans. on Mechatronics*, 22(5):2308–2318, 2017.

[35] MA Copeland and GR Slemon. An analysis of the hysteresis motor i-analysis of the idealized machine. *IEEE Trans. on Power Apparatus and Systems*, 82(65):34–42, 1963.

[36] Mohammad Imani Nejad. *Self-bearing motor design & control.* PhD thesis, Mechanical Engineering, Massachusetts Institute of Technology, 2013.

[37] Ahmad Darabi, Hamed Tahanian, Shayan Amani, and Mohammadreza Sedghi. An experimental comparison of disc-type hysteresis motors with slotless magnetic stator core. *IEEE Trans. on Industrial Electronics*, 64(6):4642–4652, 2017.

[38] KR Rajagopal. Design of a compact hysteresis motor used in a gyroscope. *IEEE Trans. on Magnetics*, 39(5):3013–3015, 2003.

[39] Lei Zhou, Mohammad Imani Nejad, and David L Trumper. One-axis hysteresis motor driven magnetically suspended reaction sphere. *Mechatronics*, 42:69–80, 2017.

[40] Mohammad Zare and Abolfazl Halvaei Niasar. A novel sensorless vector control of high-speed hysteresis motor drive. *Journal of Power Electronics & Power Systems*, 2(3):1–7, 2013.

[41] D O'Kelly. Eddy-current and hysteresis effects in rotating machines. *Proceedings of the Institution of Electrical Engineers*, 116(3):391–394, 1969.

[42] M Azizur Rahman. Analytical models for polyphase hysteresis motor. *IEEE Trans. on Power Apparatus and Systems*, (1):237–242, 1973.

[43] D O'Kelly. Theory and performance of solid-rotor induction and hysteresis machines. In *Proceedings of the Institution of Electrical Engineers*, volume 123, pages 421–428. IET, 1976.

[44] S Miyairi and T Kataoka. A basic equivalent circuit of the hysteresis motor. *Elect. Engng. Japan (USA)*, 85:41–50, 1965.

[45] T Kataoka. Unified analysis of solid rotor induction and hysteresis motors. *Electrical Engineering in Japan*, 95(3):60–67, 1975.

[46] SM Mirimani, ABOLFAZL Vahedi, MOHAMMAD REZA Ghazanchaei, and AMIR Baktash. Electromagnetic analysis of hysteresis synchronous motor based on complex permeability concept. *Iranian Journal of Electrical and Electronic Engineering*, 9(2):88–93, 2013.

[47] Reza Nasiri-Zarandi and Mojtaba Mirsalim. Finite-element analysis of an axial flux hysteresis motor based on a complex permeability concept considering the saturation of the hysteresis loop. *IEEE Trans. on Industry Applications*, 52(2):1390–1397, 2016.

[48] SF Rabbi, Matthew P Halloran, Tyler LeDrew, Alex Matchem, and Md Azizur Rahman. Modeling and v/f control of a hysteresis interior permanent-magnet motor. *IEEE Trans. on Industry Applications*, 52(2):1891–1901, 2016.

[49] Hong-Kyu Kim, Hyun-Kyo Jung, and Sun-Ki Hong. Finite element analysis of hysteresis motor using the vector magnetization-dependent model. *IEEE Trans. on magnetics*, 34(5):3495–3498, 1998.

[50] Thomas A Lipo. *Vector control and dynamics of AC drives*, volume 41. Oxford university press, 1996.

[51] Riccardo Marino, Patrizio Tomei, and Cristiano M Verrelli. *Induction motor control design*. Springer Science & Business Media, 2010.

[52] T Kataoka, T Ishikawa, and T Takahashi. Analysis of a hysteresis motor with overexcitation. *IEEE Trans. on Magnetics*, 18(6):1731–1733, 1982.

[53] D Andessner, R Kobler, J Passenbrunner, and W Amrhein. Measurement of the magnetic characteristics of soft magnetic materials with the use of an iterative learning control algorithm. In *2011 IEEE Vehicle Power and Propulsion Conference*, pages 1–6, 2011.

[54] Cang Kim Truong. *Analysis of Hunting in Synchronous Hysteresis Motor*. PhD thesis, Massachusetts Institute of Technology, 2004.

[55] Jun Young Yoon and David L Trumper. Friction modeling, identification, and compensation based on friction hysteresis and dahl resonance. *Mechatronics*, 24(6):734–741, 2014.

[56] Reto Schoeb and Natale Barletta. Principle and application of a bearingless slice motor. *JSME International Journal Series C Mechanical Systems, Machine Elements and Manufacturing*, 40(4):593–598, 1997.

[57] Jiro Kuroki, Tadahiko Shinshi, Lichuan Li, and Akira Shimokohbe. Miniaturization of a one-axis-controlled magnetic bearing. *Precision Engineering*, 29(2):208–218, 2005.

[58] Quang Dich Nguyen and Satoshi Ueno. Modeling and control of salient-pole permanent magnet axial-gap self-bearing motor. *IEEE/AsmE Transactions on mechatronics*, 16(3):518–526, 2011.

[59] Hiroya Sugimoto, Seiyu Tanaka, Akira Chiba, and Junichi Asama. Principle of a novel single-drive bearingless motor with cylindrical radial gap. *IEEE Transactions on Industry Applications*, 51(5):3696–3706, 2015.

[60] Theeraphong Srichiangsa, Hiroya Sugimoto, and Akira Chiba. Torque density improvement of a one axis actively positioned single-drive bearingless motor. In *2018 IEEE Energy Conversion Congress and Exposition (ECCE)*, pages 6908–6913. IEEE, 2018.

[61] Junichi Asama, Yuki Hamasaki, Takaaki Oiwa, and Akira Chiba. Proposal and analysis of a novel single-drive bearingless motor. *IEEE Transactions on Industrial Electronics*, 60(1):129–138, 2013.

[62] David Trumper, Lei Zhou, and Ruvinda Gunawardana. Transportation system having a magnetically levitated linear stage, November 22 2018. PCT/US2018/033662.

[63] Akira Chiba, Tadashi Fukao, Osamu Ichikawa, Masahide Oshima, Masatugu Takemoto, and David G Dorrell. *Magnetic bearings and bearingless drives*. Elsevier, 2005.

[64] Leon E Weisbord and Francis W Wessbecher. Hysteresis synchronous motor utilizing polarized rotor, February 21 1984. US Patent 4,433,260.

[65] Arthur Eugene Fitzgerald, Charles Kingsley, Stephen D Umans, and B James. *Electric machinery*, volume 5. McGraw-Hill New York, 2003.

[66] Marco Cossale, Martin Kitzberger, Gereon Goldbeck, Gerd Bramerdorfer, Dietmar Andessner, and Wolfgang Amrhein. Investigation and modeling of local degradation in soft magnetic materials. In *2018 IEEE Energy Conversion Congress and Exposition (ECCE)*, pages 5365–5370. IEEE, 2018.

[67] David Meeker. Finite element method magnetics. *FEMM*, 4:32, 2010.

[68] Ekkes Bruck. *Handbook of Magnetic Materials*, volume 26. Elsevier, 2017.

[69] Jun Young Yoon. *Linear iron-core permanent magnet motor with high force and low acoustic noise*. PhD thesis, Massachusetts Institute of Technology, 2017.

[70] Tyler Hamer. Dynamic signal analyzer using labview, 2019. https://github.com/TyHammer125/Dynamic-Signal-Analyzer.

[71] R Munnig Schmidt, Georg Schitter, and Adrian Rankers. *The Design of High Performance Mechatronics-: High-Tech Functionality by Multidisciplinary System Integration*. Ios Press, 2014.

[72] Christof Rohrig and Andreas Jochheim. Identification and compensation of force ripple in linear permanent magnet motors. In *Proceedings of the 2001 American Control Conference.(Cat. No. 01CH37148)*, volume 3, pages 2161–2166. IEEE, 2001.

[73] Hai-Hua Mu, Yun-Fei Zhou, Xin Wen, and Yan-Hong Zhou. Calibration and compensation of cogging effect in a permanent magnet linear motor. *Mechatronics*, 19(4):577–585, 2009.

[74] Gerald Rothenhöfer and Alexander Slocum. Reducing pitch error of a linear motion system actuated by a permanent magnet open face linear motor. *Precision engineering*, 33(3):305–309, 2009.

[75] Asief Javeda, Takeshi Mizuno, Masaya Takasaki, Yuji Ishino, and Daisuke Yamaguchi. Variable stiffness approach to reduce vibration induced in passively-supported directions of an active magnetic suspension system. In *Proceedings of 16th International Symposium on Magnetic Bearings*, pages 1–4, 2018.

[76] Benjamin Richard Teare. Theory of hysteresis-motor torque. *Electrical Engineering*, 59(12):907–912, 1940.